New Developments in ^{1}H NMR-linked Metabolomics: Identification of New Biomarkers for the Metabolomic Classification of Niemann-Pick Disease, Type C1, and its Response to Treatment

Victor Ruiz-Rodado

Leicester, 2016

New Developments in ^{1}H NMR-linked Metabolomics: Identification of New Biomarkers for the Metabolomic Classification of Niemann-Pick Disease, Type C1, and its Response to Treatment

By

Victor Ruiz-Rodado

A thesis submitted in fulfilment of the requirements for the degree of Doctor of Philosophy at Leicester School of Pharmacy (De Montfort University).

1st Supervisor

Prof. Martin Grootveld (Leicester School of Pharmacy, De Montfort University)

2nd Supervisors

Dr. Cristobal J. Carmona (Languages and Computer Science, Department of Civil Engineering, University of Burgos, Burgos, Spain)

Dr. Daniel J. Sillence (Leicester School of Pharmacy, De Montfort University)

Dr. David Elizondo (School of Computer Science and Informatics, De Montfort University)

Prof. Frances M. Platt (Department of Pharmacology, University of Oxford)

This PhD research work was sponsored by De Montfort University (Leicester, UK) and Hope Against Cancer (Leicester, UK).

Leicester, 2016

CONTENTS

AKNOWLEDGEMENTS

Firstly, I would like to thank Prof. Martin Grootveld for giving me the opportunity of starting a career in Research, for his supervision throughout this work and for his help, not only in Research matters but also providing his support with personal issues, together with his wife, Kerry.

I would also like to thank the rest of my supervisory team, namely Dr. David Elizondo, Dr. Dan Sillence, and specially Prof. Fran M. Platt, for kindly hosting me every time I came down to her lab at University of Oxford. Thanks to Dr. Raluca Nicoli from Platt Lab for taking care of me every time I was there and helping with all the animal work. Thanks to Dr. Fay Probert for the useful discussions about this project and her help in some of the work described herein.

Since this project involved different research groups, I would like to thank them all for their help in the provision of biological samples, including those at Section on Molecular Dysmorphology (NIH, Bethesda, USA), National Hospital for Neurology and Neurosurgery (London, UK), The Mark Holland Metabolic Unit (Salford, UK) and St. Mary's Hospital (Manchester, UK).

Also thanks to the sponsors that funded this research work: De Montfort University for the fees scholarship award and Hope Against Cancer (Leicester, UK) for the provision of stipend.

Many thanks to Dr. Mark Edgar for taking the time to train me on NMR at Loughborough University.

Special thanks to the small Spanish family that we created here in Leicester throughout these 4 years, for creating the feeling that we were still at home and to put up with all the scientific problems that I unfortunately (for them) shared with them.

Many special thanks to my parents, Manuel and Carmen, to my brother Carlos, and more specially to my grandmother Lola, since in a very weird way she always knew that I was going to work in science. Thanks for their support and patience, and for making me feel that I never left Madrid in each Skype talk and every visit.

Finally, but by no means least, I would like to thank my awesome wife, Bea. She started all this, encouraging me to go through this PhD process, providing her support at any step and being involved in any achievement that we might have; since any good that subsequently happens is mainly because of her. Thanks as well for her 'interest' in NMR, metabolomics and 'that Niemann whatever' that she had to explain every time someone asked. This work (as everything else) is dedicated to her.

DECLARATION

This thesis has not been accepted in any previous application for a degree and contains the original work of the author except where otherwise indicated.

Patient recruitment and sample collection

The personnel involved in the NP-C1 urine sample collection included Danielle te Vruchte (Department of Pharmacology, University of Oxford, UK), Dr. Robin H. Lachmann (National Hospital for Neurology and Neurosurgery, London, UK), Prof. Christopher J. Hendriksz (The Mark Holland Metabolic Unit, Salford, UK), Dr. James E. Wraith (St. Mary's Hospital, Manchester, UK) and Jackie Imrie (St. Mary's Hospital, Manchester, UK).

All plasma samples used in this study were collected under the Eunice Kennedy Shriver National Institute of Child Health and Human Development Institutional Review Board (Principal Investigator: Dr. Forbes D. Porter). The collections took place at the National Institutes of Health clinical centre in Bethesda, Maryland, USA.

Plasma separation from 'whole blood' was performed by Danielle te Vruchte (University of Oxford, Oxford, UK).

Animal work and liver tissue collection was performed by Dr. Raluca Nicoli (University of Oxford) at University of Oxford.

Data Analysis

Data analysis performed on the urine samples collected from NP-C1 patients undergoing miglustat treatment and that performed on plasma samples was done in conjunction with Dr. Fay Probert.

PUBLICATIONS

Probert, F., Ruiz-Rodado, V., Zhang, X., te Vruchte, D., Claridge, T. D., Edgar, M., Zonato Tocchio, A., Lachmann R. H., Platt, F. M., Grootveld, M. *Urinary excretion and metabolism of miglustat and valproate in patients with Niemann–Pick type C1 disease: One-and two-dimensional solution-state ^{1}H NMR studies*. Journal of pharmaceutical and biomedical analysis, **2016,** Vol**.** 117, 276-288.

Ruiz-Rodado, V., Luque-Baena, R. M., te Vruchte, D., Probert, F., Lachmann, R. H., Hendriksz, C. J., Wraith, J. E., Imrie, J., Elizondo, D., Sillence, D., Clayton, P., Platt, F. M., Grootveld, M. *$_{1}H$ NMR-Linked Urinary Metabolic Profiling of Niemann-Pick Class C1 (NPC1) Disease: Identification of Potential New Biomarkers using Correlated Component Regression (CCR) and Genetic Algorithm (GA) Analysis Strategies.* Current Metabolomics*,* **2014**, Vol. 2, 88-121.

OUTLINE

This thesis describes the applications of NMR-linked metabolomics analysis to urine and plasma samples collected from human Niemann Pick, type C1, (NP-C1) patients and their corresponding controls, together with the analysis of hepatic tissue from a mouse model of this disease, in order to explore metabolic alterations arising from the disease process, and also to seek valuable biomarkers for the purpose of diagnosing and monitoring its progression.

The first Chapter (Chapter 1) provides an introduction to the main techniques employed in this work. A summary of NMR theory has been included in order to explain how this analytical technique operates, its applicability to the field of biofluid and tissue samples analysis, and how useful it is as a diagnostic tool. The field of metabolomics will also be described, together with the historical evolution of the methodologies employed. Chapter 1 is also focused on the disease of study, Niemann-Pick, type C1 (NP-C1). The biochemical processes underlying this disease, the pathophysiological manifestations experienced by afflicted patients (with special reference to liver dysfunction and damage), together with the current status of treatment, specifically that involving the pharmacological agent miglustat, and disease diagnosis will be also explained.

Chapter 2 describes the resolution of the urinary ^{1}H NMR profile of NP-C1 patients, which is of major utility in the metabolomics-linked data analysis performed. The information extracted therefrom was subjected to differing multivariate analysis (MVA) strategies in order to classify these patients according to their disease status. Indeed, ROC curve analysis was employed for the purpose of assessing the classification success rate of

the models developed for this urinary dataset in order to seek valuable biomarkers for this lysosomal storage disease. NMR analysis of urine samples from NP-C1 patients receiving therapies such as miglustat was also explored in order to detect this agent in their urinary ^{1}H NMR profiles; accordingly, the solution structure of this drug was also investigated by NMR analysis.

Chapter 3 outlines the ^{1}H NMR-linked metabolomics analysis performed on blood plasma samples collected from NP-C1 patients, healthy individuals, heterozygous disease carriers, together with NP-C1 patients undergoing miglustat treatment. The Random Forests (RFs) strategy was employed to classify these samples based on their classifications. A brief discussion regarding the methodology employed for the acquisition of ^{1}H NMR spectra on these samples is also included. Finally, comparisons between the ^{1}H NMR plasma profiles acquired from all the different patients/participants in the study are conducted, along with an evaluation of plasma metabolites as possible NP-C1 disease biomarkers.

Chapter 4 describes the NMR analysis performed on liver samples collected during the development of NP-C1 in a mouse model of the disease, since this organ plays a crucial role in this disorder. The dataset extracted from the multicomponent ^{1}H NMR analysis of aqueous extracts of these samples were analysed by RFs in order to extract valuable information regarding the disease classification of these hepatic tissue extracts. Additionally, the correlation of such metabolic changes to the progression of the disease was investigated, in addition to the redox status of the hepatic tissue.

In Chapter 5, the ability of a newly-developed statistical MVA method, Correlated Component Regression, to successfully perform in a metabolomics context was evaluated, along with its dependence on the number of variables and components employed to build

such classification models, specifically those arising from the urinary and hepatic NP-C1 datasets. Both datasets will also serve to compare the variables ranking obtained after a cross-validated RFs analysis to a Recursive Feature Elimination (RFE) variant of the same method for variable selection.

In Chapter 6, all the metabolic pathways and biochemical processes that can be affected in NP-C1 disease process are discussed according to the outcomes obtained in the previous sections, and will be compared and contrasted with corresponding information available in the literature. Furthermore, some metabolites will be proposed as valuable biomarkers for the diagnosis and stratificational prognosis of NP-C1 disease.

In Chapter 7 the conclusions arising from this work will be discussed, including the utility of the metabolites selected as discriminatory urinary and blood plasma biomarker features for the diagnosis of NP-C1, together with outcomes from the NMR analysis of liver tissue samples. The classificational abilities of the RFs-Recursive Feature Elimination and CCR-LDA MVA strategies in a metabolomics context is also delineated.

ABSTRACT

NMR-linked metabolomics analysis was employed to investigate urinary and human plasma profiles collected from Niemann Pick type C1 disease patients (NP-C1), in addition to aqueous extracts of liver samples of an NP-C1 mouse model. NP-C1 is a lysosomal storage disorder caused by mutations in the lysosomal proteins NPC1 and NPC2, which are involved in lysosomal cholesterol trafficking. NP-C1 disease is a fatal genetic disorder, characterised by neurodegeneration and hepatic damage. Miglustat (MGS) is the only approved drug for this disease, and consequently, plasma and urine samples collected from MGS-treated patients were also investigated.

The ability of ^{1}H NMR analysis to detect a wide range of metabolites simultaneously served to characterize the metabolic profiles of urine, plasma and hepatic tissue samples investigated in order to perform linked multivariate analysis (MVA). Additionally, MGS was identified in urine samples collected from NP-C1 treated patients. MVA employing both parametric and machine learning-based techniques was conducted to classify samples according to their disease status, and also to seek biomarkers that could aid in the diagnosis and/or prognosis of the disease. Moreover, a new technique was introduced in a metabolomics context, Correlated Component Regression (CCR), and the suitability of Random Forests (RFs) for variable selection was also explored.

We were able to differentiate urine samples collected from NP-C1 patients from those collected from heterozygous controls, and also propose several metabolites as NP-C1 urinary biomarkers such as bile acids, 2-hydroxy-3-methylbutyrate, 3-aminoisobutyrate, 5-aminovalerate, trimethylamine, methanol, creatine and quinolinate. The ^{1}H NMR linked

metabolomics study of plasma samples revealed major distinctions among the groups investigated, metabolic alterations ascribable to the disease pathology were mainly observed as changes in the lipoprotein profiles of NP-C1 patients. Hepatic tissue extracts analysed revealed major disturbances in amino acid metabolism, along with impairments in the NAD^+/NADH production and redox status. Gut microbiota and bile acid metabolism were also highlighted as features altered in NP-C1 disease.

CCR linked to Linear Discriminant Analysis was evaluated as a new tool for metabolomics analysis, giving accurate results when compared to alternative techniques tested. Additionally, the suitability of Random Forests and associated recursive feature elimination for variable selection in metabolomics studies was contrasted, suggesting that those strategies relying on a variable ranking to select the top features for discrimination are more suitable for metabolomics investigations than those that iteratively remove a percentage of the least effective features until the classification performance decays.

ABBREVIATIONS

3-AIB (3-aminoisobutyrate)

AA (Amino Acid)

AAA (Aromatic Amino Acid)

ACC (Accuracy)

ANCOVA (Analysis Of Covariance)

ANOVA (Analysis Of Variance)

AUC (Area Under the Curve)

BA (Bile Acid)

BBB (Blood Brain Barrier)

BCAA (Branched Chain Amino Acid)

BMRB (Biological Magnetic Resonance Data Bank)

BRP (Between Run Precision)

CCR (Correlated Component Regression)

CI (Confidence Interval)

Cn (CreatiNine)

COSY (Correlation Spectroscopy)

Cr (CReatine)

CV (Cross-Validation)

DG (DiacylGlicerides)

DMA (DiMethylAmine)

EMA (European Medicines Agency)

ER (Endoplasmic Reticulum)

FDA (Food and Drug Administration)

FID (Free Induction Decay)

FA (Fatty Acid)

FT (Fourier Transform)

GAs (Genetic Algorithms)

GC (Gas Chromatography)

HDL (High Density Lipoproteins)

HMDB (Human Metabolome Data Base)

HSQC (Heteronuclear Single Quantum Coherence)

INEPT (Insensitive Nuclei Enhanced by Polarization Transfer)

LC (Liquid Chromatography)

LDA (Linear Discriminant Analysis)

LDL (Low Density Lipoproteins)

LLOQ (Lower Limit Of Quantification)

LOD (Limit Of Detection)

MCCV (Monte Carlo Cross-Validation)

MLHD (Maximum LikeliHooD)

MS (Mass Spectrometry)

MVA (MultiVariate Analysis)

NAD (Nicotinamide Adenine Dinucleotide)

NADP (Nicotinamide Adenine Dinucleotide Phosphate)

NAFLD (Non-Alcoholic Fatty Liver Disease)

Nampt (NicotinAMide PhosphoribosylTransferase)

NMDA (N-Methyl-D-Aspartate)

NMR (Nuclear Magnetic Resonance)

NOESY (Nuclear Overhauser Effect SpectroscopY)

NP-C (Niemann Pick type-C)

OM (Overall Mean)

OOB (Out-Of-Bag)

PCA (Principal Component Analysis)

pRDA (Partial Redundancy Analysis)

QC (Quality Control)

QUIN (quinolinate)

RFs (Random Forests)

ROC (Receiver Operating Characteristic)

SE (Standard Error)

SPE (Solid Phase Extraction)

SVMs (Support Vector Machines)

TG (TriacylGlicerides)

TMA (TriMethylAmine)

TMAO (TriMetylAmine-N-Oxide)

TOCSY (Total Correlation Spectroscopy)

TNR (True Negative Rate)

TPR (True Positive Rate)

TSP (TrimethylSilyl Propanoic acid)

VLDL (Very Low Density Lipoproteins)

WRP (Within Run Precision)

LIST OF FIGURES

LIST OF TABLES

CHAPTER 1

INTRODUCTION

1.1. NUCLEAR MAGNETIC RESONANCE SPECTROSCOPY (NMR)

NMR is a spectroscopic technique based on the magnetic properties of nuclei. The effect of the magnetic field on the nuclei was first discovered by Rabi *et al.* in 1939 (1), when he performed an experiment based on sending a stream of hydrogen atoms through an homogeneous magnetic field which was additionally subjected to a radiofrequency field; these researchers found that some energy was absorbed by the molecules at a defined frequency, and this absorption caused a small-but-detectable deflection of the beam (1). This was the first observation of NMR, and Rabi received the Nobel Prize in 1944 based on his contribution towards the birth and development of this technique.

Nuclear spin (*I*) is an intrinsic form of angular momentum (*p)* possessed by atomic nuclei which contain an odd number of protons or neutrons. The value of *I* is characteristic for each isotope.

$$p = I\frac{h}{2\pi} \quad (1)$$

A proton has a spin associated about an axis, which is a form of angular momentum, p. This spin presents an associated magnetic moment, μ. The correlation between both parameters is given by the gyromagnetic ratio, γ.

$$\gamma = \frac{\mu}{p} \tag{2}$$

Without a magnetic field, nuclear spin are orientated randomly; however, when the sample is placed in an external magnetic field, nuclei with positive spin are orientated in the same direction as this magnetic field, in the minimum energy state. However, nuclei with negative spin are orientated in the opposite direction, and this anti-parallel orientation has the higher energy. This effect on the orientation of nuclei in a magnetic field is known as the *Zeeman Effect*.

When a bulk sample of hydrogen nuclei (protons) is placed in a magnetic field, it is expected that such particles are distributed equivalently, following the Boltzmann distribution, in both low and high energy states, through their parallel and anti-parallel spin orientations. The allowed orientations (*m*) are determined by the relation *2I + 1*, and which is described by the magnetic quantum number, which takes values from *-I* to *+I*. For instance, in the proton case where *I* = 1/2, then *m* assumes values of -1/2 and +1/2. However, after a certain time (known as relaxation time), this sample of protons will attain thermal equilibrium with respect to the magnetic field (2).

It is possible to induce the movement from the lower energy state to the higher energy state by applying radiation in the radiofrequency region to the sample. The energy of this transition, and hence, the frequency associated with it, and which is absorbed by the nuclei to accomplish the transition to the higher energy state, is given by the *Bohr condition*:

$$\nu = \frac{\gamma B_0}{2\pi} \quad (3)$$

The nucleus under the magnetic field B_0 along the z-axis (in this case) draws a *precession* movement around this axis [Figure 1(b)] since the alignment with B_o cannot be completely achieved. The angle has a defined value since it is quantizated ($\cos \theta = m/I$). The angular velocity of this precession movement is given by the *Larmor equation*:

$$\omega_0 = \gamma B_0 \quad (4)$$

This radiation has the same energy as the differing orientations, which is the resonance frequency of the system, known as *Larmor frequency*. In order to detect this effect, a vector M_0 (magnetization vector) must be rotated away from z-axis towards the x,y-plane. In view of the strong B_0 applied to the sample, the only means to displace M_0 is to supply an RF pulse orthogonal to B_0 (along the x-axis) oscillating at the *Larmor frequency* of our nuclei, i.e. achieving resonance (3). This pulse is known as a 90º pulse [Figure 1(c)], since it rotates the magnetization 90º. Once the magnetization has been transferred to the x,y-plane, and therefore nuclei are precessing about it, the electrical current generated can be detected by a receiver coil.

Resonance causes transitions between both energy states [Figure 1(a)], and therefore nuclei can move to the maximum energy state. These two orientations are termed α (m = ½) and β (m = -½) respectively. Since more protons will have the lower-energy parallel orientation, a radio signal at the resonance frequency will be absorbed, and hence generate more upward transitions. When nuclei return to their minimum energy state, they are

required to lose that energy since it is a non-equilibrium state; subsequently, they emit the electromagnetic signal, termed Free Induction Decay (FID), which is detected by the receiver coil. The loss of this energy is conditioned by two parameters, T_1 and T_2. T_1 is the spin-lattice or longitudinal relaxation time which leads to the recovery of M_z (achievement of thermal equilibrium); and T_2 is the spin-spin or transverse relaxation time which involves the decay of the M_{xy} magnetization.

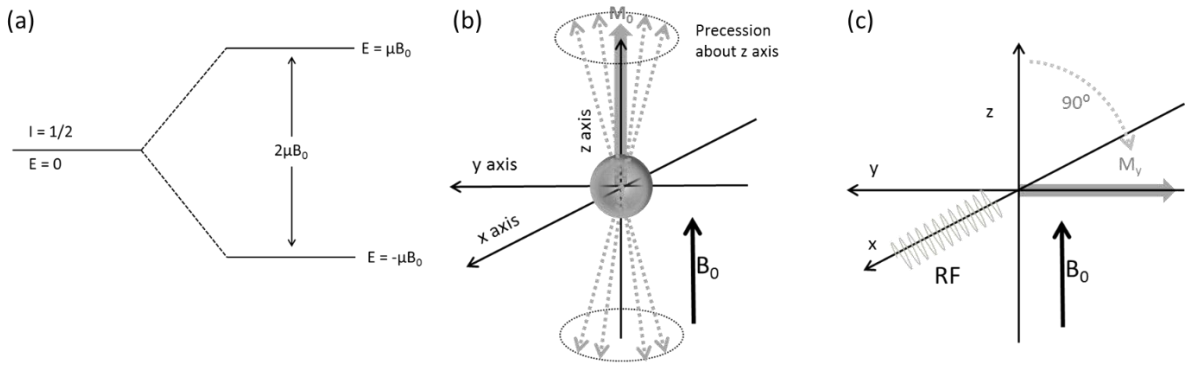

Figure 1.1. (a) Energetic sub-levels present when a nucleus with non-zero spin (1/2 in this case) is placed in a magnetic field. (b) Precession movement of nuclei around the z-axis at which B_0 has been applied. (c) Direction of the magnetization vector M_y in the rotating frame system. Abbreviations: RF, RadioFrequency pulse emitted along x-axis.

In order to simplify the explanation of the pulse sequences employed in this work, the 'vector model' proposed by Block (4) will serve as a reference: after applying B_1, M_0 moves towards B_1, and both M_0 and B_1 are precessing around B_0, originating a system that is complicated to represent. Furthermore, the rotating frame is introduced for purposes of clarity; this representation takes the frame of reference to precess at a frequency ω_{RF}, hence B_1 seems static and M_0 precess around B_0 at an offset frequency $\omega_0 - \omega_{RF.}$ (3).

The subsequent Fourier Transform (FT) of the FID provides a normal NMR spectrum with absorption signals at frequencies that represent the energy difference between the basal and excited states (2). This operation was implemented in 1966 by Anderson and Nerst (5), and was based in the previous discoveries made by Lowe and Norberg in 1957 (6). In summary, this transformation converts a signal described as a function of time into one within the frequency domain.

In nuclear magnetism, not only are the nuclei involved, but also the electrons surrounding them, and these electronic effects are responsible for the differences in the locations of the resonances in conventional spectra. Nuclei's behaviours in the magnetic field can be influenced by different effects, providing information such as:

Environment and atoms linked to each nucleus (chemical shift, δ): In molecules, the nuclei are magnetically-deshielded or -shielded; the effective field at the position of nuclei is different from the externally-applied field. This phenomenon is attributable to the distribution of 'electron density' within the molecule, mainly around the protons and bonds involving these. Those groups with more electronic density around themselves experience an effective magnetic field lower than the one originally applied, this is the case for the methyl group at the terminus of a hydrocarbon chain, for example. Contrarily, those groups with less electronic density experience a more intense magnetic field ($\leq B_0$, though), so that they are deshielded, such as those adjacent to carbonyl groups. The chemical shifts are therefore considerably affected by substituents which specifically influence this electron distribution; for instance, electronegative groups will pull away the electrons of neighbouring groups towards themselves, generating a deshielding effect, and therefore giving rise to a more downfield-shifted signal.

Number of nuclei (peak integral): The relative intensity from a resonance signal can be correlated with the number of nuclei that generate that signal. It is therefore possible to quantitatively estimate the proportions of different protons within the molecule, and this involves determinations of the area under the resonance peak.

Number and placement of nuclei (multiplicity): In view of the electronic distributions in a bond, two linked nuclei retain the spin information of each other. The energy difference between the two energy levels is modified by the other nuclei, and therefore if electrons of one nucleus are in the excited state (higher energy level), the energy difference of contiguous nuclei will be increased, and vice-versa. Furthermore, two different energy sub-levels will appear for each case, both of them higher or lower than the initial state. This phenomenon is known as spin-spin coupling, and consequently, the splitting of resonances is observed. The separation between the different multiplet lines of the same resonance signal is known as the coupling constant, *J*. It is calculated as the distance in Hz between these resonance lines.

1.1.1. Water suppression experiments

A simple pulse sequence involves the application of a 90^{o} pulse (this value can be diminished to speed up the experiment) followed by the data acquisition, in which the FID is recorded. However, in NMR-linked metabolomics studies, the presence of water in the samples investigated is a common issue, since serum, urine, cerebrospinal fluid (CSF), etc., are all water-based biofluids. The relative concentration of metabolites in these fluids is minimal when compared to that of water, and therefore, the signal arising from H_2O dominates the majority of the ^{1}H single pulse spectra. In order to overcome this issue, water

suppression experiments are employed. The pulse sequences utilised in these experiments remove (partially) the water signal through different approaches. Two of the most commonly employed techniques used in metabolomics are NOEPR (Nuclear Overhauser Effect pulse train with presaturation during relaxation and mixing time) (7), and PRESAT (Presaturation) (8). Single-pulse spectra without suppression of the solvent signal present the main issue of signal overlap, and also overloading of the receiver, generating baseline distortions (wiggles) if the receiver gain value is very high, or inadequately digitized signals if this value is set very low to allow the acquisition of the massive solvent peak (9).

PRESAT: This is a two-pulse experiment that utilizes a relatively long (seconds), low power RF pulse to selectively saturate (the solvent) at a specific frequency by irradiating during the relaxation delay (RD), and with a non-selective pulse to excite the full spectrum of resonances (8). The long power pulse is of the order of the solvent T_1, so that it does not allow it to relax, and consequently its signal is suppressed. As noted above, this presaturation pulse is relatively long, so that the hydrogen atoms of -OH, -NH and $-NH_2$ groups that chemically exchange with water are also saturated, and therefore they are unobservable or attenuated (for instance, the urea signal detectable in urine) (10). The pulse sequence works as follows: Presat (RD) - 90^{o}_{x}. It should be noted that the duration of a pulse is inversely proportional to the width of the area excited, and hence the longer the pulse, the narrower the spectral bandwidth (11).

NOEPR: This method is usually employed in conjunction with PRESAT, so that suppression of the solvent signal is performed during both the recycle delay and mixing time in a pulse sequence structured similarly to that of a NOESY (2D experiment employed to

observe connections through space). The structure of the pulse sequence is RD-[$90°_x$ - t_1 - $90°_x$ - t_m - $90°_x$]. RD is the relaxation delay, during which the water resonance is selectively irradiated (presaturation); t_1 is a short delay, and t_m is the mixing time in which the water resonance is again selectively irradiated. The mixing time is that in which the cross-polarization takes place, transferring magnetization to another atom; this process is a function of the mixing time increment in a 2D-NOESY experiment. Nevertheless, in this case there is no such increment, and therefore no indirect dimension is detected.

1.1.2. CPMG pulse sequence

In the NMR-linked metabolomics analysis of plasma samples, the investigators face the problem of poor 'wiggly' baselines attributable to protein signals, and broad envelope regions arising from the -CH_3 groups of triacylglycerols, proteins, cholesterol and phospholipids at *ca.* 0.80 ppm. This effect arises from the small T_2 values of these large biomolecules. Two alternatives are proposed in order to solve this issue, i.e. the physical filtering of larger biomolecules through ultrafiltration, or protein precipitation using organic solvents, or alternatively applying an NMR pulse sequence that acts as a T_2 filter, known as the CPMG pulse sequence (Carr-Purcell-Meiboom-Gill), which attenuates signals from macromolecules which have short T_2 relaxation times. Small metabolites experience rapid molecular motion, e.g. tumbling, contrarily to macromolecules such as proteins, which show slow motion, and consequently have shorter T_2 (spin-spin relaxation time) values, that gives rise to broad resonances in spectra acquired.

Immediately after applying a 90^o_x pulse, the maximum M_y magnetization is achieved and this decays over time, following T_2. This is the loss of coherence of the total M_y, and it is caused by the spin-spin relaxation, so that nuclei initially structured along M_y start fanning

out. The different effective magnetic field that each nucleus experiences leads them to precess at different *Larmor frequencies*, so they spread out with time, a process guided by the T_2 value. Another 180^o_x pulse can then be applied after a certain time (τ), refocusing the individual M_y of nuclei and therefore obtaining a coherent magnetization, known as an echo, at M_{-y} after τ. This is known as the spin-echo pulse sequence developed by Carr and Purcell (12) following the work on T_2 determination by Hahn in 1950 (13); it can be depicted as 90^o_x - τ - 180^o_x - τ - 1^{st} echo - τ - 180^o_x - τ - 2^{nd} echo - … $(\tau - 180^o_x - \tau)_n$, in which the intensity of each echo decreases exponentially with a time constant equivalent to T_2 (14). As a result of the recovery of coherence after the 180^o pulse, the echoes are formed along the -y and y-axes. Meiboom and Gill noted that if the 180^o pulse does not exactly rotate the magnetization 180^o, then the vector moves away from the x,y-plane in an accumulative manner, and then the decay of the echo intensity will not correspond to T_2 (14). These authors addressed the problem by replacing the rotation of the magnetisation around the x-axis (180^o_x) with that around the y-axis (180^o_y). With this modification, an amplitude deviation of the 180^o pulses will not be cumulative, and the echo is generated at an even number of 180^o_y pulses always along the positive y-axis. These modifications introduced by these four researchers to the original Hahn spin-echo pulse sequence gave rise to the Carr-Purcell-Meiboom-Gill pulse sequence, termed CPMG, which is widely employed in the NMR analysis of plasma samples to remove the broad signals attributable to macromolecules (Figure 1.2). As noted above, large molecules have shorter T_2 times, and hence during the τ delay the magnetization vector will have fanned-out. Small molecules with larger T_2 times will only commence fanning-out after the 90^o pulse, and therefore will be refocused after the 180^o_y pulse and detected in view of their orientation in the x,y-plane (15).

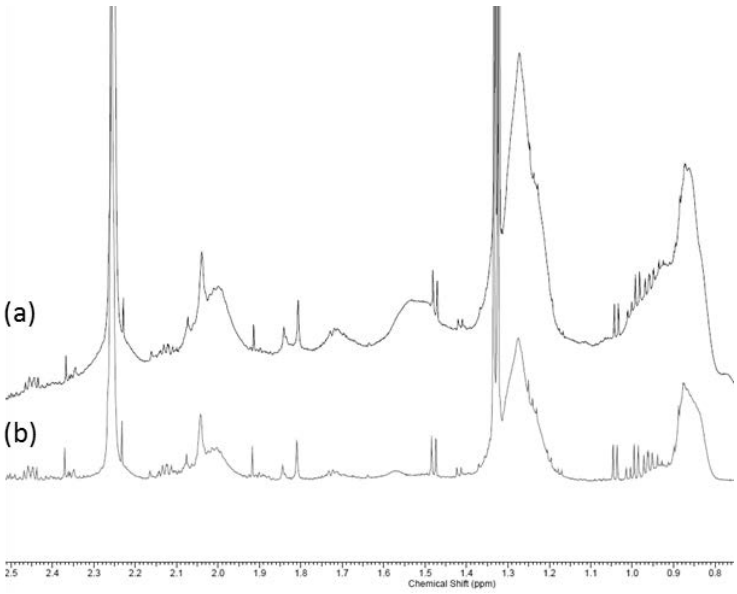

Figure 1.2. Stack plot of a 1D plasma spectrum acquired through (a) a NOEPR pulse sequence, and (b) a CPMG pulse sequence with water suppression: broad signals arising from lipids are diminished, and the wiggly baseline caused by protein signals is corrected.

1.1.3. Two-dimensional NMR

When studying complex mixtures (urine, plasma, etc.) or macromolecules (proteins, polysaccharides, etc.) 1D NMR may not offer enough clear information about the structure, and consequently the identity, of biomolecules investigated. Instead of acquiring a spectrum displaying intensity *vs*. frequency in only one dimension, by 2D spectroscopic experiments we obtain a 2D plot showing intensity as a function of two frequencies, usually known as *F1* and *F2*. The position of each peak is defined by 2 coordinates (*F1*, *F2*) showing a signal ('cross-peak') away from the main diagonal if two different resonances are coupled within the molecule; or on the diagonal, centred around the same *F1* and *F2* frequency co-ordinates ('diagonal-peak'), i.e. the own-connection of a resonance signal. The intensity of these 'cross-peaks' is represented by a contour plot, depicting contour lines drawn at suitable intervals, and similar to a topographical map (3). 2D experiments are composed of different phases:

preparation, evolution (t_1, indirect detection of an additional dimension), mixing (transference of coherence amongst spins), and detection (t_2).

COrrelation SpectroscopY (COSY): This 2D NMR technique shows how proton-containing functions within molecules are connected to each other in spectra (16). These experiments are applied to identify molecules through the study of ^1H-^1H couplings arising from their structure. In this type of experiment, magnetization is transferred by scalar coupling. Protons that are more than three chemical bonds away do not generate cross peaks because the ^4J coupling constants are very close to 0. Therefore, only signals of protons which are two or three bonds apart are visible in a COSY spectrum**.**

The common pulse sequence is 90^o_x - t_1 - 90^o_x - t_2, where t_1 is the evolution phase and t_2 the detection one. After the first pulse, in a two proton coupling system (A, X), four different vectors will rotate along the x,y-plane, each of those with a different frequency, and consequently, fanning out at different velocities from the y-axis. Then, the second pulse rotates the y component vectors to the -z-axis (which is not detected) and maintains the x component. Associated with this step, there is transference of magnetization determined by the spin system situation at t_1, which depends in turn on the *Larmor frequencies* of each proton A (ν_A) and X (ν_X). The x-components of magnetization vectors give an FID, which after FT with respect to t_2 gives a 4 line spectrum containing signals at the frequencies: A_1, ν_A + ½ J (A, X); A_2, ν_A - ½ J (A, X); X_1, ν_X + ½ J (A, X) and X_2, ν_X - ½ J (A, X), which in turn are associated with the transitions depicted in Figure 1.3. The second FT along t_1 yields the 2D spectrum with 4 groups of 4 signals, two centred around ν_A, ν_A and ν_X, ν_X (diagonal peaks), and 2 around ν_A, ν_X and ν_X, ν_A (cross-peaks) (17). t_1 is sequentially-incremented from 0 in Δ intervals, giving

for each value for t_1 an FID acquired at t_2, so that a matrix is composed of rows containing t_2 data for $t_1 = 0$ in the first row, with the second row containing t_2 data for $t_1 = \Delta$, etc. This whole process is repeated until sufficient data is acquired, typically 50 to 500 increments of t_1 (3).

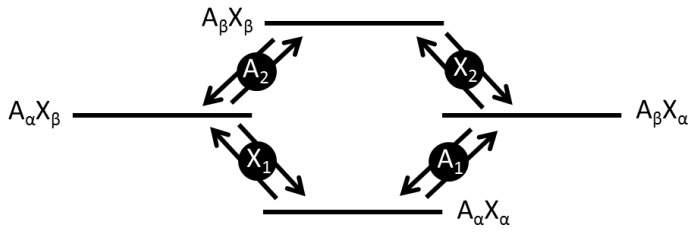

Figure 1.3. Energy levels scheme and transitions for a two spin AX system conformed for two ^{1}H nuclei.

TOtal Correlation SpectroscopY (TOCSY): In a TOCSY experiment (18, 19) magnetization is transferred over a complete spin system within the molecule by successive scalar couplings. The TOCSY experiment involves all protons of a spin system, even if they are not directly connected.

This experiment is similar to the COSY technique, but in this case we can observe the whole coupling system, and the second 90° pulse is substituted for a spin-lock stage (90° - t_1 - spin-lock - FID) which is equivalent to the mixing period. This stage consists of a low energy pulse or a series of short pulses in the y-axis direction that locks the M_y. In order to lock all the nuclei with regard to their difference *Larmor frequencies* defined by their nuclear environments, the spin lock pulse must be tuned in strength and duration. Moreover, the mixing time (t_m) is directly correlated to the spin-system observation; the longer the t_m, the further the whole spin system is extended. The goal of the spin lock stage is to reduce the

chemical shift differences (spin locking field << B_0), and therefore, those arising from the scalar coupling will dominate the process (17). This is ascribable to the much lower energy of B_1 when expressed relative to B_0. In order to achieve the transference of energy between nuclei, the Hartman-Hahn condition (20) is required to be accomplished, i.e. different sets of nuclei all precessing at the same frequency (ν) in order to allow the transfer of energy (cross polarisation), a condition which is relatively easier to reach in homonuclear systems since all nuclei have the same γ value (21). The spin-locking field guides the relaxation across My, yielding a new relaxation time $T_{1\rho}$, which differs from T_1 and T_2, but is very similar to T_2 when $T_1 \approx T_2$.

Heteronuclear Single Quantum Coherence (HSQC): This experiment reveals the connections through a direct bond between ^1H and a heteronucleus (i.e., one which differs from ^1H), particularly ^{13}C in a metabolomics context, as cross-peaks in a 2D spectrum. This experiment was first described by Bodenhausen and Ruben in 1980 (22), who investigated ^{15}N NMR spectra. The pulse sequence is depicted below:

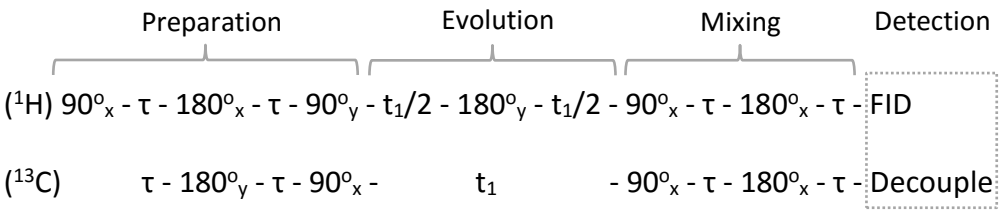

The first part of the pulse sequence (preparation) is the same as INEPT (Insensitive Nuclei Enhanced by Polarization Transfer), an experiment employed to enhance the intensity of ^{13}C resonances through the transfer of polarization from directly attached ^1H. Then the system evolves over t_1, which is changed incrementally, and finally the ^{13}C polarization is

transferred back to ^{1}H by a reverse INEPT, and its resonance signal subsequently recorded (17). Polarization transfer occurs when the excitation of one transition of a nucleus modifies the overall spin population distribution.

Initially, ^{1}H nuclei are flipped towards the y-axis, and then those coupled to either C_{α} or C_{β} start rotating about this axis at different frequencies during a time τ. After the 180^{o}_{x} pulse, both vectors ($M_H^{C\alpha}$ and $M_H^{C\beta}$) are oriented oppositely, i.e., about -y-axis. If the system is left to freely evolve, then an echo would be formed along -y, as noted above, but since 180^{o}_{x} is also applied in the ^{13}C channel, the populations of both levels are inverted, and move towards the -x and x-axis in the opposite directions from which they started, generating a 180^{o} angle between $M_H^{C\alpha}$ and $M_H^{C\beta}$ after τ. Subsequently, the 90^{o}_{y} pulse places the vectors along -z and z-axis, with $M_H^{C\beta}$ in the starting position (z-axis) again, and $M_H^{C\alpha}$ facing the opposite one (-z-axis) aligned with M_C. The 90^{o}_{x} to ^{13}C permits polarization transfer from proton to carbon. After these 90^{o} pulses, the preparation period ends. $M_C^{H\beta}$ and $M_C^{H\alpha}$ start refocusing on the x-axis to form an echo for a $t_{1/2}$ period, although the 180^{o}_{x} applied to the adjacent proton inverts proton magnetization along z-axis where they were residing, and consequently $M_C^{H\beta}$ and $M_C^{H\alpha}$ start fanning out for another $t_{1/2}$ time, until they form a 180^{o} angle (antiphase) along the y-axis. This procedure is repeated many times with different t_1 increments in order to permit the acquisition of the indirect dimension during this evolution time. After t_1, with the two 90^{o}_{x} pulses in both the ^{13}C and ^{1}H channel, the transfer back of polarization from ^{13}C to the ^{1}H nucleus is achieved. At this point, transverse magnetization is attributable to the evolution of protons according to heteronuclear coupling, and therefore this mixing period corresponds to a reverse INEPT. Subsequent 180^{o}_{x} pulses interchange the vectors for $M_H^{C\alpha}$ and $M_H^{C\beta}$ until they are phased, for both $M_C^{H\beta}$ and $M_C^{H\alpha}$. This last phase allows observation of the frequency of the more insensitive ^{13}C nucleus as ^{1}H magnetisation.

The resulting spectrum shows the ^{1}H resonances on F1, and the ^{13}C ones on F2, and as both spectra are different, there are not diagonal peaks; only cross-peaks reveal direct connections between ^{1}H and ^{13}C.

1.2. METABOLOMICS

Metabolomics is the systematic study of the unique 'chemical fingerprints' arising from specific cellular processes, diseases, environmental conditions, mutations, etc. It has been defined as 'the quantitative measurement of the multi-parametric metabolic response of living systems to pathophysiological stimuli or genetic modification' (23).

The metabolic connections amongst these cellular processes, and particular biofluid profiles arising therefrom have been noted since the beginning of Medicine as a discipline, in addition to the possibility of extracting valuable information regarding a disease and/or its status.

The colour, smell, and taste of urine, for example, were used as diagnostics from ancient China and India, where clinicians began using ants to detect the sugar content in urine, as well as tasting it (24). In Greece, since 450 BC Hippocrates developed the theory that the physical state of a person was correlated with the excess or lack of his/her body fluids. Galen (AD 131–200) continued with the theory that the health or temperament of a person was conditioned by the state of the 4 humours: black bile, yellow bile, phlegm and blood (25). This theory remained until nearly the 18th century. In that age, doctors tended to purge, bleed or apply pro-emetic techniques in order to equilibrate patient humours and heal them. In the middle ages, urine was used as a biofluid with a great value in diagnosis through its smell, taste and colour (Figure 1.4) (26).

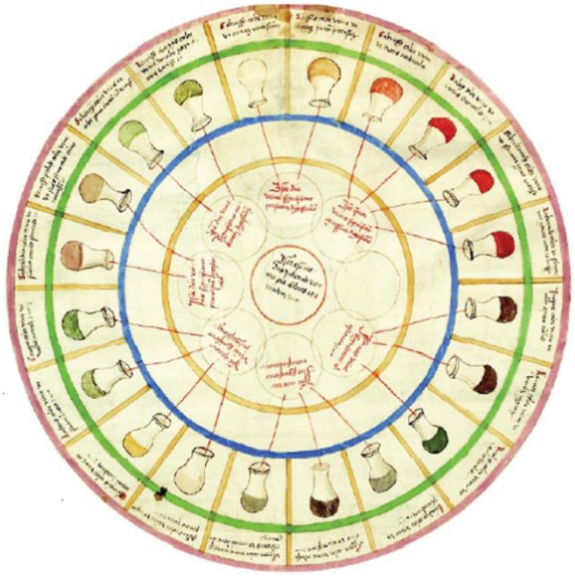

Figure 1.4. 16th Century diagnostic urine wheel: this urine wheel was published in 1506 by Ullrich Pinder, in his book *Epiphanie Medicorum*. It describes the possible colours, smells and tastes of urine, and their use as a diagnostic tools (26).

In the 1940s, Roger Williams working at Texas University, explored the ability of a simple method, such as paper chromatography, in order to investigate whether a metabolic profile can be obtained through the analysis of saliva and urine, this work being the first proposal for the existence of a metabolic pattern derived from biofluid analysis (27). He demonstrated that the taste thresholds and the excretion patterns of a variety of molecules presented inter-individual variability (Figure 1.5), but were homogeneous for each individual (27).

The technological improvements accomplished in the 1960s and 1970s (first quadrupole GC/MS instrument) allowed investigators to carry out a detailed quantitative analysis of metabolic profiles. Accordingly, the Horning group in the 1970s demonstrated how gas chromatography-mass spectrometry (GC-MS) could be employed to investigate a wide range of compounds present in human urine and tissue extracts; they also created the

term ‘metabolic profile’ (28-30). The investigations conducted by the Horning group, together with that of Linus Pauling and Arthur B. Robinson led to the development of GC-MS methods to detect and identify metabolites present in urine (31).

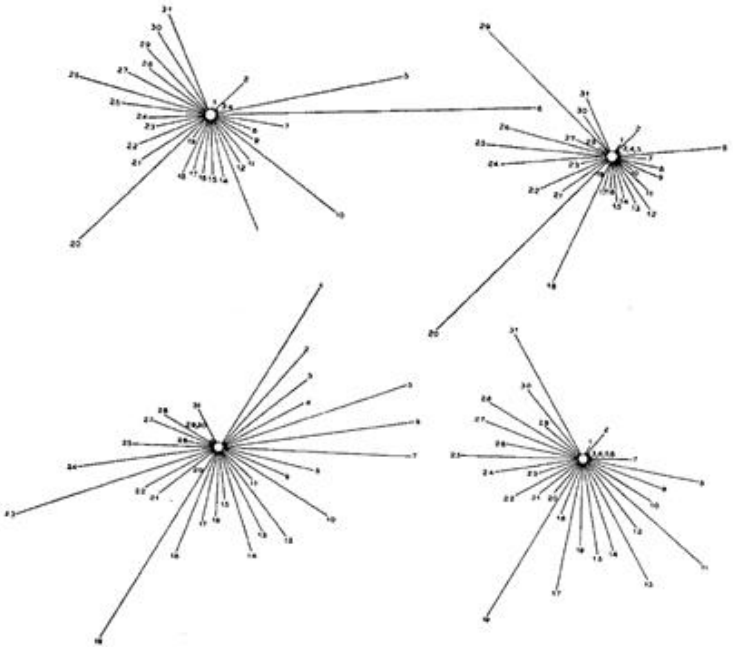

Figure 1.5. Polar co-ordinates of the metabolic patterns of 4 subjects studied by R. Williams in 1940: data were obtained by measurements of taste thresholds (numbers 1-17), and urinary metabolites (numbers 18-31). The lengths of the lines are indicative of the amounts of compounds determined (27).

The establishment of metabolic profile determinations in biological samples using high-resolution NMR analysis provides a detailed and specific view into cellular metabolic processes under normal and altered (disease-related) conditions. Indeed, continuing the work performed on GC-MS for biofluid profiling in previous years, McConnell, M. L. *et al.* published their work on pattern recognition using this technique (32).

In 1974, the NMR analysis of tissue began its development with investigations conducted by Hoult *et al.* focused on the ^{31}P NMR analysis of intact biological samples (Figure 1.6). They analysed muscle tissue in order to explore the complexation of ATP with magnesium (33); this is known to be the first NMR analysis applied to a biopsy. One year later, an NMR analysis of intact frog muscle was also reported by Bárány and co-workers (34). Therefore, these studies of organs and tissues by NMR analysis that led to the development of modern *in vivo* NMR spectroscopy (35) commenced 40 years ago.

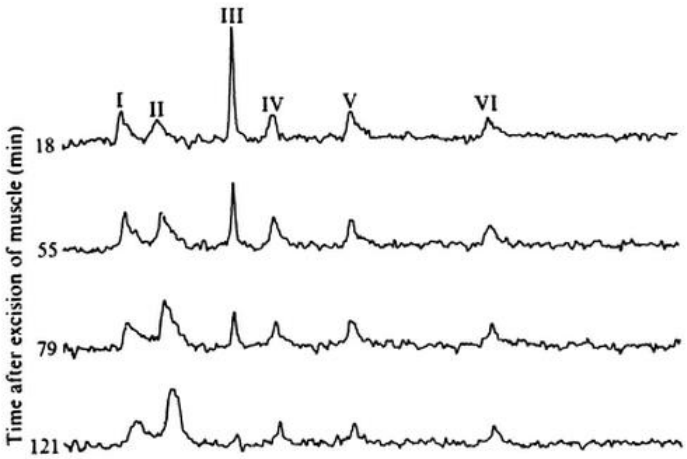

Figure 1.6. Experiment performed by Hoult *et al.* involving ^{31}P-NMR analysis (129 MHz) of muscle: intact muscle from the hind leg of a rat. Peak assignments: I, sugar phosphate and phospholipids; II, inorganic phosphate; III, creatine phosphate; IV, γ-ATP; V, α-ATP; VI, β-ATP (33).

In the late 1970's ^{1}H NMR analysis started to be proposed as a non-invasive technique for the metabolic profiling of biofluids and tissue by D. Rabenstein and co-workers (36, 37). A few years later, in the middle 1980s, Jeremy Nicholson and Peter Sadler at Birkbeck College (University of London, UK), and later at Imperial College (London, UK) demonstrated how ^{1}H

NMR spectroscopy could be utilised as a valuable diagnostic tool, and applied this technique to establish a diabetic metabolic profile and subsequently developed the study of NMR spectroscopy linked to pattern recognition in the mid- to late 1980s (38). This work performed by Nicholson and co-workers on plasma analysis by ^{1}H NMR was based on the application of the newly-introduced pulse sequences utilised to supress the broad signals arising from the macromolecules such as proteins and lipids by Daniels *et al.* in 1976 (39), and in the previous investigations conducted by Bock in 1982 (40), in which this author analysed blood plasma by NMR for the first time, exploring the ^{1}H NMR plasma spectral change in patients suffering from lactic acidosis, those undergoing phenobarbital treatment, and also investigating the detection of ethanol resonances in his own plasma profile following vodka consumption.

In 1985, Arús *et al.* were the first investigators to assign the ^{1}H NMR resonances in spectra of excised rat brain (41). In frog, rat and human skeletal muscle, the ^{1}H resonances found were virtually the same as those detected in rat brain. Furthermore, the $=N\text{-}CH_3$ resonance signal of creatine at 3.02 ppm was proposed to be used as internal reference for chemical shift values (42).

Interestingly, all this early metabolomics research work was devoid of a name to define the class of research performed, so that the first paper using the word metabolome was Oliver S. G. *et al.* (*Trends. Biotechnol*. 1998. **16**:373).

In 2005, the Siudzak group at The Scripps Research Institute (CA, USA) developed the first Metabolomics web database (METLIN), which contained over 10,000 metabolites and tandem MS data. On 23th of January of 2007, the Human Metabolome Project, led by David Wishart (University of Alberta, Canada), completed the first draft of the human metabolome, and this database primarily contained approximately 2,500 metabolites, 1,200 drugs and

3,500 food components (43). An additional database available that contains NMR spectra of metabolites is the Biological Magnetic Resonance Data Bank (BMRB) run by the University of Wisconsin, which also hosts spectra from peptides, proteins and nucleic acids (44). Moreover, the Spectral Database for Organic Compounds (SDBS), created by the National Institute of Advanced Industrial Science and Technology (Japan) contains not only NMR spectra, but also MS, Electron Spin Resonance (ESR), Infra-Red (IR) and Raman ones. These databases have incredibly aided the identification of metabolites, and the information contained therein has been updated and enlarged with recently published works regarding the identification and resolution of the majority of resonances present in urinary (45), blood serum (46) and salivary (47) ^{1}H NMR profiles.

The future of NMR-linked metabolomics is moving towards both the automation of all the analytical steps performed after spectral acquisition, and also the standardization of experimental conditions. Accordingly, automated assignment web-based software has been developed, i.e. COLMAR (48), and software developed by the Wishart group allows the automatic resonance signal deconvolution for quantitative Metabolomics, BAYESIL (49). The next step in a metabolomics investigation after the completion of all resonance assignments is multivariate analysis, and this can be performed by the web-based tool MetaboAnalyst 3.0 (50) that allows researchers to analyse datasets through a wide battery of multivariate and univariate analysis techniques, and also includes modules for time-series and pathway analyses. The standardization of NMR-linked Metabolomics investigations is a major concern for the scientific community, mainly in the field of urine NMR analysis as a diagnostic tool (51), since plasma analysis investigations are still being subjected to new developments, both in terms of signals assignments [mainly lipoprotein subclass identification (52)] and the dichotomy between physically (ultrafiltration, organic solvent precipitation) (53) or NMR-

based suppression of the broad signals attributable to macromolecules present in this biofluid. Nevertheless, Nicholson and co-workers have reported a set of protocols for human urine, serum, and plasma NMR-linked metabolomics analysis in order to provide standardized steps in metabolomics investigations (54). This effort for standardizing the experimental procedures in NMR-linked urinary metabolomics analysis includes all the steps involved in such investigations, from sample collection and preparation to the manner in which investigators should report their results (55). In order to accomplish this ambitious objective, the Metabolomics Society released the Metabolomics Standards Initiative in 2007 (56). In 2012, a further initiative known as the coordination of standards in metabolomics (COSMOS) was set up to bring together metabolomics researchers to develop guidelines and standard workflows for metabolomics applications (www.cosmosfp7.eu). Additionally, the standardization of urinary metabolite quantification serves as a further step, since it would translate the investigations from laboratory to clinic, since proposing metabolites as biomarkers irremediably requires the provision of accurate threshold metabolite values in order to distinguish healthy from diseased patients in a diagnostic test (57).

In the NMR-linked metabolomics field, the major instrumental advances are driven towards a decrease in the spectral acquisition duration for homo- and heteronuclear 2D spectroscopy in order to facilitate the assignment of resonances within reduced time periods. Throughout the last five years, the development of ultrafast NMR experiments has allowed the acquisition of 2D NMR spectra in a single scan (58), which may permit the development of high-throughput 2D NMR-based metabolomics studies (59). Moreover, Rai and Sinha (2012) reported a new J-compensated HSQC pulse sequence which reduces the data collection time 22 times, and which does not show any deficiency in the quantification of low abundance metabolites (60).

1.3. MULTIVARIATE STATISTICAL ANALYSIS TECHNIQUES

1.3.1. Principal Component Analysis (PCA)

The PCA technique is attributable to Hotelling (61), although its origins are in the orthogonal least-squares adjustments introduced by K. Pearson, who first proposed it over 100 years ago (62). By applying PCA, we seek to maximize the percentage of variance explained using linear combinations of 'predictor' variables, the so-called components. PCA is an unsupervised technique, since these components are selected without any assumption about the group classification and hence clusterings that might underlie the dataset; therefore, no grouping of observations is assumed. The information lies in the correlation structure, and both clustering tendency and outliers can be detected.

A dataset with *K*-variables can be geometrically represented by a plane of *K*-dimensions. The goal of PCA is to reduce the number of dimensions, together with an explanation, with those few dimensions, of the maximum variation of the dataset (Figure 1.7).

Each sample/observation is represented in the PCA space as a point with *K*-coordinates. The samples in that space have to be centred first, by subtracting the mean, and PCA then draws a line through the *K*-dimensions that best approximate the data (ordinary least squares technique), which would represent the first component. It is usually convenient to standardize the variables prior to principal component analysis computations, since those variables which present a higher contribution towards the total variance dominate computation of the first PC. This first PC is obtained as a linear combination of the variables with the aim of achieving maximal variance; then, the second PC is obtained as a linear combination of the original variables, with the same purpose of achieving maximal variance, in an orthogonal direction to the first PC, and so on (63).

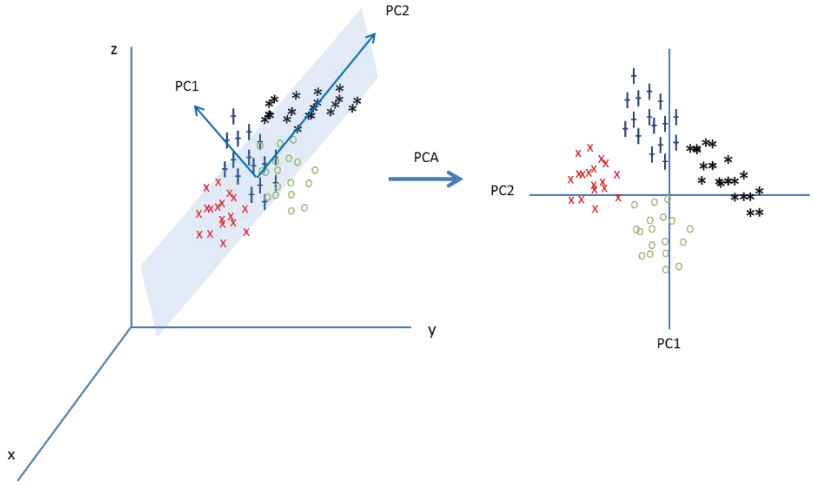

Figure 1.7. PCA representation in a 3D space: the 4 groups depicted in the 3D space (left) are represented by PCA in a 2D space (right) in which PC1 and PC2 explain the maximum variance achievable.

The projections of the samples/observations in the new plane with *A*-dimensions (*A*, number of principal components) are the scores *T* (Figure 1.8). The proximity between objects/samples indicates the presence of similar properties amongst those samples, and vice-versa.

The weights of the variables in the PCs are known as loadings (*P*). They express how the original variables are linearly combined to form the scores, and how the variables are related to the components. The residual matrix represents the distance between each point in *K*-dimensions, and its projections in the new dimension-reduced plane, and therefore it is the variation unexplained by the PCs (10).

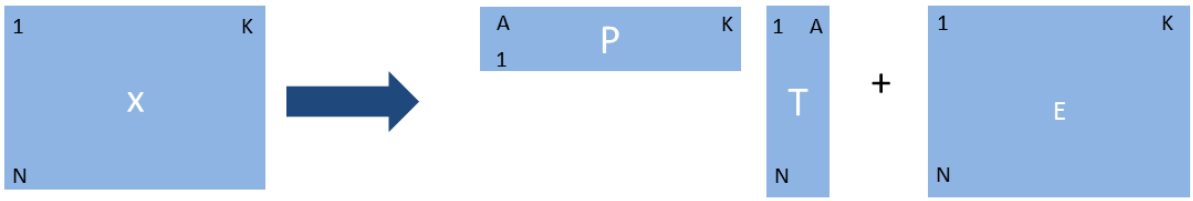

Figure 1.8: Matrix representation of a PCA model: *X,* original dataset; *P*, loadings matrix; *T*, scores matrix; *E*, residual matrix.

In some situations, loadings of some variables might have medium correlation values to the factors, which may lead to a difficult interpretation of the results. In order to facilitate this interpretation, the factors can be rotated to make the correlations of the variables to the factors more polarized. Rotation can be either orthogonal or oblique, the former being the most widely employed since the factors arising from the components' rotation remain orthogonal, as are the PCs from which they are generated. Through a rotation of the components [linear combination of the original factors such that the variance of the squared loadings is maximized (64)], the explained variance changes from the PCs to the new rotation-derived factors, but the total amount of explained variance remains the same, i.e. the only change is the partition of the variance into factors. Varimax (65) is the most widely used rotation technique, and it attempts to reduce the number of variables with higher loadings within a factor, and also the number of variables associated with several factors simultaneously (64).

1.3.2. Linear Discriminant Analysis (LDA)

Linear discriminant analysis (LDA) is a statistical method which seeks a linear combination of the variables in order to achieve the best discrimination between the initial

groups investigated (66). Moreover, it can be employed to define decision rules in order to classify a new sample, the class of which is unknown.

This method finds the linear combination of the features that maximizes the ratio of 'between-class' variance to the 'within-class' variance in any particular dataset, thereby guaranteeing maximal separation (67).

If the dataset is represented by the matrix $X = (x_1, x_2, \ldots x_n)$, where n is the number of observations, x_i being an observation described by q features, then μ_k is the mean of a class C_k and μ is the overall mean of all the observations:

$$S_B = \sum_k (\mu_k - \mu)(\mu_k - \mu)^t \quad (5)$$

$$S_w = \sum_k \sum_{x_i \epsilon C_k} (\mu_i - \mu)(\mu_i - \mu)^t \quad (6)$$

S_B and S_W represent the 'between-class' and 'within-class' scatter matrices respectively. The sum of both gives the covariance matrix for the whole dataset.

The aim is to seek and find a projection of the dataset, in the d dimensional plane, where it achieves a maximum separation between the mean values of projected classes, and minimum variance within each projected class so that $w^t S_B\, w$ is maximized and $w^t S_W\, w$ is minimized. This dual objective can be reached through the vector w_{opt}, which attemps to maximize the following function:

$$J(w) = \frac{w^t S_b w}{w^t S_w w} \quad (7)$$

This LDA approach is similar to PCA, but in this case we not only seek to find the components that maximize the variance, but additionally, we attempt to achieve a maximal

separation between classes, differentiating between variability 'between-groups' (S_B) and 'within-groups' (S_W). If the structure underlying the dataset reveals that $S_B >>> S_W$, then PCA also performs well for classification purposes.

1.3.3. Partial Redundancy Analysis (pRDA)

RDA is a technique that combines regression and PCA in order to model multivariate response data (68). Indeed, RDA (69) with a single 'response' variable is equivalent to multiple linear regression modelling. The operation of this method can be viewed as a multivariate linear regression of *Y* (response variables matrix, *n* x *p*) on *X* (explanatory variables matrix, *n* x *m*), yielding a matrix of fitted values, known as $\hat{Y}$. Subsequently, a PCA on $\hat{Y}$ is performed in order to obtain a matrix of the canonical axes (similar to the scores matrix in a PCA).

Permutation tests are usually employed to check if the linear combinations of *X* are truly explaining Y, and consequently the R^2 value, a parameter that represents how well a model fits the original data (with a score of 0 indicating an absolute lack of fitting, and 1.00 a perfect fitting of the data), together with the *p*-value obtained when the observed case is tested against those obtained after randomly permuting the y_i variables within the *Y* matrix, perhaps several thousand or more times.

Partial Redundancy Analysis (pRDA) is method first proposed by Davies & Tso in 1982 (70), in which an additional matrix of covariables *W*, influences the response variables *Y*. This approach is applied to control the known effects of a covariable, when analysing the effect of a set of variables *X* on *Y* (71). Another application of this model is to isolate the effect of a single explanatory variable or factor.

1.3.4. Correlated Component Regression (CCR)

Correlated Component Regression (CCR) is an ensemble dimension reduction regression technique that provides reliable predictions even with near multicollinear data (72). Correlation amongst variables, known as multicollinearity, is a common problem encountered when dealing with large datasets, and consequently, traditional regression techniques may estimate unstable coefficients (73). Situations where the number of predictor variables *P* approaches or exceeds the sample size *N* give rise to major problems, and such instability is often accompanied by perfect or near perfect predictions of the regression model developed. However, this seemingly good predictive performance is usually associated with overfitting, and is not accurate when new samples are employed to test the model (72).

CCR proposes the prediction of the dependent variable based on *K* correlated components. If $K = 1$, CCR is equivalent to the corresponding Naïve Bayes solution (probabilistic classifier based on the application of Bayes' theorem with independence assumptions) (74). It is further suggested that for $K > 1$, CCR represents a natural extension of a Naïve Bayes model applied to multiple dimensions (74).

Estimation of components: CCR utilizes $K < P$ correlated components in place of the *P* predictors to estimate the response variable (75). Each component S_k is an exact linear combination of the variables, $X = (X_1, X_2, \ldots X_P)$. The first component S_1 captures the effects of those predictors that have direct effects on the outcome (72). Unlike PCA, the objective is not to explain the correlation/covariance matrix through the weights of the components (percentage of variance explained), but to compute the weights with the aim of maximizing

the ability to predict the outcome (75). The CCR-linear model (CCR-LM) algorithm proceeds as follows:

Estimate the loading $\lambda_g^{(1)}$, on S_1, for each predictor g = 1, 2,…*P*, as the simple regression coefficient of the regression of *Y* on X_g. Component S_1 captures the direct effects of *X* for the regression *y* on *X* as a weighted average of the one predictor model.

$$\lambda_g^{(1)} = \frac{Cov\,(Y,X_g)}{Var(X_g)} \tag{8}$$

$$S_1 = \sum_{g=1}^{P} \lambda_g^{(1)} X_g \tag{9}$$

The first component S_1 is computed as a linear combination of *X* using $\lambda_g^{(1)}$ as weights. Similarly, predictions for the 2-component CCR model are obtained from the simple OLS regression of *Y* on S_1 and S_2. Components are related to each other, and they are not orthogonal as in other techniques (PCA, Partial Least Squares); this correlation allows the mutual enhancement of the predictive abilities of the whole set of components, so that S_2 improves the performance of predictor S_1, S_3 improves that for S_2, and so forth, with the aim to achieve the desired effect of removing 'extraneous variation'.

Component $S_{k'}$ for $k' > 1$, is defined as a weighted average of all 1-predictor partial effects, where the partial effect for predictor *g* is computed as the partial regression coefficient in the OLS regression of *Y* on X_g, and also on all previously computed components S_k,k = 1,… k' -1 (75).

$$Y = \alpha + \gamma_{1.g}^{(2)} S_1 + \lambda_g^{(2)} X_g + \varepsilon_g^{(2)} \tag{10}$$

With the aim of representing the model developed in a simpler fashion by regression coefficients, the CCR model can be expressed as follows:

$$\hat{Y} = \alpha^{(k)} + \sum_{k=1}^{k} b_k^{(k)} S_k = \alpha^{(k)} + \sum_{k=1}^{k} b_k^{(k)} \sum_{g=1}^{P} \lambda_g^{(k)} X_g = \alpha^{(k)} + \sum_{g=1}^{P} \beta_g X_g \quad (11)$$

Therefore, the regression coefficient β_g is the weighted sum of the loadings, where the weights are the regression coefficients for the components (75):

$$\beta_g = \sum_{k=1}^{k} b_b^{(k)} \lambda_g^{(k)} \quad (12)$$

M-fold Cross Validation (CV): The purpose of CV is to improve the performance of the classification model by assigning a fraction of the original sample size to a training set and the remaining to a 'test set'. The first of these contains the samples employed to develop the model, whilst the second one is employed to check how effective the model is when these samples are tested in order to predict their classification status.

CCR employs M-fold validation, and runs this procedure several times iteratively. Each round provides one set of CV performance statistics. One round of M-fold validation randomly divides a sample of n cases into M mutually-exclusive sub-groups, known as folds, and obtains a similar number of samples within each fold.

The first fold is the 'test sample', and the remaining folds are used as 'training samples' employed to estimate the model performance. The Q^2 statistic is typically used to evaluate the performance of the model in the validation fold. Q^2 is the cross-validated R^2 value and is computed utilising the Predictive Error Sum of Squares (*PRESS*) and the Total Sum of Squares (*TSS*) (Equation 9). Q^2 values are always ≤1, and it can indeed assume

negative values when *PRESS* > *TSS*, revealing that the model performs worse when it is evaluated with the 'test set' than the mean response of the 'training set' (76):

$$Q^2 = 1 - \frac{PRESS}{TSS} = 1 - \frac{\sum_{i=1}^{n}(y_i - \hat{y}_i)^2}{\sum_{i=1}^{n}(y_i - \bar{y})^2} \quad (13)$$

This result on fold 1 is then stored, and the process is repeated for the second fold. The model's predictive performance is then tested on this 2nd validation fold, and the results aggregated with the previous CV performance (from fold 1). The process is then repeated for the remaining folds.

Step-Down Procedure: This approach works in conjunction with M-fold cross-validation. For a particular value of *K* (number of correlated components), a model with all possible predictors is initially estimated. Subsequently, the least important predictors are left out based on their standardised effect (Equation 14), and the Q^2 value for the new model is obtained using the original set of predictors minus the 'worst' (75). This process then repeats until we have Q^2 values for every possible model (75).

$$\beta_g^* = \left(\frac{\sigma_g}{\sigma_y}\right)\beta_g \quad (14)$$

CCR uses a step-down variable selection algorithm in order to remove irrelevant predictors, which commences using all the variables for developing the model; subsequently, it eliminates those variables with the smallest standardised coefficients one by one, re-estimating the model at each step (72).

1.3.5. ROC curve analysis

ROC (Receiver Operating Characteristic) curve analysis represents a relative balance between the benefits (true positives) and costs (false positives) of MVA models (77), and is widely considered to be the most objective and statistically-valid method for biomarker performance evaluation (50). ROC curves are often summarized into a single metric known as the area under the ROC curve (AUC) depicted in a 2D plot in which the True Positive Rate (TPR) is plotted on the y-axis, and False Positive Rate (FPR) is plotted on the x-axis.

	TRUE CLASS			
DISEASE	**HEALTHY**			
True positives (TP)	False positives (FP)	**DISEASE**	**PREDICTED**	
False negatives (FN)	True negatives (TN)	**HEALTHY**	**CLASS**	

Table 1.1. General confusion matrix

$$TPR\ (sensitivity) = \frac{TP}{TP+FN} \quad (15)$$

$$TNR\ (specificity) = \frac{TN}{TN+FP} \quad (16)$$

$$ACC\ (accuracy) = \frac{TP+TN}{TN+TP+FP+FN} \quad (17)$$

Sensitivity is the ability of the model to classify diseased patients as diseased (or controls as control), and specificity is the ability of the model developed to correctly classify control (non-diseased) participants. Both terms are major parameters utilised to assess the performance of a diagnostic/classification rule. Indeed, the AUC is conditioned by both values, which inform us about the suitability of the model proposed, i.e. AUC values are

considered excellent if they lie between 0.90 - 1.00, good for 0.80 - 0.90, fair for 0.70 - 0.80, poor for 0.60 - 0.70 and of no value for ≤0.6) (78).

1.4. ARTIFICIAL INTELLIGENCE BASED TECHNIQUES

1.4.1. Random Forests (RFs)

Random Forests is a prediction/classification model technique consisting of an ensemble of classification and regression tree-structured classifiers (79).

Decision trees are classifiers which use a single feature at each non-terminal node, so that a sample is classified to the left or the right branch at that specific node if its value for that feature is greater or less than the threshold specified at that node. At each split, the data is partitioned in two mutually-exclusive groups, and attempts to achieve as much homogeneity as possible in each group; subsequently, the splitting is repeated for each group in order to improve this homogeneity within them, but with the constraint of having a tree relatively small and easy to interpret (80). Once the tree is unable to continue the splitting of samples into different groups, the process completes. The tree can then be 'pruned' back to the desired size.

In 1984, Brieman, Olshen, Friedman and Stone published the book '*Classification and Regression Trees'*, and developed the *CART* software (81). This book presented the applicability of RFs and its successful performance when attempting to solve a range of problems that one of the researchers faced when he was working at the UC San Diego Medical School.

RFs uses an ensemble of classification trees; each of these trees is grown by random feature selection from a 'bootstrap' sample ['training set' sub-samples with replacements

obtained from the original dataset (82)] at each branch (83). Class prediction is based on the average classification performance of the aggregate of trees. The process of building up a tree consists of selecting a bootstrap sample of 63.2% (on average) from the original whole sample set, and then a random group of variables are chosen for splitting at a particular node. The remaining 36.8% sub-set is then employed to obtain an unbiased estimate of the classification error (out-of-bag error, OOBE error) (84). Since the OOB observations are not used for fitting the trees, this is a cross-validated accuracy estimate, and hence it represents an unbiased estimation of the generalization error (79). Variable importance is evaluated *via* measurements of the increase of the OOB error value when it is permuted (79). The OOB error estimate ranges from 0 (if the model is able to predict with a 100% in accuracy the class of the test set) to a value of 1.00 (no sample from the test set was correctly classified).

1.4.2. Support Vector Machines (SVMs)

Support Vector Machines were originally developed in 1982 by Vapnik (85), and the most relevant outcome appeared in 1992 with the seminal Boser, Guyon and Vapnik paper: '*A training algorithm for optimal margin classifiers*', in which this technique was formally proposed (86).

SVMs is a classification algorithm that operates by finding the decision surface that can more clearly separate samples from different classes, and hence has the largest distance between borderline samples (*support vectors*). Separation is then achieved by identifying these *support vectors* for the respective classes, identifying the separating *hyperplane* (space of *K-1* dimensions constructed in a *K*-dimensional space, where $K > 3$) in between, so that these points are the most influential ones over the parameters selected to 'draw' this hyperplane in such a manner that moving a support vector moves the hyperplane. However,

the remaining samples do not have any influence in the process of seeking of this hyperplane. Therefore, the algorithm generates the weights, and only considers the support vectors to define their values, and hence the boundary. Nevertheless, if this decision surface does not exist, then the dataset has to be mapped onto a higher dimensional space where this decision surface exists. This transformation is known as the *Kernel trick.*

If the training set $x_i \in R^n$, $i = 1 \ldots m$ where each of the x_i (samples) belong to one of the two categories y_i, indicated by either -1 or 1, SVMs finds a hyperplane with the parameters *(w,b),* using the following convex optimization problem to obtain them (86):

$$\min_{w,b,\epsilon} \frac{1}{2} w^t w + c \sum_{i=1}^{N} \epsilon_i \qquad (18)$$

subject to $y_i(w^t x_i + b) \geq 1 - \epsilon_i$, where $\epsilon_i \geq 1$, for $i = 1,\ldots N$

In Equation 18, *c* works as a regularization parameter which acts as a 'slack' constant, and which is a 'trade-off' between the ability of the system to model accurately using the training set, and its predictive performance (87). If *c* is small, then the margin is large, so constraints are easily ignored; however, if *c* is large, then the margin is narrow, and therefore constraints are hard to ignore, so that *c* controls the margin width. ϵ_i is a measure of misclassification rate and is also known as the *'slack variable'.* The function of this term is to reduce the overfitting problem, enhancing the performance of SVMs, but also allowing a fraction of training sample objects to be within the margin or even misclassified in order to not introduce more complexity within the model (i.e., a 'soft' margin classifier).

1.4.3. Genetic Algorithms (GAs)

GAs are randomized search and optimization algorithms inspired by Darwin's theory of evolution that were introduced by Holland in 1975 (88). GAs function as a simulation of an evolutionary process, in which a population of solutions evolve over a sequence of generations (89) (Figure 1.9). Each chromosome represents a potential solution, and the fitness value associated with each chromosome indicates its relevance to obtain the best possible solution (90).

***Encoding and Initial Population*:** A chromosome is a string of 'bits' with a length determined by the total number of variables. The presence/absence of a variable in the chromosome is given by the value 1 or 0 in the corresponding *i*-th place within the chromosome; this assignment is generated randomly. Consequently, each chromosome represents a different sub-set of features.

Selection, Crossover and Mutation: The selection process involves the principle of '*Survival of the fittest'*, i.e. improved solutions are selected to get through to the next generation; notwithstanding, 'bad' solutions are discarded. The 'good & bad' criteria are given by the fitness function.

Crossover causes a structured yet randomized exchange of genetic information amongst solutions/chromosomes, with the aim that effective solutions could be crossed with other high-performance ones in order to generate improved models. This process is applied with a probability, called *crossover rate*, i.e. the probability that a chromosome (solution) experiences cross-over during its reproduction process. A *crossover rate* of 1.00 indicates that all the chromosomes experience crossover, so no unchanged solutions go through to

the next generation. For instance, a value of 0.75 indicates that a chromosome may go through to the next generation unchanged with a probability of 0.25.

Mutation works by modifying the value of each gene with a certain probability. This operator then restores missed or unexplored genetic material stored in the population in order to prevent the premature convergence of the GAs to sub-optimal solutions (89).

Fitness function: The fitness function is a measure of the 'goodness' of a solution, and can be used to rank chromosomes/solutions against the other chromosomes. It can also be employed to assess feature sub-set selection, in order to simplify the model using less features, achieving at least the same level of success when classifying samples according to their correct class. In a classification problem context, the fitness is equivalent to evaluations of the predictive ability of the model using a sub-set of genes (variables).

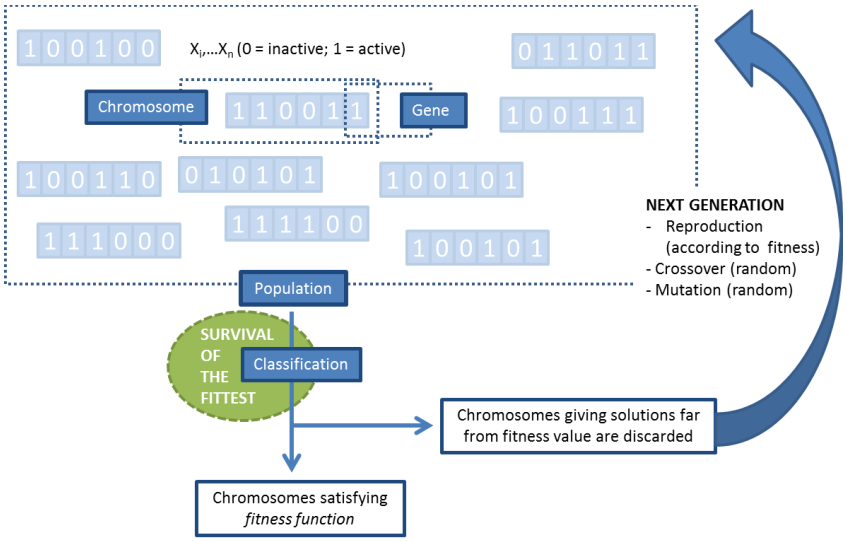

Figure 1.9. Schematic representation of a GAs procedure for a classification problem: variables (x_i...x_n) are coded in chromosomes as 1 or 0 if they are or are not included in the model respectively. The whole process moves on for *N* number of generations, or until the fitness value is attained.

1.5. NIEMANN PICK TYPE C1 DISEASE

1.5.1. Description

Niemann-Pick type C (NP-C) disease is a neurodegenerative lysosomal storage disorder caused by mutations in the *NPC1* and *NPC2* genes, the hereditability of which is autosomic recessive (91). Approximately 95% of patients have mutations in the *NPC1* gene (mapped at 18q11) which encodes a large membrane glycoprotein located in late endosomes (92) . The remaining 5% have mutations in the *NPC2* gene (mapped at 14q24.3) which encodes a small soluble lysosomal protein that binds cholesterol in the lumen of this organelle (92). Patients with NP-C1 and NP-C2 diseases are indistinguishable, both clinically and in terms of the standard biochemical tests for NP-C diagnosis (93).

In 1984, Pentchev and colleagues made the highly significant discovery that the major biochemical feature of NP-C disease is lysosomal accumulation of LDL-derived, unesterified (free) cholesterol, and consequently, these patients develop a dysregulated sterol biosynthesis, uptake and esterification (94). The estimated incidence of the disease is approximately 1:120,000 live births, based on studies performed during the past 20 years (95).

1.5.2. Cell biology of cholesterol

Cholesterol, which is the major steroid present in animal tissues, stabilizes the structure of plasma membranes, regulates membrane permeability, and reinforces the liquid ordered phase of lipid bilayers (96). It is essential for myelin formation (97), and during development it has a major signalling pathway function, specifically in the hedgehog signalling pathway, in which cholesterol covalently modifies the proteins involved in order

to render them functional (98, 99). Cholesterol binds to the amino terminal peptide arising from the autoproteolitic cleavage of the original protein (i.e. those involved in the hedgehog pathway), and it is only this N-terminal peptide which has signalling activity, involved for example in skeletal (100) and cerebellum development (101). Cholesterol is a precursor of corticosteroids, vitamin D, bile acids and steroid hormones.

Not all mammalian cells are able to metabolize cholesterol. In fact, only liver and steroidogenic tissues do. Nevertheless, other tissues unable to metabolize this molecule are capable of modulating its concentration in the membranes by regulating the biosynthesis, uptake, and export of cholesterol from the cell through ATP-binding cassette (ABC) transporters (102).

Cholesterol can be obtained by cells through two routes. Firstly, it can be acquired from the diet associated with plasma low-density-lipoproteins (LDLs), in which cholesterol from the liver can be transported through the circulation to extra-hepatic tissues, being initially packaged in very-low-density-lipoproteins (VLDLs). In the circulation, VLDLs are converted to LDLs by the action of lipoprotein lipase.

LDLs are taken up by cells *via* LDL receptor-mediated endocytosis. The interaction of LDLs with LDL receptors requires the presence of apoB-100, the exclusive apolipoprotein of LDLs. The endocytosed vesicles (endosomes), derived from the internalization of the membrane, then fuse with lysosomes, where the apoproteins (originally contained in LDLs), are degraded; subsequently, cholesteryl esters are hydrolysed within the lysosome yielding free cholesterol. This cholesterol moiety is then incorporated into the plasma membranes where required, predominantly at the cytoplasmic membrane, where LDL-cholesterol released from lysosomes can be rapidly detected (103). The caveolae (special region within the membrane which is rich in cholesterol and sphingomyelin) are the first destination for

the free cholesterol carried by LDL. However, to elicit homeostatic responses and to be transformed to cholesteryl esters and bile acids, or indeed incorporated into lipoproteins, cholesterol must first reach the endoplasmic reticulum (ER) (103).

Alternatively, cholesterol can be generated via *de novo* synthesis in the endoplasmic reticulum. LDLs are not able to go through the blood-brain barrier (BBB) and supply the brain; furthermore, this *de novo* pathway is the only and exclusive mechanism for the central nervous system (CNS) to obtain cholesterol. Free cholesterol synthesised in the glia and complexed with apolipoprotein E is then delivered to neurons (104). Although LDL cannot cross the BBB, cholesterol can egress from the CNS as 24-hydroxy-cholesterol. Furthermore, 27-hydroxy-cholesterol can also cross the BBB in the opposite direction (105).

1.5.3. NPC1 and NPC2 proteins

The multivesicular late endosomes accommodate two proteins, NPC1 and NPC2, which are crucial for moving cholesterol out from the endosomal system (Figure 1.10). Therefore, deficiencies in the levels or activity of these proteins lead to the accumulation of LDL-derived unesterified cholesterol in LE (106).

In NP-C disease, the movement of LDL-derived cholesterol to the endoplasmic reticulum and plasma membrane is delayed, resulting in altered regulation of cholesterol homeostasis in the ER. Hence, cholesterol and LDL-receptor synthesis is enhanced to compensate for the apparent lack of cholesterol detected by the cell; additionally, cholesterol esterification is diminished (107). In contrast, intracellular transport of cholesterol delivered from exogenously-supplied high-density-lipoproteins (HDLs) seems to be unaffected in the disease, and this is presumably ascribable to this source of cholesterol not entering late endosome/lysosome via endocytosis (107).

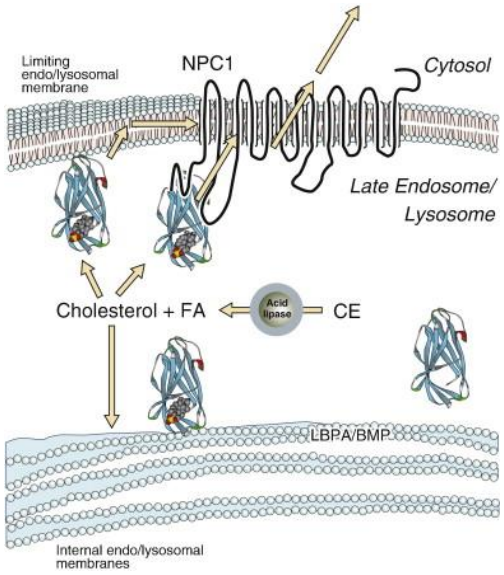

Figure 1.10. Potential mechanism for NPC1/NPC2-mediated cholesterol export from late endosome/lysosome: CE, cholesteryl ester; FA, unesterified fatty acid; LBPA/BMP, lyso-*bis* phosphatidic acid, also known as *bis*-(monoacylglycerol)phosphate (108). NPC2 (soluble protein) binds unesterified cholesterol in the late endosome/lysosome with the iso-octyl chain in the binding pocket, an event that may be enhanced by *bis*-(monoacylglycero)phosphate. NPC2 transfers cholesterol to the N-terminal loop of NPC1 (a multi-pass membrane protein) which binds cholesterol, accommodating the hydroxyl group in the binding pocket. Cholesterol is exported from late endosome/lysosome by an unknown mechanism (109). [Figure taken from (108)]

Other biomolecules are also stored within the lysosome in this disease, including complex gangliosides such as GM_1 and GM_2, glucosyl and galactosylcerebrosides (108). NPC1 and NPC2 proteins have been proposed to be involved in the endosomal/lysosomal processing of these lipids, since simple gangliosides (e.g. GM_2, GM_3) can be delivered to Golgi after being endocytosed by the late endosome/lysosome system to generate more complex

structures as an alternative to the *de novo* synthesis pathway (110). Therefore, mutated NPC1 and/or NPC2 lead to the accumulation of these gangliosides.

A sequential process of pathological effects derived from NPC1 gene mutation/inactivation has been recently proposed, in which the first consequence of this genetic alteration is sphingosine storage, folllowed by deficient calcium homeostasis within the lysosome which leads to a reduced calcium release and consequently a block in late endosome/lysosome fusion that finally causes unsterified cholesterol storage (111). Accordingly, the storage of cholesterol, which was previously thought to be the main activator of the molecular disease process, is actually the trigger of all the neurodegenerative processes that subsequently occur.

1.5.4. Disease manifestations

The manifestation of NP-C1 disease is very heterogeneous, and actually it can vary between siblings (95), which leads a delay in in diagnosis of 5–6 years from the onset of neurological symptoms (112, 113). Therefore, the individual features illustrated in Figure 1.11 are not NP-C1-specific, but the conjunction of all of them generates a clinical picture which is considered disease-specific.

Neurological features include abnormal saccadic eye movements, ataxia, dystonia, dysarthria and dysphagia. In the cerebellum, Purkinje cells die in a characteristic pattern that exacerbates with age and disease state (114). The age of onset of these neurological manifestations has a major impact on the severity of the disease; however, the progression remains essentially the same (Figure 1.11) (114).

Systemic symptoms include hepatosplenomegaly and pulmonary failure (115), the latter being more associated with the most severe cases of the disease (116); indeed, the

strongest visceral hallmark of NP-C1 is splenomegaly, which is a more powerful indicator when it presents along with the neurological symptoms delineated above.

Psychiatric symptoms are also part of the disease process, including cognitive decline, psychosis which typically appears in adolescence or early adulthood, and disruptive or aggressive behaviour presenting at the same stage (117).

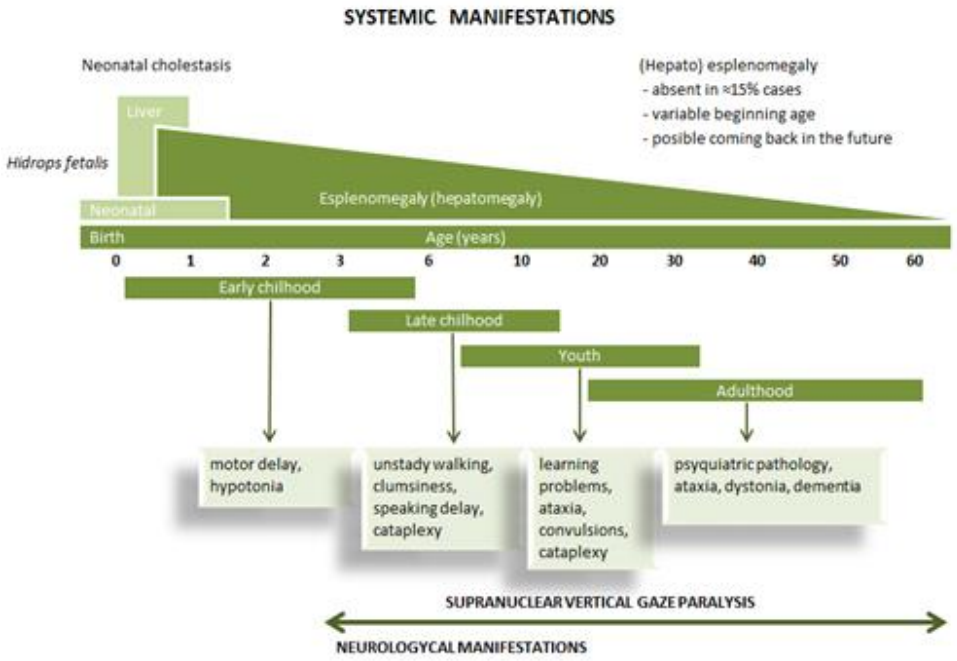

Figure 1.11. Major clinical disease manifestations and age at onset of neurological symptoms. [Figure adapted from (91)]

1.5.4.1. Hepatic manifestations

NP-C1 is mainly a neurodegenerative disease associated with major organic manifestations, in which the liver is affected. A percentage of NP-C1 patients (approximately 50%) suffer from liver disease, and approximately one tenth of these patients die from liver failure before the first year of age (118). Moreover, NP-C1 disease is one of the most

common disorders responsible for neonatal cholestasis, a disorder in which bilirubin excretion is altered, and consequently, bile salt levels are decreased in the gastrointestinal tract, causing a decreased or even null absorption of fats and hydrophobic vitamins (i.e., vitamins A, D, E and K). In a 20-year investigation conducted at King's College Hospital (London, UK), NP-C disease was found to be the second major cause of neonatal cholestasis, only one place below alpha-1-antitrypsin deficiency (119). Another 2-year study, performed in the USA revealed that NP-C was the first cause amongst all metabolic/genetic disorders of neonatal cholestasis (120).

The liver controls lipoprotein, glucose and cholesterol homeostasis within the body; it has a major synthetic function producing most of the clotting factors, bile, albumin and some vitamins. Additionally, the liver has an excretory function (i.e. bilirubin), participates in the immune response through Kuppfer cells filtering antigens and damaged cells out of the organ, and has a relevant function in the storage of glycogen and certain vitamins. All these functions that are performed by this organ, along with the fact that liver disease is one of the major pathological symptoms of NP-C1, renders investigations involving this organ as a valuable approach to the disease process.

The majority of investigations on NP-C1 liver have been previously focused on the lipid profiles of the hepatic cells (121, 122) or alternatively explore hepatocyte gene expression (123). However, to date low-molecular-mass polar compounds present within hepatic tissue have not been investigated. Indeed, such metabolites are involved in metabolic pathways that may be altered in NP-C1 disease.

Studies previously performed using an NP-C mouse model (124) indicate that this animal model develops a pathological hepatic phenotype similar to that observed in NP-C1 infants (121, 125), showing cholesterol storage, increased levels of liver damage biomarkers

such as alkaline phosphatase, aspartate and alanine aminotransferase, hepatomegaly and the presence of apoptotic cells (122).

1.5.5. Diagnosis

When a patient is suspected to be suffering from NP-C disease, then a genetic test is carried out to check for mutations in either the *NPC1* or *NPC2* genes. If at least 1 pathogenic mutation is detected, then this patient is diagnosed with NP-C (126). Contrarily, if these pathogenic mutations are not detected, then the filipin test is performed. This diagnostic test involves the staining of cultured skin fibroblasts from a biopsy obtained from patients, in order to demonstrate free cholesterol accumulation within lysosomes (127), since this dye specifically binds unesterified but not esterified cholesterol.

The LDL-induced cholesterol esterification rate assay also represents a useful complementary evaluation (92). More recently, a preliminary diagnosis of NP-C disease using the filipin test in a blood smear has been proposed (128), but this demonstrated that there were no morphological differences between blood samples collected from healthy controls and NP-C patients; nevertheless, filipin signal intensities were much higher in NP-C patients than those of healthy controls (128). However, the filipin test gives inconclusive results in 15% of cases (129). If after these tests the NP-C diagnosis is not absolutely clear, further DNA, mRNA and protein analyses is required.

Recently, diagnostic markers for NP-C such as plasma oxysterols (130) have been proposed and also the measurement of intracellular acidic compartment volume (mean equivalent of fluorescence - MEFL/LysoTracker) (131). However, both are complementary to the above diagnostic methods, and they are required to be more focused on the development of the disease, its assessment, and its response to treatment. More recently, a new blood biomarker has been proposed, specifically lysosphingomyelin-509 (a derivative of

lyso-sphingomyelin), which is detectable at higher levels in blood collected from NP-C1 patients by LC-MS/MS (132).

1.5.6. Treatment

NP-C presents a complex and wide spectrum of symptoms derived from the pathophysiology associated with this disease, and different pharmaceutical approaches have been explored in order to ameliorate the disease process.

NP-C disease also involves behavioural disturbances, catatonia, psychosis and depression (133); indeed, general psychotic symptoms appear in early adulthood in approximately 35% of NP-C patients (113). Moreover, in view of the high incidence of epilepsy in these patients [seizures are common manifestations of the disease in young patients (134)], anti-epileptic drugs are also employed, including sodium valproate (VPA), iamotrigin and levetiracetam (135). VPA is also an inhibitor of histone deacetylases (HDACi), a process that will be further described as a target. However, VPA is one of the weakest and simplest HDACi, and indeed its performance was not recognized until long after preliminary studies were performed on its therapeutic properties (136).

Differing medication strategies have been proposed for the treatment of NP-C disease according to the different classes of its clinical development. Disease-induced apoptosis has been proposed as one of the targets, so that an inhibitor of protein tyrosine kinase, imatinib (Gleevec, STI571), was tested against the c-Abl/p73 system, proteins involved in cerebellar neurodegeneration in NP-C (137). By inhibiting these proteins, Alvarez *et al.* reported an increase in Purkinje cell survival, and also a reduction of the apoptotic process in the cerebellum of NP-C mice; accordingly, neurological symptoms of this mice

model were improved, together with a reduction of weight loss coupled with a longer mean lifespan (137).

A different approach is the therapeutic use of cyclodextrins, which are cyclic polysaccharides with a truncated cone shape that has the ability to carry hydrophobic molecules inside its crevice whilst having a hydrophilic outer surface that renders this polymer soluble in polar solvents and fluids. Cyclodextrin has been proven to ameliorate the neurological symptoms in NP-C1 disease in the NP-C1 mouse model (BALBc/*NPC*^{nih}) (138) in view of its ability to remove cholesterol from neurons; although this process remains unclear. Furthermore, a cyclodextrin derivative, 2-hydroxypropyl-cyclodextrin has also been proven to reduce the activation and influx of macrophages in both liver and brain, together with a corresponding improvement in Purkinge cell survival and consequently a longer lifespan (139).

Another group of compounds tested for the treatment of NP-C disease are histone deacetylases. These agents increment the expression of some chaperones that allow mutant NPC1 proteins to be delivered from the ER to LE/L system. If these NP-C1 mutant proteins exhibit sufficient activity to export cholesterol from the lysosome, then its accumulation may be ameliorated as well as the clinical manifestations derived therefrom (140).

In view of the inflammatory processes that take place in the brain of NP-C1 patients some treatment strategies targeted on the amelioration of this symptom have also been investigated. The activation of microglial cells and macrophages in the NP-C1 mouse brain also gives rise to oxidative stress, which has been targeted in combination therapies such as ibuprofen/aspirin plus vitamin C (141); indeed, in the work performed by Smith *et al.*, they show how the use of an NSAID such as ibuprofen can improve the lifespan of animals in a mouse model of NP-C1, based on survival curves (141). Another combined therapy using

ibuprofen as an anti-inflammatory agent is its employment with both curcumin and MGS, in order to target GSL storage (MGS), inflammation (ibuprofen) and calcium homeostasis (curcumin) (142). In this work, the authors showed how a combination therapy comprising curcumin and MGS was more efficient than the three drugs together, and then suggested how anti-inflammatory treatment can 'act as a double-edged sword', ameliorating the symptoms in the first instance and then becoming gradually detrimental, as previously reported for Sandhoff disease (143), another LSD.

1.5.6.1. Miglustat

One sub-group of iminosugars is the N-iminosugars, in which the anomeric carbon and the intracyclic oxygen have been replaced by an -NH and a methylene group respectively. One of the members of this group is miglustat (MGS).

MGS (OGT 918, N-butyl-deoxynojirimycin) is a small molecule (MW = 218) derivative of a family of polyhydroxylated alkaloids extracted from some plants and micro-organisms, specifically, a deoxynojirimicyn derivative.

This agent inhibits glucosylceramide synthase and the synthesis of all glucosylceramide-based GSLs, including lactosylceramide and gangliosides (Figure 1.12), since this is the first step in glycosphingolipid synthesis (144). The type of inhibition of this drug was determined by using ceramide as an acceptor, and revealed that glucosyltransferase activity was competitive for ceramide and non-competitive for UDP-glucose, confirming that this inhibition was performed by ceramide mimicry (145).

MGS can effectively pass the blood-brain-barrier (BBB), and has the potential to be effective in treating LSD with neurologic manifestations; indeed, the observational cohort study carried out by Pineda *et al*. (115) indicates that MGS stabilizes neurological disease in

the majority of patients with NP-C. MGS also provides protection against oxidative stress (146), which appears to be part of the pathological cascade of symptoms of the disease (146, 147). Moreover, beneficial effects on axonal degeneration were also shown in patients receiving MGS treatment (148).

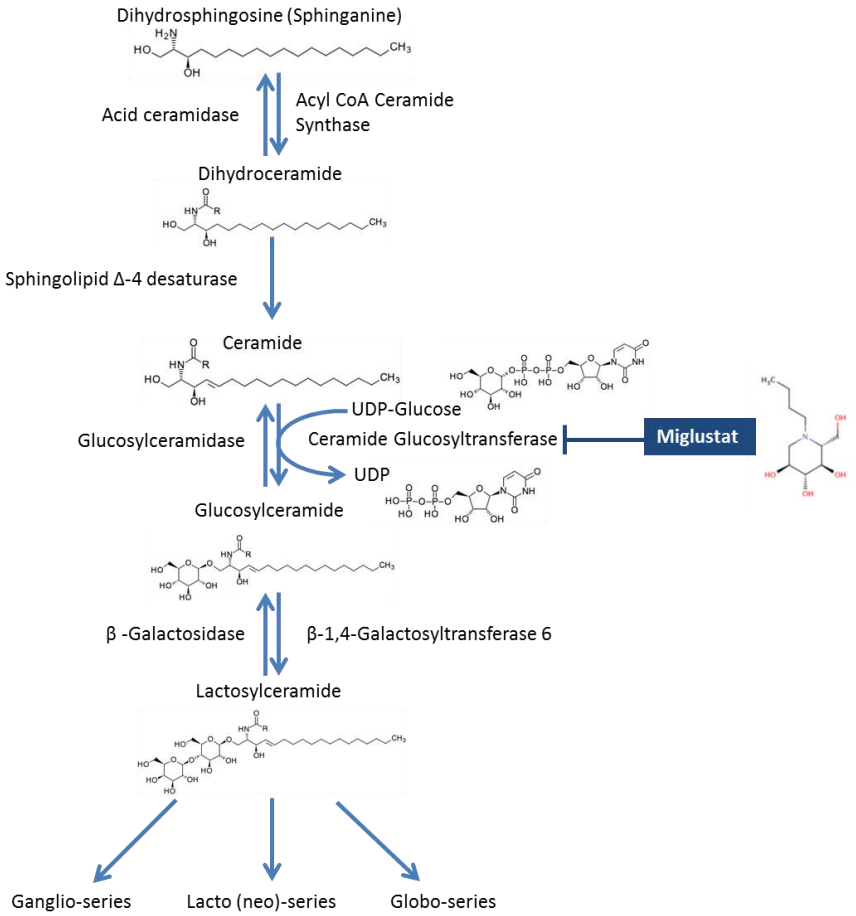

Figure 1.12. Key steps in the biosynthesis of GSLs: ceramide glucosyltransferase gives rise to ceramide glycosylation generating glucosylceramide, a step inhibited by MGS. This glycosphingolipid is subsequently converted to lactosylceramide which is the precursor of all the glycosphingolipid series shown.

Prior to the approval of MGS as a therapeutic agent for NP-C1 disease, it had been used to treat other GSL diseases such as Tay-Sachs and Sandhoff diseases (149). Indeed, it was approved by the European Medicines Agency (EMA) in 2002, and by the USA Food and Drug Administration (FDA) in 2003 for the treatment of type I Gaucher disease (150, 151). However, for the treatment of NP-C disease it was only approved in 2009 by the EMA; in fact, despite its use being approved in most countries, this has not been accomplished in the USA. It was first proposed for the treatment of this condition based on evidence of slower disease progression and prolonged survival in animal models (108). Subsequently, clinical studies demonstrated the stabilization of neurologic disease in both children and adults treated with MGS (152).

The recommended daily dose is 200 mg 3 x daily in adults, and is adjusted according to body surface area in patients under 12 years of age (EMA). It was shown to be rapidly absorbed, and maximal plasma concentrations are attained on average 2.0 - 2.5 hr. after dosing, on average. Renal clearance is about 150 mL/min (no biotransformations have been reported), suggesting that the renal elimination is mainly through filtration and also that the risk for interactions with drugs which are eliminated by active secretion is low (EMA).

MGS was firstly discovered to improve neurological dysfunctions together with an increase in lifespan in murine and feline NP-C models after its daily administration (153). Saccadic eye movement velocity, a parameter for disease progression exploration, is decreased in both the vertical and horizontal direction in NP-C1 patients (154-156); nonetheless, when these patients receive MGS treatment, this defect is improved (157). Moreover, about 72% of patients treated with this drug over 12 months presented stabilized disease status (based on ambulation), swallowing and cognition (158).

CHAPTER 2

^{1}H NMR LINKED METABOLOMICS ANALYSIS OF URINE COLLECTED FROM NP-C1 PATIENTS, MIGLUSTAT-TREATED PATIENTS AND HETEROZYGOUS CARRIERS

2.1. URINE SAMPLES PREPARATION FOR NMR ANALYSIS

107 urine samples collected from untreated NP-C1 patients, heterozygote carriers as controls and miglustat (MGS)-treated patients were stored at -80^{o}C prior to ^{1}H NMR analysis. Urine samples were provided by Prof. Platt and colleagues at the Department of Pharmacology, University of Oxford (Oxford, UK); these samples were collected with informed consent and approved by the appropriate Research Ethics Committee (06/MRE02/85). Samples were thawed at room temperature, and 0.60 mL of each sample was centrifuged (5 min., 10,000 x *g*) in order to remove cells and debris; 0.55 mL of the supernatant was collected from each sample and subsequently spiked with 0.05 mL of D_2O, thoroughly mixed, and 0.60 mL aliquots of the supernatants were then transferred to 5-mm diameter NMR tubes (Norell, UK).

Disease class	NP-C1	Heterozygotes	MGS-treated NP-C1
Samples (male/female)	14 (6/8)	47 (6/26)*	46 (14/32)
Mean age in years (range)	9.9 (0.5-29.6)	57.8 (42.6 - 64.0)**	18.3 (3.0 - 33.0)

Table 2.1. General characteristics of participants included in the urinary NP-C1 metabolomics investigation. *Information regarding the gender of the remaining participants was unavailable. **Mean and range computed only from 8 HET participants in view of a lack of information availability.

Urine samples were collected from 21 NP-C1 disease patients at differing time points throughout a 4 year period, both prior and subsequent to treatment with MGS, yielding a total of 47 samples from patients treated with this therapeutic agent. MGS dose is calculated and based on body surface area for children, whilst adult patients typically receive 600 mg/day. Eight of the patients in the cohort received 3 × 200 mg daily doses, two patients a reduced dose of 2 × 200 mg daily, four patients received a single 100 mg dose, and one patient received 2 × 200 mg daily doses followed by a 100 mg nightly dose. Unfortunately, dosages of valproate received by the relevant NP-C1 disease patients were unavailable to the author; however, those for the control of epileptic seizures in adults typically range from 1 to 2 g daily, and children 10-15 mg/kg/day up to a maximum of 600 mg daily.

Spiking experiments: Standard solutions of authentic biomolecules were prepared in the mM range concentrations in 0.10 M phosphate buffer (pH 7.00). In the case of bile acids (Sigma-Aldrich, UK), they were firstly dissolved in a pH 7.00 buffer solution to reach a final concentration of 10 mM; then, 450 µL of urine samples were spiked with 100 µL of these bile

acids, and 50 µL of D_2O containing 0.05% wt. *d*-TSP) as a lock reference. Subsequently, the mixture was thoroughly mixed and transferred to a 5-mm diameter NMR tube (Norell, UK).

2.2. NMR ANALYSIS OF NP-C1 URINE SAMPLES

1D ^{1}H NMR: Single-pulse ^{1}H NMR spectra experiments were acquired at 298 K on a Bruker AX 600 MHz spectrometer (Queen Mary University of London facility, London, UK). Each spectrum was acquired for 128 scans, 5.6 µs pulses, 32 K (subsequently filled to 65 K) data points and a spectral width of 12.00 ppm. The intense residual H_2O/HDO signal (δ = 4.80 ppm) was supressed using *Presaturation* (Bruker *zgpr* pulse sequence). Spectra were acquired in an automated manner using a sample changer for continuous sample delivery.

^{1}H-^{1}H COSY*:* These experiment were conducted at 300 K on a Bruker AV 400 MHz spectrometer (Leicester School of Pharmacy, De Montfort University). The pulse sequence employed was *cosygpprqf* (Bruker) with presaturation during relaxation delay using gradient pulses for selection. The spectral width in the F1 and F2 axes were 4000 Hz, and 2048 data points were collected in F2. For the urine samples, 256 increments and 32 scans per increment were used. The relaxation delay was 4.5 s for a total acquisition time of ~ 7 hr. Prior to Fourier transformation, a sine function was applied in both time domains.

^{1}H-^{1}H TOCSY: This experiment was carried out at 300 K on a Bruker AV 400 MHz spectrometer (Leicester School of Pharmacy, De Montfort University). Spectra of urine were acquired using *dipsi2esgpph* pulse sequence (Bruker) in which 72 transients per increment and 256 increments were collected into 2k data points over a spectral width of 12 ppm in both dimensions applying the MLEV17 spin-lock scheme with a spin-lock power of 6 kHz. A

recycle delay of 1.43 s was used, and water suppression was achieved using excitation sculpting with gradients, and DIPSI2 sequence was employed for mixing. The total acquisition time per sample was ~ 18 hr.

***1D-TOCSY*:** 1D TOCSY spectra were acquired using the SELMLGP pulse sequence (1D homonuclear Hartman-Hahn transfer using MLEV17 sequence for mixing using selective refocusing with a shaped pulse). This experiment was carried out at 300 K on a Bruker AV 400 MHz spectrometer (Leicester School of Pharmacy, De Montfort University). The mixing time was set to 0.2 s, 256 FIDs were acquired. The duration of the selective 180° shaped pulse was optimized to 80 ms and the power level Gauss shape to 63 dB. The 1D-TOCSY pulse sequence selectively excites only the peak of interest at the specified chemical shift value in the spectrum, which corresponds to a particular proton/group of protons in a molecule, for a period of time (the mixing time), in order to transfer this magnetization *via J*-couplings to all protons throughout the spin system which it is part of.

2.2.1. ^{1}H NMR Urinary profiles of NP-C1 patients

The identities of metabolites present in the urinary ^{1}H NMR spectra acquired were assigned according to chemical shift values, coupling patterns and coupling constants and also from a range of literature sources (45, 159, 160), and then cross-checked with the Human Metabolome Database (HMDB) (161). A combination of both 1D and 2D COSY and TOCSY techniques were employed to confirm these assignments, as was the 'spiking' of these biofluids with appropriate small (μL) volumes of solutions of authentic biomolecules prepared at mM concentrations.

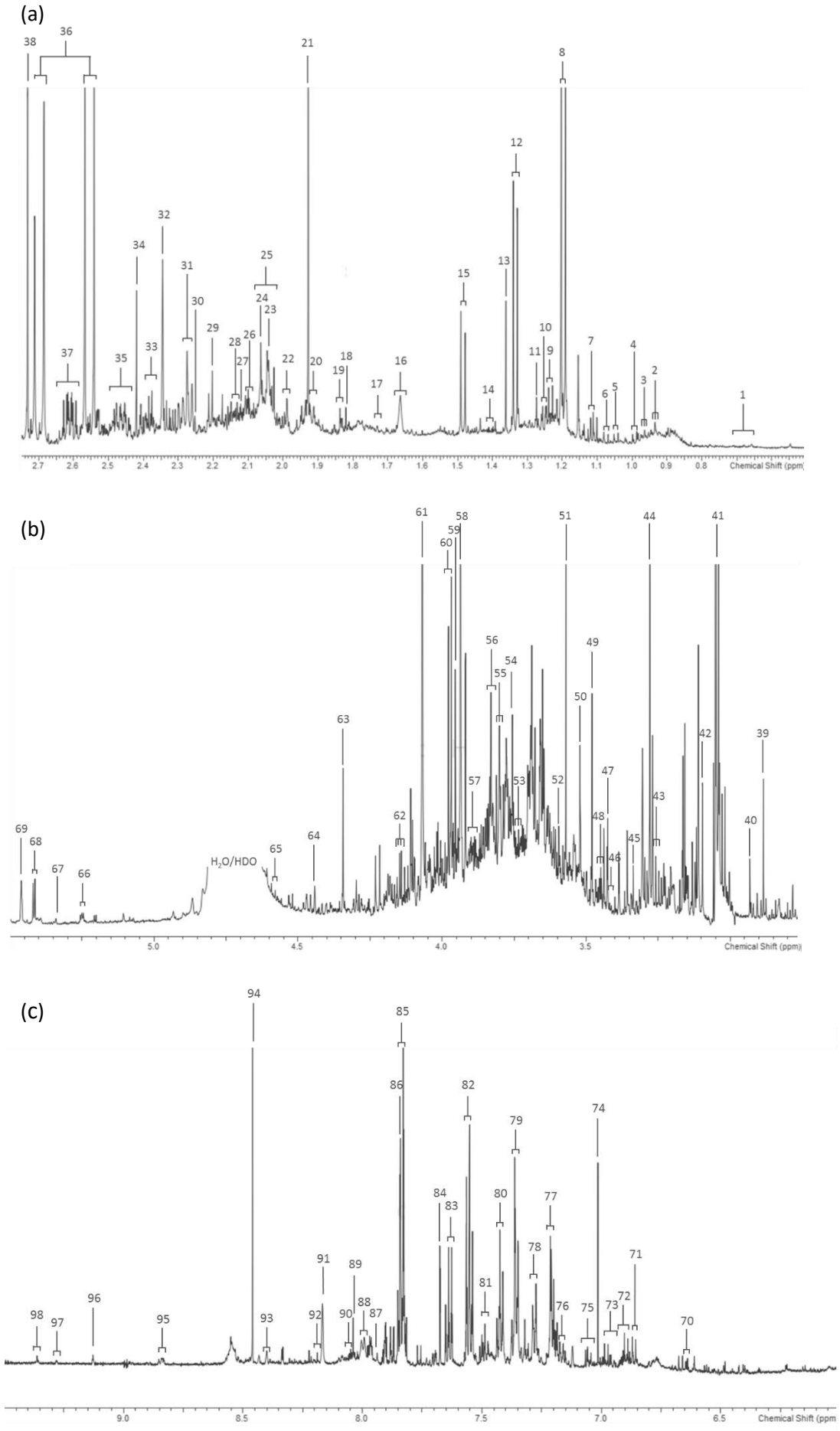
(a)
(b)
(c)
H2O/HDO
Chemical Shift (ppm)

Figure 2.1. (a), (b) and (c), 0.50-2.75, 2.75-5.50 and 6.00-9.50 ppm regions, respectively, of the 600 MHz urinary ^{1}H NMR profile of an NPC1 patient (a typical spectrum is shown): Abbreviations: 1, Bile acids-C18-CH_3; 2, Ile-CH_3; 3, Leu-CH_3; 4, Val-CH_3; 5, Val-CH_3'; 6, Methyl-succinate-CH_3; 7, 2-Oxoisovalerate-CH_3's; 8, 3-Aminoisobutyrate-CH_3; 9, 3-D-Hydroxybutyrate-CH_3; 10, L-Fucose-CH_3; 11, 3-Hydroxyisovalerate-CH_3; 12, Lactate-CH_3; 13, 2-Hydroxyisobutyrate-CH_3's; 14, Lysine-C4-CH_2; 15, Alanine-CH_3; 16, 5-Aminovalerate-C3/4-CH_2; 17, Lysine-C5-CH_2; ; 18, Thymine-C5- CH_3; 19, 2-Hydroxyglutarate-C3-CH_A; 20, Lysine-C3-CH_2; 21, Acetate-CH_3; 22, 2-Hydroxyglutarate-C3-CH_B; 23, N-acetylaspartate-CH_3; 24, N-acetylneuraminate-CH_3; 25, N-acetyl-X-CH_3; 26, Glutamine-C2-CH_2; 27, Methionine-S-CH_3; 28, Glutamine-C3-CH_2; 29, Acetoin-C1-CH_3; 30, Acetoacetate-CH_3; 31, 2-Hydroxyglutarate-C4-CH_2; 32, Pyruvate-CH_3; 33, Glutamate-C3-CH_2; 34, Succinate-CH_2's; 35, Glutamine-C4-CH_2; 36, Citrate-CH_{2A}/CH_{2B}; 37, 3-Aminoisobutyrate-C2-CH_2; 38, Dimethylamine-CH_3's; 39, Trimethylamine-CH_3's; 40, Dimethylglycine-CH_3's; 41, Creatinine-CH_3/Creatine-CH_3; 42, Malonate-CH_2; 43, Taurine-CH_2-NH_3^+; 44, Trimethylamine-N-oxide-CH_3's; 45, Methanol; 46, Cystine-C3/C6-CH_2; 47, *cis*-Aconitate-CH_2; 48, Taurine-CH_2-SO_3^-; 49, 3-Hydroxyphenylacetate-CH_2; 50, Phenylacetate-CH_2; 51, Glycine; 52, Phenylacetylglycine-CH_2; 53, Lysine-C2-CH; 54, Guanidoacetate-CH_2; 55, Ethanolamine-CH_3; 56, Mannitol; 57, Serine-C2/3-CH_2; 58, Creatine-CH_2; 59, Glycolate-CH_2; 60, Hippurate-CH_2; 61, Creatinine-CH_2; 62, Lactate-CH; 63, Tartrate-CHOH; 64, Trigonelline-CH_3; 65, β-Glucose-C1-CH; 66, α-Glucose-C1-CH; 67, Allantoate-CH; 68, Sucrose-C1-CH; 69, Allantoin-CH; 70, 2-Furoylglycine-C3-CH; 71, Tyrosine-C3/C5-CH; 72, 3-(3-hydroxyphenyl)-3-hydroxypropanoate-C1/C6-CH; 73, Phenol-C2/C4/C6-CH; 74, Histidine-C5-CH; 75, Phenol-C3/C5-CH; 76, Tyrosine-C2/C6-CH; 77, Indoxyl-sulphate-C8/C7/C2-CH; 78, Indoxyl-sulphate-C6/C9-CH; 79, Indoxyl sulphate-C2-CH and Phenylalanine-C2/C6-CH; 80, Phenylalanine-C3/C4/C5-CH; 81, Indoxyl sulphate-C6-

CH and Benzoate-C3/C5-CH; 82, Hippurate-C3/C5-CH: 83, Hippurate-C4-CH; 84, 1-Methylhistidine-C4-CH; 85, Hippurate-C2/C6-CH; 86, Histidine-C2-CH; 87, 3-Methylhistidine-C2-CH; 88, Quinolinate-C5-CH; 89, 3-Methylxanthine-C7-CH; 90, Trigonelline-C5-CH; 91, Hypoxanthine-C2/C7-CH; 92, 1-Methylnicotinamide-C5-CH; 93, Quinolinate-C6-CH; 94, Formate-H; 95, Trigonelline-C4/C6-CH; 96, Trigonelline-C2-CH; 97, N-methylnicotinamide-C2-CH; 98, N-Ribosylnicotinamide-C2-CH.

Typical 600 MHz single-pulse ^{1}H NMR spectra of urine samples collected from NP-C1 disease patients and their heterozygous carrier controls contained a multitude of prominent, sharp signals assignable to a wide range of low molecular-mass metabolites (Figure 2.1). Indeed, resonances ascribable to a very wide range of amino acids [e.g. glycine (Gly), alanine (Ala), leucine (Leu), isoleucine (Ile), valine (Val), tyrosine (Tyr) and taurine, etc.], short-chain organic acid anions (e.g., acetate, citrate, formate, fumarate, lactate, pyruvate, succinate, etc.), amines such as methyl-, dimethyl- and trimethylamines, and bile acids, together with many further classes of biomolecules, were readily observable. Indeed, > 100 different metabolites were unambiguously assigned on the basis of the 107 spectra acquired. Some resonances present in the spectra required further work in order to confirm assignments in addition to the simple acquisition of a 1D spectrum, and therefore correlation spectroscopic techniques were applied, such as TOCSY (in both 1D and 2D versions) and COSY. The coupling patterns of the metabolites can be explored by performing these correlation spectroscopy experiments, as can be observed in Figure 2.2, in which 3-aminoisobutyrate (3-AIB) was identified in urine samples using a 1D-TOCSY experiment.

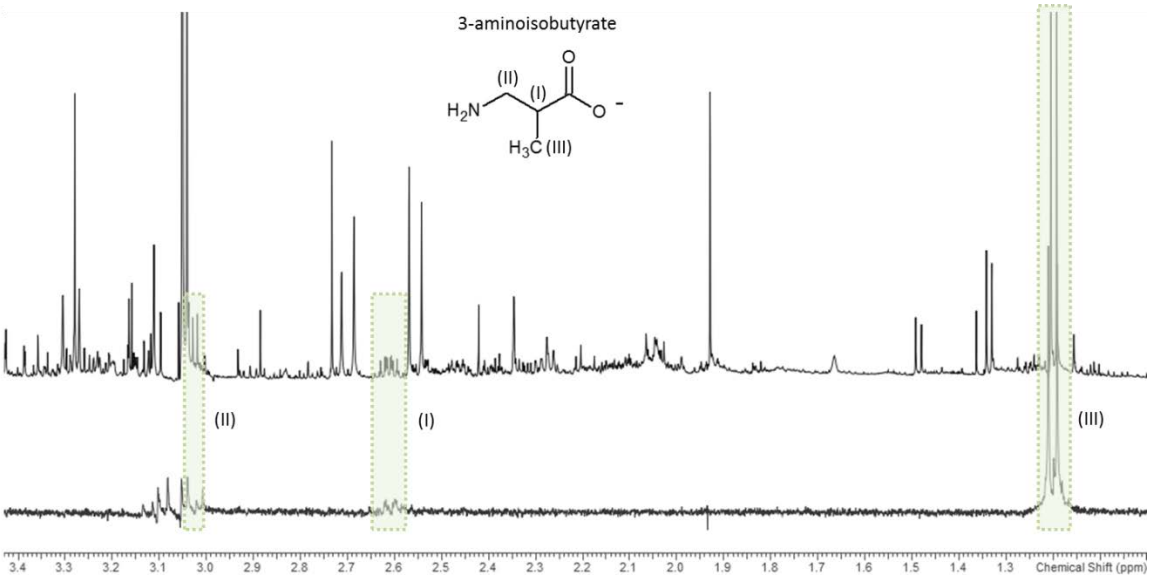

Figure 2.2. 400 MHz 1D-TOCSY spectrum of a human urine specimen collected from an NP-C1 disease patient: this selective TOCSY experiment confirms couplings between each of the 3-aminoisobutyrate (3-AIB) resonance assignments. The signal centred at 1.21 ppm was the one selectively irradiated in this experiment.

The assignments of some metabolites were not accomplished in view of their low concentration or overlap with other resonance peaks in view of the great complexity of the urinary ^{1}H NMR profiles explored, since more than 200 compounds are identifiable (45).

2.2.2. Identification of bile acids in urine samples

The C18-CH_3 group of bile acids (BAs) have urinary resonances located within the 0.60 and 0.75 ppm region of ^{1}H NMR spectra. The importance of the resonances encountered therein for further MVA will be detailed in the following sections. Assignments for the bile acids' C18-CH_3 group signals were confirmed *via* the acquisition of ^{1}H NMR spectra on selected urine samples which had been 'spiked' with authentic bile acid standard solutions (Figure 2.3), i.e. chenodeoxycholate, glycocholate, glycochenodeoxycholate,

taurochenodeoxycholate, taurodeoxycholate and tauroursodeoxycholate. Lithocholate solubility in water is only *ca.* 0.05 µM (162), and therefore, it is unobservable by either 400 MHz or 600 MHz NMR spectrometers; accordingly, its C18-CH_3 resonance was not observed in Figure 2.3(a).

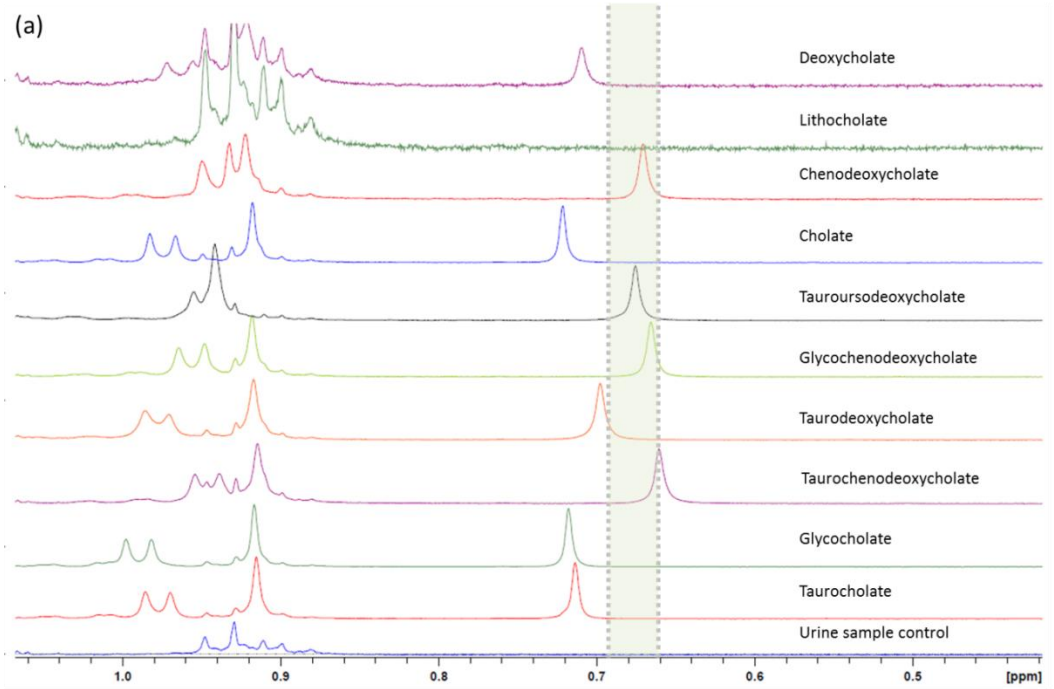

R_2	R_3	Bile Acid anion specie
H	OH	Chenodeoxycholate
OH	OH	Cholate
OH	H	Deoxycholate
H	H	Lithocholate

Figure 2.3. (a) 0.4 - 1.1 ppm region from a 400 MHz ^{1}H NMR spectra of a urine sample 'spiked' with different bile acids (BAs): the C18-CH_3 group signal can be clearly observed as a singlet between 0.65 and 0.75 ppm. The green shadowed rectangle highlights the 0.66 - 0.69 ppm bucket. (b) BAs general chemical structure together with a table listing those BAs arising from the different possible substitutions in those groups highlighted. Glycine or taurine adducts resulting from further conjugations are located at R_1.

BAs that do not present an -OH group in either C7 or C12 [Figure 2.4 (b)] positions are responsible for this signal, since BAs that do have a downfield-shifted C18-CH_3 resonance contain a hydroxyl group. Indeed, the more pronounced effect is ascribed to C12, as expected in view of its proximity to C18. The conjugation with either taurine or glycine does not exert any major observable effects on the chemical shift value of this C18-CH_3 resonance [Figure 2.3 (a)]. Additionally, *p*-values arising from the ANOVA model depicted in Equation 19 for adjacent regions to the 0.66-0.69 ppm bucket were not significant for the comparison between HET and NPC groups [*p* (0.61 - 0.66 ppm) = 0.211), *p* (0.69 - 0.72 ppm) = 0.728].

2.3. DATA PREPROCESSING

61 urine samples were initially included for statistical analysis: 14 untreated NP-C1 patients (NPC) and 47 heterozygous carriers as controls (HET). The binning process gave a table of 61 rows (samples) x 199 columns (variables), containing the sum-normalised intensities of each spectrum. Spectral regions containing resonances arising from ethanol (*t*, 1.22 - 1.24 ppm; *q*, 3.63 - 3.67 ppm), which were detectable in several of the heterozygous carrier urine samples and urea (*br*, 5.59 - 5.99 ppm) were removed from all the urinary ^{1}H NMR profiles for further MVA.

An exponential line-broadening function of 0.30 Hz was routinely applied to the FIDs prior to FT for all the spectra that were subsequently phased, baseline corrected and referenced to the formate (*s*, 8.46 ppm) resonance since no internal standard was added to the samples. Moreover, the formate-H resonance is readily visible as a singlet in a clear region of the urinary NMR profiles, and therefore it is easily identifiable. The intense δ = 4.65 - 5.15 ppm residual H_2O/HDO signal region was also removed from all the ^{1}H NMR profiles acquired prior to the performance of MV data analysis strategies.

Spectral data were analysed using *NMR Spectrus Processor 2012* (Advanced Chemistry Development Inc., ACD/Labs, Toronto, Canada) and binned using the 'Intelligent Bucketing' procedure implemented in the software noted above. This technique splits the spectra into chemical shift buckets, given the position of a particular resonance peak in every spectrum, so that the same signal in different spectra always is incorporated into the same bucket, even if pH or ionic strength effects have shifted it somewhat. The bucket width selected was 0.04 ppm with a 50 % looseness factor (width variation of the bucket in order to accommodate the resonance peak). This algorithm for binning the spectra (in different integral regions) aims at overcome the problem which arises from setting buckets' limits in the middle of a resonance peak, then yielding inaccurate integral values and biased results when the statistical analysis is performed on the dataset obtained.

2.3.1. Creatinine normalisation

Significant differences between the mean urinary creatinine (Cn) concentrations of the two disease classification groups were analysed in order to explore the possibility of performing Cn-normalization, since both groups investigated, i.e. NP-C1 patients and heterozygous carriers as controls, were not age-matched, and Cn urinary concentration is known to increase with age (157). Therefore, a preliminary ANOVA (Equation 19) was carried out for Cn only (Figure 2.4); for this purpose, the dataset was sum-normalised, cube-root transformed and Pareto scaled prior to this analysis. The bucket selected for this univariate analysis was 4.05 - 4.10 ppm, since the Cn resonance peak at 3.03 ppm presents some overlap with the creatine (Cr) and phosphocreatine-CH_3 resonances.

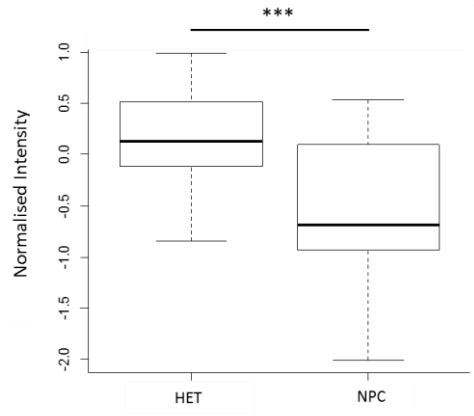

Figure 2.4. Box plot for Cn signal (4.05 - 4.10 ppm): Cn levels for both disease classification groups were compared using the ANOVA model depicted in Equation 19, showing a significant difference. $p = 4.45 \times 10^{-7}$ for the disease classification contribution ($p < 0.05$, *; $p < 0.01$, **; $p < 0.001$, ***).

In view of the significant differences between both classification groups (NPC and HET) for the 4.05 - 4.10 ppm Cn bucket, the dataset was constant sum normalised (the sum of all individual integral buckets yields 1 for each spectrum) and not Cn-normalised. After this normalisation, the dataset was cube-root transformed and Pareto scaled for all further MVA performed.

The main aim of Cn-normalisation has always been to reduce the potentially large intra-and inter-individual differences in diuresis, and therefore, prevent the occurrence of false negative or false positive values attributable to very dilute or very concentrated urine samples (163). Nevertheless, Cn-normalisation has only been proven to be useful when no differences in diet or kidney disease were assumed, or if the kinetics of excretion of the selected biomarker(s) is(are) similar to Cn (164); indeed, some authors prefer not to Cn-normalise their data if the metabolites of interest do not have the same kinetics of excretion as Cn. In view of the participants' age in this study, where the NP-C1 patients are all below

32 years of age and the HET participants are the parents of those donors, the expected result for Cn levels matches with the one obtained in the ANOVA performed. The *p*-values obtained therefrom indicated significatively higher Cn levels for the HET group, and therefore, Cn-normalisation was discarded for MVA of the urinary dataset.

Prior to performing both univariate and MVA, samples were visually checked for any major disturbances. One NP-C1 patient was found to be receiving valproate treatment by detecting a triplet at 0.84 ppm and its coupling with the remaining valproate-$CH_{2's}$ resonance signals, and 6 heterozygous carriers plus another NP-C1 patient taking acetaminophen, since their characteristic resonance signals were identified at 7.13 and 7.35 ppm for its glucuronide metabolite, 7.31 and 7.45 ppm for the sulphate one and 2.16 ppm for its acetamido methyl group (Figure 2.11). All these samples were removed for the purpose of all further analysis.

2.4. UNIVARIATE AND MULTIVARIATE ANALYSIS OF THE ^{1}H NMR URINARY DATASET

2.4.1. Univariate data analysis: ANOVA

ANOVA analysis of the urinary dataset was performed according to the model depicted in Equation 19 to explore any significant differences between the metabolites for each disease group, and also to isolate the variance attributable to the disease status, removing any further effect attributable to kinship. In this ANOVA model, Y_{ijk} represents the (univariate) predictor variable value observed, μ is the overall population mean value in the absence of any significant, influential sources of variation. D_i, F_j and DF_{ij} are components of variation ascribable to between-disease classifications, family, and the disease classification-family interaction sources, and e_{ij} *is* the unexplained error (residual) contribution.

$$Y_{ij} = \mu + D_i + F_j + DF_{ij} + e_{ij} \quad (19)$$

2.4.2. Multivariate data analysis

2.4.2.1 Preliminary data analysis: PCA

PCA [MetaboAnalyst 3.0 (50), this software was utilised for all the PCA performed in this work] was employed in order to explore any underlying classification patterns within the urinary NP-C1 dataset. In the PCA 3D scores plot depicted in Figure 2.5, the clustering of samples based on their disease status is not readily visible. Although NPC urine samples have lower values for PC3 than of the HET group, there is some overlap for that PC. PC1 and PC2 do not accomplish any clear separation. However, combination of these 3 PCs allows the best visualization of the clustering by disease class.

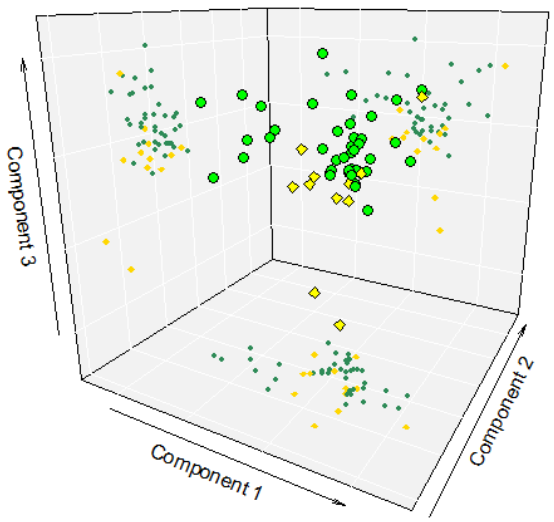

Figure 2.5. PCA 3D score plot for the NP-C1 urinary dataset: representation of the 3 first PCs in a 3D scores plot with the projections on the 2D planes as the scores plot for each 2 PCs. (green circles = HET, yellow diamonds = NPC).

2.4.2.2. Classification performance

Random Forests (RFs): The RFs technique was employed for classification and variable selection purposes using the *randomForest* R package (165) (this software was utilised for all the RF analysis performed in this work).

RFs parameters were tuned in order to improve its performance, so the number of trees was set up to 500 and the number of variables selected at each split was 8 based on the Out-Of-Bag (OOB) error values obtained. RFs was applied over 100 iterations; at each iteration, the OOB and the confusion matrix was stored in order to obtain classification performance parameters (Table 2.2). Additionally, variable importance (mean decrease accuracy criterion, MDA) values for variable selection were extracted and their mean and standard error of the mean (SEM) values computed. For each set of 100 iterations, a column of 65 rows (number of samples) was generated containing random numbers from 0 to 1, so that samples with values > 0.66 were included in the test-set, whilst samples with values ≤ 0.66 were included in the training-set. This procedure, also known as Monte Carlo Cross-Validation (MCCV) was applied to each class (NPC and HET) independently.

Genetic Algorithms (GAs): The GAs strategy was applied using the GALGO R-package (166) that allows the selection of different parametric and non-parametric classification techniques such as k-nearest-neighbours, discriminant functions (Maximum Likelihood), nearest centroid, SVMs, RFs and neural networks. In this work we have used SVMs and MLHD.

For this GAs methodology, the chromosome size was selected to be 10 (maximum number of variables in each model/chromosome). These chromosomes evolved generating 500 solutions (chromosomes/models) with the aim of achieving a fitness value of 0.9. To

build up the models, the methods employed were Maximum LikeliHooD (MLHD, a modification of LDA that uses Bayes' rule as the discriminant function assigning a sample to the class with highest conditional probability) and SVMs, using a radial Kernel. The performance of the models generated using the techniques delineated above was computed by using a 5-fold cross validation procedure and the outcomes are listed in Table 2.2.

Correlated Component Regression-Linear Discriminant Analysis (CCR-LDA): CCR-LDA was set to a maximum of 1, 2 and 3 components and to a maximum of 5, 10, 15 and 20 variables for developing the classification models. Each of the combinations was repeated 5 times, resulting in 60 different models. The validation procedure was a 5-fold cross-validation over 10 rounds. Results from this CCR-LDA analysis are shown in Table 2.2.

MVA Technique	OOB (SEM)	Accuracy (SEM)	Sensitivity (SEM)	Specificity (SEM)
RFs	0.224 (0.00012)	0.835 (0.001)	0.695 (0.001)	0.831 (0.003)
GA-MLHD/SVM	-	0.827 (0.002)	0.752 (0.002)	0.903 (0.001)
CCR-LDA	-	0.810 (0.013)	0.583 (0.032)	0.926 (0.012)

Table 2.2. Classification performance of the techniques employed for the analysis of the NP-C1 urinary dataset: the OOB error value is also indicated for the RFs approach. Standard error of the mean values for each of the parameters computed are provided in brackets.

All the MVA techniques were able to succesfully classify urine samples regarding their disease status (NPC *vs*. HET); indeed, they all gave very good results for specificity and accuracy. However, values obtained for sensitivity were not very efficient, the CCR-LDA technique having the lowest sensitivity and the highest variablity, not only for sensitivity, but

for the remainder of the classification performance parameters computed, as observed for the SEM values displayed in Table 2.2. However, these SEM values cannot be considered high, since the maximum value accounts for only 5.49% of the averaged sensitivity parameter. Nevertheless, the CCR-LDA model gave the highest specificity value (0.926). The RFs and CCR-LDA strategies gave the highest accuracy and specificity values respectively when applied to the NP-C1 urinary dataset.

The limitations introduced for GAs and CCR-LDA classifications technique with regard of the number of variables that could be included to the model building process were aimed at reducing the neglective effect of overfitting, i.e. the employment of a number of variables highly exceeding the number of samples, which results in very accurate models which usually fail when new samples are tested. Additionally, cross-validation procedures were implemented in the model development process in order to also overcome this issue.

2.4.2.3. Variable Selection

Random Forests (RFs): Throughout the 100 iterations applied in the RFs analysis outlined above, MDA value for variable importance was computed, and consequently, the mean value of those 100 MDAs obtained for each variable; so that a variable ranking was obtained on completion of the process (Table 2.3).

Genetic Algorithms (GAs): The GALGO package saves the frequency at which each variable is selected to generate a successful classification (i.e., reach a fitness of 0.9). The variables can then be ranked and averaged for both techniques (SVMs and MHLD) based on these frequencies (Table 2.3).

Correlated Component Regression-Linear Discriminant Analysis (CCR-LDA): The average presence of the variables in the models built by this CCR technique was computed in order to generate a ranking. This ranking was based exclusively on the number of times a specific variable is included within a model, so their loadings in each component were not considered (Table 2.3).

Bucket (ppm)	Assignment	Multiplicity (J, Hz)	*p*-value for Disease	Fold Change	RF	GA-MLHD/SVM	CCR-LDA
0.66 - 0.69	BAs-C18-CH_3	*s*	9.39×10^{-5}	8.54	(7)	(1)	(8)
0.72 - 0.76	Unknown-1	*d* (6.6)	2.79×10^{-5}	-11.86	(3)	(2)	(2)
0.81 - 0.83	2-OH-3-MeBu-CH_3	*d* (6.7)	8.47×10^{-3}	-10.22	(>15)	(4)	(7)
0.98 - 1.03	Val-CH_3's/Ile-CH_{3a}	2 x *d*	1.65×10^{-2}	5.06	(>15)	(>15)	(14)
1.17 - 1.22	3-AIB-CH_3	*d* (7.4)	8.58×10^{-9}	2.81	(2)	(>15)	(1)
1.36 - 1.41	2-HydroxyisoBu-$CH_{3's}$	*s*	3.65×10^{-2}	1.84	(15)	(>15)	(>15)
1.50 - 1.56	*n*-Butyrate-C3-CH_2	*m*	6.18×10^{-4}	13.00	(13)	(>15)	(>15)
1.58 - 1.63	5-Aminovalerate-C3/4-CH_2	*m*	3.87×10^{-2}	-5.04	(>15)	(10)	(12)
2.02 - 2.08	N-acetyl-CH_3	*s*	2.15×10^{-2}	1.25	(>15)	(>15)	(10)
2.08 - 2.12	Gln-C3-CH_2	*m*	2.61×10^{-2}	1.49	(6)	(>15)	(>15)
2.12 - 2.18	Unknown-2	*m*	2.98×10^{-1}	-1.09	(>15)	(15)	(>15)
2.25 - 2.31	2-Hydroxyglutarate-CH_2	*m*	3.91×10^{-3}	-1.52	(>15)	(12)	(>15)
2.87 - 2.89	TMA-$CH_{3's}$	*s*	2.09×10^{-2}	2.29	(10)	(7)	(>15)
3.24 - 3.29	TMA-N-oxide-$CH_{3's}$	*s*	1.26×10^{-3}	-1.51	(8)	(3)	(12)
3.29 - 3.33	Methanol	s	2.39×10^{-3}	-1.96	(11)	(>15)	(15)
3.46 - 3.48	3-HydroxyPheAc-CH_2	*s*	1.73×10^{-1}	1.38	(>15)	(11)	(>15)
3.63 - 3.67	Glycerol-C1/3-CH_{2a}	*m*	5.21×10^{-1}	1.06	(>15)	(14)	(>15)

3.67 - 3.71	AAs-α-CHs/3-OH-isoBu-β-CH_2	*m*	7.23×10^{-2}	1.19	**(>15)**	**(13)**	**(>15)**
3.88 - 3.92	Hippurate-CH_2	*d* (5.9)	1.04×10^{-1}	1.02	**(12)**	**(>15)**	**(>15)**
3.92 - 3.95	Cr-CH_2	*s*	1.52×10^{-5}	1.59	**(14)**	**(6)**	**(4)**
4.05 - 4.10	Cn-CH_3	*s*	4.45×10^{-7}	-1.33	**(1)**	**(9)**	**(6)**
8.40 - 8.42	Quinolinate-C6-CH	*dd*	3.83×10^{-5}	30.32	**(9)**	**(>15)**	**(13)**
8.80 - 8.86	Trigonelline-C4/6-CH	*m*	4.96×10^{-4}	-6.70	**(4)**	**(5)**	**(5)**
9.11 - 9.16	Trigonelline-C2-CH	*s*	2.92×10^{-4}	-5.27	**(5)**	**(8)**	**(3)**

Table 2.3. Discriminatory variables for the urinary NP-C1 dataset: top 15 variables selected by the three techniques employed for analysis (RFs, CCR, GAs) are listed along with their assignment, multiplicity, ANOVA *p*-value for 'Disease', fold change (positive values for variables with higher levels in NPC group and negative for those with lower values) and the ranking for each MVA technique specified in the last column. The colour codes in the last 3 columns will serve to correlate the disease related-metabolic pathways discussed in *Chapter 6* with the MVA techniques employed to select the metabolites involved in those pathways. Abbreviations: Val, Valine; Ile, Isoleucine; 2-OH-3-MeBu, 2-Hydroxy-3-methylbutyrate; 3-AIB, 3-aminoisobutyrate; 2-HydroxyisoBu-$CH_{3's}$, 2-Hydroxybutyrate-$CH_{3's}$; Gln, Glutamine; 3-HydrohyPheAc, 3-Hydroxyphenylacetate; AAs, amino acids; 3-OH-isoBu-β-CH_2, 3-Hydroxyisobutyrate-β-CH_2.

50% of the variables listed in Table 2.3 were ranked in the top 15 for at least 2 different techniques, and the 0.66 - 0.69, 0.72 - 0.76, 3.24 - 3.29, 3.92 - 3.95, 4.05 - 4.10, 8.80 - 8.86 and 9.11 - 9.16 ppm buckets were featured as top variables for all three MVA methods, which might indicate that these variables were the more robust features to differentiate samples according to their disease status. Indeed, all these variables were ranked as top 10

features for all the techniques, and only the 1.17 - 1.22 ppm bucket, despite not being selected by the GAs approach, it should be included as a top important variable since it was ranked 2nd and 1st by RFs and CCR-LDA respectively.

The major discriminatory variables include branched chain amino acids (BCAAs) such as Ile and Val, and products of their degradation pathways such as 3-AIB, 2-hydroxy-3-methylbutyrate and 3-hydroxyisobutyrate; moreover, Gln, 3-hydroxyphenylacetate (a tyrosine metabolite) and the α-group resonance signal from amino acids were also selected.

This bile acid bucket has been highlighted as one of the most important features as well, although the exact bile acids species contributing to this signal are somewhat unclear.

n-Butyrate is a gut microbiota metabolite arising from carbohydrate fermentation. Further metabolites listed in Table 2.3 that can also be attributed to gut microflora are TMA (choline degradation product) and 5-aminovalerate, the latter a product of lysine catabolism.

Higher levels of TMA-N-oxide (TMAO), trigonelline and Cn were observed in the HET participants; however, these three metabolites are well known age-correlated metabolites which may arise from diet (TMAO and trigonelline) and muscle tissue (Cn).

Three metabolites listed in Table 2.3, could arise from exogenous sources as 2-hydroxyisobutyrate and methanol (although methanol also arises from microflora metabolism), in addition to hippurate, a metabolite of benzoate mainly encountered in plant dietary sources and a gut microbial-mammalian co-metabolite generated through the conjugation of benzoate with glycine (167).

The N-acetyl-group signals arise from the acetamido (-NHCOC$\underline{H}_3$) groups of some metabolites as a result of a common chemical modification, frequently encountered in amino acids and sugars, mainly occurring in brain.

2-Hydroxyglutarate is a hydroxy-acid resulting from the reduction of ketoglutarate, an intermediate in the Krebs cycle.

Quinolinate is a product of kynurenine metabolism and a precursor of niacin nucleotides, such as NAD, NADP, etc. that can also act as a neurotransmitter.

Glycerol is a structural metabolite being the frame for the addition of fatty acids to form triacylglycerols (TG), diacylglycerols (DG) and monoacylglycerols (MG).

One of the most important variables selected was the 0.72 - 0.76 ppm bucket, which remains unassigned, although it has been previously reported in urine (168); indeed, the coupling constant (*J*) value of this resonance signal (6.6 Hz) is very similar to that determined in (168) (6.8 Hz), and these researchers have suggested that it arises from the $-CH_3$ unit of an isopropyl group, which is linked to a magnetically-distinguishable, second $-CH_3$ group doublet resonance located at $\delta = 0.88$ ppm. Both these $-CH_3$ units were found to be connected (albeit in a MV statistical context) to a suggested asymmetrical carbon atom methine (-CH) fragment (centred at $\delta = 2.18$ ppm), although these investigators did not confirm these connectivities *via* the application of neither 1D or 2D ^{1}H-^{1}H NMR COSY/TOCSY techniques.

2.4.2.4. ROC curve analysis

Biomarker selection was investigated through ROC curve analysis. This analysis was conducted using the ROC curve analysis option included in MetaboAnalyst 3.0 [(169) this software was utilised for all the ROC curve analysis performed in this work]. Those metabolites selected as discriminatory features for more than 1 of the techniques in Table 2.3, excluding those likely arising from age differences between both disease-classification groups, were subjected to ROC curve analysis in order to explore their ability as NP-C1 disease urinary biomarkers. The variables selected were those assigned to bile acids (0.66 -

0.69 ppm), unknown metabolite (0.72 - 0.76 ppm), 2-hydroxy-3-methylbutyrate-CH_{3a} (0.81 - 0.83 ppm), 3-AIB-CH_3 (1.17 - 1.22 ppm), 5-aminovalerate-C3/4-CH_2, (1.58 - 1.63 ppm), trimethylamine-CH_3's (2.87 - 2.89 ppm), methanol (3.29 - 3.33 ppm), creatine (3.92 - 3.95 ppm) and quinolinate (8.40 - 8.42 ppm). However, the presence of methanol must be taken cautiously since their higher levels in the HET group could be attributable to the lowest exposure to methanol vapours (cleaning products) and alcohol consumption in the younger NP-C1 patients (170).

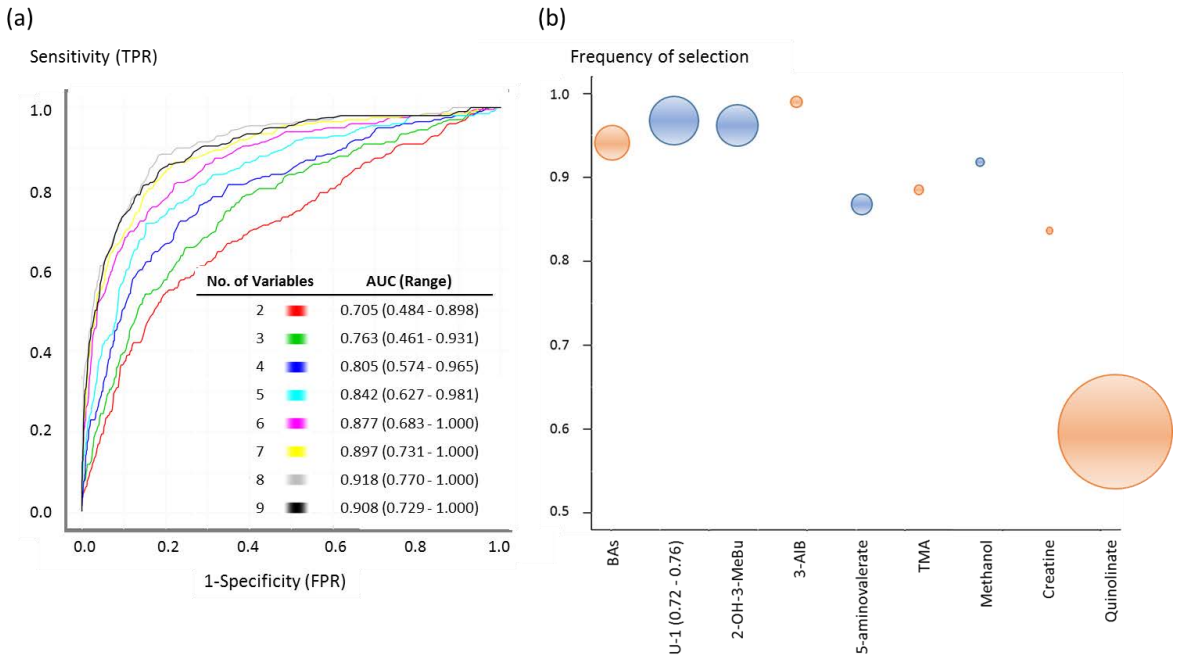

Figure 2.6. (a) ROC curves and (b) bubbles diagram for variable importance in the NP-C1 urinary dataset: different combinations of variables gave different AUC values ranging from 0.705 for 2 variables, up to 0.918 with 8 variables, as indicated in the table inserted in (a). Variable ranking arising from ROC analysis is depicted in the vertical axis in (b), blue bubbles indicate metabolites with lower levels in NPC group, and the orange ones, those with higher levels. The size of each bubble is correlated with the FC (fold change). Abbreviations: U-1,

unknown metabolite; 2-OH-3-MeBu, 2-Hydroxy-3-methylbutyrate; TPR, True Positive Rate; FPR, False Positive Rate.

The assessment of model performance is evaluated through MCCV, so that two-thirds of the samples were utilised in order to generate a RFs classifier which were validated on the one-third of the remaining samples excluded from the model building process; the sensitivity and specificity of the models developed were computed from the confusion matrix arising from the multiple MCCV iterations. 100 rounds of CV were performed, and results were depicted in the form of a ROC curve by plotting the sensitivity against 1-specificity showing the performance of biomarkers subsets. Through this method, the models generated combine different features in each case from the maximum number of variables entered.

As expected, mean AUC values were decreasing along with the number of variables employed for the model, apart from the model built up with 8 variables that has higher values than the 9 variables one. AUC values were all above 0.7, a performance which is consider fair, in terms of classification success. The selection frequencies of those 9 variables included in the ROC analysis are illustrated in Figure 2.6 along with their fold change (FC). Bile acids, an unknown doublet within the δ = 0.72-0.76 ppm bucket, 2-hydroxy-3-methylbutyrate and 3-AIB were the metabolites most frequently selected for construction of the models.

2.5. POTENTIAL AGE-CORRELATED URINARY METABOLITES

One of the limitations of the urine NP-C1 dataset analysis is the difference in age amongst the sample donors, so that the NP-C1 patients are all below 32 years of age and the heterozygote carriers are the parents of these individuals (Table 2.1).

Trigonelline, TMAO and Cn were selected as important discriminatory features for all the MVA techniques employed to differentiate NP-C1 patients from HETs by their NMR urine profile, all showing higher levels for the control group (HET) (Table 2.3). It has been previously observed that all these metabolites were elevated in people over 40 years old (171). Accordingly, since these three metabolites were elevated in the HET group and these samples were collected from the NP-C1 patients´ parents, such a difference is likely to be ascribable to the older urine sample donors. Therefore, these metabolites will not be considered as possible urinary biomarkers or as indicators of any alteration in the metabolism of NP-C1 patients in Chapter 6.

Trigonelline is a pyridine found in coffee beans amongst some other vegetables, so its presence in urine may attributable to differences in dietary habits in the older participants, mainly regarding coffee and tea consumption.

TMAO is the oxidation product of TMA, a reaction that takes place in the liver, when either carnitine or choline that are not absorbed are degraded by the flora of the large intestine yielding TMA, amongst other metabolites (172). Approximately 75% of the total body carnitine originates from food sources of either carnitine or its precursors, such as lysine and methionine. Indeed, the primary sources of this metabolite are meat. Additionally, increased levels of TMAO in urine have been reported after consumption of fish (173) and diets with high salt content (174).

Cn is a by-product of muscle metabolism arising from Cr-phosphate breakdown, which is subsequently excreted into urine. Urinary excretion of Cn correlates positively with body weight, reflecting skeletal muscle mass (175, 176), and therefore, higher concentrations are expected in adults. Daily urinary excretion of Cn derived from muscles occurs at a ratio of *ca*. 1 g per 20 kg of muscle mass (177).

2.6. NMR ANALYSIS OF URINE SAMPLES COLLECTED FROM NP-C1 PATIENTS UNDERGOING MIGLUSTAT TREATMENT

2.6.1 NMR characterization of miglustat

Prior to the detection of MGS in urine, the signals arising from this agent had to be assigned for its further identification in urine samples collected from treated patients. NMR spectra obtained for the elucidation of MGS assignments samples were acquired at 298 K on a Bruker AV 400 MHz spectrometer (Leicester School of Pharmacy facility, DMU, Leicester, UK) operating at a frequency of 399.94 MHz. All data were processed in Topspin 2.1 (Bruker, UK). MGS was obtained from Monsanto/Searle when used as a standard or via prescription of the drug to NP-C1 patients. MGS samples were prepared at a concentration of 20.0 mM in 17.0 mM phosphate buffer [pH 7.10, 90% H_2O/10% D_2O, the latter containing 0.05% (w/w) TSP].

1D ^{1}H NMR: Single-pulse ^{1}H NMR spectra were acquired with 64 scans, 6.5 μs pulses, 32,768 data points and a spectral width of 4,800 Hz. Water suppression was achieved using

the NOESY-presaturation pulse sequence (Bruker *noesygppr1d* pulse sequence) with irradiation at the water frequency during the recycle and mixing time delays.

^{1}H-^{1}H COSY: Bruker *cosygpprqf* pulse sequence was employed. The spectral width in the F1 and F2 axes were 2500 Hz, and 2048 data points were collected in F2. For the urine samples, 32 increments and 32 scans per increment were used. The relaxation delay was 2.5 s for a total acquisition time of ~ 4 hr. Before the Fourier transformation, a sine function was applied in both time domains.

^{1}H-^{13}C HSQC: Bruker *hsqcedetgpsp.3* pulse sequence was employed. 64 scans for 128 increments were acquired for each spectrum. The F2 and F1 spectral widths were 6,340 and 16,600 Hz, respectively. 1D ^{13}C spectra for displaying along the vertical axis in HSQC spectra were acquired using the *zgpg30* Bruker pulse sequence with 1024 scans, a spectral width of 23,980 MHz, and 65,536 data points for a total acquisition time of 1.37 s.

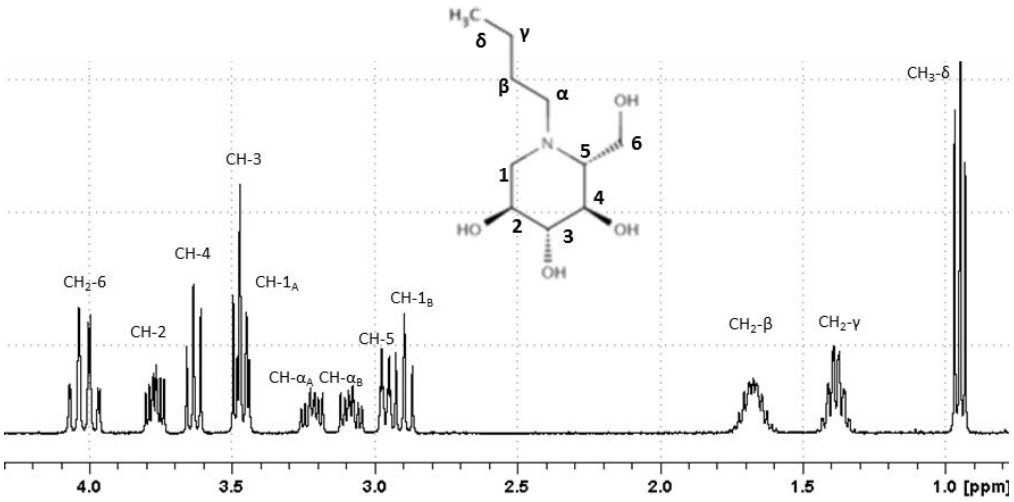

Figure 2.7. Assigned 1D ^{1}H-NMR spectrum of MGS 20 mM in 17.0 mM phosphate buffer, pH 7.10 (90% H_2O/10% D_2O).

There are two distinct regions in the MGS spectrum (Figure 2.7), the more shielded resonances attributable to the n-butyl chain [δ = 0.95 (t), 1.39 (m) and 1.68 ppm (m)], and the deshielded resonances ascribable to the piperidine ring protons within the 2.8-4.1 ppm chemical shift range together with the -CH_2-α from the butyl chain. The proximity of this group to the piperidine ring nitrogen atom causes its resonances to be deshielded (with two magnetically-inequivalent ^{1}H nuclei signals centred at 3.10 and 3.23 ppm).

In order to confirm the assignments displayed in Figure 3.8, 2D NMR experiments were carried out, such as ^{1}H-^{1}H COSY [Figure 2.8(a)] and ^{1}H-^{13}C HSQC [Figure 2.8(b)]. The assignments, together with the coupling constants and multiplicities for all the resonances observed in the NMR spectra acquired are listed in Table 2.4.

Moiety	**^{1}H**	**^{13}C**
CH_3-δ	0.95 (*t*, *J* = 7.4 Hz, 3 H)	15.71
CH_2-γ	1.39 (*dsext*, *J* = 7.4, 1.8 Hz, 2 H)	22.34
CH_2-β	1.68 (*m*, 2 H)	27.43
CH_2-α_A	3.23 (*m*, 1 H)	55.25
CH_2-α_B	3.10 (*m*, 1 H)	-
CH-1_A	3.47 (*dd*, *J* = 13.4, 4.2 Hz, 1 H)	56.25
CH-1_B	2.92 (*t*, *J* = 11.7 Hz, 1 H)	-
CH-2	3.77 (*m*, 1 H)	69.50
CH-3	3.47 (*t*, *J* = 9.4 Hz, 1 H)	79.25
CH-4	3.64 (*t*, *J* = 9.9 Hz, 1 H)	70.61

CH-5	2.99 (*ddd*, *J* = 10.3, 2.3 Hz, 1 H)	66.08
CH-6	4.02 (2 x *dd*, *J* = 13.4, 3.0, 1.8 Hz, 2 H)	57.42

Table 2.4. Chemical shifts together with the coupling patterns and coupling constants for ^{1}H and ^{13}C NMR spectra acquired on MGS in aqueous media.

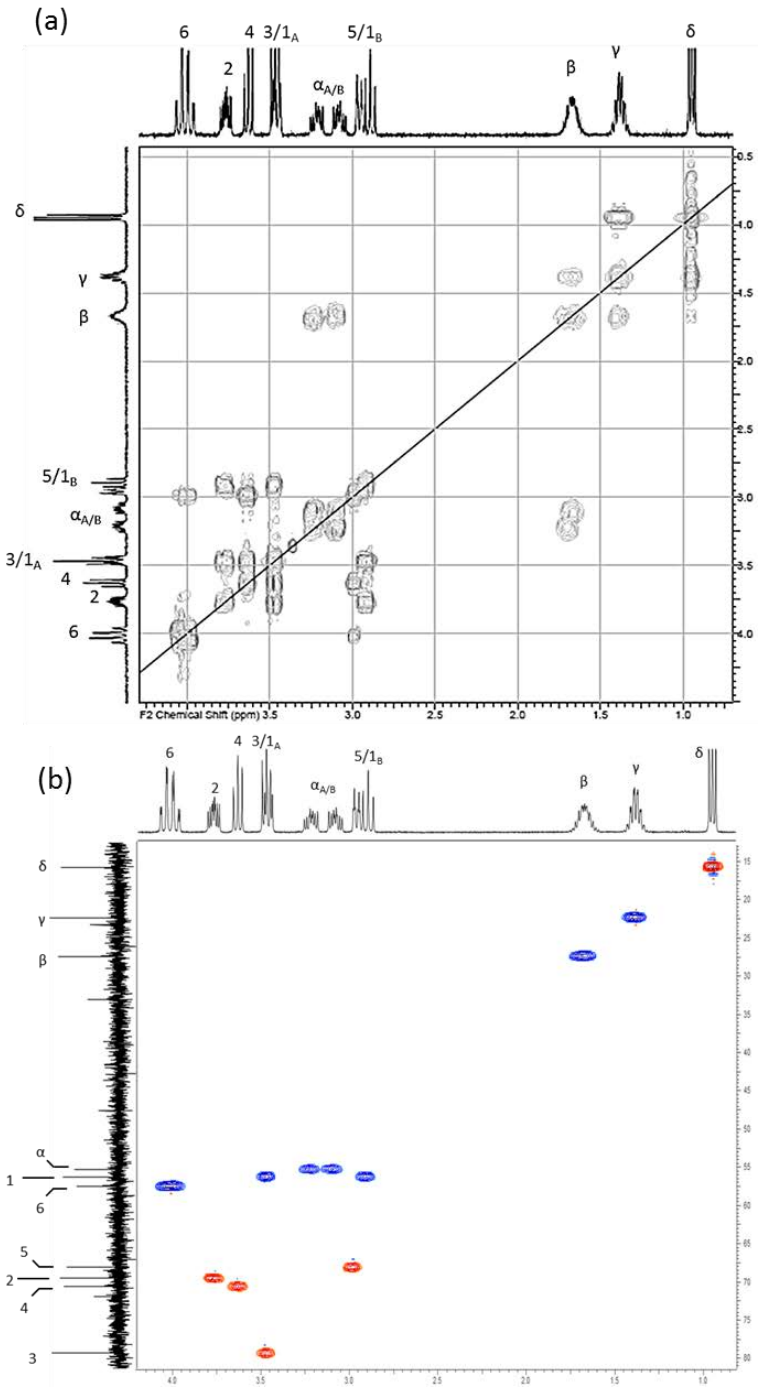

Figure 2.8. (a) 400 MHz ^{1}H-^{1}H COSY and (b) HSQC spectrum of 20 mM MGS in 17.0 mM phosphate buffer, pH 7.10 (90%/10% D_2O/H_2O): ^{1}H resonances along with the assignments are displayed in the horizontal axis, whilst ^{13}C ones are displayed in the vertical axis. Red cross-peaks indicate either a -CH_3 or -CH group, and blue ones represent CH_2 functions.

2.6.2. Miglustat detection in urine

Representative ^{1}H NMR spectral profiles of urine samples collected from an NP-C1 patient subsequent and prior to treatment with MGS are shown in Figures 2.9 (a) and (b) respectively. Resonances corresponding to MGS are detectable in the urinary ^{1}H NMR profile of the patient when receiving MGS treatment, predominantly those arising from the butyl chain.

***Spiking experiments*:** The presence of MGS in the urine collected from NP-C1 patients undergoing this treatment was further confirmed via the addition of a final concentration of 1.00 x 10^{-3} M MGS to additional urine samples collected from untreated NP-C1 patients [Figure 2.9(c)]. Following this *in vitro* treatment, a series of MGS resonances were also clearly visible in the ^{1}H NMR urinary profiles, most notably a strong triplet located at 0.95 ppm corresponding to the terminal n-butyl chain CH_3 group protons of MGS, together with its β- and γ-CH_2, and piperidine ring-CH-$1_{A/B}$, -CH-3, -CH_2-6, -CH-4, and -CH-5 protons.

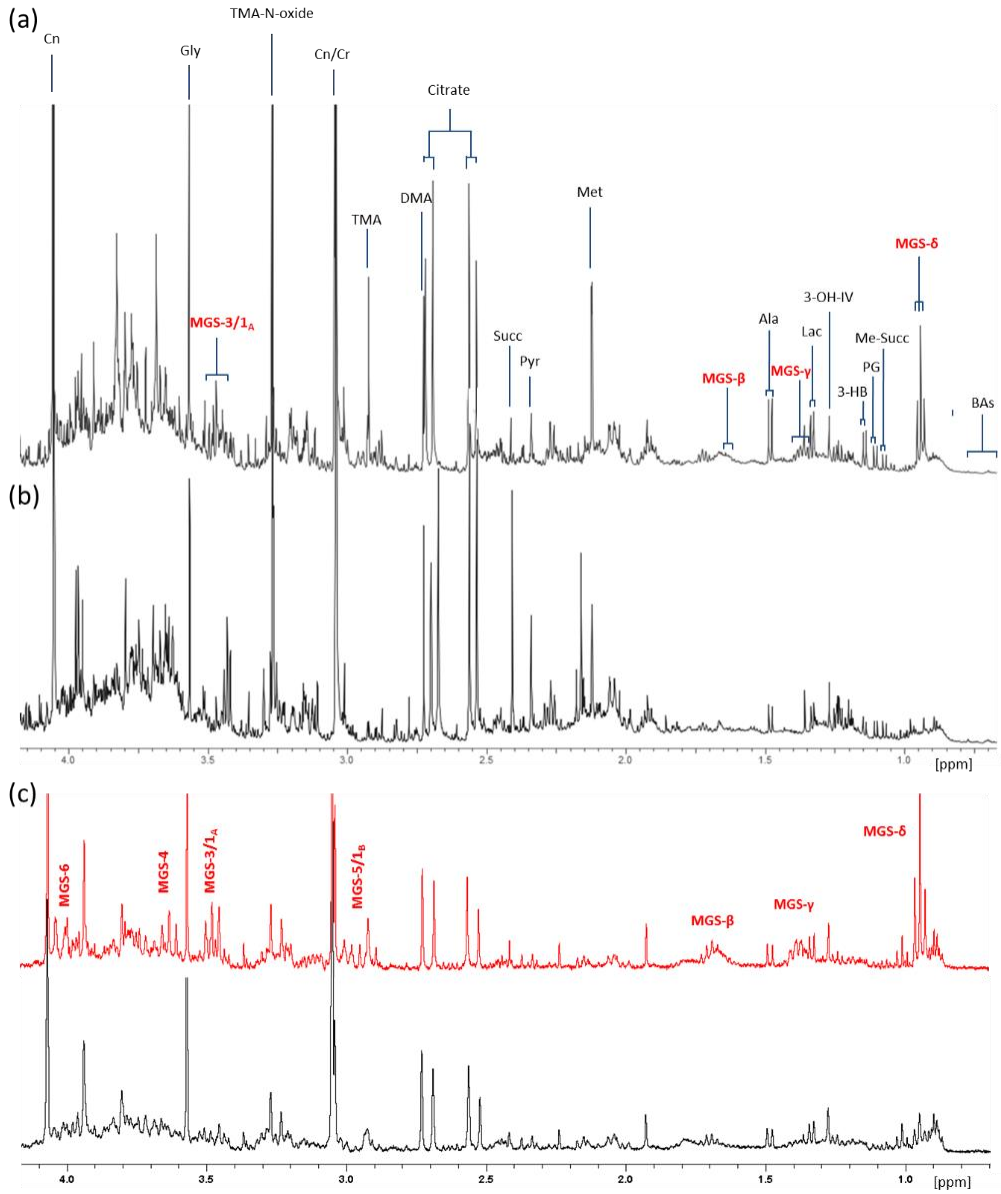

Figure 2.9. 400 MHz 1D spectra of urine collected from an NP-C1 patient before (b) and after (a) MGS treatment; (c) healthy urine sample spiked with MGS (red) and the same urine sample untreated (black): MGS assignments are displayed in red. For purposes of clarity only selected resonances are labelled. Abbreviations: BA, Bile acids; Me-Succ, Methylsuccinate; PG, Propylene glycol; 3-HB, 3-Hydroxybutyrate; Lac, Lactate; Pyr, Pyruvate; Succ, Succinate; DMA, Dimethylamine; TMA, Trimethylamine; Cn/Cr, Creatinine/Creatine.

2.6.3. ^{1}H NMR analysis of urine collected from NP-C1 patients undergoing miglustat treatment

MGS was detected in urine samples through 1D and 2D NMR techniques, together with spiking experiments, as previously described. Moreover, valproate, together with its major metabolite O-acyl-β-glucuronide was detected in 14 of the samples examined in this cohort. The identity of this metabolite was confirmed by the addition of β-glucuronidase to urine samples in which the glucuronide adduct was present, and also to untreated samples serving as negative controls.

β-Glucuronidase equilibration: Urine samples were treated with 400 units of β-glucuronidase (Sigma–Aldrich, UK) in 0.10 M phosphate buffer (pH 7.00), and then incubated for a period of 24.0 h. at 37 °C prior to ^{1}H NMR analysis.

The shifts experienced by the resonance peaks arising from glucuronate, along with the appearance of those from the free drug released, revealed the presence of this metabolite (Figure 2.10). Additionally, MGS, acetaminophen along with its glucuronide and sulphate metabolites (Figure 2.11), valproate and 1-O-Valproyl-β-glucuronide were unambiguously identified in urine samples labelled as MGS-treated utilising both 1D and 2D NMR techniques, despite the structural similarities between the n-alkyl chain moieties in the structures of MGS, valproate and the latter's 1-O-valproyl-β-glucuronide metabolite. Valproate metabolites have been previously identified in urine samples *via* application of NMR, i.e. ^{1}H-^{1}H TOCSY and ^{1}H-^{13}C HMBC techniques (178, 179). These results obtained complemented previous reports which demonstrate that valproate is largely excreted as the 1-O-valproyl-β-glucuronide metabolite (178, 180, 181). Quantification of both MGS and 1-O-

valproyl-glucuronide *via* the integration of their resonances located at the 0.93 - 0.97 and 5.53 - 5.57 ppm buckets respectively is described in detail in the Appendix 1.

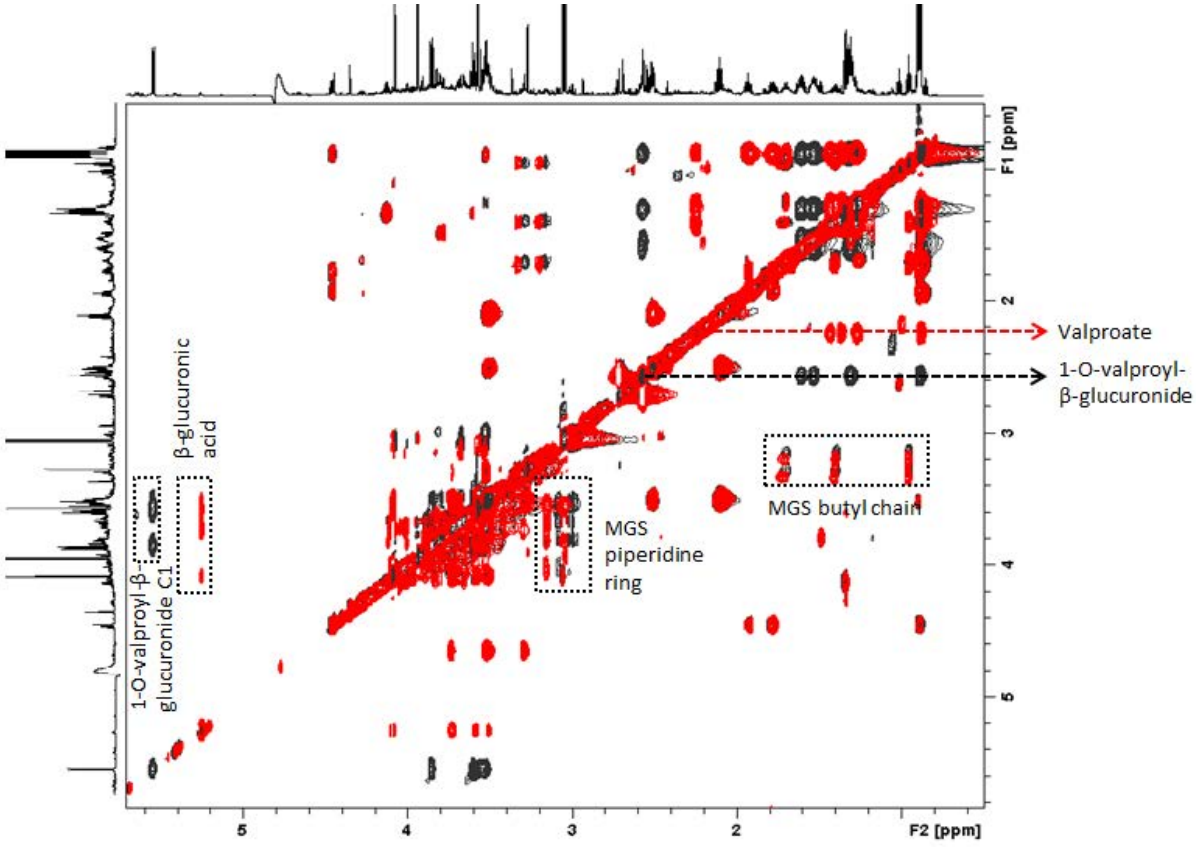

Figure 2.10. 400 MHz ^{1}H-^{1}H TOCSY spectrum of urine collected from an NPC1 patient receiving MGS treatment, before (black) and following (red) equilibration with β-glucuronidase: ^{1}H NMR signals arising from valproate, the valproate-O-acyl-β-glucuronide metabolite and MGS are labelled. A typical spectrum is shown.

MGS concentrations in biological fluids have been previously reported in human plasma and cerebrospinal fluid (CSF) (182), and also mouse plasma (183) by LC-MS/MS. Lachmann and co-workers quantified MGS using cationic exchange chromatography coupled with pulsed amperometric detection (184). Treiber *et al*. investigated the distribution of this

agent, after administration in rats, in different tissues and biofluids, including urine, using HPLC and radiolabeled MGS together with a perbutyrated derivative acting as a prodrug (185). However, all the techniques mentioned above required previous preprocessing (separation) steps.

Analytical technique	Preprocessing steps	Sample analysed	Run time	LOD	Ref
LC-MS/MS	SPE	Human Plasma	<2 min.	*ca*. 60–180 nM	(186)
LC-MS/MS	Collection of HPLC fractions, evaporation (N_2) and reconstitution in water followed by extraction with ethyl acetate.	Human liver microsomal samples	6 min.	*ca.* 0.10 nM	(187)
UPLC-MS/MS	SPE	Human Blood	4 min.	*ca*. 600 nM	(188)
HPLC-UV	Acidification of samples (pH 4.0) and extraction with ethyl acetate, followed by pre-column derivatization with 2,4 - dibromoacetophenone	Human plasma	15 min.	5 and 0.5 g/ml for valproate and 2- propyl-4-pentenoate	(189)

Table 2.5. Reported methods for valproate and/or its metabolites quantification and detection in biofluids and tissue: techniques listed along with any further preprocessing steps and major features of the analysis. Abbreviations: SPE, Solid Phase Extraction; LOD, Limit Of Detection; Ref, Reference.

The range values of the urinary excretion levels for both MGS and 1-O-valproyl-β-glucuronide in this patient cohort was 78 - 680 µmol/mmol Cn and 47 - 1154 µmol/mmol Cn respectively. However, such values are, of course, influenced by differences in the dose of MGS and valproate administered to the patients involved and by the time-point of urine sample collection subsequent to dosing, together with any between patient variations in the

renal clearance of these agents. Moreover, valproate is mainly excreted as this glucuronide adduct, although some other metabolites have been found in urine (187); therefore, the inter-individual variability with regard to valproate biotransformations can be an additional source of variation. MGS metabolism is still unclear, since it has been reported that 5% MGS is excreted in urine as a glucuronide adduct (190); however, we could not confirm it in a recent investigation involving a rat microsomal system and to the best of our knowledge there are not any reports published with that regard.

As with MGS, previous methods available for the analysis of valproate and its metabolites in urine include LC-MS/MS (186, 187), together with UPLC-MS/MS (188) and more conventional HPLC-UV analytical approaches (189) (Table 2.5).

A further advantage of ^{1}H NMR urinalysis is that 1-O-valproyl-β-glucuronide is particularly sensitive to pH value (i.e., it has a limited hydrolytic stability) and elevated temperatures (191), and hence the use of techniques which do not require the exposure of biofluid samples to such methodological stresses is recommended.

Xenometabolome: NMR analysis provides a holistic view of the urine samples analysed, which permits the exploration of the presence of further resonances arising from exogenous molecules, such as drugs and their metabolites. These observations encourage the use of NMR for the resolution of complex mixtures such as biological fluids, where it is likely to find metabolites from exogenous compounds like drugs, the so called *Xenometabolome* (26, 192). The ability of NMR to detect these kind of metabolites will serve of tremendous aid when dealing with epidemiological studies where patients are likely to be self-medicated (193), exposed to toxic substances or in cases in which patients undergo dual or multiple therapies, as notable in the NP-C1 disease cases explored here. It has to be

considered that in some countries such as the USA, MGS is not approved, even when this drug is the only available therapy worldwide, so the risks of self-medicating patients is high.

The biofluid profile of an individual is mainly composed for endogenous metabolites; nevertheless, the presence of molecules arising from diet or the exposure to hazardous compounds offers much valuable information to the investigator, since metabolomics analysis not only reveals the endogenous metabolome, but also how it responds to these exogenous compounds, and the behaviour of sample donors, e.g. either passively or through self-administration of medicines and drugs, tobacco and alcohol consumption, etc.

Furthermore, for urine ^{1}H NMR-based metabolomics investigations of NP-C patients, the assignment of MGS affords valuable information regarding the empirical removal of such potentially interfering xenobiotic relevant spectral bucket regions prior to conducting such analyses.

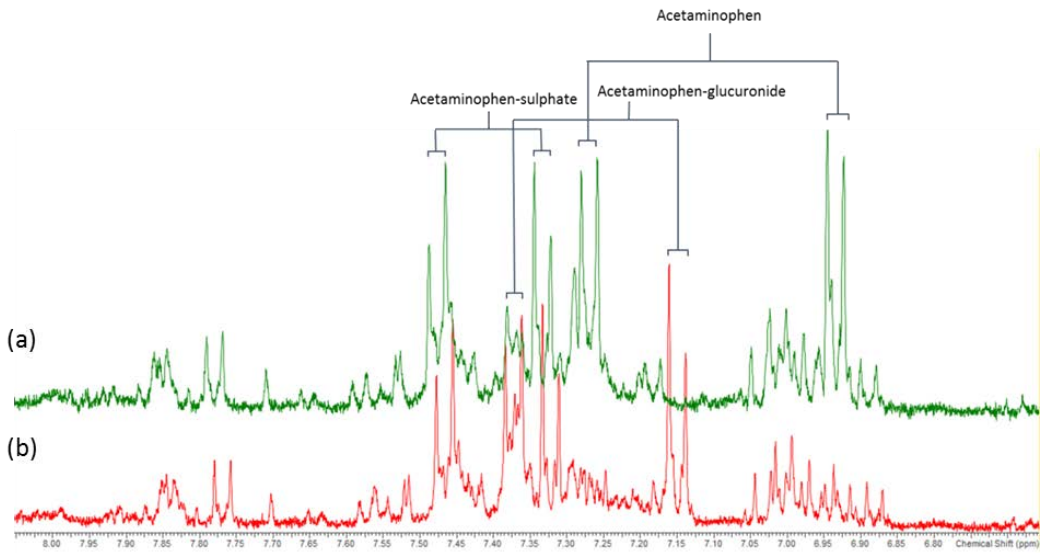

Figure 2.11. Aromatic region from a ^{1}H-NMR 400 MHz urine spectra collected from a NP-C1 MGS-treated patient before (b) and after (a) β-glucuronidase incubation: acetaminophen aromatic ring C2/6-CH signals are labelled for its different metabolites detectable in urine.

2.6.4. ^{1}H NMR-linked metabolomics investigations of the response to miglustat treatment of NP-C1 patients

In order to explore the possible changes in the ^{1}H NMR urine profiles of NP-C1 patients conceivably attributable to MGS treatment, the urine levels of those metabolites identified as discriminatory variables in the previous section were analysed in an univariate sense using the Tukey's HSD (Honest Significant Difference) test for pairwise comparisons (Figure 2.12).

However, it should be noted that such MGS as valproate and further glucuronide adducts of this agent have chemical shift values very close or even identical to those of the selected metabolites listed in Table 2.4. Therefore, some of these biomolecules were not employed for this analysis in view of their overlap with those signals attributable to the exogenous metabolites previously mentioned. Metabolites labelled as age-correlated in section 2.5 were also excluded from this analysis.

Chemical shift bucket (δ, ppm)	Assignment	Obscuring signal
0.98 - 1.03	Val-CH_3's/Ile-CH_{3a}	MGS-δ-CH_3
1.36 - 1.41	2-HydroxyisoBu-$CH_{3's}$	MGS-γ-CH_3
1.50 - 1.56	*n*-Butyrate-C3-CH_2	Valp-C3-CH_2
1.58 - 1.63	5-Aminovalerate-C3/4-CH_2	Valp-glucuronide-C3-CH_2
2.25 - 2.31	2-Hydroxyglutarate-CH_2	Valp-C2-CH_2
2.87 - 2.89	TMA-$CH_{3's}$	MGS-C5-CH/C1-CH_b
3.46 - 3.48	3-HydrohyPheAc-CH_2	MGS-C3-CH
3.63 - 3.67	Glycerol-C1/3-CH_{2a}	MGS-C4-CH
3.67 - 3.71	AAs-α-CHs/3-OH-isoBu-β-CH_2	Valp-glucuronide-C4'-CH

3.88 - 3.92	Hippurate-CH_2	Valp-glucuronide-C5'-CH

Table 2.6. List of discriminatory variables with resonances overlapping those arising from drugs and corresponding metabolites found in urine samples collected from NP-C1 patients receiving MGS treatment: the exogenous metabolite resonances are listed in the third column. Chemical shift values employed for assignments are listed in Table 2.3 and Figure 2.10. Abbreviations: 2-HydroxyisoBu-$CH_{3's}$, 2-Hydroxybutyrate-$CH_{3's}$; 3-HydrohyPheAc, 3-Hydroxyphenylacetate; AAs, amino acids; 3-OH-isoBu-β-CH_2, 3-Hydroxyisobutyrate-β-CH_2.

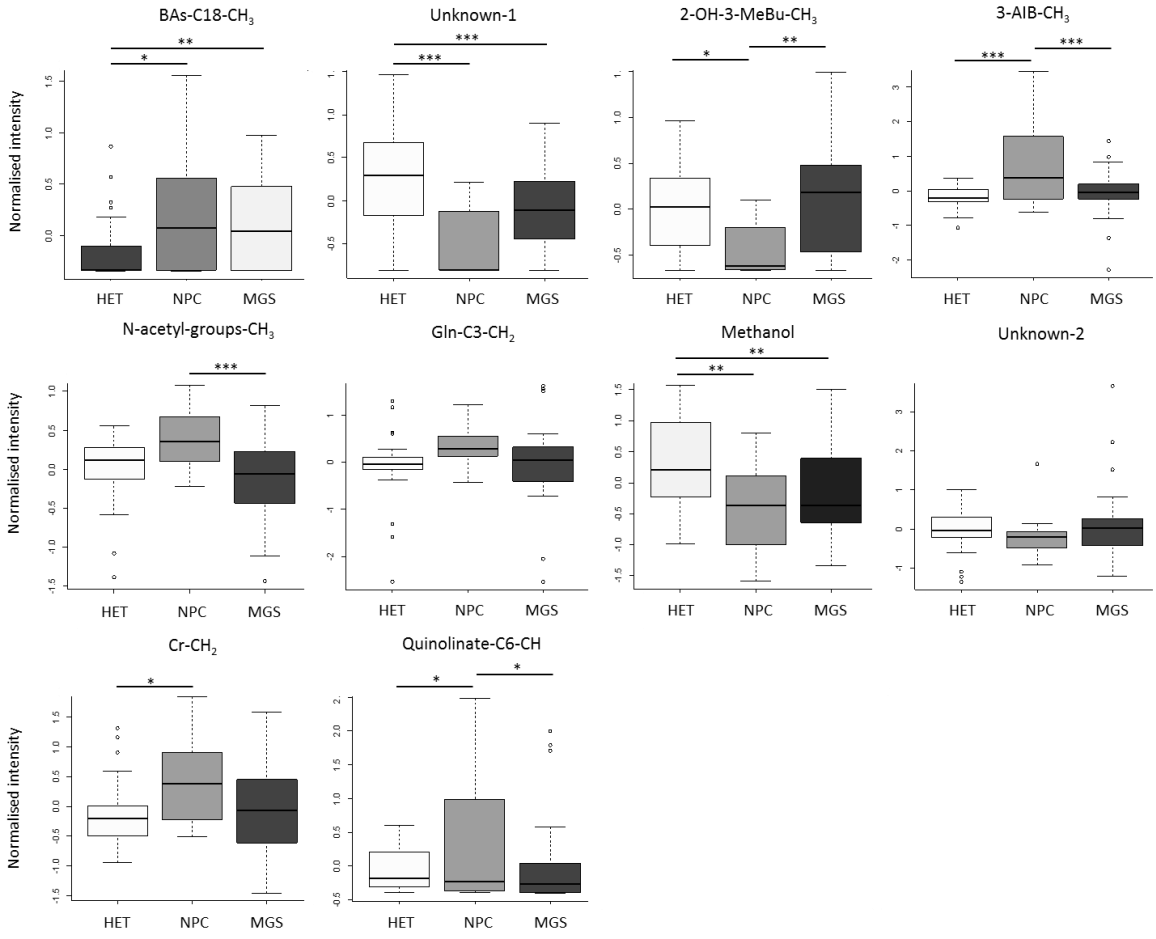

Figure 2.12. Analysis of discriminatory metabolites levels amongst heterozygotes controls (HET), NP-C1 patients (NPC) and MGS-treated NP-C1 patients (MGS): box plots for discriminatory variables that represent their normalised intensities for each group

(heterozygote, NP-C1 and NP-C1 MGS treated). Statistically significant differences obtained from the Tukey's HSD test are indicated by asterisks ($p < 0.05$, *; $p < 0.01$, **; $p < 0.001$, ***). Abbreviations: BAs, bile acids; 2-OH-3-Me-Bu, 2-Hydroxy-3-methylbutyarte; 3-AIB, 3-aminoisobutyrate; Cr, creatine. Unknown-1 corresponds to the 0.77 - 0.80 ppm bucket.

Bile acids levels remain the same for NP-C1 and MGS-treated patients, their levels being higher than those for the HET group, and somewhat lower than that of the NPC group. As expected, since MGS has no effect on bile acid synthetic pathways, nor cholesterol metabolism. Additionally, the increase in urinary BAs levels is mainly ascribable to hepatic problems in NP-C1 patients, and MGS mainly improves their neurologic status, although in some Gaucher disease patients the hepatomegaly has been partially resolved after MGS treatment (194, 195).

2-Hydroxy-3-methylbutyrate, 3-AIB, Cr and Gln show similar levels for MGS and HET groups, being all 4 metabolites correlating with muscle tissue breakdown as will be discussed in section 6.4.

MGS has been proved to improve the neurological symptoms and concomitantly the ability of NP-C1 patients to move and walk. Those functions require muscular activation, which may prevent atrophy, and consequently the release of muscle breakdown products into the bloodstream, that would be subsequently filtered out into the urine. MGS-treated NP-C1 patients are usually studied from a functional point of view, focusing in the neurological symptoms, in which common analysis are ambulation, swallowing, acoustic response, etc. (115, 196), mainly based in a test originally developed by Iturriaga *et al*. (197). Improvements for the majority of these characteristics have been observed after MGS treatment. Therefore, an increase in patients mobility triggered by an improvement in their

neurological status caused by MGS treatment would explain these results. Nevertheless, these outcomes might contrast with some well-known adverse effects of MGS treatment as diarrhoea and weight loss (198, 199); however, diarrhoea is directly related to the loss of liquids and the body weight is usually recovered after 24 months of treatment (199, 200). Both issues have their source in gastrointestinal problems caused for the intake of this drug and not in endogenous protein degradation.

Higher N-acetylated metabolites levels in urine is a common feature of some LSD such as Sandhoff and Tay-Sachs diseases. These biomolecules are mainly gangliosides, the degradation pathway of which is affected by mutations in one of the catabolic enzymes involved. Indeed, the accumulation of gangliosides in the brain is the cause of some of the neurological symptoms occurring in NP-C1 patients (201, 202). The presence of these N-acetylated biomolecules can be monitored by ^{1}H NMR analysis of urine (203). The 2.02 - 2.08 ppm bucket was selected by CCR-LDA and ranked 10th, showing higher levels for the NPC group (p = 2.15 x 10^{-2}, FC = 1.25). The well-known effects of MGS in reducing glycosphingolipid concentrations in brain can lead to the significant decrease observed in this study for urinary N-acetyl-metabolites in NP-C1 patients undergoing MGS treatment. Indeed, investigations conducted with animal models of Tay-Sachs and Sandhoff under MGS treatment revealed the delayed accumulation of GM_2 ganglioside in the brain (149, 204).

Methanol levels, despite experiencing a slightly increase with regard to NPC group, remain significatively lower than the HET group. Hence, MGS has no effect on this metabolite. The absence of more resonances available arising from bacterial metabolites prevent generalisation of the effect of MGS on microbiota activity/population in NP-C1 disease.

Quinolinate (QUIN) levels are significantly lower for the MGS-treated group than for the NPC one, showing a similar pattern to HET participants. Since the source of this metabolite is somewhat unclear (macrophages infiltrate, imbalance in NAD^+/NADH synthesis, muscle wasting, etc.), the results observed here are difficult to attribute to a specific physiological change caused by MGS treatment. Nevertheless, recent studies suggest that the inflammation process associated to the NP-C pathophysiology is secondary to the tissue damage, so it is a response from the body to fight back the disease (205); and therefore, as MGS corrects some of the symptoms arising from the disease process, then the lower levels of QUIN may reflect the reduced inflammatory process as an indirect consequence of the treatment.

CHAPTER 3

^{1}H NMR LINKED METABOLOMICS ANALYSIS OF PLASMA SAMPLES COLLECTED FROM NP-C1 PATIENTS, HETEROZYGOUS CARRIERS, HEALTHY PARTICIPANTS AND MIGLUSTAT TREATED NP-C1 PATIENTS

3.1. PLASMA SAMPLES COLLECTION AND PREPARATION FOR NMR ANALYSIS

75 plasma samples collected from NP-C1 patients, 89 from MGS treated NP-C1 patients, 31 from heterozygous carriers and 30 collected from healthy participants (as controls) were stored at -80°C. NP-C1 patients untreated and MGS treated together with heterozygotes were fasted prior to sample collection. However, healthy participants were not fasted. Plasma was separated from whole-blood using a histopaque column (gradient density column). Samples were thawed on ice and centrifuged for 3.0 min. at 850 x *g*. 200 µL of plasma was diluted with 300 µL Mili-Q H_2O and 55 µL D_2O (the latter to provide an NMR field frequency lock). Samples were transferred to standard 5 mm-diameter NMR tubes (Norell, UK) for analysis.

Disease class	NPC	MGS	HET	WT
Number (male/female)	75 (42/33)	89 (54 /35)	31 (15/13)*	30 (23/6)
Average age in years (range)	19 (0.3 - 54)	11 (1 – 28)	N/A	~15 (0.4 - 18)**

Table 3.1. Participants' information included in the NP-C1 plasma dataset: Abbreviations: NPC, NP-C1 disease patients; MGS, NP-C1 patients undergoing miglustat treatment; HET, heterozygous carriers; WT, healthy participants. *Information relative to the gender of some heterozygous carriers was not available; **, the age of all healthy participants was not available.

3.2. NMR ANALYSIS OF PLASMA PROFILES

NMR spectral acquisition was performed on a Bruker AVIII 700 spectrometer equipped with a ^{1}H ($^{13}C/^{15}N$) TCI cryoprobe (Department of Chemistry, University of Oxford) with sample temperature stabilised at 310K. ^{1}H NMR spectra were acquired using a 1D NOESY presaturation (*noesygppr1d* pulse sequence, Bruker) scheme for attenuation of the water resonance with 2 s presaturation. Low molecular weight metabolite spectra were acquired using a spin-echo sequence [Carr-Purcell-Meiboom-Gill (CPMG)] with presaturation for water suppression (*cpmgpr1d* pulse sequence, Bruker) with a τ interval of 0.39 ms, 80 loops, and echo time of 0.40 ms, 32 scans, an acquisition time of 1.46 s, a relaxation delay of 2 s, and a fixed receiver gain.

3.2.1. ^{1}H NMR plasma profiles of NP-C1 patients

^{1}H NMR resonances were assigned on the basis of chemical shifts, coupling constants and literature values (46, 206, 207). Spectra acquired from plasma samples contained

different resonance signals ascribable to amino acid, small organic acid anions, glucose, lipoproteins and glycoproteins. Additionally, some other signals from exogenous agents were observed in the NMR spectra such as Ca-EDTA^{2-} and Mg-EDTA^{2-} complexes resonances arising from the chelation of these metal ions by this agent, which was present in the sample collection tubes as an anticoagulant (Figure 3.2); resonances arising from the plasma separation procedure can also be observed in the spectrum such as a singlet at 2.26 ppm and signals around 1.80 ppm. Broad resonances from 3.40 to 4.45 ppm and from 5.40 to 5.62 ppm are attributable to the polymer (polysucrose-based) contained in the histopaque column employed for plasma isolation (Figure 3.1).

Histopaque is a method employed to separate the different phases present in blood, i.e. those conformed by plasma from that containing lymphocytes, monocytes and platelets, and an additional phase conformed of granulocytes and erythrocytes, through a density gradient media composed of polysucrose, which is the broad signal observed in Figure 3.1, in 3.40 - 4.45 and 5.40 - 5.62 ppm NMR spectral regions. This solution incorporates sodium diatrizoate, observable as a singlet at 2.26 ppm. Additional signals were found after running a sample of water, as control, *ca*. 1.80 ppm, which probably arises from the histopaque treatment of blood samples. In view of the exogenous NMR-visible signals assignable to the sucrose polymer and further agents derived from histopaque treatment that overlayed some resonance signals of biological interest, this plasma isolation method presents limitations for NMR-based metabolomics studies.

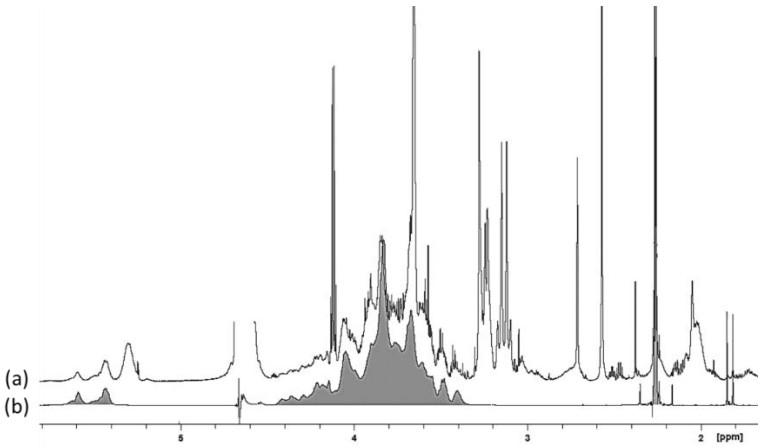

Figure 3.1. Stack plot of (a) a plasma sample separated by histopaque and (b) a water sample also passed through a histopaque column.

The usual methods employed to avoid anticoagulation during blood sample collection include the usage of sample tubes containing lithium-heparin, citrate or the sodium salt of EDTA. Both citrate and EDTA give ^{1}H NMR-visible resonance peaks in plasma spectra, subsequently acquired, at the concentrations typically used (208), whilst plasma samples collected in heparin-Li^{+} present only a weak and broad spectrum that can be removed through CPMG pulse sequences for spectral acquisition. However, the presence of EDTA signals in the ^{1}H NMR plasma spectra could offer additional information, since the resulting Ca and Mg-$EDTA^{2-}$ resonances are clearly observable, and can be employed to monitor both metal ions. Although other metal ions (Zn^{2+}) could be interfering in the complex equilibrium that involves Ca-$EDTA^{2-}$:Ca^{2+}:Mg-$EDTA^{2-}$:Mg^{2+}:Free-EDTA. Barton *et al*. (209) explored the influence of the differing anticoagulants noted above on NMR metabolomics plasma investigations, and concluded that only a few resonances are completely masked by EDTA and EDTA-metal ions resonances, such as acetylcarnitine-$N(CH_3)_3$ resonance at 3.60 ppm (Ca-$EDTA^{2-}$-N-CH_2CH_2-N- peak), carnitine resonances at *ca.* 3.21 ppm (free EDTA-N-CH_2-CO- peak), ornithine-C4-CH_2 resonances at 3.07 ppm (Ca-$EDTA^{2-}$-N-CH_2CH_2-N- peak) and cis-

aconitate-CH_2 resonance at 3.44 ppm (Ca-$EDTA^{2-}$-N-CH_2CH_2-N- peak). Their final conclusion was that NMR metabolomics investigations utilising plasma samples collected in EDTA tubes can be conducted without any major drawbacks.

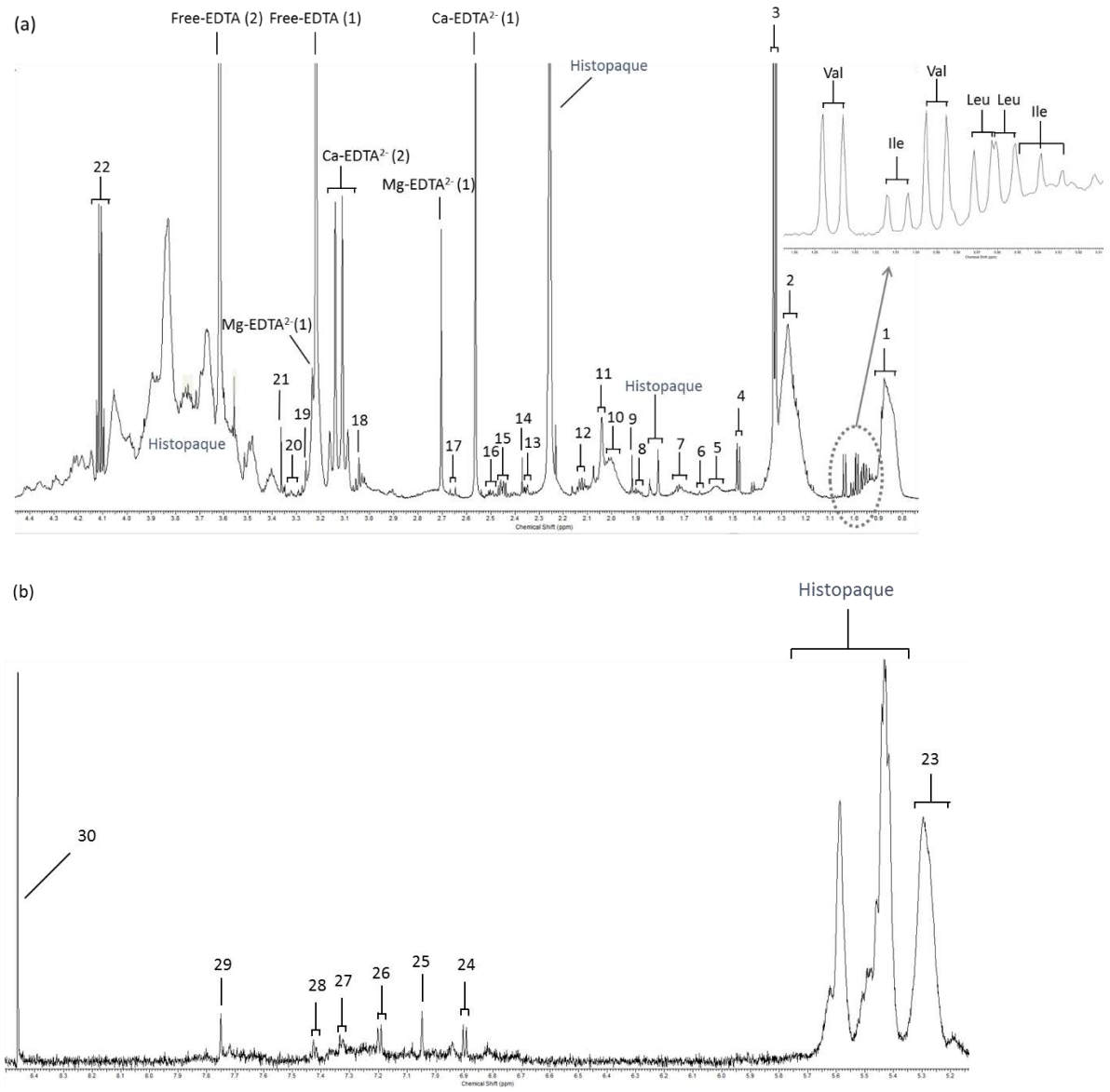

Figure 3.2. (a) 0.75 - 4.45 and (expansion of the BCAA region is included as an insert) (b) 5.10 - 8.50 ppm regions from an NP-C1 patient ^{1}H NMR plasma profile: 1, CH_3-VLDL/LDL; 2,-$(CH_2)_n$-VLDL/LDL; 3, Lactate-CH_3; 4, Alanine-CH_3; 5, TG-C**H$_2$**CH_2CO; 6, Arginine-C4-CH_2; 7, Lysine-C5-CH_2; 8, Arginine-C3-CH_2; 9, Acetate-CH_3; 10, CH_2C**H$_2$**CH=-; 11, N-acetyl-glycoprotein-CH_3; 12,

Proline-1; 13, Glutamate-C2-CH_2; 14, Pyruvate-CH_3; 15, Glutamate-C3-CH_2; 16, Glutamine-C4-CH_2; 17, Citrate-CH_{2a}; 18, Creatine-CH_2; 19, TMAO-$CH_{3's}$; 20, Proline-2; 21, Phosphocholine-NCH_3; 22, Lactate-CH; 23, =C-C**H₂**-C=, -C**H**=C**H**-; 24, Tyrosine-C3/5-CH; 25, Histidine-C5-CH; 26, Tyrosine-C4/6-CH; 27/28-Phenylalanine; 29, Histidine-C6-CH; 30, Formate-H.

3.3. DATA PREPROCESSING

Any resonances arising from histopaque contamination, i.e., the 1.80 - 1.86, 2.18 - 2.31, 3.30 - 4.50, and 5.37 - 5.68 ppm spectral regions were removed. Additionally, the 1.15 - 1.17 ppm region was excluded in view of ethanol contamination, likely as a result of skin disinfection prior to sample collection. Regions containing only noise across all spectra were also excluded, so that a dataset containing 38 columns (variables) and 252 rows (samples) was obtained. Prior to any statistical analysis, the whole dataset was sum-normalised, Pareto scaled and cube-root transformed.

3.4. UNIVARIATE AND MULTIVARIATE ANALYSIS OF THE ^{1}H NMR PLASMA DATASET

3.4.1. Univariate data analysis: Tukey's HSD test

Since some information concerning the age and gender of participants was not available, an ANOVA/ANCOVA model similar to those employed in previous and next sections cannot be accurately employed. However, a *post-hoc* Tukey's range test (honest significant test, HSD) was applied to the sum-normalised, cube-root transformed and Pareto-scaled plasma dataset. Those variables selected by the RFs technique as discriminatory

features are supplemented in Table 3.3 by a '*' sign to indicate the level of significance based on their ^{1}H NMR plasma profiles.

3.4.2. Multivariate data analysis

3.4.2.1. Preliminary analysis: PCA

PCA scores plots illustrated in Figure 3.2 reveal that WT is the most distinct classification group, since a clear cluster can be observed when plotted against the NPC, HET and MGS groups. However, the HET and NPC groups do not form clear clusterings in the scores plot, and hence there is no separation between these groups. The influence of miglustat (MGS) treatment on the ^{1}H NMR plasma profiles of NP-C1 patients was also explored. Scores plot of PC1 *vs*. PC2 in Figure 3.3 did not show any differences between both groups (MGS *vs*. NPC). Indeed, apart from WT, the MGS plasma profiles were found to be very similar to the remaining disease classification groups (NPC and HET).

3.4.2.2. Classification performance

Random Forests (RFs): The procedure described in section 2.4.3 for RFs analysis was also employed for the plasma dataset. Since in this case the number of groups is 4, this analysis was applied for each pair of different groups, with the exception of MGS *vs.* HET one, since that comparison was irrelevant for this study (Table 3.2) as heterozygous carriers do not present any symptomatology associated to NP-C1 disease, and therefore, they are not treated with MGS.

(a)

OOB error

Disease class	WT	NPC
NPC	0.106 (0.003)	
HET	0.175 (0.005)	0.226 (0.003)
MGS	0.160 (0.003)	0.353 (0.004)

(b)

Accuracy

Disease class	WT	NPC
NPC	0.904 (0.005)	
HET	0.818 (0.007)	0.765 (0.007)
MGS	0.832 (0.006)	0.646 (0.006)

(c)

Sensitivity

Disease class	WT	NPC
NPC	0.926 (0.005)	
HET	0.824 (0.011)	0.754 (0.020)
MGS	0.864 (0.007)	0.664 (0.008)

(d)

Specificity

Disease class	WT	NPC
NPC	0.853 (0.011)	
HET	0.823 (0.012)	0.778 (0.007)
MGS	0.729 (0.015)	0.632 (0.010)

Table 3.2. RF classification performance for all 4 groups analysed in the plasma dataset: tables showing mean and SEM values (the latter between brackets) for OOB error (a), accuracy (b), sensitivity (c) and specificity (d) values.

It should be noted that accuracy, sensitivity and specificity show lower values for the HET *vs*. NPC classification comparison, and even lower values for MGS *vs*. NPC one (Table 3.2), and this confirms the absence of differences between the ^{1}H NMR profiles of the HET and NPC groups, and the unaltered profile of NP-C1 patients despite of being under MGS treatment. However, the remaining group pair comparisons were successfully classified by RFs as illustrated in the multidimensional scaling plots shown in Figure 3.3, where the classification of the test set is exhibited.

The RFs performance on WT *vs*. NPC groups resulted in an OOB error value of 0.106 ± 0.003 (mean ± SEM), which reveals a successful classification of the training set. The multidimensional scaling plot of the proximity matrix calculated from one of the RFs

iterations (Figure 3.3) serves as an illustration of this discrimination. Additionally, no discrimination was identified in the untreated NP-C1 patient group based on gender or age.

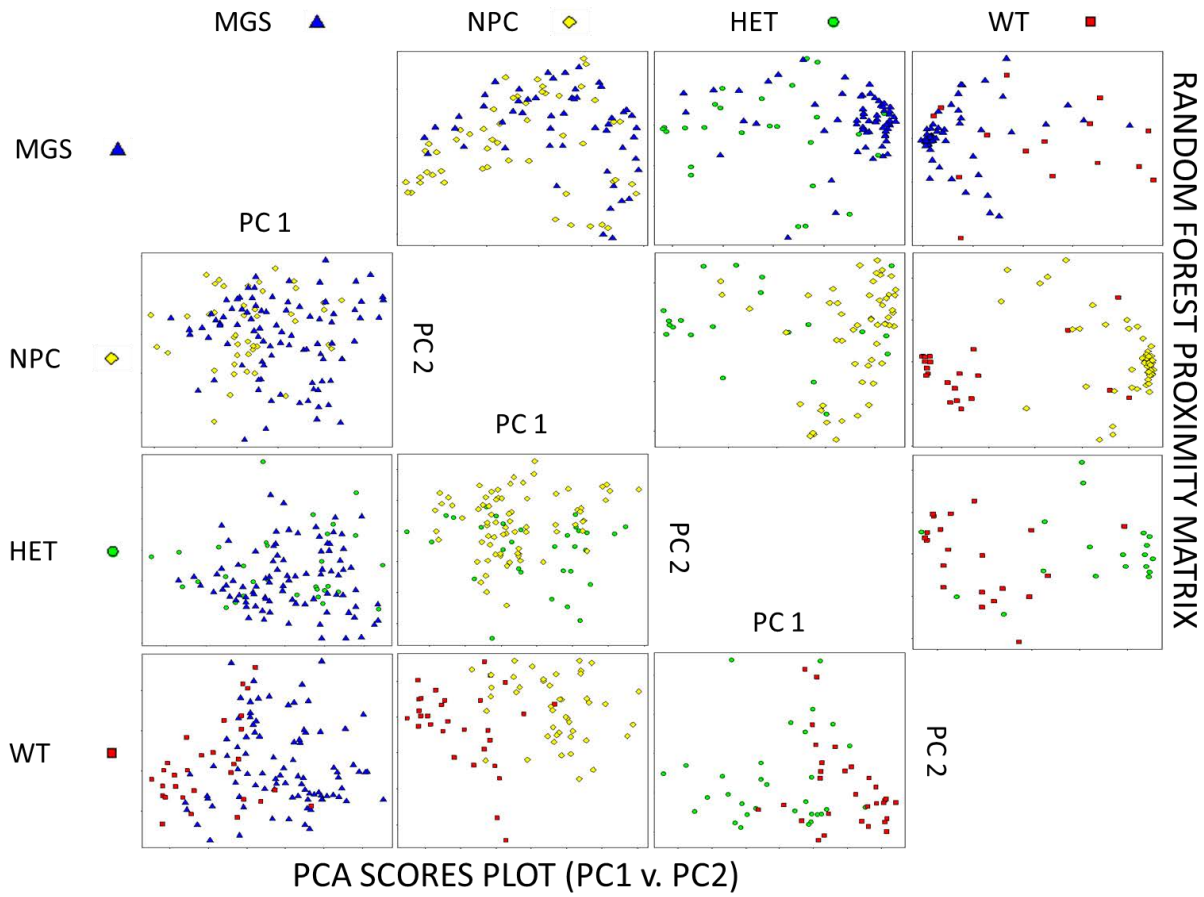

Figure 3.3. PCA scores plots for PC1 *vs.* PC2 for each pair of comparisons, and multidimensional scaling plot from a RFs proximity matrix showing success of discrimination from a single RFs iteration for the NP-C1 plasma dataset.

3.4.2.3. Variable selection

Table 3.3 summarises the top nine discriminatory variables selected by the RFs analysis, for each pair of disease status classifications compared, along with their corresponding assignments. HET *vs.* MGS is not shown as noted above, and RFs analysis of

the NPC *vs*. MGS comparison did not show any classification success, and therefore no ranking was extracted from that analysis.

Bucket (ppm)	Assignment	Multiplicity (J, Hz)	NPC *vs.* WT	HET *vs.* WT	MGS *vs.* WT	NPC *vs.* HET
0.81 - 0.83	HDL-CH_3	br				$\downarrow^{**}$(2)
0.83 - 0.89	VLDL-CH_3	br	$\uparrow^{***}$(6)	$\uparrow^{***}$(2)	$\uparrow^{***}$(6)	
0.89 - 0.95	Isoleucine-C5-CH_3	t (7.3)	$\uparrow^{***}$(9)			$\uparrow^{*}$(9)
1.13 - 1.15	2,3-butanediol-$(CH_3)_2$	d (6.1)			$\uparrow$(9)	
1.21 - 1.23	HDL-$(CH_2)_n$	br		$\uparrow^{***}$(7)		$\uparrow$(8)
1.23 - 1.25	LDL-$(CH_2)_n$	br	$\uparrow^{***}$(5)	$\uparrow^{***}$(3)	$\uparrow^{***}$(4)	
1.25 - 1.31	VLDL-$(CH_2)_n$	br	$\uparrow^{***}$(2)	$\uparrow^{***}$(5)	$\uparrow^{***}$(1)	$\uparrow^{*}$(7)
1.31 - 1.37	Lactate-CH_3	d (6.8)	$\uparrow^{***}$(7)		$\uparrow^{***}$(7)	
1.53 - 1.61	-C**H_2**CH_2CO	br	$\uparrow^{***}$(1)	$\uparrow^{**}$(8)	$\uparrow^{***}$(3)	$\uparrow^{**}$ (3)
1.94 - 1.96	Proline 1	m		$\uparrow^{***}$(9)		
1.96 - 1.98	Proline 2	m		$\uparrow^{***}$(6)		
2.03 - 2.09	N-acetylglycoprotein/CH_2-C**H_2**-CH=	s/br	$\uparrow^{***}$(8)			
2.52 - 2.58	Ca-EDTA	s			$\uparrow^{***}$(8)	$\uparrow^{***}$(1)
5.26 - 5.32	Unsaturated lipid 2	br	$\uparrow^{***}$(3)	$\uparrow^{***}$(1)	$\uparrow^{***}$(2)	
5.32 - 5.37	Unsaturated lipid 1	br	$\uparrow^{***}$(4)	$\uparrow^{***}$(4)	$\uparrow^{***}$(5)	$\downarrow$ (5)
7.02 - 7.08	Histidine-C2-CH	s				$\uparrow^{*}$(6)
7.74 - 7.85	Histidine-C5-CH	s				$\downarrow^{*}$(4)

Table 3.3. RFs discriminatory variables for the NP-C1 plasma dataset: Arrows indicate an increase/decrease in the measured metabolite with respect to the WT samples (or with respect to the HET samples in the case of the NPC *vs*. HET comparison). The results of the Tukey's HSD test for each metabolite identified by RFs analysis are indicated by asterisks ($p < 0.05$, *; $p < 0.01$, **; $p < 0.001$, ***). The RFs ranking is based on their MDA value, and is

represented in brackets. Unsaturated lipid 1 and 2 refer to =C-C**H**$_2$-C= and -C**H**=C**H**- protons respectively.

Since some of the variables listed in Table 3.3 were highlighted in more than one classification comparison as discriminant features, their levels are then illustrated as box plots in Figure 3.5.

3.4.2.4. ROC curve analysis

In order to seek those variables that more efficiently contribute to the classification of NP-C1 patients when compared to healthy control ones, a ROC curve analysis was performed including WT and NPC classes using RFs as a tool for classification. Metabolites selected as important features for discrimination listed in Table 3.3 were employed for this analysis.

The majority of variables selected for classification for the NPC *vs*. WT comparison were assignable to lipoprotein-associated TGs, being actually able to successfully classify the WT and NPC groups with only 2 variables [AUC (mean) = 0.912; range, 0.772 - 0.982]. Isoleucine (Ile) and lactate were also included in the models, being selected in *ca*. 86% of those constructed [Figure 3.4 (b)].

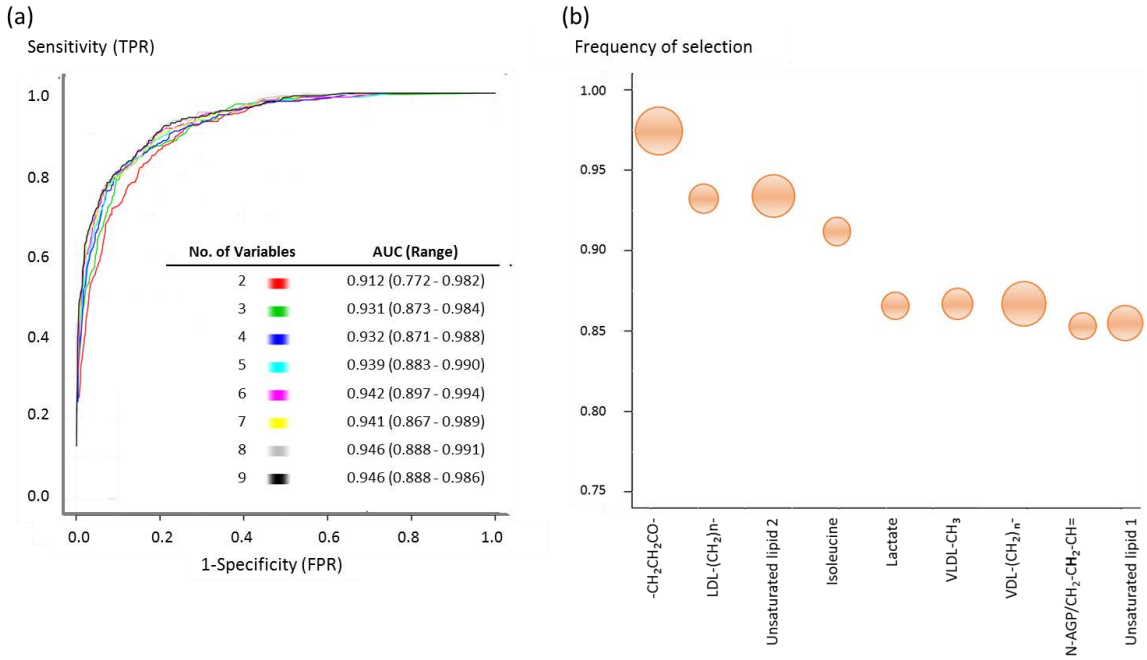

Figure 3.4. (a) ROC curves and (b) bubble diagram for variable importance for the NP-C1 blood plasma dataset: different combinations of variables gave different AUC values, ranging from 0.912 for 2 variables, and up to 0.946 with 9 variables, as indicated in the Table inserted in (a). (b) Variable rankings arising from ROC analysis (depicted in the vertical axis in); blue bubbles indicate metabolites with lower levels in the NPC group, and orange ones those with higher levels. The size of each bubble is correlated with the fold change (FC). Abbreviations: N-AGP, N-acetylglycoproteins; TPR, True Positive Rate; FPR, False Positive Rate.

3.5. ^{1}H NMR PLASMA PROFILES OF NP-C1 PATIENTS, HETROZYGOUS CARRIERS, HEALTHY PARTICIPANTS AND MIGLUSTAT TREATED NP-C1 PATIENTS

Fasting at least 8 hours prior to lipid determination in blood or plasma is a common requirement in order to prevent increased lipid levels ascribable to food intake, specifically TGs. Although samples collected from healthy participants are not fasting samples, levels of several lipidic species for NPC, HET and MGS groups are higher than those for this WT group

(Figure 3.5) and recent studies have reported only a low correlation between fasting times and plasma lipid levels (210). However, the results shown herein present some limitations.

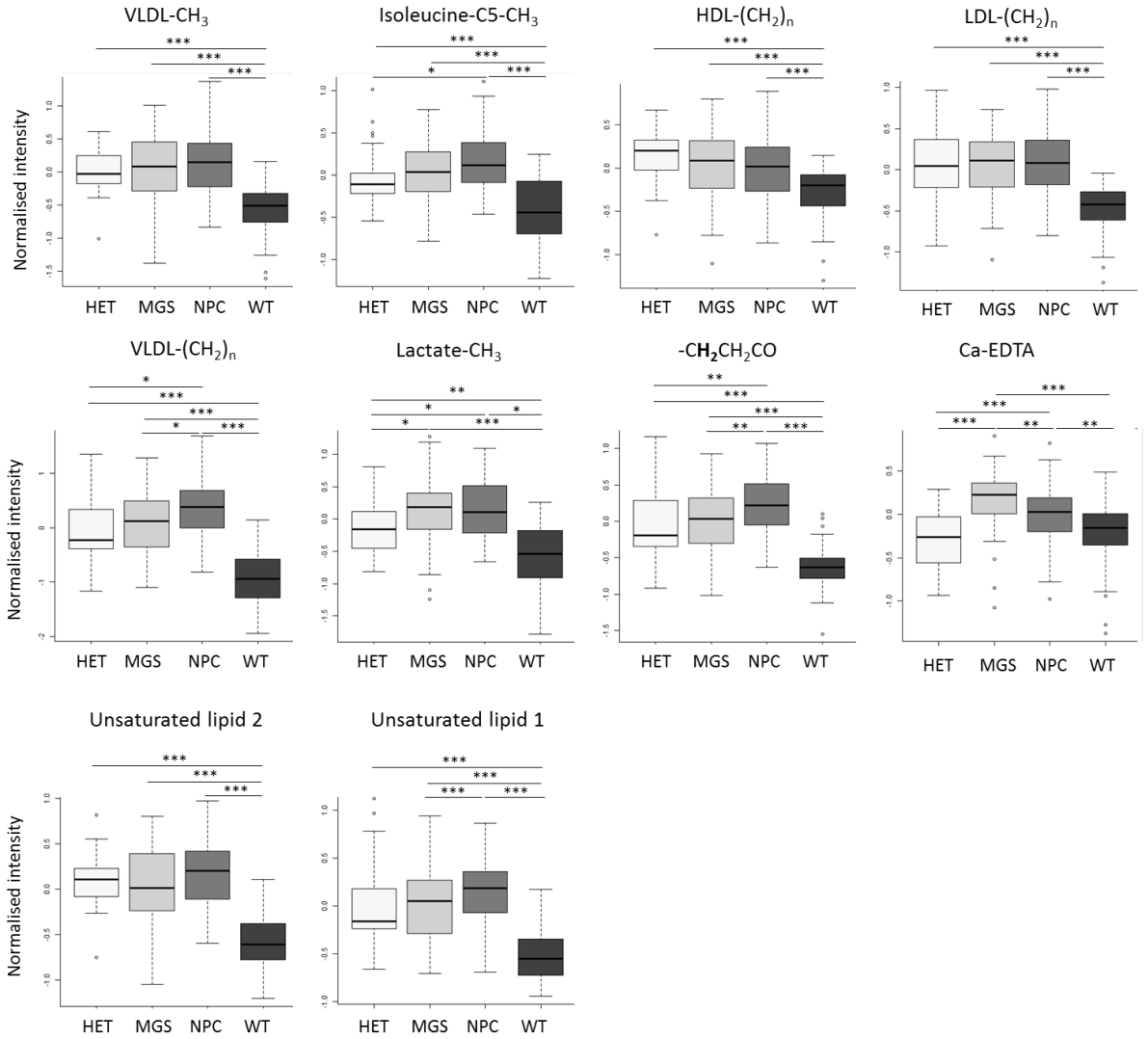

Figure 3.5. Box plots for metabolites selected in more than one classification problem for the NP-C1 plasma dataset: those metabolites selected by the RFs models and also showing significant differences are indicated by asterisks ($p < 0.05$, *; $p < 0.01$, **; $p < 0.001$, ***).

NP-C1 is a disorder mainly affecting lipid and cholesterol trafficking. Table 3.3 reveals that differences in such lipid resonances were selected as important features for

discrimination between untreated NPC patients and the WT participants. Most notably, NP-C1 patients exhibit an increase in both VLDL lipid signals [i.e. VLDL-CH_3 and VLDL-$(CH_2)_n$-], LDL-$(CH_2)_n$-, HDL-$(CH_2)_n$-, lipid -C**H_2**CH_2CO, and vinylic TGs spectral regions. In addition, lactate is significantly increased for all the groups when expressed relative to the WT one. The N-acetylglycoproteins and lactate spectral regions were also highlighted as important variables for discrimination in view of their higher levels in the NP-C1 group.

The MGS group's ^{1}H NMR plasma profiles show a very similar pattern to the NPC one for those spectral regions assignable to lipids, except for the -C**H_2**CH_2CO and unsaturated lipids-1, for which the MGS group has lower levels (Table 3.3). Interestingly, the isoleucine bucket was neither selected as a discriminatory variable for MGS-treated samples, nor did it attain any statistical significance (showing very similar levels to the NPC group). However, some additional variables were required for discrimination between MGS-treated patients and the healthy controls (WT group), including increases in the Ca-EDTA^{2-} and 2,3-butanediol buckets.

The HET group exhibited an intermediary phenotype for plasma lipoproteins between the MGS/NPC and WT ones, since the pattern for VLDL-CH_3, Ile, VLDL-(CH_2)n-, TG-C**H_2**CH_2CO and unsaturated lipid-1 in the ^{1}H NMR plasma spectra is NPC > MGS > HET >> WT, similar to WT although the unsaturated lipid 2 resonance signal is of higher intensity than that of the MGS group. Similar to the NP-C1 patients, the key variables responsible for discrimination between the HET and WT groups are dominated by lipid resonances. Two variables responsible for discrimination between NPC and control spectra were not identified in the HET *vs*. WT analysis (N-acetyl glycoprotein/CH_2-CH_2-CH= and lactate), whilst an increase in proline resonances is observed only for the HET samples. This HET group was successfully classified when compared to the WT one, but the profiles exhibited were closer

to the NPC group; RFs analysis for this pair (HET *vs.* NPC) of groups gave fair values for accuracy, specificity and sensitivity. Additionally, both histidine buckets contributed to the discrimination between the NPC and HET classes, this being the only case in which this amino acid resonances were featured as discriminatory variables.

These similarities between the HET and NPC groups are somewhat surprising, since heterozygous carriers do not manifest any pathological symptoms, and this may indicate an irrelevant role of lipoprotein metabolism in the disease process.

CHAPTER 4

^{1}H NMR LINKED METABOLOMICS ANALYSIS OF LIVER SAMPLES COLLECTED FROM AN NP-C1 MOUSE MODEL

4.1. LIVER AQUOEUS METABOLITES EXTRACTION FOR NMR ANALYSIS

NP-C1 mutant (BALB/cNctr-Npc1m1N/J, *Npc1*$^{-/-}$; NP-C1), control (*Npc1*$^{+/+}$; WT) and NP-C1 heterozygous mice (*Npc1*$^{+/-}$; HET), were generated from heterozygote matings and the genotype of offspring was determined by polymerase chain reaction (PCR), as described previously (211). Mice were bred and housed under standard non-sterile conditions at the University of Oxford. All animal procedures were conducted using protocols approved by the UK Animals (Scientific Procedures) Act (1986). In total, 65 liver samples from gender-matched heterozygous carrier (HET), NP-C1 disease (NPC) and wild type (WT) mice were collected at 3, 6, 9 and 11 weeks.

	Collection Time Point (weeks)			
Disease Class	3	6	9	11
Wild type (WT)	4 (3/1)	3 (0/3)	7 (5/2)	8 (5/3)
Heterozygotes (HET)	0 (0/0)	0 (0/0)	9 (5/4)	10 (5/5)
NP-C1 (NPC)	4 (2/2)	6 (4/2)	11 (6/5)	3 (0/3)
	Number (male/female)			

Table 4.1. Liver samples available for ^{1}H NMR-linked metabolomics analysis at time-points of 3, 6, 9 and 11 weeks.

Aqueous metabolites extraction for NMR analysis: The extraction protocol employed was based on the procedure described by Waters *et al*. (212) with slight modifications. A portion of hepatic tissue (*ca*. 80 mg) was taken, for each piece of liver 0.02 mL of ice-cold extraction solvent (H_2O/CH_3CN, 1:1) per mg of tissue were added. The sample was then mechanically homogenized using an electric pestle rotor (Sigma-Aldrich UK, UK). The homogenates were centrifuged at 10,000 × *g* for 10 min at 4 °C. Supernatants (hydrophilic metabolites) were freeze-dried and reconstituted in 500 µL of D_2O containing 0.05 % wt. TSP, and 50 µL of pH 7 phosphate buffer to reach a final concentration of 0.01 M, then vortexed and centrifuged at 5,000 x *g* for 10 min. at room temperature. Supernatants were transferred into 5-mm NMR glass tubes (Norell, UK) for NMR analysis.

4.2. NMR ANALYSIS OF LIVER EXTRACTS

1D ^{1}H NMR: Single-pulse ^{1}H NMR spectra experiments were carried out on a Bruker Avance AM-400 spectrometer (Leicester School of Pharmacy facility, DMU, Leicester, UK) operating at a frequency of 399.94 MHz and a probe temperature of 298 K. Spectra were

acquired using *noesygppr1d* (Bruker) pulse sequence for water suppression. For each spectrum 128 scans were acquired, a relaxation delay of 3 s, spectral width of 4,800 Hz and a time domain of 32 K points. Spectra were acquired in an automated manner using a sample changer for continuous sample delivery.

***^{1}H-^{1}H COSY**:* This experiment was carried out at 27 ˚C on a Bruker AV 400 MHz (Leicester School of Pharmacy, DMU, Leicester, UK) using the same parameters as those delineated above for urine samples.

^{13}C-^{1}H HSQC: Heteronuclear Single Quantum Coherence (HSQC) spectra were acquired on a Bruker Avance AM-400 spectrometer (Leicester School of Pharmacy, DMU, Leicester, UK). For the HSQC experiments, *hsqcedetgpsp.3* pulse sequence (Bruker) was employed, and 256 scans for 128 increments were acquired for each spectrum. The F2 and F1 spectral widths were 6,340 and 16,600 Hz, respectively.

4.2.1. ^{1}H NMR hepatic profiles of NP-C1 mice

Typical 400 MHz single-pulse ^{1}H NMR spectra of liver samples (Figure 4.1) collected from NP-C1 disease mice and their heterozygous carrier, plus wild type specimens controls contained a large number of different types of polar low molecular weight metabolites, including amino acids [alanine (Ala), isoleucine (Ile), lysine (Lys), tyrosine (Tyr), phenylalanine (Phe)] and derivatives such as sarcosine, small organic acids (2-aminobutyrate, 2-hydroxybutyrate, lactate), carbohydrates (glucose, glycogen), nucleotides (GMP,GTP), etc.

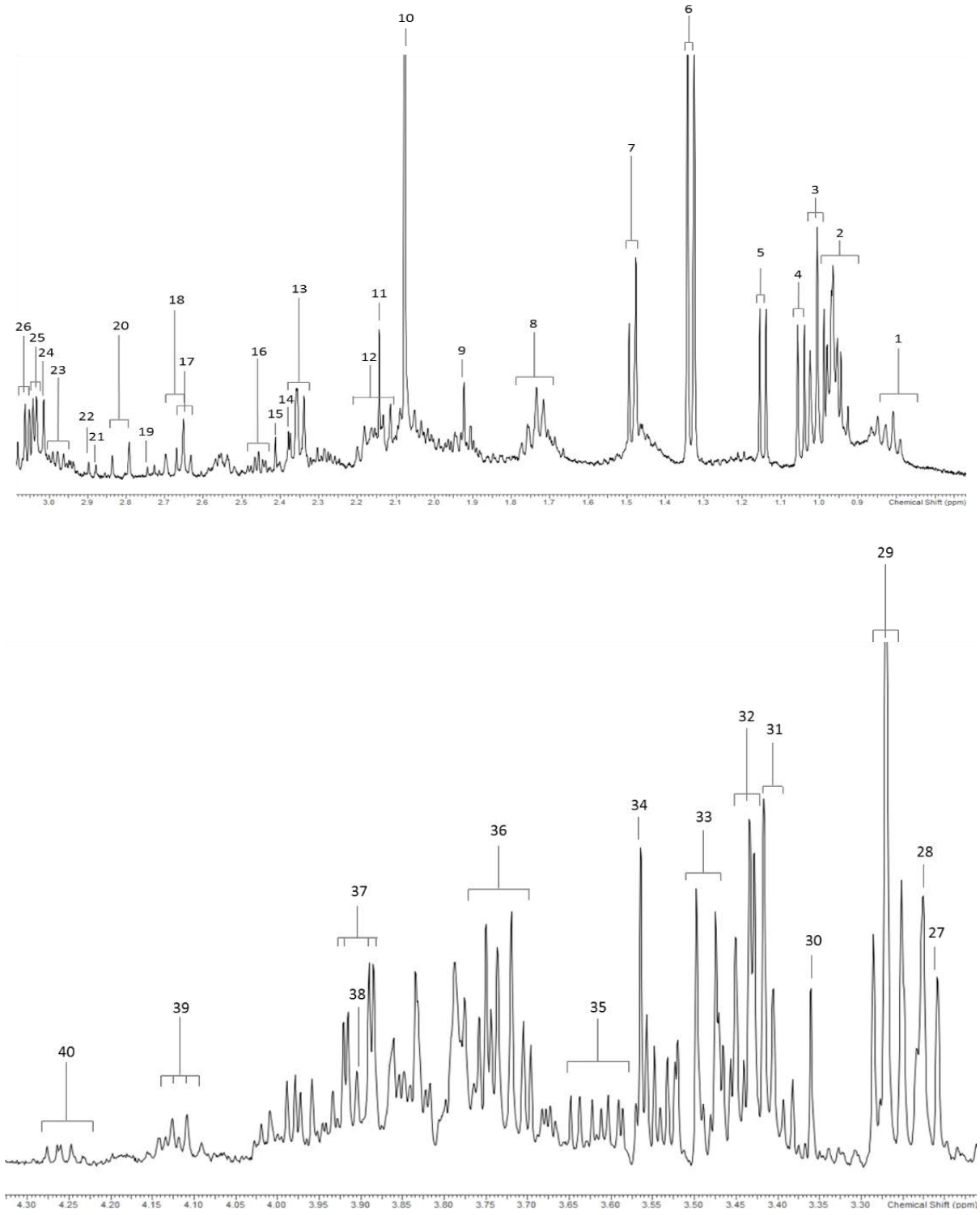
1
2
3
4
5
6
7
8
9
10
11
12
13
14
15
16
17
18
19
20
21
22
23
24
25
26
27
28
29
30
31
32
33
34
35
36
37
38
39
40
Chemical Shift (ppm)
Chemical Shift (ppm)

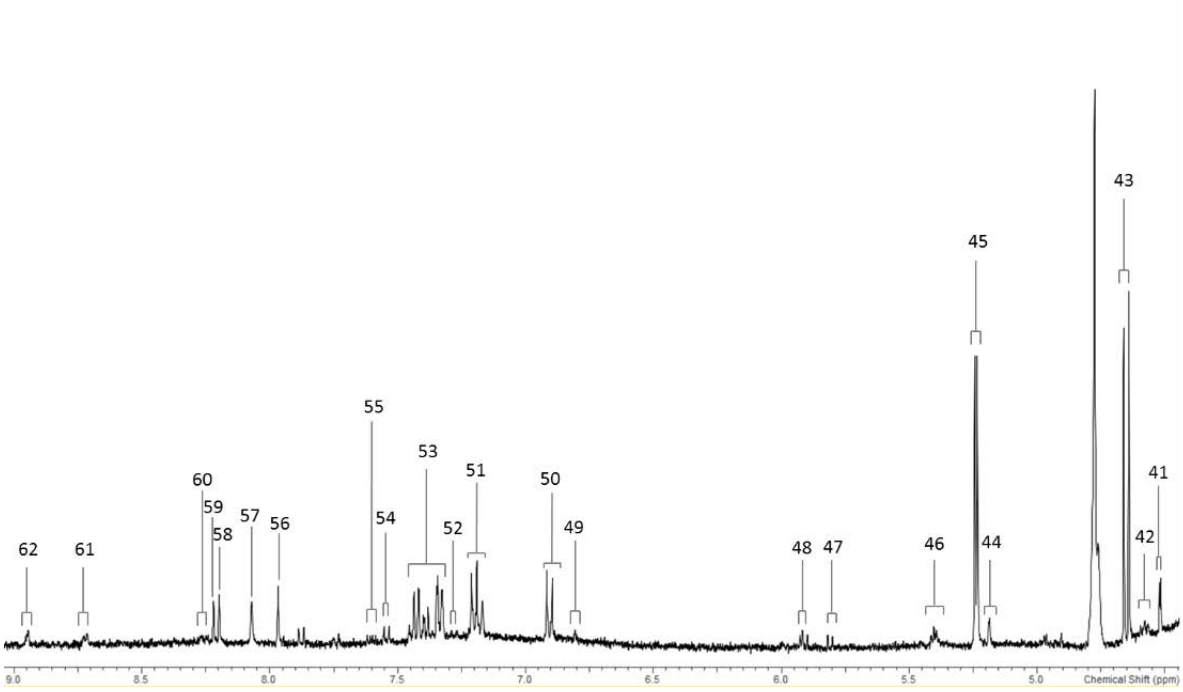

Figure 4.1. ^{1}H NMR spectrum of an NP-C1 mouse liver aqueous extract: 1, Unassigned-1; 2, Leu-CH_3/Ile-C5-CH_3/Val-CH_{3a}; 3, 2-Aminobutyrate-CH_3; 4, Val-CH_{3b}; 5, Propylene glycol-CH_3; 6, Lactate-CH_3; 7, Ala-CH_3; 8, Lys-C5-CH_2/Orn-C4-CH_2; 9, Acetate-CH_3; 10, Acetonitrile; 11, Met-CH_3; 12, GSSH-Glu-C3-CH_2/Gln-C3-CH_2; 13, Glu-C4-CH_2; 14, Oxalacetate-CH_2; 15, Succinate-CH_2; 16, Gln-C4-CH_2; 17, Met-C4-CH_2/Hypotaurine-C4-CH_2; 18, Asp-CH_{2a}; 19, Sarcosine-CH_3; 20, Asp-CH_{2b}; 21, TMA-$CH_{3's}$; 22, Dimethylglycine-$CH_{3's}$; 23, GSSH-Cys-C3-CH_2; 24, Creatine-CH_3; 25, Lys-C6-CH_2; 26, Orn-C5-CH_2; 27, Choline/Phosphocholine-$CH_{3's}$; 28, Glycerophosphocholine-CH_3's; 29, Taurine-S-CH_2/β-Glucose-C2-CH; 30, Methanol; 31, β/α-Glucose-C4-CH; 32, Taurine-N-CH_2; 33, β-Glucose-C3/5-CH; 34, Glycine; 35, Glycerol-C1/3-CH_2; 36, β-Glucose-C6-CH_a/α-Glucose-C3-CH/6-CH_2; 37, β-Glucose-C6-CH_b; 38, Betaine-CH_2; 39, Lactate-CH_2; 40, Thr-CH_2; 41, Ascorbate; 42, GSH-Cys-CH; 43, β-Glucose/Glucose-6P-C1-CH; 44, Phosphoenolpyruvate-CH_{2a}; 45, α-Glucose/Glucose-6P-C1-CH; 46, Phosphoenolpyruvate-CH_{2b}/Glycogen; 47, Uracil-CO-CH; 48, GTP-C1'-CH; 49, 3-Hydroxyphenylacetate-CH2; 50, Tyr-C2/6-CH; 51, Tyr-C3/5-CH; 52, 3-Hydroxyphenylacetate-C4/6-CH; 53, Phenylalanine; 54, Uracil-NH-CH; 55, Niacinamide-C5-CH; 56, Guanosine-C8-

CH; 57, GTP/GMP-C8-CH; 58, GMP-C8-CH/Hypoxanthyne-C2-CH; 59, Hypoxanthine-C8-CH; 60, Nicotinate-C4-CH; 61, Nicotinate/Niacinamide-C6-CH; 62, Nicotinate/Niacinamide-C2-CH.

4.3. DATA PREPROCESSING

After 1D spectral acquisition, an LB = 0.30 Hz was applied to all spectra prior FT and subsequent baseline and phase corrections were carried out using *NMR Spectrus processor*. The *intelligent bucketing* procedure applied gave a dataset of 65 rows (samples) and 207 columns (variables). The integral intensity values for each bucket were normalised and referenced to the TSP signal (*s*, δ = 0.00 ppm). Spectral regions which did not contain any resonances were removed, so that a final dataset of 65 samples x 143 variables was obtained for further analysis.

Prior to further analysis, NMR spectra were visually checked for any major disturbances. None of the spectra was excluded for subsequent statistical analysis.

4.4. UNIVARIATE AND MULTIVARIATE ANALYSIS OF THE ^{1}H NMR MURINE HEPATIC DATASET

4.4.1. Univariate data analysis: ANCOVA

The experimental design for univariate analysis of the ^{1}H NMR buckets from the NP-C1 liver dataset involved an ANCOVA model that incorporates 3 factors and 6 primary sources of variation: (1) 'between-disease classifications' (qualitative NPC disease-active *vs.* the combined HET/WT control group), fixed effect (D_i); (2) 'between-genders' fixed effect (qualitative) 'nested' within 'disease classifications' (G_j); (3) experimental sampling time-

point fixed effect (quantitative, T_k); (4, 5 and 6) disease classification x gender, disease classification x time-point and gender x time-point first-order interaction components (DG_{ij}, DT_{ik} and GT_{jk}) respectively. This experimental design is represented by Equation 20, in which Y_{ijk} represents the (univariate) predictor variable value observed, μ its overall population mean value in the absence of any significant, influential sources of variation, and e_{ijk} the unexplained error (residual) contribution.

$$Y_{ijk} = \mu + D_i + G_j + T_k + DG_{ij} + DT_{ik} + GT_{jk} + e_{ijk} \quad (20)$$

4.4.2. Multivariate data analysis

4.4.2.1. Preliminary analysis: PCA

PCA was employed in order to explore any clustering present within the data regarding the 3 groups initially studied. PCA analysis revealed that there was a significant clustering of the NP-C1 disease classification which was distinct from both the HET and WT groups; however, no discrimination between the latter two disease status classifications was found. Indeed, PC 4 *vs*. PC 3 *vs*. PC 2 score plot obtained with the unsupervised PCA approach (Figure 4.2) provided the best visualisation of this NPC *vs*. the combined HET/WT group discrimination. The NPC cluster exhibited significantly higher and lower scores vectors than those of the combined HET/WT ones for components 2 and 4 respectively; there appeared to be no 'between-classification' differences between these scores vectors for component 3 as can be observed in the projections of the 3D plot on the 2D planes.

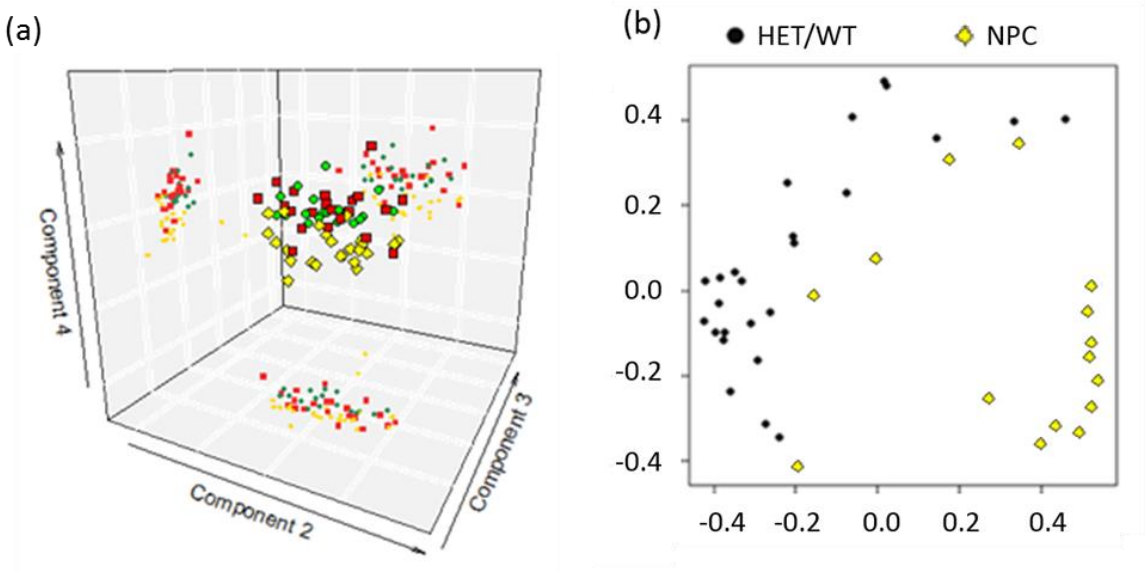

Figure 4.2. (a) Three-Dimensional (3D) PC4 *vs*. PC3 *vs*. PC2 scores plot arising from PCA of the liver NP-C1 dataset (yellow diamonds, NPC; red squares, WT; green circles, HET). (b) Multidimensional scaling plot of a random forests proximity matrix from HET/WT *vs*. NPC analysis: this plot demonstrates the success of discrimination from a single RFs iteration.

4.4.2.2. Classification performance

Random Forests (RFs): The RFs classification methodology for these liver samples was performed in the same way as described previously for the urinary and plasma datasets, but in this case the RFs tuning gave optimised values of 1,000 for the number of trees and 12 variables selected at each split. Initially, 3 groups were analysed using RFs: HET, WT and NPC mice. RFs performed on HET *vs*. WT gave OOB = 0.428, meaning a 57.2% out of sample accuracy. However, lower values for OOB error were obtained when RFs was employed with NPC *vs*. HET (OOB = 0.175) and NPC *vs*. WT (OOB = 0.190). In view of this situation, HET and WT were merged in one group (HET/WT) for further analysis. This analysis gave OOB error mean values of 0.190 ± 0.00041. For prediction performance, the values for sensitivity, specificity and accuracy were 0.799 ± 0.0013, 0.843 ± 0.0034 and 0.810 ± 0.00084

respectively. A plot representing the classification performance of RFs for the test set is depicted in Figure 4.2 (b).

4.4.2.3. Variable selection

The variable importance values for the 143 variables were computed in the same way as previous datasets (urine and plasma) using the mean decrease accuracy value (MDA). This value is computed from permuting OOB data, so that for each tree the prediction error on the OOB portion of the data is recorded as an error rate for classification. Subsequently, the procedure is repeated after permuting each feature. The difference is then averaged over the ensemble of trees, and normalized by the standard deviation of the differences (165). The top 15 variables, together with their respective ranking, *p*-values and assignments are presented in Table 4.2.

Variable Ranking	Bucket (ppm)	Assignment	Multiplicity	ANCOVA *p*-value for disease	Fold change
1	7.30 - 7.35	Phenylalanine-C1/C2-CH	*d* (6.8)	1.60×10^{-4}	+1.56
2	7.17 - 7.23	Tyrosine-C3/C5-CH	*d* (8.6)	1.70×10^{-4}	+1.38
3	6.88 - 6.93	Tyrosine-C2/C6-CH	*d* (8.2)	1.45×10^{-3}	+2.25
4	8.92 - 8.97	Nicotinate-C2-CH	*d* (2.1)	1.30×10^{-3}	-1.49
5	2.99 - 3.05	Lysine-C6-CH_2/Ornithine-C5-CH_2	*t*/*t*	2.00×10^{-4}	+1.51
6	2.62 - 2.67	Hypotaurine-C4-$C\underline{H}_2SO_2^-$/Methionine-C4-CH_2	*m*	2.40×10^{-3}	+1.96
7	6.78 - 6.81	3-Hydroxyphenylacetate-C4-CH	*m*	3.80×10^{-4}	-3.45
8	0.94 - 0.99	Valine-CH_3	*d* (7.1)	1.49×10^{-2}	+1.35
9	4.24 - 4.27	Threonine-C3-CH	*m*	3.40×10^{-4}	+1.30
10	8.69 - 8.74	Niacinamide-C6-CH	*dd* (4.4, 1.7)	0.26	-1.01
11	8.23 - 8.29	Nicotinate/Niacinamide-C4-CH	*m*/*dd*	8.11×10^{-2}	-1.37

12	7.35 - 7.41	Phenylalanine-C3/4/5-CH	*m*	1.22×10^{-2}	+3.21
13	0.77 - 0.80	Unassigned	*t* (7.5)	0.20	-1.27
14	8.90 - 8.92	Niacinamide-C2-CH	*s*	0.25	-1.79
15	2.67 - 2.72	Aspartate-C2-CH_{2a}	*dd* (8.9)	3.90×10^{-3}	+2.06

Table 4.2. Key ^{1}H NMR variables derived from the application of the RFs strategy to the liver NP-C1 dataset: variables are ranked from 1 to 15 based on their MDA value. 'Between-disease classifications' ANCOVA *p*-values are provided, along with their fold changes. ^{1}H NMR resonances, their coupling patterns and assignments were confirmed *via* the methods outlined in section 4.2. Fold changes for TSP-normalised hepatic metabolite concentrations are expressed relative to NP-C1 disease group, so that a positive value indicates upregulation in NP-C1 disease, whereas a negative value indicates a higher level in the HET/WT group.

The acquisition of 2D ^{1}H-^{13}C HSQC and ^{1}H-^{1}H COSY NMR techniques confirmed the structural identities of those metabolites selected as discriminatory features. Thus, the assignment of phenylalanine, tyrosine, nicotinate and niacinamide was facile since their ^{1}H NMR signals are clearly visible in unobscured regions of the 1D ^{1}H NMR spectra acquired, and in some cases further supporting evidence for such assignments was obtained, since two or more resonances arising from individual metabolites were indicated as discriminatory variables. Although, both nicotinate and niacinamide presented low concentrations so their ^{13}C resonances were unobserved in the HSQC spectra acquired. However, application of 2D-NMR experiments was required to confirm assignments of the valine resonances since they are located at chemical shift values close to those of leucine and isoleucine. Additionally, both methionine and hypotaurine have triplet resonances located at *ca.* 2.65 ppm, coupled to a multiplet located at 2.15 ppm for the former, and a triplet at 3.35 ppm for the latter; both these linkages were observed in the 2D COSY NMR experiments conducted (Figure 4.4)

and their respective ^{13}C resonances were also observed in the HSQC experiments performed [Figure 4.3 (a)]. The 3-hydroxyphenylacetate resonance was detectable, at low intensity, in 17 of the HET and WT liver samples, but only in 2 of the NP-C1 samples, specifically the 6.78-6.81 ppm bucket (generally, an uncrowded region for all the tissue spectra acquired). Assignments for aspartate resonances were also confirmed by such 2D-NMR experiments. The ABX coupling system of the C2-CH_b proton resonance of this amino acid lies within the 2.79-2.81 ppm bucket. For the combined lysine-C5-CH_2/ornithine-C4-CH_2 resonances (δ = 1.70-1.74 ppm), ^{1}H-^{13}C HSQC spectra acquired confirmed the identities of these amino acids, and hence this ^{1}H NMR bucket did not arise from further metabolites with similar δ values (for example, putrescine and spermidine).

These variables included significantly elevated hepatic spectral intensities of amino acids (Phe, Tyr, Asp, Lys/Orn, Met, Thr and Val, and also the β-amino acid hypotaurine), along with reduced ones for nicotinate and nicotinamide, 3-hydroxyphenylacatate and an unassigned species with a triplet resonance located within the 0.77-0.80 ppm bucket. Whilst this latter resonance remains unassigned, ^{1}H-^{1}H COSY NMR (Figure 4.4) analysis demonstrated that this triplet signal was linked to a multiplet centred at δ = 1.99 ppm, an observation indicating that the latter is attributable to a proton located α- to a carboxylate function, i.e. these coupled resonances appear to arise from a carboxylic acid anion species. Additionally, its ^{13}C chemical shift value is 10.98 ppm.

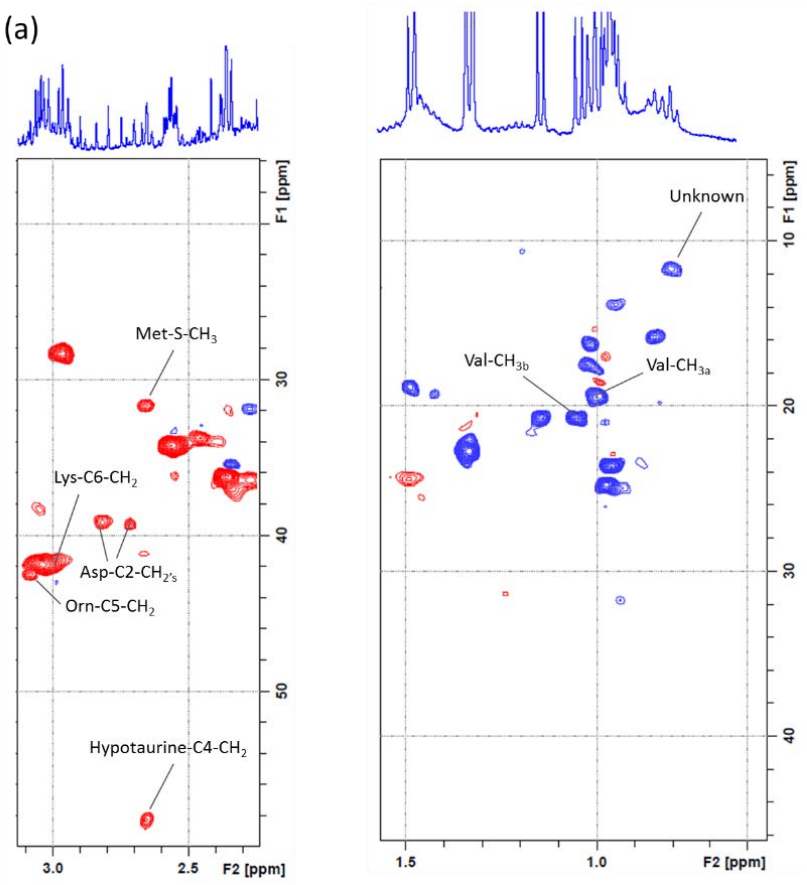
(a)
Met-S-CH3
Lys-C6-CH2
Asp-C2-CH2's
Orn-C5-CH2
Hypotaurine-C4-CH2
Unknown
Val-CH3b
Val-CH3a
F1 [ppm]
F2 [ppm]

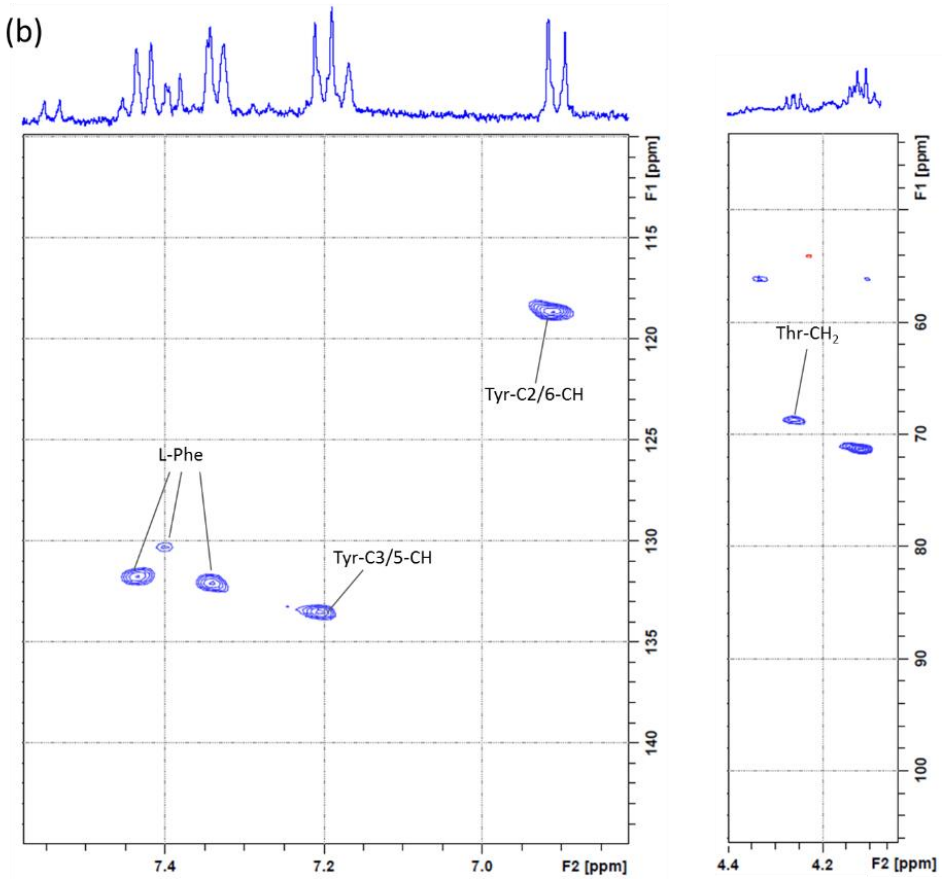
(b)
Tyr-C2/6-CH
L-Phe
Tyr-C3/5-CH
Thr-CH2
F1 [ppm]
F2 [ppm]

Figure 4.3. 400 MHz ^{1}H-^{13}C HSQC spectrum of an NP-C1 mouse liver aqueous extract: only those resonances that were selected as discriminatory features and observable in a ^{1}H-^{13}C HSQC spectrum (low concentrated metabolites are not visible in view of the low natural abundance of ^{13}C) are assigned in this Figure for purposes of clarity. Red cross-peaks indicate either a -CH_3 or -CH group, and blue ones represent -CH_2- functions.

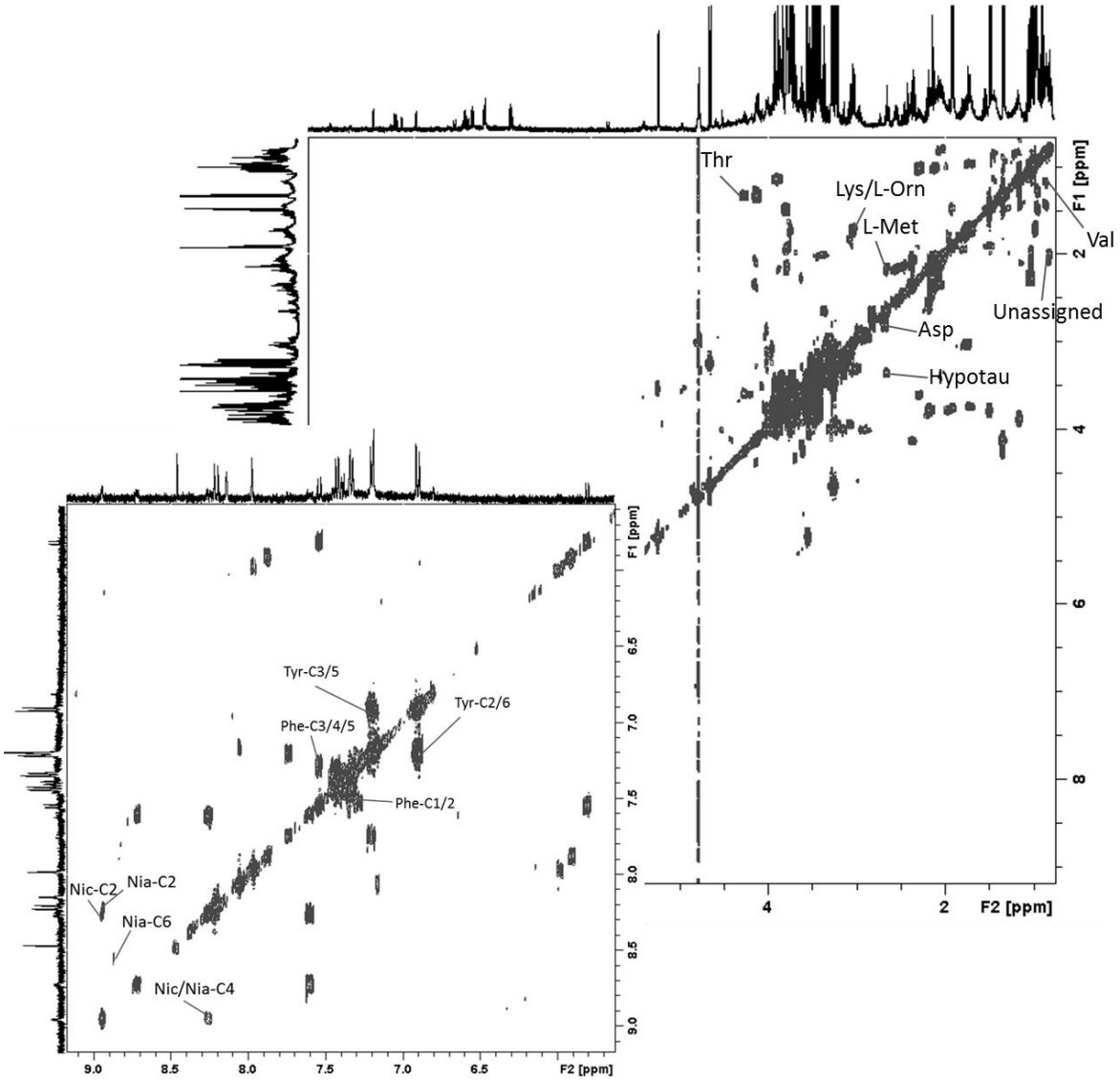

Figure 4.4**.** 400 MHz ^{1}H-^{1}H COSY spectrum, of an aqueous extract of an NP-C1 liver sample. Typical spectra is shown (aromatic region expanded). Only the cross-peaks for the selected metabolites are indicated in the spectrum. Abbreviations**:** Phe-C1/C2, Phenylalanine-C1/C2-

CH; Tyr-C3/C5, Tyrosine-C3/C5-CH; Tyr-C2/C6, Tyrosine-C2/C6-CH; Nic-C2, Nicotinate-C2-CH; Lys/Orn, Lysine-C6-CH2/Ornithine-C5-CH_2; Hypotau, Hypotaurine-C4-$CH_2SO_2^-$; Met, Methionine-C4-CH_2; Val, Valine-CH¬3; Thr, Threonine-C3-CH; Nic/Nia-C4, Nicotinate/Niacinamide-C4-H; Nia-C6, Niacinamide-C6-CH; Phe-C3/4/5, Phenylalanine-C3/4/5-CH; Nia-C2, Niacinamide-C2-CH; Asp, Aspartate-C2-CH_{2a}.

4.4.2.4. ROC curve analysis

In order to evaluate the ability of RFs to classify and predict using these variables, a ROC analysis was carried out, using the corresponding option in MetaboAnalyst 3.0. Only those variables detailed in the previous section were retained to perform the analysis outlined above. Then, with only 11 variables (out of 143 initial variables) attributable to Phe, Tyr, Val, Met/Hypotaurine, Niacinamide, Nicotinate, Lys/Orn, Thr, Asp, 3-hydroxyphenylacetate and the unassigned bucket (0.77 - 0.80), RFs gave a maximum AUC value of 0.939 (range = 0.823 - 1.000) (Figure 4.5).

In the ROC analysis observed in Figure 4.5, the number of variables is permuted to generate different RF models containing different sets of variables from those previously selected; furthermore, the number of features employed also changes. In this case, 2, 3, 5, 7, 10 and 11 variables were used for developing the models. For each model the respective AUC value together with the range is stored and depicted in Figure 4.5.

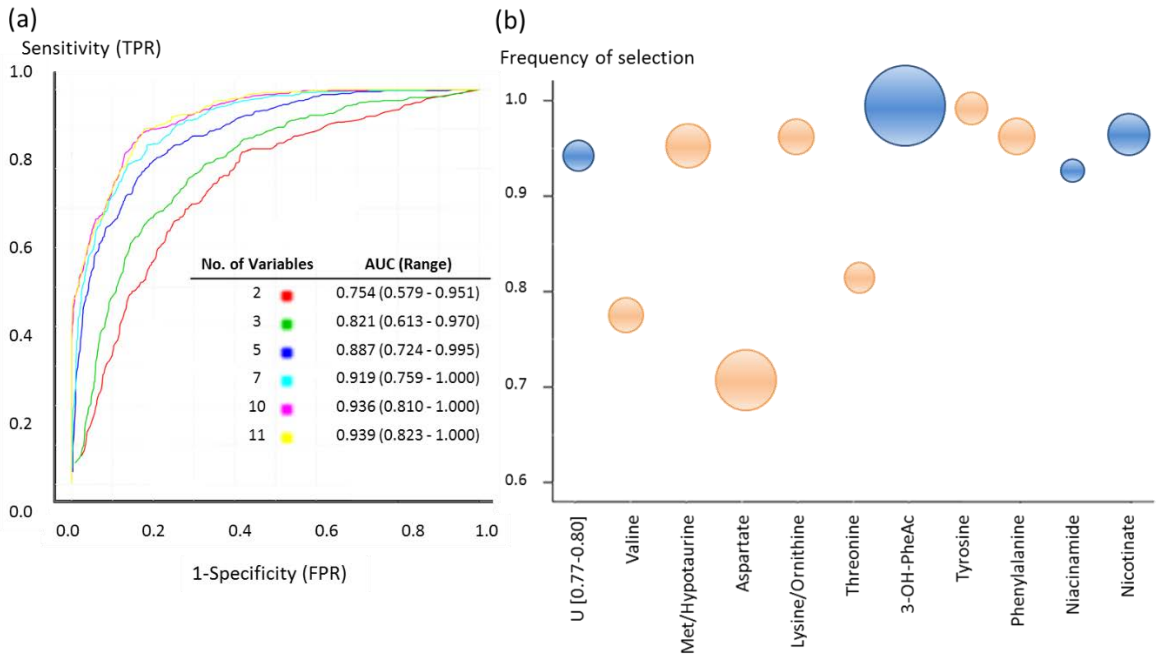

Figure 4.5. (a) ROC curves analysis for the liver NP-C1 dataset and (b) blue bubbles indicate metabolites with lower levels in NPC group and orange ones, those with higher levels. The size of each bubble is correlated with the FC (fold change): different combination of variables gave different AUC values ranging from 0.754 for 2 variables, up to 1 with 7, 10 and 11 variables, as indicated in the table inserted in the left plot. Abbreviations: TPR, True Positive Rate; FPR, False Positive Rate; AUC, Area Under the Curve; U, unknown; 3-OH-PheAc, 3-hydroxyphenylacetate.

ROC curve analysis revealed that the buckets attributable to 3-hydroxyphenylacetate and tyrosine were the variables with higher frequency of selection for building up the classification RFs models, additionally the models involving only 2 variables accomplished an AUC range of 0.579 - 0.951 showing a good extent of success. These facts together with the phenylalanine frequency of selection (0.96, ranked the 4th) indicate that the most affected pathway in NP-C1 liver disease, and therefore the one with higher value as a discriminant feature, is that involving aromatic amino acids.

4.4.3. Time-dependency of ^{1}H NMR NP-C1 hepatic profiles

As the samples were collected at different time points, ASCA was performed using the *MetaboAnalyst 3.0* option for *Time Series Analysis*. ASCA splits the total variance into different parts due to the factors involved in the experiment, and extracts the variance arising from the interaction of these factors (213). No significant differences were found for sampling time; indeed, 'between-time-points' component gave a *p*-value = 0.185, revealing no correlation with metabolite levels. Furthermore, the 'disease x time-point' interaction component of variance was also found not to be significant for the first two (major) PCs explored (p = 0.530). Partial redundancy analysis performed focused on the collection time-point variable revealed no significant differences (p = 0.069) attributable to this variables regarding the levels of the hepatic metabolites monitored.

Since some variables selected were ascribable to the same metabolite, only those with the highest MDA values arising from that biomolecule were retained in order to explore the time dependency of the variables. Therefore, the top 15 features were attributed to 11 metabolites. Plots of normalised intensity values v. collection time-point for those 11 discriminatory metabolites selected by RFs are shown in Figure 4.6.

Lower intensity values for Val, Asp, Thr, Tyr, Lys/Orn and the unassigned δ = 0.77-0.80 ppm resonance were observed at the week 3 time-point than those for NP-C1, and these observations appear to be consistent with the pre-symptomatic nature of this time-point, i.e. elevated levels of these biomolecules appear at the early (6 week) and late (≥ 9 week) symptomatic points. Indeed 'time point' x 'disease classification' interaction effect was found to be marginally significant for Val (p = 0.025) and the bucket 0.92 - 0.94 ppm was also found significant (p = 0.042), which is ascribable to the other methyl group of Val. Interestingly, other regions showing statistical significance for 'time point' x 'disease

classification' interaction effect were 1.70 - 1.74 and 1.74 - 1.79 ppm (p = 0.030 and 0.039) which are ascribable to Lys-C5-CH2/Orn-C4-CH2 and 7.41 - 7.47 ppm (part of Phe multiplet, p = 0.031). Nevertheless, those values may be considered marginally significant due to their proximity to the threshold 0.05.

However, there appeared to be no time-dependence of the 3-hydroxyphenylacetate, phenylalanine and nicotinate levels, although Val, Asp, Thr, Tyr and Phe NP-C1 hepatic levels were higher than those of HET/WT group at all the post-symptomatic time-points, together with lower ones for 3-hydroxyphenylacetate and nicotinate in this group. Although niacinamide shows some descending tendency over time, such differences are clearly not significant. Moreover, with the exception of 3-hydroxyphenylacetate, the liver content of all metabolites appeared to be time-independent in the combined HET/WT group.

Performance of the above RF procedure, but excluding the pre-symptomatic week 3 samples, gave rise to a slight improvement compared to that achieved without removal, specifically a mean OOB error of 0.13 ± 0.003, and prediction performance values for sensitivity, specificity and accuracy of 0.86 ± 0.0014, 0.89 ± 0.0016 and 0.865 ± 0.00082 respectively. These results are consistent with the pre-symptomatic nature of samples collected at the week 3 time-point in NP-C1 mice.

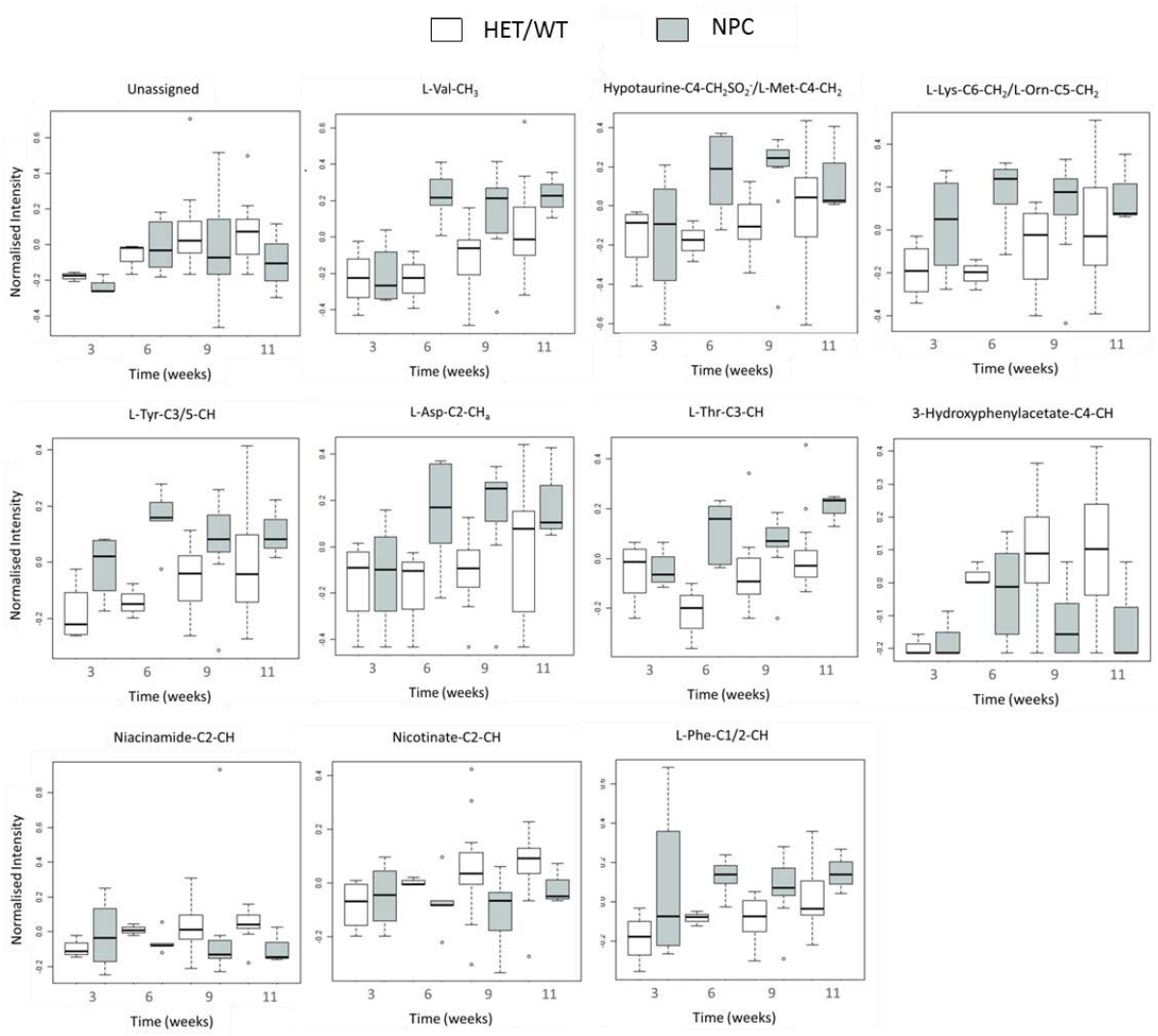

Figure 4.6. Box plots of the 11 metabolites identified as discriminatory variables for the NP-C1 liver dataset by RFs analysis *vs.* time-point (weeks) for the NPC (grey) and HET/WT (white) classifications.

The ANCOVA model revealed some regions attaining statistical significance for the 'Time point' effect, such as 3.44 - 3.50 (p = 0.023), 3.39 - 3.44 (p = 0.026), 5.22 - 5.28 (p = 0.017), 8.44 - 8.47 (p = 0.034) and 3.69 - 3.71 ppm (p = 0.046) ascribable to glucose moieties and formate (8.44 - 8.47 ppm). These values may arise from a differential energetic metabolism over time for mice, although these values were very close to 0.05, the threshold for statistical significance.

4.4.4. Gender contribution to ^{1}H NMR NP-C1 hepatic profiles

The same RF procedure described above was applied to the dataset, but in this case the *y* response variable was gender. This analysis was performed to check that the variables selected were not conditioned by gender differences and hence represent a true separation between NP-C1 and healthy mice (WT/HET). The OOB obtained was 0.461 which reveals no differences attributable to gender. Corresponding partial redundancy analysis-based permutation testing analysis focused on the gender variable revealed that gender was not significantly related to any of the discriminatory variables (p = 0.100). The only signals that gave significant p-values for 'gender' contributions were 3.35 - 3.37 (p = 0.0065) , 5.17 - 5.20 (p = 0.0083), 3.44 - 3.50 (p = 0.024), 8.44 - 8.47 (p = 0.029), 5.88 - 5.93 (p = 0.035), 5.22 - 5.28 (p = 0.035) and 1.45 - 1.51 ppm (p = 0.040), ascribable to methanol, phosphoenolpyruvate-CH_{2a} (PEP), β-Glucose-C3/5-CH, formate-H, GTP-C1'-CH and α-glucose/glucose-6P-C1-CH and alanine-CH_3 respectively. Most of these metabolites are correlated with the glycolysis pathway, since glucose subsequent transformed to glucose-6P yields PEP prior to the final product, i.e. pyruvate, which can also arise from alanine in the alanine-pyruvate cycle. The same variables shown significant *p*-values in the ANCOVA model for the factor 'time point' x 'gender', revealing no effect of the collection time point in those variables gender-dependent. None of the variables presented a significant *p*-value for the interaction factor 'disease' x 'gender'.

The variables listed in Table 4.2 failed to attain statistical significance for the 'gender' factor or any of the combinations with others, such as 'disease' and 'time-point', which indicates that gender is not conditioning the classification of mice liver extracts according to their disease class.

4.5. HEPATOCYTE REDOX STATUS BASED ON GSH:GSSG RATIO

Although not featuring as significant biomolecule variables in the RF and further MV analysis models developed, we also explored differences between the mean hepatic concentrations of glutathione (GSH) and its corresponding disulphide oxidation product (GSSG), and in particular that of the [GSH]:[GSSG] concentration ratio between the NP-C1 and HET/WT classifications investigated. [GSH]:[GSSG] ratio is a valuable and reliable indicator of the REDOX status of tissue, mainly in the liver, since this organ is the site of GSH synthesis (214). GSH provides reducing equivalents to cells, and the GSH/GSSG couple is recognised as a major thiol-disulfide cellular 'redox buffering system', since the combined cellular concentrations of these biomolecules are much higher than those of the other two major redox-active systems, i.e. $NADP^+$/NAPH and thioredoxin (215). The levels of both correlated metabolites can be utilised as indicator for the redox environment of the cell (215). Glutathione is a tripeptide conformed for Glu-Cys-Gly, in which Cys is the key component, since its reactive thiol group is the one involved in the formation of a disulphide linkage with an additional GSH molecule to yield GSSG (Equations 21 and 22).

$$GSH + {}^{\bullet}OH \longrightarrow GS^{\bullet} + H_2O \quad (21)$$

$$GS^{\bullet} + GS^{\bullet} \longrightarrow GSSG \quad (22)$$

The buckets selected to explore the levels of GSH and GSSG were 4.55 - 4.61 ppm and 3.31 - 3.35 ppm (Figure 4.7), attributable to GSH-Cys-CH and GSSG-Cys-CH_{2a} respectively, according to the chemical shift values provided in (216) and (217) respectively.

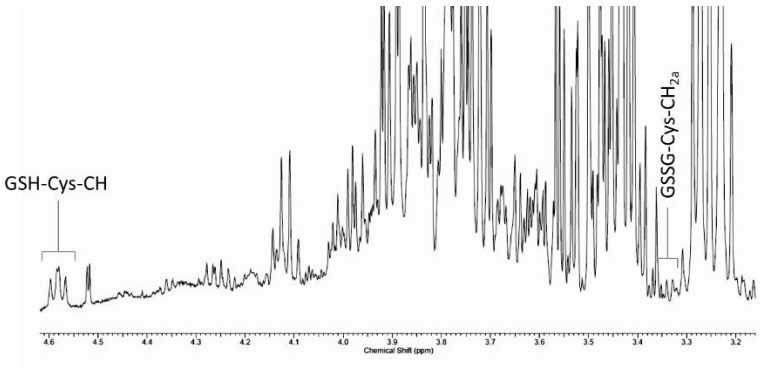

Figure 4.7. Typical spectra from an aqueous liver tissue extract from 3.15 ppm to 4.62 ppm showing the resonance signals employed for the [GSH]:[GSSG] computation.

Primarily, it was found that hepatic GSH levels were significantly reduced in NP-C1 patients (p = 0.036), although no such differences were noted for GSSG (ANCOVA model depicted in Equation 20) for the 'between-disease classifications' factor However, there was a much more highly significant decrease in the mean [GSH]:[GSSG] ratio of the NP-C1 group when compared to that of the HET/WT control one ($p = 8.65 \times 10^{-4}$).

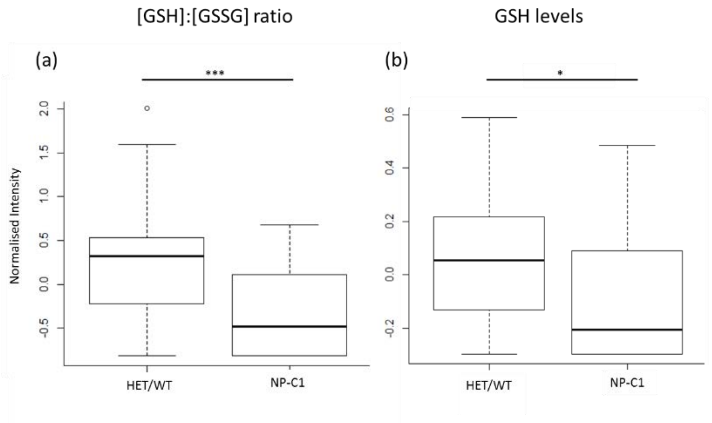

Figure 4.8. (a) Box plot for hepatic mice GSH:GSSG ratio [4.55 - 4.61]:[3.31 - 3.35] and (b) for hepatic mice GSH levels for both disease classification groups: Both GSH and GSH:GSSG ratio were analysed using the ANCOVA model depicted in Equation 20, showing a significant difference ($p < 0.05$, *; $p < 0.01$, **; $p < 0.001$, ***).

CHAPTER 5

CLASSIFICATION AND VARIABLE SELECTION BY RANDOM FORESTS AND CORRELATED COMPONENT REGRESSION IN A METABOLOMICS CONTEXT

5.1. RANDOM FORESTS RANKING FOR VARIABLE SELCTION *vs.* RANDOM FORESTS-RECURSIVE FEATURE ELIMINATION

NP-C1 Disease Urinary dataset: In order to identify the variables which were more important for the discrimination of samples according to their disease classification, MDA values for each variable were saved at each iteration and finally averaged to obtain final rankings. Additionally, it was possible to track the ranking and MDA value of any variable along all those 100 repetitions (Figure 5.1) in order to explore their variability. At each iteration the whole sample set was partitioned as 2/3 for training and 1/3 for test sets, and hence 100 different sub-sets of training and test sets were employed.

An alternative methodology for variable selection is Recursive Feature Elimination (RFE), an approach which is linked to the RFs technique (RFs-RFE). RFs-RFE is a strategy

proposed by Diaz-Uriarte (218) in which 20% of variables with lowest ranking are removed after RFs performance, and then the classification is performed again without those variables. The ability of this process is assessed by the OOB error value, i.e. variables with lowest contribution for classification will be removed until this value (OOB error) increases or becomes unstable.

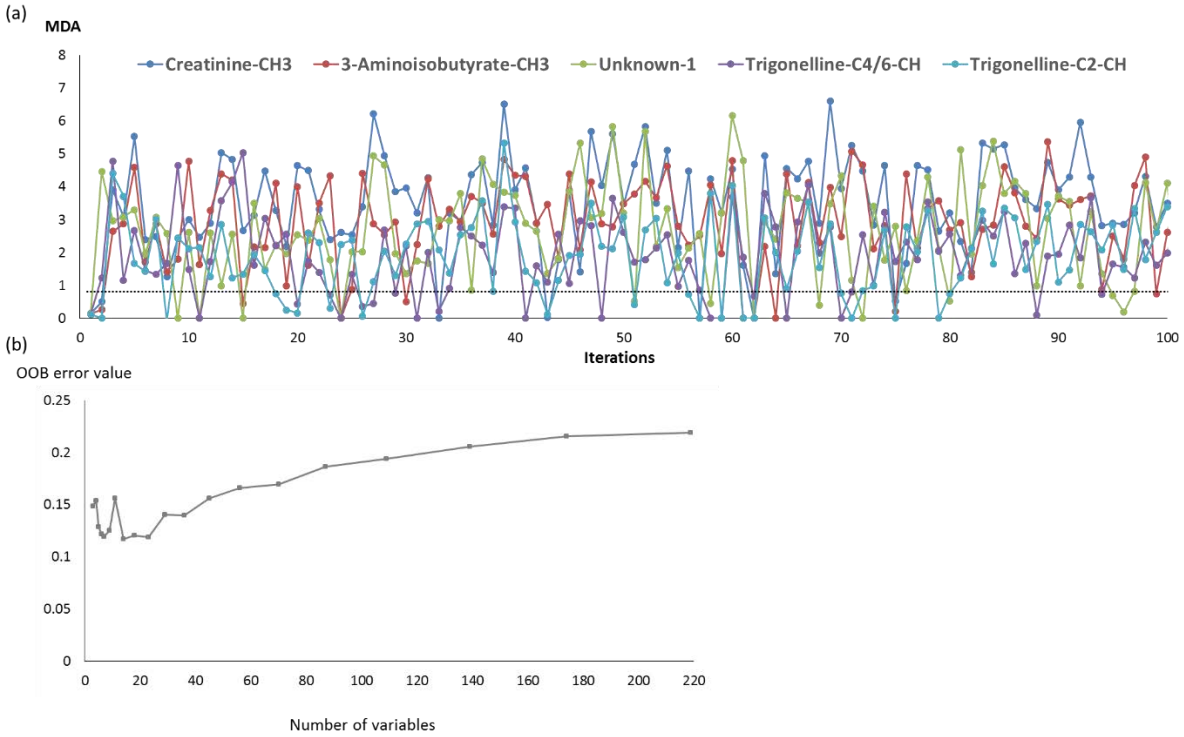

Figure 5.1. (a) MDA values for top-5 variables ranked by RFs over 100 iterations in which the black line represents the MDA mean value (0.88) of the 15th variable selected by RFs for the urinary NP-C1 dataset, and this acts as a threshold for variable selection. (b) Recursive Feature Elimination (RFE) for the urinary NP-C1 dataset showing changes in the OOB error value as a function of the number of variables employed by the RFs analysis.

Creatinine-N-CH_3 (4.05 - 4.10 ppm), 3-aminoisobutyrate-CH_3 (1.17 - 1.22 ppm), unknown-1 (0.72 - 0.76 ppm), and both trigonelline signals [-C4/6-CH (8.80 - 8.86 ppm) and -C2-CH (9.11 - 9.16 ppm)] were selected below the mean MDA value obtained for the 15th top variable (2-Hydroxyisobutyrate-$CH_{3's}$, 1.36 - 1.41 ppm) 7%, 10%, 13%, 19% and 20% respectively. The 16th ranked variable was the 1.58 - 1.63 ppm bucket assignable to 5-aminovalerate-C3/4-CH_2, with an MDA value of 0.79. This metabolite was selected by the CCR and GAs techniques as the 12th and 10th most important variable respectively.

In Figure 5.1 (b) the OOB error value decreases until the number of variables is 23, then it becomes stable and then starts to fluctuate as the number of variables further decreases. However, even with only 3 variables, the OOB error value obtained was 0.149, a value below 0.220 which is the starting OOB value with 219 variables. These last 3 variables were the 0.72 - 0.75 ppm, 1.17 - 1.22 ppm and 4.05 - 4.10 ppm buckets, the latter two assigned to 3-AIB and Cn respectively.

Mice hepatic dataset: The variability of the variables ranking, and consequently, the features selected after the full cross-validated process was also explored for the NP-C1 liver dataset. The combined top-5 ranked variables' MDA value was explored over each of those 100 repetitions, and is depicted in Figure 5.2. The performance of RFs-RFE was also explored to compare with the RFs variable selection procedure.

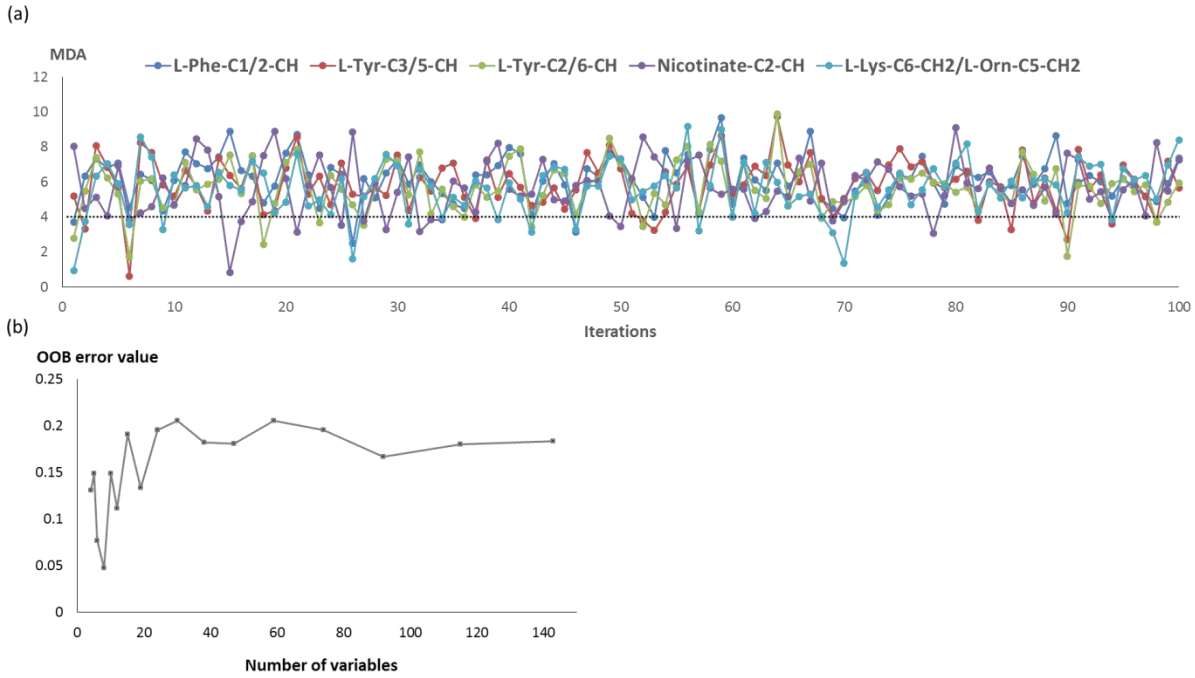

Figure 5.2. (a) Mean decrease in accuracy (MDA) values computed for the 5 most effective discriminatory variables throughout 100 iterations. The black pointed line represents the mean MDA value for the 15th most important selected variable (aspartate), which acts as a threshold for variable selection. (b) Recursive Feature Elimination (RFE) for the mice liver NP-C1 dataset showing the changes in the OOB value as a function of the number of variables employed by RFs.

MDA computations indicated that the top 5 variables selected would not have been selected in 7, 11, 12, 16 and 19% for the first, second, third, fourth and fifth of these respectively in the CV testing cases. As expected, this percentage increases for those variables selected with lower rankings. The 2.67 - 2.72 ppm bucket attributable to a proton from the ABX system of aspartate (Asp) was the threshold for this dataset, with an MDA value of 4.11, with the next one being the 2.79 - 2.81 ppm bucket assignable to the other Asp proton from that coupling system, which gave an MDA value of 3.94.

In this study, the RFs strategy was applied for the classification of human urine and plasma, together with mice liver samples according to their disease status. In this case, RFs was employed with the major aim of determining the variables that can group samples based on their disease class; in this manner, we can enhance our knowledge of disturbances in metabolic pathways arising from the NP-C1 disease process, and moreover propose some of these metabolites as biomarkers.

A wide range of different MVA techniques are available for variable selection (219), but RFs attain effective results when dealing with outliers, it does not overfit and provides excellent results even if some variables are noise (220). Several MVA strategies have been successfully utilised for the analysis of datasets in which the number of possible predictor variables (*P*) exceeds the number of samples (*n*) available, i.e. $P > n$ situations; one of these techniques is the RFs approach, which has been successfully applied throughout a range of metabolomics studies (221, 222).

Our RFs model was primarily tuned in order to improve its performance, and this approach has been previously investigated by Diaz-Uriarte *et al.* (218), in which the investigators demonstrated that both the number of variables included in the generation of each individual tree, and the maximum number of trees included in the final RFs model can be tuned separately since they are independent parameters. Moreover, the computational time required proportionally increases with the number of trees, and selecting a very large number does not necessarily provide an improved performance, as reported in (218) and explored in this investigation. The number of variables selected for tree partitioning has been shown to be the most critical parameter to tune; nevertheless, the default value was found to be an effective choice for the liver and plasma NP-C1 datasets, in which it was set at a value of $(143)^{1/2} \approx 12$ for liver, and 7 for plasma, given the presence of a total of 39

variables in the latter dataset (for this model, 6 or 7 variables for tree partitioning would have matched the $\sqrt{n}$ rule). Nevertheless, when RFs strategy was applied to the urinary NP-C1 dataset, the optimal value for tree partitioning was 8, a very low value considering the total number of variables in the original dataset (199 variables).

The variable selection process has been performed based on the MDA values, since this has been suggested to be the most reliable metric (79, 223), and therefore it is more robust than the other available metric, the Gini index (224). In view of the random sub-sampling procedure conducted by RFs for classification purposes, the variables with selectively higher MDA values can, of course, vary when this classification technique is repetitively applied to MV analysis of the same dataset; moreover, in order to explore as many combinations of samples in the training and test sets as possible, an iterative process was implemented here, although the OOB error term computation already involves a cross-validation (CV) procedure (225).

An assessment of the performance of this iterative cross-validated process was also conducted in order to test the reliabilities of the selected metabolite variables, and this revealed that with the employment of the MDA value of the 15th-ranked variable as a threshold, the top 1-, 2-, 3-, 4- and 5-ranked variables selected would not have been selected in 7, 11, 12, 16 and 19% respectively of the CV testing cases (Figure 5.2) for the liver dataset, and 7, 10, 13, 19 and 20% respectively for the NP-C1 urinary one (Figure 5.1), which shows how the variables selected change with different test and training sub-sample sets. Therefore, studies in which CV with random sub-sampling is only performed once or a few times can experience this limiting effect, since the results can be biased by the sub-sample selected. However, the robustness of this ensemble technique was confirmed by the computation of SEM values for the MDAs, which were very small.

Additionally, a further major methodology available for variable selection, the so-called Random Feature Elimination, serves as another iterative process which was first proposed by Diaz-Uriarte (218). When combined with RFs, the variable importance is primarily computed, and this process then repeated with removal of the 20% of less important variables until the OOB decreases to a stable value. This strategy was also explored herein employing our urine and hepatic datasets, which revealed how the OOB value initially decreases with the reduction of the number of variables (20% at each repetition), an observation predominantly ascribable to the removal of noisy variables that generate unsuccessful trees, and that are further averaged when computing the OOB. Additionally, this procedure has been investigated in detail in (226).

In the datasets investigated, the OOB error value reached a minimum and then became unstable, i.e. a high variability of OOB error values following the removal of certain variables; however, even using only 3 variables, the OOB error value was lower than the initial one containing the complete set of features, indicating an improved classification performance. The main issue arising from this RFE approach is that the final goal of this strategy is to reduce the number of variables to the minimum, whilst maintaining reasonably good classification performance; nevertheless, in a metabolomics context, where the selected features might be related to disorders caused by the disease and not by the disease itself, reductions in the number of variables can be detrimental, since information about affected pathways may be lost, and the reduced number of variables may represent common metabolites that usually are non-disease-specific, and therefore their value as biomarkers is severely limited.

5.2. CORRELATED COMPONENT REGRESSION: A NEW TOOL FOR METABOLOMICS ANALYSIS

5.2.1. CCR-LDA performance

Correlated Component Regression-Linear Discriminant Analysis (CCR-LDA) was applied to the urinary and liver NP-C1 datasets to evaluate its ability to classify those samples with regard to their disease status, and also to compare its performance against other well-established MVA techniques employed in metabolomics investigations. The results arising from both these classification problems are depicted in the table below.

Dataset	MVA Technique	OOB (SEM)	Accuracy (SEM)	Sensitivity (SEM)	Specificity (SEM)
URINE	RFs	0.224 (0.00012)	0.835 (0.001)	0.695 (0.001)	0.831 (0.003)
	GA-MLHD/SVM	-	0.827 (0.002)	0.752 (0.002)	0.903 (0.001)
	CCR-LDA	-	0.810 (0.013)	0.583 (0.032)	0.926 (0.012)
LIVER	RFs	0.190 (0.0004)	0.810 (0.001)	0.799 (0.001)	0.843 (0.003)
	CCR-LDA	-	0.824 (0.014)	0.719 (0.029)	0.887 (0.016)

Table 5.1. MVA performance of all the technique employed for the urinary and liver NP-C1 datasets: the top part of the Table is a copy of Table 3.2. The bottom part includes the analysis outlined in section 4.4.2.2 plus the results of the CCR-LDA applied to the hepatic dataset. The OOB error value is also indicated for the RFs approach (the standard error of the mean for each of the parameters computed is shown in brackets).

CCR-LDA only out-performs the other techniques in term of specificity, although it presents higher SEM values for all the parameters computed. The main difference, however, is the low value obtained for sensitivity. This dataset is somewhat complicated, since the 2

classes are not balanced, and the control group is almost 4 times larger than the disease one. Therefore, the CCR strategy could be more sensitive to that issue.

The main feature that CCR-LDA has when compared to alternative parametric MVA techniques is the correlation of the components, so that these are not selected with the restriction of having to be orthogonal to each other, but with the aim of improving the performance of the model, increasing the ability of the component previously selected for classification (in the case of the combination with LDA, it can be employed for regression purposes in addition). Those components contributing to the overall performance *via* enhancements of the predictive ability of the pre-built model are known as *proxy* components, and those variables with higher loading on those components and lower on the prior ones are denominated *proxy* (suppressor) variables.

5.2.2. CCR-LDA dependency of the number of components and variables employed

In order to explore the ability of the CCR-LDA technique to classify samples independently of the number of variables and/or components employed to construct the model, the number of variables was limited to 5, 10, 15 and 20, and the number of components to 1, 2 and 3 for both urinary and hepatic mouse datasets; selecting each of these combinations 5 times yields a final set of 60 different models. Specificity, sensitivity, accuracy and AUC values were computed for each of these models. For each of those 12 possible combinations of maximum number of components x maximum number of variables, the classification performance parameters were averaged.

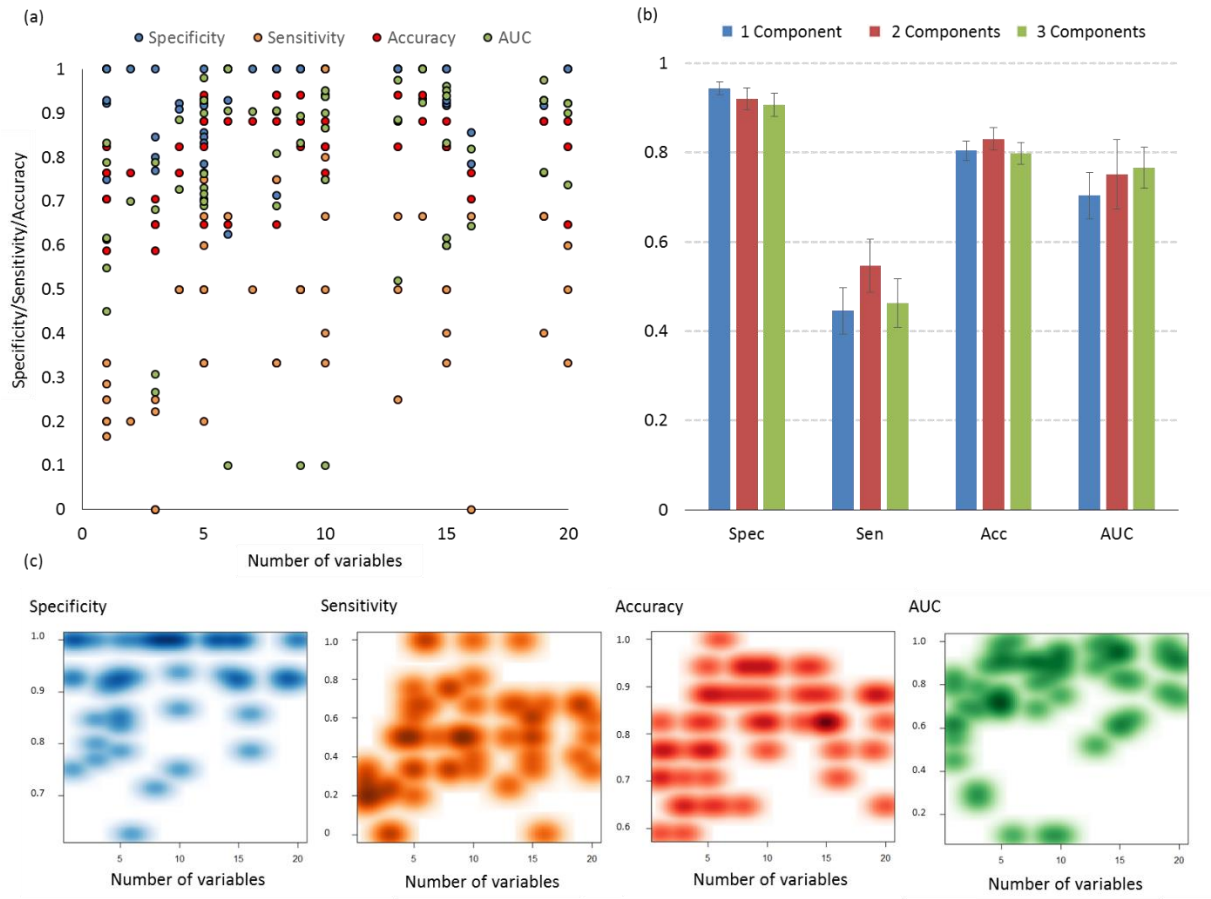

Figure 5.3. CCR-LDA results for the NP-C1 urinary dataset. (a) Scatter plot of the number of variables *vs.* the parameters employed for the 60 models generated utilising from 1 to 20 variables. (b) Mean values for specificity (Spec), sensitivity (Sen), accuracy (Acc) and area under the curve (AUC), along with their SEM values for the models generated with 1, 2 and 3 components. (c) Individual density plots for specificity, sensitivity, accuracy and AUC as a function of the total number of variables employed by the CCR-LDA strategy.

No significant correlations (linear, logarithmic or quadratic) were found between the number of variables employed for the model and their classification performance (Figure 5.3). Indeed, analysis of the classification performance as a function of the number of components did not show any tendency for sensitivity and accuracy to increase; however, it should be considered that specificity decreases as the number of components increase, and

also the opposite effect is observed for AUC values in Figure 5.3(c). In the density plots it can be observed that neither sensitivity nor accuracy show a tendency (decreasing or increasing values as the number of components increases); however, sensitivity values appear to increase with the number of variables, and for the AUC, these values increase with only a few variables, and then they remain at a high level when more variables are introduced into the model.

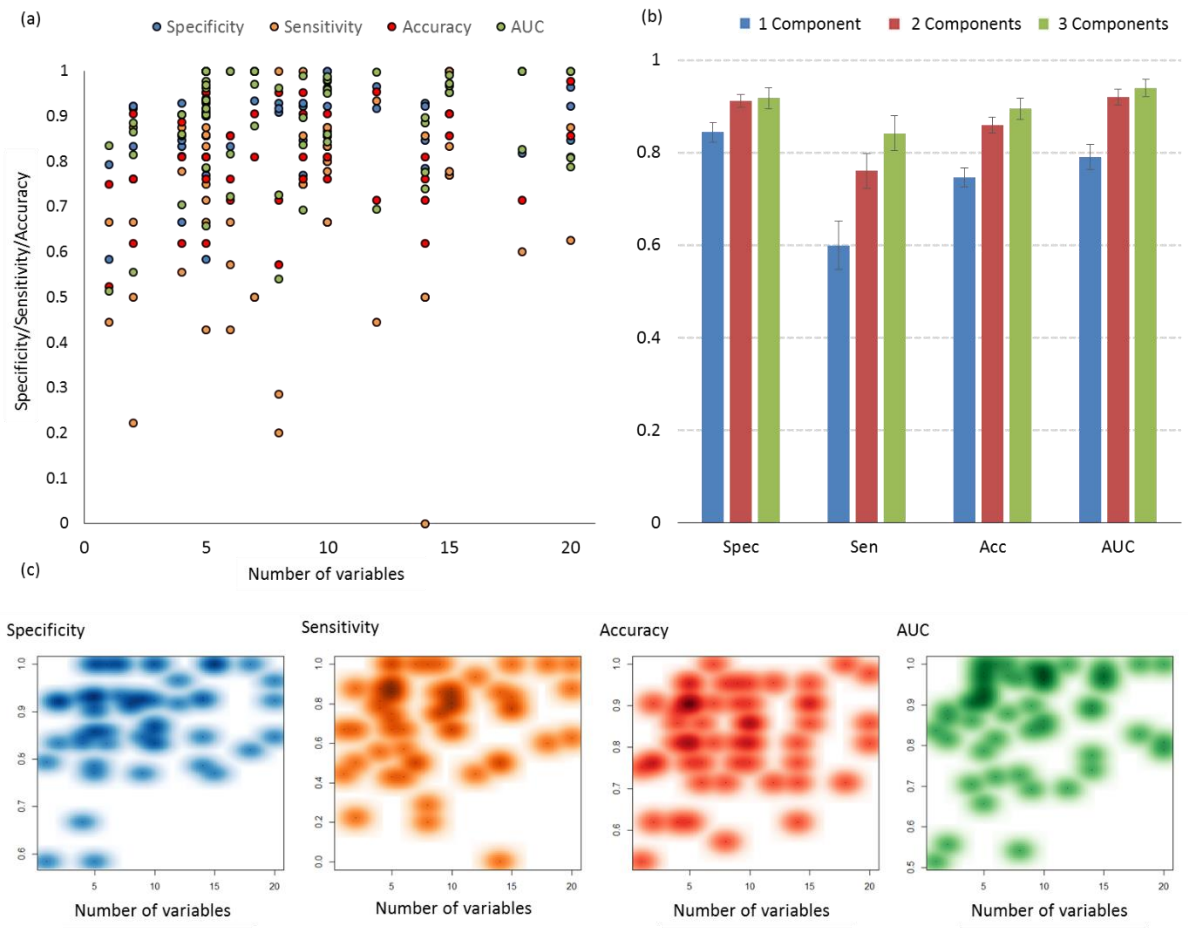

Figure 5.4. CCR-LDA results for the NP-C1 mice hepatic dataset. (a) Scatter plot of the number of variables *vs.* the parameters employed for the 60 models generated utilising from 1 to 20 variables. (b) Mean values for specificity (Spec), sensitivity (Sen), accuracy (Acc) and area under the curve (AUC), along with their SEM values for the models generated with a

maximum of 1, 2 and 3 components. (c) Individual density plots for specificity, sensitivity, accuracy and AUC as a function of the number of variables employed by CCR-LDA.

Values for specificity, sensitivity, accuracy and AUC in the NP-C1 mice liver CCR analysis of the ^{1}H NMR spectral buckets reveals a clear dependency of the number of components, these parameters increasing with the number of components involved (Figure 5.4). Nevertheless, no tendency or dependency is observed regarding the number of variables employed, although lower values for these parameters are obtained when the number of variables is less than 10, except for that of sensitivity which reaches its minimum value when the number of features employed are close to 15.

The variable selection process in CCR is analogous to the RFE one described in section 5.1, since the 'step-down' procedure incorporated in the CCR algorithm starts with the whole set of variables and they are then sequentially removed until the CV process performance decays. With regard to classification problems, the minimum number of variables is always desired for a model, so that a low number of variables can be set as an initial parameter for CCR, and then researchers may check to determine if a successful classification rate is accomplished. In this case, a limitation to only 5 variables out of 219 and 143 for the urinary and hepatic datasets, respectively, were set, and results arising from CCR-LDA model gave very promising results. Nevertheless, the lowest values for sensitivity, accuracy and AUC were obtained using 5 variables [Figure 5.3 (c)] for the urinary dataset. The same results were observed in the hepatic dataset [Figure 5.4 (c)]. However, there is not a very high density of points in Figures 5.2 (c) and 5.3 (c), an observation that may indicate that limitation of variables affects the results for these datasets, as expected.

CHAPTER 6

INTEGRATIVE METABOLOMICS: URINE, PLASMA AND LIVER ^{1}H NMR METABOLOMICS ANALYSIS TO ASSESS THE METABOLISM OF NP-C1 PATIENTS

6.1. NICOTINATE/NIACINAMIDE PATHWAY

Elevated levels of quinolinate (p = 3.83 x 10^{-5}, FC = 30.32) were found in urine specimens collected from NP-C1 patients, and the ^{1}H NMR analysis of liver samples collected from NP-C1 mice model also showed lower levels of nicotinate (p = 1.30 x 10^{-3}, FC = -1.49) and niacinamide (p = 0.26, FC = -1.01) than in healthy controls. These findings suggest an imbalance in the nicotinate/niacinamide pathway that may, in turn, lead to a depletion in NAD/NADP levels.

Dietary nicotinamide is absorbed in the intestines, and it is then converted in the intestinal lumen by bacterial nicotinamidase to nicotinate. Both nicotinamide and nicotinate are major precursors of NAD synthesis in humans (salvage pathway), even though they are required to be incorporated through the diet. Moreover, human cells have the ability to

synthesise NAD from tryptophan (Trp) (Figure 6.1). Hara and co-workers have suggested that NAD biosynthesis is tissue-specific based on the expression pattern of the enzymes involved in its metabolism (227). Hence, it occurs predominantly from nicotinate in the small intestine and from nicotinamide in skeletal muscle, whereas in the liver and kidney, both metabolites, along with Trp, contribute to the synthesis of NAD (227). Moreover, NADP is synthetised through the phosphorylation of NAD, and particularly noteworthy is the diminished mean hepatic concentration of GSH present in the NP-C1 mouse classification ($p = 0.036$), which may reflect a disease-mediated imbalance in hepatocyte $[NADP^+]$:$[NADPH^+]$ concentration ratios, since GSH is required for the conversion of NADP to NADPH (228).

The first step in NAD synthesis from nicotinamide is the generation of its mononucleotide, a reaction mediated by the enzyme nicotinamide phosphoribosyltransferase (Nampt). A recent investigation has reported an upregulation of Nampt mRNA, and increased levels of NAD in the liver of mice fed with a high-fat diet (229), and also in non-alcoholic fatty liver disease (NAFLD) (230). Additionally, *Nampt* mRNA expression levels were also found to be higher in fibrotic human livers (231), fibrosis being a major feature of the development of NP-C1 mice liver pathophysiology (122). Therefore, the hepatic stress experienced by the NP-C1 mice could lead to an increase in NAD production in order to load enzymatic reactions that require this cofactor, such as β-oxidation and tricarboxylic acid metabolism which are enhanced in other hepatic disorders such as NAFLD (232). Indeed, in NAFLD liver tissue, there is an imbalance in bile acid duct transporters (233), a complication also observed in NP-C1 mice liver as discussed below. This enhanced requirement of NAD may be responsible for the low nicotinate/nicotinamide levels observed in NP-C1 mice liver extracts, since they appear to be overutilised to generate NAD.

Moreover, the increased levels of quinolinate (QUIN) found in urine collected from NP-C1 patients, together with the lower levels of both nicotinate and niacinamide in NP-C1 mice hepatic tissue, could indicate an imbalance between *de novo* and salvage pathways, i.e., an overloading of the latter in NP-C1 liver. The synthesis of NAD from Trp *via* QUIN mainly occurs in the liver (234); therefore, a defect in the QUIN to nicotinate mononucleotide stage may lead to an increased activity of the salvage pathways enzymes, hence reducing the levels of nicotinate/niacinamide and therefore the accumulation of QUIN that is then released from hepatocytes. Healthy individuals, with sufficient dietary levels of nicotinamide, present relatively low levels of QUIN production in the liver, and consequently its levels, together with those of further kynurenine pathway metabolites in other tissues and the systemic circulation are relatively low (235).

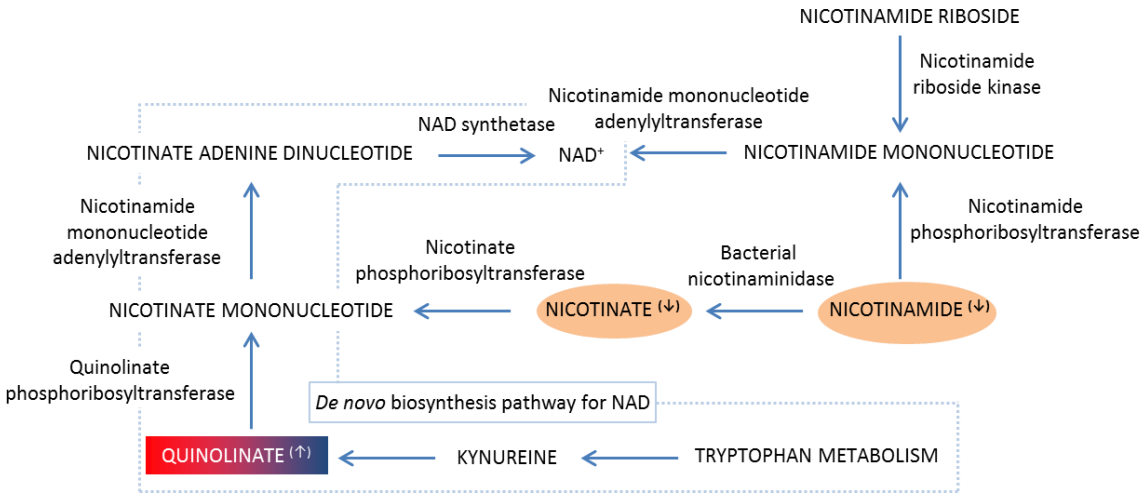

Figure 6.1. NAD metabolism: schematic representation of NAD synthesis highlighting those metabolites selected as discriminatory variables, and indicating the tissue/biofluid where they were found, and their levels in NP-C1 samples expressed relative to those from healthy controls. Urinary metabolites selected by the different strategies applied are indicated by coloured boxes (red = RFs; green = GAs-SVMs/MLHD; blue = CCR-LDA). Metabolites

highlighted in orange refer to those selected in mice liver samples analysis. Arrows illustrate higher (↑) or lower (↓) levels in the NPC group.

Quinolinate (QUIN) is generated and released by infiltrating macrophages and activated microglia in the brain (236). It is produced through the kynureine pathway, which is the route involved in the degradation of Trp and the production of NAD (Figure 6.1). QUIN acts as an agonist of the N-methyl-D-aspartate (NMDA) receptors, mainly in the forebrain, and as such is considered to be an endogenous brain excitotoxin. This gives rise to a wide range of deleterious processes within the brain through its triggering of ionic imbalances in neurons via a Ca^{2+} influx which activates a NMDA-receptor (237). Moreover, activation of neuronal nitric oxide synthase and nitric oxide activity (238), together with and cytoskeleton destabilization (239), may also lead to cell death. Since QUIN does not have a specific transporter to cross the BBB (240), the increased levels of this metabolite found in NP-C1 urine samples presumably arise from other tissues, since macrophages have a 20-fold higher ability to generate QUIN than that of microglial cells (241). Additionally, the liver also has the ability to generate QUIN (242).

The increase of QUIN levels in biofluids has been previously reported, with elevated concentrations in blood serum and cerebrospinal fluid (CSF) being correlated to early renal insufficiency (243). Indeed, a method to quantify QUIN in urine using LC-MS/MS (244) has recently been proposed for the diagnosis of renal cell carcinoma, i.e., urinary QUIN may serve as a biomarker (245). Furthermore, its levels have been also observed to be elevated in sepsis processes (246), such levels being linked to an immune system response mainly dominated by macrophage activation. Elevated levels of QUIN in urine could arise from a macrophage infiltration, which has been observed in several tissues such as lungs (247) and liver (120) in

both human and mice afflicted with NP-C1 disease. Indeed, more recently increased serum levels of QUIN have also been observed in hepatic dysfunction (248).

6.2. BLOOD PLASMA LIPOPROTEIN PROFILES

A major cellular process in NP-C1 disease is the disruption of cholesterol transport from the lysosome. This cholesterol arises from LDL particles that are transported *via* the bloodstream. Given these pathological features, it may be expected that significant changes occur in lipoprotein homeostasis in NP-C1 patients. Indeed, recent studies have revealed that the plasma lipoprotein profile of NP-C1 patients is characterised by low HDL, LDL and total cholesterol levels, and higher TG levels (249). It has also been observed that a reduction in HDL-cholesterol levels is correlated with the impairment of cholesterol trafficking within the cell (249, 250).

Intriguingly, in this work, the LDL-$(CH_2)_n$ spectral region presented a similar pattern following the NPC ≈ MGS ≈ HET >> WT classifications. The ^{1}H NMR plasma profiles of NP-C1 patients revealed higher levels for both VLDL signals than the WT one (Figure 4.4). Since the -$(CH_2)_n$, -C**H$_2$**CH_2CO, and N-acetyl glycoprotein/CH_2-C**H$_2$**-CH= mobile lipid regions of the NMR spectra acquired have been previously shown to be strongly correlated with plasma triglyceride levels in both humans and mice (251, 252), this is consistent with elevated lipoprotein-associated TG levels in the NP-C1, MGS and HET groups over those of the WT one observed in this study, even though the WT samples were collected under non-fasting conditions.

Interestingly, nicotinate is an inhibitor of hepatocyte microsomal diacylglycerol acyltransferase 2 (DGAT2), an enzyme involved in the synthesis of TGs from DGs (253). When this metabolite inhibits hepatic DGAT2, TG synthesis is decreased, and concomitantly, its

availability for VLDL assembly; as a consequence, apoB degradation is increased and the secretion of VLDL/LDL particles is diminished (254). Therefore, in cases of diminished nicotinate levels, VLDL particles should be increased in plasma, as observed in this work. Intriguingly, a study performed by Beltroy *et al*. (122) showed that TGs levels in the hepatic tissue of NP-C1 mice are lower than those of corresponding healthy controls. In contrast, in another study performed by Garver and co-workers, lipid levels in both NP-C1 and WT mice were found to be not significatively different, with surprisingly elevated levels of TGs in a HET mice group (121). In this work, the HET group involved also exhibited enhanced levels for the VLDL-CH_3 and -$(CH_2)_n$ spectral regions when expressed relative to those of the WT group, indicating that heterozygotes may also present increased plasma TGs levels, and suggesting that this increase is not directly linked to disease pathology [which is consistent with the lack of correlation between TGs and age of death in previous reports (249)] or that they present an intermediate phenotype for VLDL metabolism.

The HDL-$(CH_2)_n$- variable exhibits a pattern in the classification order HET > MGS > NPC >> WT, and this was selected by RFs analysis as the 2nd most important variable when determining differences between the NPC and HET groups. The higher levels of this lipoprotein contrast with those found in other cholesterol storage disorders (besides NP-C1), such as Tangier disease (255) and cholesterol ester storage disease (256). HDL levels in heterozygotes have been previously reported as not generally affected (250), an observation contrary to the results reported here. MGS-treated patients show a slight increase in their HDL levels when compared to those from the NPC group, which is in accordance with investigations using MGS with Gaucher patients (257); in contrast, this improvement in HDL metabolism was not observed when treating Tangier disease patients with this agent (258). This effect on HDL levels is potentially attributable to the imbalance in ABCA1 protein

activation that occurs in NP-C1 cells, since ABCA1 is the central protein involved in HDL metabolism (250).

6.3. BILE ACID METABOLISM

Increased levels of bile acids (BAs) were observed in the urinary profiles of NP-C1 patients (p = 9.39 x 10^{-5}, FC = 8.54); indeed, the variable 0.66-0.69 ppm was selected within the top 8 features for classification by all the MVA techniques employed for the urinary dataset analysis employed. This bucket contains resonances ascribable to the C18-CH_3 group of glycochenodeoxycholate, chenodeoxycholate, taurochenodeoxycholate, taurodeoxycholate and tauroursodeoxycholate, the latter being a BA encountered in humans at very low levels (259); indeed, about 4% of total bile is ascribable to this BA (260). The primary bile acids are cholate and chenodeoxycholate, since they are synthetized in the liver by the action of human enzymes; subsequently, further biotransformations carried out by human microbiota lead to the formation of lithocholate, deoxycholate and ursodeoxycholate.

As previously noted, urinary concentrations of BAs are increased in pathological situations where the hepatobilary system is compromised. These increased urinary levels of BAs could arise from the cholestasis and liver disease that are features of NP-C1 disease (91). Erickson *et al*. have shown how mRNA levels for the BA transporters Mrp1, 2, 3, 5 (multi-drug resistance proteins) and Ntcp (Na^+-taurocholic co-transporting polypeptide) were elevated in NP-C1 mice, an observation suggesting that this transcriptional upregulation is a compensatory mechanism in hepatic stress situations, and is required to potentiate the excretion of any potentially toxic agents (125). The increased expression of these sinusoidal excretion transporters may cause an enhancement in BA excretion from the liver into the

bloodstream, and consequently, urinary levels of these metabolites are elevated. Additionally, the enhanced excretion levels of cheno, urso and lithocholate may indicate an imbalance between both synthetic pathways (Figure 6.2), since BAs generated through the neutral pathway, involving ER enzymes, did not contribute to the signal located within the 0.66 - 0.69 ppm bucket.

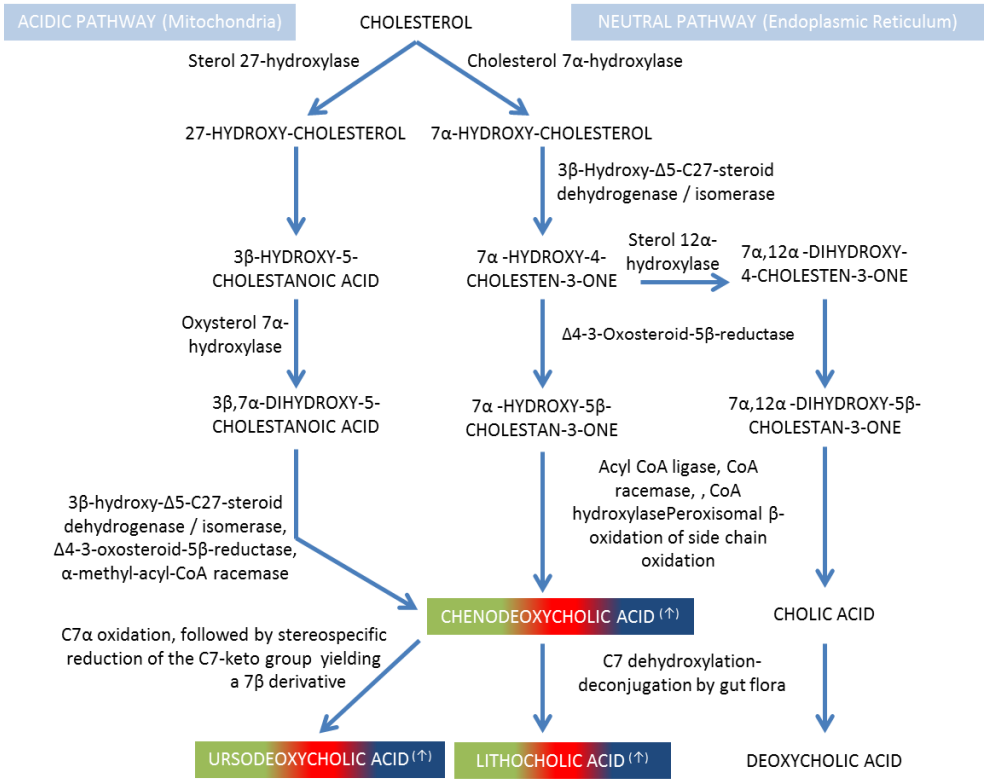

Figure 6.2. Bile acid synthesis pathway: Synthesis route for bile acids from cholesterol. Note that in view of the overlay of the C18-CH_3 group resonance in the urinary ^{1}H NMR profiles obtained, the main bile acids highlighted in this Figure are undistinguishable, so they have all been selected. Metabolites selected as urinary discriminatory variables in this work are shown within a coloured box, indicating that the technique selected that variable (red = RFs; green = GAs-SVMs/LDA; blue = CCR-LDA). Arrows illustrate higher (↑) or lower (↓) levels in the NP-C1 group.

Increased BA levels observed in the urinary profiles of NP-C1 patients may also (or alternatively) arise from the unusual bile acid 3β,7β-dihydroxy-5-cholen-24-oate (which is doubly-conjugated with sulphate at C-3, and N-acetylglucosamine at C-7), and/or its glycine and taurine C-24 position adducts (261), agents which may serve as valuable urinary biomarkers for this disease and perhaps reflect associated liver trauma in these patients (262). Moreover, in the work published by Alvelius *et al.* (263), higher urinary levels of C24 3b-sulfooxy-7b-N-acetylglucosaminyl-5-cholen-24-oic bile acid (SNAG-D5-CA), together with its glycine and taurine-conjugates, were found to be elevated for NP-C1 patients when compared with healthy controls, and a LC-MS/MS methodology has been recently reported for the measurement of this BA in urine (262). Based on the chemical structures of both BAs in which the position 12 is not hydroxylated, they may contribute towards the signal located within the 0.66 - 0.69 ppm bucket.

6.4. MUSCLE BIOMASS WASTING

Common clinical features of NP-C1 disease are weight loss and loss of muscle biomass (264, 265). Consequently, the release of muscle breakdown products, such as branched-chain amino acids (BCAAs) and correlated metabolites into the bloodstream, which can then be filtered out into urine may serve as an indicator of this process.

BCAAs can be neither stored nor biosynthesised in the human body; therefore, their levels are conditioned by the diet, the proteolysis of endogenous proteins and the degradation that takes place in mitochondria. BCAA catabolism occurs in skeletal muscle, liver, kidney, heart, brain and adipose tissue. Although they cannot be synthetized *de novo*, their degradation products can be incorporated into other biomolecules such as lipids, since Val, Leu and Ile ultimately yield propionyl-CoA and/or acetyl-CoA from their catabolism.

Muscle protein contains a higher proportion of BCAAs than that of proteins in other tissues, and muscle is the predominant site of their degradation. Indeed, a urinary ^{1}H NMR-based metabolomics study on muscle wasting revealed that the concentrations of BCAAs, together with their oxidation products, are increased in urine collected from patients suffering from this debilitating condition (266).

In this study, the Val-$CH_{3's}$/Ile-CH_{3a} bucket (0.98 - 1.03 ppm) was selected as a discriminant feature by the CCR-LDA approach in view of its higher level in the NP-C1 ^{1}H NMR urinary profiles (p = 1.65 x 10^{-2}, FC = 5.06), and Ile was also highlighted in plasma, having considerably higher levels in NP-C1 patients (p = 5.51 x 10^{-11}, FC = 1.47), along with those of the HET and MGS groups. Additionally, 3-AIB (p = 8.58 x 10^{-9}, FC = 2.81) was selected by the RFs and CCR techniques with very high rankings (2nd for RFs, 1st for CCR-LDA), this being a common metabolite for the valine and thymine degradation pathways. Therefore, this may serve as a hallmark of muscle wasting, since increased BCAA levels have been previously reported to be correlated to rises in muscle protein deterioration (267). Another two BCAA metabolites were selected as discriminatory features in our urinary dataset, specifically 2-hydroxy-3-methylbutyrate (p = 8.47 x 10^{-3}, FC = -10.22) and 3-hydroxyisobutyrate (p = 7.23 x 10^{-2}, FC = 1.19). 2-hydroxy-3-methylbutyrate is generated through the reduction of 2-oxoisovalerate, a catabolite of Val, and 3-hydroxyisobutyrate is a further metabolite in the same pathway (Figure 6.3). The lower levels of this metabolite, together with those higher values for 3-AIB urinary concentrations, may indicate an increased activity of the enzymatic system that yields isobutyryl-CoA from 2-oxoisovalerate (Figure 6.3). Nevertheless, the spectral region to which 3-hydroxyisobutyrate was assigned may indeed contain other resonances arising from the α-CH group of amino acids, which may represent a confounding factor.

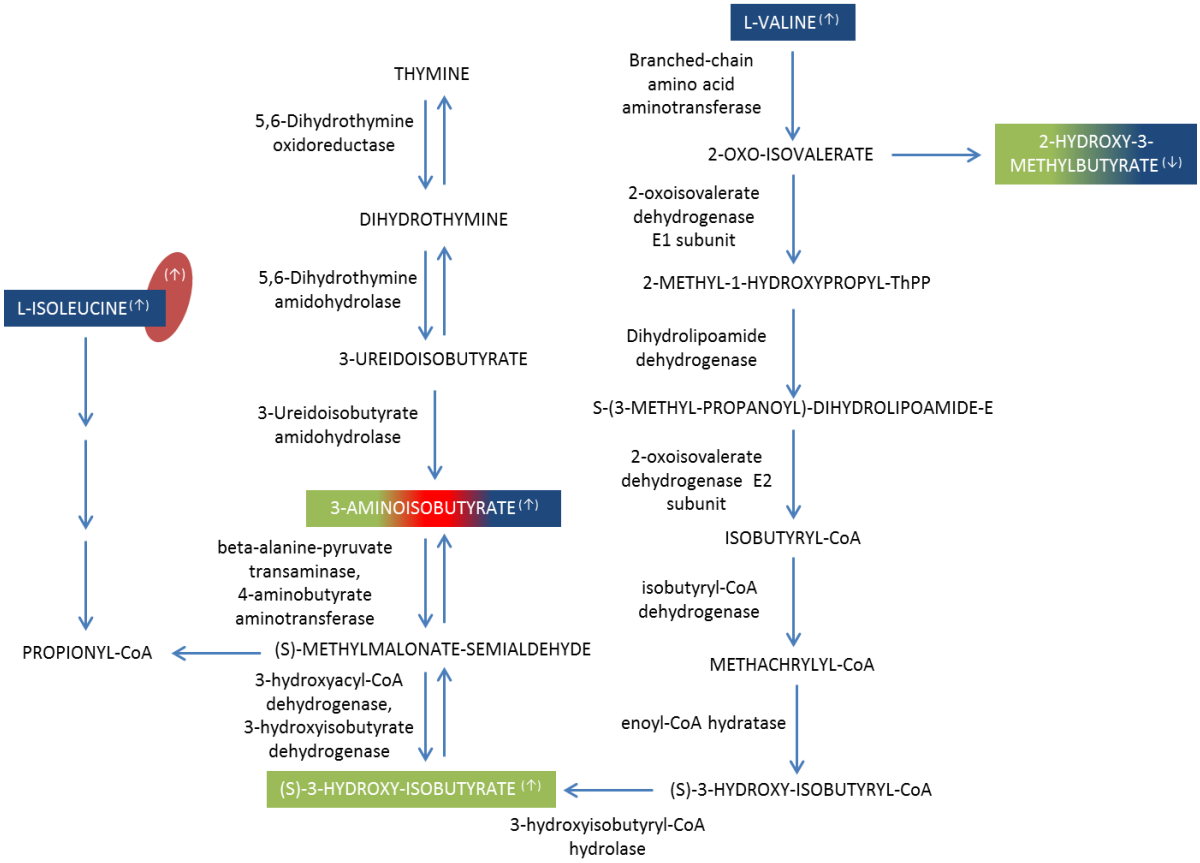

Figure 6.3. BCAA degradation metabolic pathway: this route, as part of the BCAA catabolism process, was indicated as one of the major pathways affected in the disease (leucine catabolism is not included). The thymine catabolism route is also incorporated into this diagram since its final product is common to that of the valine degradation pathway. Urinary metabolites selected as discriminatory variables are visible within a coloured box, which also indicates the technique that selected that variable (red = RFs; green = GA-SVM/LDA; blue = CCR). Plasma discriminatory features for the NP-C1 *vs*. WT comparison are indicated by a red coloured circle. Arrows illustrate higher (↑) or lower (↓) levels in the NPC group.

Intriguingly, loading evaluations with both thymine and L-Val have revealed that urinary 3-AIB predominantly arises from thymine catabolism, with ≤ 10% generated from L-Val degradation (268, 269). High 3-AIB urinary levels have also been observed in cases of

methylmalonic semialdehyde dehydrogenase deficiency (268), an enzyme involved in the catabolic breakdown of both Val and thymine. Metabolism of valine produces the intermediate (S)-3-hydroxyisobutyric acid, a metabolite that may be elevated in urine from NP-C1 patients ($p = 7.23 \times 10^{-2}$, FC = 1.19), although its ^{1}H NMR signal at 3.67 - 3.71 ppm overlaps with that from the α-CH group of amino acids, so this assignment remains tentative. 3-Hydroxyisobtyrate is then oxidized to (S)-methylmalonate semialdehyde by 3-hydroxyisobutyrate dehydrogenase. Thymine metabolism generates 3-AIB, which is then deaminated to (R)-methylmalonate semialdehyde. These two enantiomers are substrates for methylmalonate semialdehyde dehydrogenase, which catalyses their oxidative decarboxylation to propionyl-CoA (Figure 6.3).

Glutamine (Gln) was also selected as a urinary discriminatory feature, but only by the RFs approach (and ranked as the 6th most important), having higher levels for NP-C1 patients ($p = 2.61 \times 10^{-2}$, FC = 1.49). The plasma pool of Gln has been proposed to arise from its release from skeletal muscle (270, 271), which may be another indicator of muscle wastage. Indeed, increased levels of the Gln bucket were also found in our plasma dataset ($p = 7.95 \times 10^{-7}$; FC = 1.23) for the NP-C1 group when expressed relative to those of the WT classification.

Moreover, increased urinary levels of Cr ($p = 1.52 \times 10^{-5}$, FC = 1.59), a distinctive metabolite of muscular tissue, were also increased in the urine collected from NP-C1 patients (the 3.92 - 3.95 ppm bucket was selected for all three MVA techniques employed), which may serve as another indicator of muscle tissue breakdown in view of the debilitating process which is characteristic of the disease. Nevertheless, a limiting factor could be the increased levels of Cn in HET participants in view of their age differences, and also the link between Cn generation from Cr-phosphate arising from muscle tissue. Gu *et al.* reported increasing levels of Cr in urine collected from children from 0 to 3 years of age, followed by

a decrease (272). Despite there are only 2 NP-C1 patients below 3 years, out of 12 in the cohort investigated herein, this may be an additional limiting factor for the consideration of Cr as an specific NP-C1 biomarker.

Interestingly, in a metabolomics study of muscle wasting through ^{1}H NMR urinanalysis, QUIN was selected as the 3rd most important variable (266), showing increased levels in those patients suffering from this condition. This was also observed in urine samples collected from NP-C1 patients (p = 3.83 x 10^{-5}, FC = 30.32).

6.5. GUT MICROFLORA IN NP-C1 DISEASE

Several metabolites arising from microbial activity within the human body (i.e., co-metabolites) were highlighted as discriminatory features in the urinary (*n*-butyrate acid: p = 6.18 x 10^{-4}, FC = 13.00; TMA: p = 2.09 x 10^{-2}, FC = 2.29, methanol: p = 2.39 x 10^{-3}, FC = -1.96, and 5-aminovalerate: p = 3.87 x 10^{-2}, FC = -5.04); the liver (3-hydroxyphenylacetate: p = 3.80 x 10^{-4}, FC = -3.45) and plasma datasets (2,3-butanediol: p = 0.38, FC = 1.73 for MGS). However, the latest was only relevant for the discrimination between the ^{1}H NMR plasma profiles of MGS-treated patients *vs*. the WT ones, and did not attain statistical significance. Accordingly, an imbalance in gut microbiota population/activity in NP-C1 patients may be implicated in this disease.

n-Butyrate is a by-product of complex carbohydrate degradation by bacteria under anaerobic conditions in the intestines. *n*-Butyrate, acetate and propionate are also generated in this degradation process (273); however, these metabolites can be also produced through human metabolism as hydrolysis products of acetylCoA, or in FA oxidation. Therefore, *n*-butyrate is a gut bacterial status biomarker, and hence increased levels observed in urine may indicate an increased gut permeability (274) since *n*-butyrate is

converted to ketone bodies and CO_2 in colon cells (275), and no α-keto-acids have been highlighted as discriminatory metabolites in either plasma or urine herein.

TMA is generated exclusively from the metabolic activity of the gut microbiome using choline, carnitine and mainly TMA-N-oxide (TMAO) as substrates (276). TMA is then oxidized in the liver by the hepatic enzyme FMAO3 (flavin-dependent monooxygenase 3) yielding TMAO; this connection between microbial and human host metabolism has been correlated with NAFLD, with increased levels of urinary methylamines in a NAFLD high-fat diet-induced mouse model (277). Dumas and co-workers (277) found a correlation of higher urinary TMA excretion and a lower phosphatidylcholine level circulating in plasma; however, in view of the problems caused by the histopaque separation of plasma involved in this study, phosphatidylcholine could not be accurately determined in plasma. Nevertheless, this may not be the case, since the proposed mechanism of this limitation in choline availability by gut microbiota can lead to a decrease in the synthesis of phosphatidylcholine, which is necessary for the secretion of VLDLs (278), contrary to our observations of higher VLDL levels in NPC/MGS/HET patients' plasma levels when compared to those of the WT group.

Methanol can also arise from pectin degradation in the colon by microflora (279). Pectin is a biomolecule of vegetable origin, present in fruits, jellies, etc (280). Moreover, it has been proposed as a urinary marker of Crohn's disease and ulcerative colitis in view of its higher levels in the urine collected from these patients in a recent metabolomics investigation (281).

5-Aminovalerate is produced by metabolism of the polyamine cadaverine, which is synthesised by bacteria *via* decarboxylation of lysine (282). Increased levels of this amino acid derivative, and lower ones of urinary 2-hydroxyglutarate, were proposed as part of a battery of biomarkers for Crohn's disease in a metabolomics study (283). Intriguingly, lower

urinary levels of 2-hydroxyglutarate have also been observed in NP-C1 patients herein. Interestingly, this similarity between Crohn's disease and NP-C disease has become more plausible in view of the recent publication by Schwerd and co-workers (284), in which they report a direct correlation between Crohn's disease and NP-C1 gut pathophysiology based on the higher predominance in NP-C1 patients of a mutation in the *NOD2* gene involved in bacterial handling. Deleterious variants in NOD2 are the strongest genetic risk factor for Crohn's disease (285, 286). In their cohort of 150 NP-C1 patients based in Manchester (UK), these authors estimated a 3 - 7% occurrence of intestinal bowel disease in patients with NP-C1, an observation contrasting with values obtained for the general carrying population, in which one of the three most common *NOD2* mutations (homozygous and compound heterozygous) is only about 1.5% (287). Both *NPC1* and *NOD2* genes were found to be correlated to a defective response of macrophages against bacteria, specifically in the autophagic process.

3-Hydroxyphenylacetate can arise either form dietary sources (288) or from gut microflora (289), i.e. from quercetin degradation, through a prior conversion of 3,7-dihydroxyphenylacetate from the C-ring fission of a de-glycosylated quercetin derivative (290). Therefore, imbalances in the activity of such microflora in mutant NP-C1 disease mice may also account for the significantly lower hepatic levels of this metabolite found in this group. Furthermore, this metabolite has been proposed as a marker of dysbiosis (291), which is discussed in the following section.

Interestingly, in a very recent study, Mardinoglu *et al*. (292) found that gut microbiota modulates host amino acids and GSH metabolism in mice, both featured as discriminatory hepatic metabolites herein.

6.6. HEPATIC STATUS IN NP-C1 DISEASE

Liver dysfunction/disease is a major feature of the NP-C1 condition, and this hepatic damage is exacerbated with the disease progress, since the liver accumulates more lipids and unesterified cholesterol. The mouse model of NP-C1 disease serves as a valuable tool for studying the hepatic damage caused. Indeed, several investigations in NP-C1 mouse models have reported hepatic cell death associated with cholesterol-rich diets (122), and increased levels of oxidation products (293). Interestingly, a reduction in the antioxidant capacity of liver NP-C1 in humans has also been reported (147), findings linked with the diminished GSH levels observed herein. Additional investigations reported a decrease in hepatic GSH concentration in *Npc1*$^{-/-}$ mice (294), these values correlating with an excessive level of oxidative stress within hepatic tissue.

These results are also supported by our finding regarding the GSH:GSSG molar concentration ratio, which is very significatively reduced in the liver extracts analysed here (Figure 4.8). Additionally, rats treated with CCl_4, an agent that induces cirrhosis, showed a decrease in the liver levels of this critical antioxidant (295), and this was also observed in patients suffering from non-alcoholic steatohepatitis (296). N-acetylcysteine (NAC) has been employed therapeutically in a NP-C1 mouse model (297) based on its ability to replenish GSH levels (as a cysteine precursor), and also as a ROS (reactive oxygen species) scavenger (298); accordingly, it has been recently employed in clinical trials (297). Hepatic GSH levels were found to be restored after NAC treatment in these mice, a phenomenon offering protection against oxidative stress, results matching those obtained in investigations focused on the cerebellum (294) and primary neurons (299). Also particularly noteworthy is the correlation between GSH and NAD/NADP pathways, since GSH is required for the reconversion of NADP to NADPH (228). Therefore, the results obtained in this study (lower levels of GSH, nicotinate

and niacinamide in NP-C1 mouse liver) may reflect a disease-mediated imbalance in hepatocyte [$NADP^+$]:[NADPH] concentration ratios.

The role of hypotaurine as a potential biomarker for NP-C1 disease-associated liver dysfunction is complicated in view of the partial overlap of its C4-$C\underline{H}_2SO_2^-$ resonance with that of methionine's-C4-CH_2 one, as noted in section 4.4.2.3. Hypotaurine serves as a key antioxidant defence in mitochondria and other intracellular environments, and it is oxidised by ROS to yield taurine, which is subsequently excreted through its transporter into extracellular media (300). The production of ROS has been indicated as one of the pathogenic effects arising from NP-C1 disease pathogenesis, and consistent with this hypothesis, elevated levels of cholesterol oxidation products have been reported in the blood plasma of NP-C1 disease patients, and also in the liver of NP-C1 mutant mice (301). In view of the involvement of oxidative stress in this disease process (146), the increased hepatic generation of hypotaurine noted here may arise as an essential metabolic response stimulated to combat against it (302).

Several previous studies performed in NP-C1 mice indicate that hepatocyte apoptosis may serve as a primary cause of progressive liver degeneration and failure in this animal model (122, 303), and/or an increased activation of macrophages (139); such considerations may also be applicable to human NP-C1 patients. If confirmed, higher hepatic hypotaurine levels observed here in NP-C1 mutant mice may be consistent with an enhanced metabolism of cysteine by the hepatic cysteine dioxygenase/cysteine sulphinate decarboxylase pathway, which is stimulated by an upregulation of oxidative stress episodes, which in turn, serve as key mediators of hepatocyte apoptosis. However, with regard to macrophage activation, we found no evidence for NP-C1 disease-mediated increases in levels of nitric oxide ($NO^\bullet$)-producing arginine in the NP-C1 mouse group, although quinolinate (macrophage activation-

related metabolite) was found to be elevated (p = 3.83 x 10^{-5}, FC = 30.32) in the urine samples collected from NP-C1 patients when compared to the HET carrier group.

In addition to symptoms described above, livers from NP-C1 mice exhibit an elevated level of fibrosis and proliferation of hepatic stellate cells (122, 303, 304). Of these processes, fibrosis plays a predominant role. It is characterised by the replacement of liver tissue by fibrous scar tissue, in addition to regenerative nodules (cirrhosis, which is responsible for major alterations to liver tissue, represents the irreversible end-stage of these developments). Hence, fibrosis gives rise to a progressive loss of liver function, and to a modified liver metabolism (305-308). Taken together, collagen and hydroxyproline levels serve as valuable hallmarks for liver fibrosis, the latter as an index of collagen metabolism (309). However, hydroxyproline was not selected as a significant biomarker by the MVA strategies in this study, and nor was it by similar NMR-linked metabolomics investigations of fibrosis-cirrhosis referenced in this section.

Several amino acids were found to be elevated in the aqueous extracts obtained from NP-C1 mice liver samples, i.e. Phe (p = 1.60 x 10^{-4}, FC = 1.56), Tyr (p = 1.70 x 10^{-4}, FC = 1.38), Lys/Orn (p = 2.00 x 10^{-4}, FC = 1.51), Met (p = 2.40 x 10^{-3}, FC = 1.96), Val (p = 1.49 x 10^{-3}, FC = 1.35), Thr (p = 3.40 x 10^{-4}, FC = 1.30) and Asp (p = 3.90 x 10^{-5}, FC = 2.06). Higher hepatic levels of Phe, Tyr and Met were also increased in a metabolomics investigation conducted by Waters *et al.*, in which they employed ^{1}H NMR analysis to explore liver samples collected from rats undergoing thioacetamide treatment (310), a fibrosis/cirrhosis-inducting agent that causes liver damage, including lipid oxidation and apoptosis (311, 312); both these processes are also involved in NP-C1-associated liver dysfunction/disease. These researchers suggested that necrosis of liver parenchyma and necrosis-induced protein degradation are the main causes of this upregulation in hepatic amino acids levels. An additional ^{1}H NMR-

linked metabolomics study on rats treated with this agent revealed elevated levels of Val, but only after 3 months of treatment (313). Both these investigations showed common features to our study, such as the upregulations of hepatic Phe, Thr, Tyr, Met and Val.

In a further study, Rajendraa *et al.* (314) explored modifications to the hepatic concentrations of free amino acids induced by repeated administration of hexachlorophene (HCP) to male adult mice; this agent exerts pathological modifications to liver structure and morphology (315). These researchers found that Phe, Tyr, Leu, Ile, Val, Thr, Asn (asparagine), Glu (glutamate) and Gln levels were significantly elevated following HCP treatment, whereas that of aspartate was markedly decreased. Moreover, reductions in the specific activity patterns of enzymes involved in amino acid metabolism, i.e. those featuring aminotransferases and glutamate dehydrogenase, indicated a suppression of liver amino acid oxidation. The abnormal upregulations in BCAAs and AAAs observed were ascribed to a reduced catabolism in view of a depleted skeletal muscle mass and hepatic dysfunction respectively; these phenomena may also account for the upregulated liver valine and phenylalanine/tyrosine concentrations observed in this study.

In humans, valine degradation, together with that of BCAAs in general, have been previously shown to be disturbed in a microarray expression analysis of serum biomarkers (123), and also in our analysis performed on the urinary NP-C1 dataset. The upregulated hepatic valine levels observed in NP-C1 disease mice here, however, may be consistent with those of Ishigure *et al.* (316), who found that human liver disease (specifically cirrhosis or hepatocellular carcinoma) diminishes the activities of methacrylyl-CoA hydratase and β-hydroxyisobutyryl-CoA hydrolase (enzymes involved in valine catabolism), and that decreased levels of these hepatic enzyme activities are derived from post-transcriptional regulation in the damaged liver.

Previous investigations have revealed that the application of treatments comprising selected methionine metabolites in experimental animal models of liver disease exhibit striking hepatoprotective effects (317). However, since the Met-C4-CH_2 resonance signal observed here (2.62 - 2.67 ppm) overlapped somewhat with the more intense hypotaurine-$CH_2SO_2^-$ resonance, and therefore additional experiments are required to explore this.

The accumulation of aspartate, along with increased plasma concentrations of this amino acid have been observed in patients with liver disease (170), and this has been suggested to arise from the downregulation of urea cycle enzymes. Interestingly, our ^{1}H NMR-based dataset provided some evidence for upregulated hepatic ornithine in mutant NP-C1 disease mice, a key intermediate of this cycle. However, this pathway has not been highlighted as a significantly affected feature in any previous studies focused on liver dysfunctions/diseases.

In NP-C1 disease mice, decreases in the hepatic ^{1}H NMR bucket intensities of both nicotinate and niacinamide were observed. Indeed, FCs of -1.49 and -1.79 respectively were noted for these metabolites, and as noted above, that this pathway may indeed be affected in NP-C1 patients. In view of their roles as NAD^+/NADH and $NADP^+$/NADPH precursors, which are employed in a wide range of metabolic redox processes, these observations may be linked to highly significant biochemical and hepatocellular effects. For example, cytochrome P450 activity featured in microsomal oxidation systems are critically dependent on the $NADP^+$/NADPH coenzyme system. Similarly, the $NADP^+$/NADPH system is involved in the phenylalanine hydroxylase-mediated oxidative transformation of phenylalanine to tyrosine.

A further example from BCAA catabolism involves the oxidative, irreversible decarboxylation of substrates to form branched-chain acyl-CoA adducts (a reaction catalysed by mitochondrial branched-chain α-keto acid dehydrogenase), which features the

NAD^+/NADH cofactor system (318). The investigation conducted by Waters *et al.* (310) found a down regulation of hepatic niacinamide in their ^1H NMR-linked metabolomics study of thioacetamide-driven fibrosis/cirrhosis in experimental animals, and this was ascribed to an enhanced level of this metabolite's methylation to 1-methylnicotinamide in cirrhotic liver. Furthermore, Varela-Rey *et al.* (319) found that orally-administered niacinamide ameliorated fatty liver and fibrosis in glycine N-methyltransferase knockout mice, and concluded that this agent acted through the prevention of hepatic fat accumulation and apoptosis via reductions in liver S-adenosylmethionine content.

Intriguingly, the intensity of the 3-hydroxyphenylacetate bucket was found to be significantly lower in the NP-C1 group than that of the HET/WT one. 3-Hydroxyphenylacetate is involved in the human tyrosine metabolism pathway, in which it is transformed to 3,4-dihydroxyphenylacetate (Figure 6.4). This reaction also requires NAD^+/NADH as a coenzyme system, which is synthesised through the nicotinate/niacinamide pathway, metabolites of which were also identified as discriminatory variables here. Furthermore, this metabolite can also arise from gut microbiota activity, and is a biomarker of dysbiosis, an alteration found in other cases of liver damage (320).

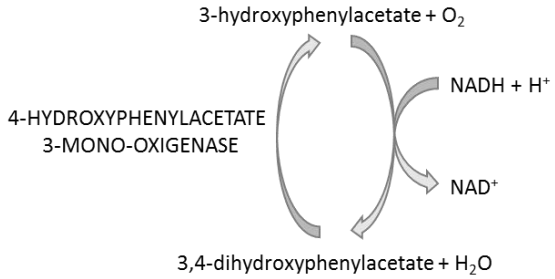

Figure 6.4. Enzymatic biotransformation of 3-hydroxyphenylacetate to 3,4-dihydroxyphenylacetate.

6.7. BIOMARKERS FOR NP-C1 DISEASE

A biomarker must be a metabolite in a biofluid or tissue biopsy sample ideally collected by a non-/minimally-invasively technique, and that is found at highly significantly elevated or reduced levels in the disease investigated. Then it may be employed to diagnose the disease, predict patient response towards therapies, and also monitor the evolution of the patient throughout the disease process. Biomarkers may only be validated if such alterations are found to be reversible via the actions of an approved therapeutic agent for the disease concerned.

As mentioned in the introductory section, the only one available for NP-C disease is the filipin staining of unesterified cholesterol in cultured fibroblasts obtained from a skin biopsy; however, this test carries some limitations regarding the detection of NP-C patients with 'variant' phenotypes (>1/3 NP-C cases) (112), and fails in 15% of the tests performed. Additionally, genetic sequencing of *NPC1* and *NPC2* genes detects mutations on both alleles in only 85% cases, and is confounded by the highly polymorphic nature of NPC1 (> 400 known mutations) (112). Both tests are time-consuming and expensive; therefore, the discovery of new biomarkers for the disease that can improve on these limitations is a major focus in this research area.

Efforts are currently being made in order to find valuable biomarkers for NP-C1 disease which might out-perform those currently available. Indeed, cholesterol oxidation products present in plasma and detected by LC-MS/MS have been proposed as biomarkers (301) for this disease, and tested in different centres (321, 322), in addition to comparisons of results acquired to additional samples collected from patients afflicted with other lipid storage disorders (323). Although cholestane-3β,5α,6β-triol (triol) and 7-ketocholesterol (7KC) have been proposed as biomarkers to assess the diagnosis of NP-C1, and have been

incorporated to the battery of clinical tests for diagnosis in some centres, a recent investigation conducted by Polo and co-workers (324) have revealed that these increases in both cholesterol oxidation products are common to cholestasis in new-born children, and hence their specificity for NP-C disease should be re-evaluated. Additionally, lysosphingomyelin and glucosylsphingosine, were recently proposed as biomarkers in view of their elevated levels in plasma samples collected from NP-C1 patients observed *via* LC-MS/MS (325).

Additional biomarkers have been reported in a microarray analysis of blood serum, including the pro-inflammatory protein galectin-3 (LGALS3) and lysosomal aspartic protease cathepsin D (CTSD) (123).

A chitriosidase assay has been also included as a possible screening test for NP-C1 disease. This enzyme is secreted by activated macrophages, and presents an enhanced activity in a wide variety of LSDs (326-329). Nevertheless, it has been proven to deliver normal (as healthy) results in NP-C1 patients (126), and 10% of the population carry a mutation showing similar levels to those of such patients, making this test inconclusive (330). Moreover, serum levels of this biomarker are also elevated in some other disorders (331).

In addition, 3β-sulfooxy-7β-N-acetylglucosaminyl-5-cholen-24-oate acid, along with its glycine and taurine amides, have been highlighted as potential biomarkers in urine, although the endogenous synthesis pathway of this BA was not confirmed (263). Furthermore, an additional bile acid has also been proposed as a urinary biomarker of NP-C1, specifically 3β,7β-dihydroxy-5-cholen-24-oate and its glycine or taurine conjugates (261).

The lysotracker assay was also proposed as a valid assay system for the diagnosis of NP-C1 disease. This test involves the fluorescent probe Lysotracker, which measures the relative acidic compartment volume in live cells (184), and shows higher levels for NP-C1

patients when expressed relative to those of healthy controls, and also suggesting a correlation with responses to MGS treatment (131).

More recently, lyso-SM-509, a compound related to lyso-sphingomyelin (lyso-SM), has been proposed as an NP-C1 biomarker, and its specificity has been tested against similar diseases such as NP-A and NP-B, yielding 95.5, 91.0 and 100.0% values for accuracy, specificity and sensitivity respectively (132).

In this work, we have explored the potential of NMR-linked metabolomics technologies as diagnostically-valid methodologies for NP-C1 diagnosis, in view of its ability to provide information on wide a range of metabolites simultaneously, and without the need for lengthy time-consuming sample preparation processes. Data arising from the NMR measurements of the different biofluids and tissue investigated herein were then subjected to MVA in order to highlight those metabolites which were efficient for classifying samples according to their disease status (NPC *vs*. HET *vs.* WT). By applying ROC curve analysis to the variables selected, their ability to serve as NP-C1 biomarkers was evaluated.

Metabolic evidence which demonstrates that the metabolites highlighted in section 6.4 serve as indicators of muscle wasting in NP-C1 is presented; however, most of these have already been identified as biomarkers in other diseases, or are very common metabolites such as amino acids, and hence their specificity for NP-C1 disease is compromised. Nevertheless, 3-AIB has only been proposed as urinary biomarker of methylmalonic semialdehyde dehydrogenase deficiency, an alteration never observed in NP-C1 to date; additionally, the urinary levels of this metabolite are reduced in those samples obtained from MGS-treated NP-C patients analysed herein, showing similar values to the HET group; accordingly, I propose 3-AIB as a specific biomarker of BCAA degradation/muscle wasting in NP-C1.

The increased levels of quinolinate (QUIN) in urine have been suggested herein to arise from the inflammatory process, hepatic damage and/or deregulation of the NAD/NADP synthesis pathway. These increased levels were resolved after MGS treatment, as shown in Figure 2.13. Indeed, the first and second of these processes are typical clinical features of NP-C1 disease. This metabolite has been proposed as a biomarker for renal failure, a feature not previously reported in NP-C1 disease; hence, this Trp metabolite can be considered as a specific urinary biomarker for inflammation, specifically macrophage activity, or it may arise from a defect/imbalance in the conversion of QUIN to nicotinate mononucleotide in these patients.

Higher levels of bile acids were also found in urine collected from NP-C1 patients. Such increases are correlated to liver damage, a common feature in young NP-C1 patients. The NMR analyses performed here were not, however, able to distinguish between the specific bile acid anion species responsible for the higher intensity 0.66 - 0.69 ppm spectral bucket region, although chenodeoxycholate and/or its taurine and glycine conjugates are presumably the predominant bile acid species contributing to that bucket. However, some other bile acids that may contribute to this signal have already been proposed for the diagnosis of NP-C1 (section 6.3).

Metabolites arising from imbalances in gut microflora activity/populations were highlighted in this work as important discriminatory features. 5-Aminovalerate, TMA, methanol and *n*-butyrate were detectable in urine with differential levels when expressed relative to our control group. Although these biomolecules may have a diagnostic utility, their origins are unclear since they may arise either from a direct enhanced/diminished activity of selected microbial strains, or their differential levels between healthy individuals and disease patients could be attributable to a physiological defect that leads to an

increase/decrease in their urinary levels, as may indeed be the case of intestinal permeability and related increased levels of *n*-butyrate in urine. Moreover, the value of these metabolites as biomarkers has to be considered cautiously, since gut microbiota in childhood evolves to a more complex population of microorganisms with age (332, 333), and our urinary dataset is not age-matched. Gut microflora also present some inter-individual variability that may affect these results, and considering the limited number of NP-C1 patients included in our urine NP-C1 cohort, this may be another limitation. Despite considerations that these microbial metabolites lack specificity in view of the complex variations in gut microflora populations, the elevated number of biomolecules featuring as discriminatory variables reveals disease-related imbalances in these metabolites.

Whilst defects in lipid distribution are key clinical manifestations of NP-C1 disease, the extent of these changes are not correlated with disease severity, and are not unique to NP-C1 disease; indeed, high TG plasma levels are a common feature in many diseases such as cardiovascular disorders, obesity, renal failure, excess alcohol consumption, etc., and this is an additionally characteristic in another lysosomal cholesterol-related disorder such as lysosomal acid lipase deficiency. Therefore, these biomarkers may have limited diagnostic value, although they may also serve as complementary tools for NP-C1 diagnosis.

A comparison of hepatic metabolites highlighted in this study as discriminatory features for the classification of NP-C1 mice liver samples with the combined HET/WT group revealed an imbalance in the nicotinate/niacinamide pathway that can lead to the generation of NAD^+/NADP. Therefore, monitoring of the metabolites involved therein can provide disease-related information for the progression of liver dysfunction in mice, and if these results are confirmed in humans, the translation to applicable clinical tests may be possible. However, further metabolites selected in the analysis of the ^{1}H NMR mice hepatic

dataset are very common (amino acids), together with well-known liver disorder-related metabolites, specifically BCAAs and AAAs, and hence their utility as biomarkers is again somewhat limited. A further hepatic metabolite selected was 3-hydroxyphenylacetate; although not being highlighted before in any NP-C1 investigation focused on liver dysfunction, its source is difficult to determine (i.e. endogenous, bacterial or food), and therefore, its employment as biomarker is also limited.

CHAPTER 7

CONCLUSIONS

This research programme demonstrates that the ^{1}H NMR- linked metabolomics analysis of human urine and plasma samples, together with hepatic aqueous extracts obtained from a mouse model of NP-C1 disease, provided valuable information regarding potential metabolism dysfunctions in NP-C1 patients, and also yielded valuable information regarding a battery of potential biomarkers to aid disease diagnosis. Moreover, we have identified (and quantified, Appendix 1) MGS in urine samples collected from NP-C1 patients treated with this therapeutic agent, and employing the same multivariate approach, resolved the resonances arising from multiple drug therapy/therapies in these patients.

NMR-linked metabolomics analysis of urine samples collected from NP-C1 patients and heterozygous carriers (as controls) revealed differences in the ^{1}H NMR urinary profiles of these patients which were successfully classified according to their disease class using different MVA techniques. Variables with higher rankings in the models developed were proposed as urinary biomarkers of the disease, and evaluated via a ROC test, which showed very good AUC values even with the employment of only 2 metabolites [AUC (mean, range) = 0.705, 0.484 - 0.898]. The highest-ranked urinary metabolites in the MVA performed are therefore proposed as urinary biomarkers, and also as indicators of differences in the NP-C1 patients' metabolism profiles, so that the increased bile acid concentrations in the NP-C1 group may be an indicator of hepatic damage and imbalanced BA biosynthesis; however,

further experiments are required to specify the particular bile acids excreted in urine by these patients, and consequently, to employ them as a validated biomarkers.

Additional metabolites were found to have differing levels in both groups studied (NPC and HET), such as QUIN (involved in macrophage activation and NAD synthesis), gut microflora metabolites (methanol, TMA and 5-aminovalerate), and muscle wasting by-products such as 3-aminoisobutyrate and 2-hydroxy-3-methylbutyrate, both arising from BCAA degradation pathways. Since the sample set was not conformed for age-matched patients, metabolite concentration differences arising from such age-dependent processes were removed from biomarker evaluation. An additional confounding factor may be the imbalanced sample set, so that only 12 NP-C1 patients were part of the disease class sub-set, and 41 for the control (HET) one; nevertheless, the MVA methods employed were able to successfully classify the samples, and cross-validation methodologies were implemented in the analysis to overcome this issue. Another limitation could be the use of heterozygotes as controls, since they have some genetic similarities that could be reflected in the phenotype, and therefore also perhaps in their ^{1}H NMR urinary profiles. However, these participants have the closest healthy genotype, so the ability of our models to classify such samples serves as an improvement in diagnosis. Moreover, using age-matched healthy participants should facilitate the analyses.

Urine collected from NP-C1 patients undergoing MGS treatment were analysed by high-resolution NMR analysis, identifying this drug in urine together with some other pharmaceutical agents, such as valproate and acetaminophen along with their metabolites, and hence providing an insight in the urinary profiling of patients undergoing several treatments in addition to the introduction of a new validated method for MGS detection in urine (and quantification, Appendix 1). Additionally, a series of modifications to the urinary

profiles of these patients undergoing MGS treatment (i.e., those of metabolites previously highlighted as discriminatory features) were investigated. These studies revealed substantial MGS therapy-associated changes in the urinary concentrations of N-acetylated metabolites such as N-acetylsugars and saccharides, i.e. reversals. Moreover, metabolites arising from the loss of muscle biomass (3-AIB and 2-hydroxy-3-methylbutyrate) and QUIN showed similar urinary levels to those from HETs, suggesting a recovery of normal levels for those metabolites after MGS treatment. However, this analysis presented some limitations in view of the overlap of drug/drug metabolite resonances with those of potential biomarkers, and hence not all the discriminatory features selected by the MVA could be evaluated in this manner.

^{1}H NMR-linked metabolomics analysis of plasma samples revealed major changes in plasma lipids, in addition to those of some other common metabolites. However, the specificity of these metabolites as NP-C1 plasma biomarkers is limited in view of the common lipid profile shared with other cholesterol/lipid storage diseases and the employment of non-fasting WT samples. Therefore, further analysis is required, and such investigations should include samples collected from patients with related or similar diseases. Moreover, specification of the lipoprotein subclasses should also be a major requirement, since recently-developed NMR methods are now able to distinguish many different lipoprotein subclasses, and this information should be employed for NP-C1 diagnostic purposes. Higher levels of some amino acids, such as glutamine and isoleucine in NP-C1 plasma samples, supported the results acquired from MVA of the urinary dataset, i.e. those relating to the muscle biomass degradation experienced by these patients, and therefore indicating a further complication of the disease that could assist in employing new therapies to overcome

this problem, and also potentially adding a new methodology to monitor this debilitating process.

For these plasma samples, a technical issue was faced regarding the employment of a polysucrose-based separation column (histopaque) for plasma, which generated additional resonance signals which overlapped those arising from endogenous metabolites. Moreover, free and metal ion-complexed EDTA resonances were also observable in our ^{1}H NMR plasma spectra, since this agent was an anticoagulant present in the blood collection tubes utilised. Although the use of this EDTA anticoagulant only presents minor problems, the histopaque protocol did present some major problems, particularly with the overlap of many histopaque-derived ^{1}H NMR signals with those of a range of potential endogenous biomarkers. However, major differences between the ^{1}H NMR profiles of NP-C1 patients, heterozygous carriers, healthy controls and MGS-treated NP-C1 patients were observed despite these complications, and therefore valuable information regarding the metabolic status of NP-C1 disease patients.

The hepatic levels of small polar metabolites contained in aqueous extracts obtained from NP-C1 disease, heterozygous carrier and healthy mice were investigated by ^{1}H NMR-linked metabolomics analysis. The NP-C1 mouse model studied presented common features related to other cases of liver damage, such as fibrosis leading to cirrhosis; fibrosis being a feature included in the pathophysiology of the disease, although some discriminatory metabolites were unique, such as nicotinate and 3-hydroxyphenylacetate. These findings provide support for the higher levels of QUIN observed in urine collected from NP-C1 patients, together with the lower levels of hepatic niacinamide, and these metabolic modifications suggest an imbalance in NAD/NADP synthesis, and therefore, a possible target for pharmaceutical strategies aimed at ameliorating the disease process and an additional

pathway to be monitored in order to assess the disease progression, specifically that involving associated liver dysfunctions. Moreover, the oxidative stress process putatively involved in this disease was also investigated by an analysis of GSH:GSSG molar concentration ratios, and the results acquired were consistent with those of previous investigations.

With regard to those metabolites arising from microbiota activity, and also found to be important discriminatory features in urine (5-aminovalerate, TMA and methanol) and liver aqueous extracts (3-hydroxyphenylacetate), further work is proposed to investigate the correlation between gut microbiota and NP-C1, since this approach is developing as a very useful methodology in metabolomics investigations, and reveal how the microbiota modulates some metabolic pathways, and how this modulation is modified in a range of human diseases. ^{1}H NMR-linked metabolomics studies of faeces provide a reliable insight into the gut microbiota status; accordingly, a further investigation of such samples may shed light on our findings.

The biomarkers proposed herein and discussed in section 6.7 should, in principle, be confirmed in further investigations and by other techniques in order to validate our findings. Urinary metabolites should be confirmed, including more NP-C1 urine samples and healthy individuals as controls. As noted above, plasma lipoprotein profiles can be investigated more extensively in order to check for further differences in lipoprotein sub-classes. Furthermore, newly-developed methods for ^{1}H NMR-linked metabolomics analysis of plasma samples such as methanol precipitation of plasma, followed by drying and reconstitution of the sample has revealed an increase in the number of metabolites detected, and consequently, broadens the spectrum of biomolecules, including that of putative biomarkers. With regard to the investigation of mouse liver samples, further work focused on explorations of the NAD

pathway in NP-C1 mouse liver should also be performed, since this metabolic route may reveal therapeutic points of action which may improve the pharmacological treatment of these patients.

In addition to the above valuable metabolic information provided, this work also evaluated a new method for MVA (CCR-LDA) and the accuracy of RFs when employed for variable selection purposes.

The CCR-LDA approach applied to our urinary and hepatic datasets showed excellent results for the classification of ^{1}H NMR urinary and hepatic tissue profiles according to their disease class, and values for accuracy, sensitivity and specificity derived therefrom were equivalent to those obtained by alternative techniques such as RFs, GAs and SVMs. These results encourage the use of this technique for MVA and its inclusion in appropriate data analysis 'toolboxes' by metabolomics investigators.

The combined RFs-RFE technique was evaluated as a strategy for variable selection and classification in a metabolomics context, as was previously performed for a microarray genetic analysis, and results acquired therefrom were compared with the variable selection method employed in our RFs model. We observed that despite being successful in classification tasks, it can reduce the number of variables to an extent where no relevant information can be extracted. Notwithstanding, the classification performance delivers high values for accuracy, and therefore with the whole ranking of variables after the completion of an appropriate number rounds of cross-validation, offers more information; furthermore, the ability of making decisions regarding the cut-off point for the number of variables lies with the investigator, and not on the performance of the variable selection algorithm.

In summary, these ^{1}H NMR-based metabolomics investigations have enabled the characterization of metabolites related to NP-C1 disease, providing a functional readout of

cellular disease biochemistry and possible biomarkers for its diagnosis. This metabolite profiling study has also revealed new discoveries linking cellular pathways to biological mechanisms, and hence increases our understanding of the pathophysiology associated with NP-C1 disease.

APENDIX 1: QUANTIFICATION OF MIGLUSTAT AND 1-O-VALPROIL-β-GLUCURONATE IN URINE SAMPLES COLLECTED FROM NP-C1 PATIENTS UNDERGOING MIGLUSTAT TREATMENT

MGS was quantified in those urine samples collected from NP-C1 patients undergoing treatment with this therapeutic agent *via* integration of the 0.93 - 0.97 ppm bucket intensity, which contains the resonance peak attributable to the MGS-CH_3 (*t*, 0.95 ppm), and for 1-O-valproyl-β-glucuronide quantification, the 5.53 - 5.57 (*d*, 0.55 ppm) ppm bucket was employed; the latter encompasses its CH-1 group from the glucuronide moiety. MGS integral values were expressed relative to either that of the TSP-($C\underline{H}_3)_3$ resonance (s, 0.00 ppm) bucket, i.e. -0.03 - 0.03 ppm, the concentration of which is known since it was added as an internal standard, or to that of Cn-CH_2 (*s*, 4.04 ppm), for which the 4.02 - 4.10 ppm bucket was utilised. Calibration curves were constructed in the range of 0.00 - 5.00 mM MGS in 0.10 M phosphate buffer (pH 7.10) as MGS-CH_3:TSP-($C\underline{H}_3)_3$ ratios. Since 1-O-valproyl-β-glucuronide standard was not commercially available, we could not construct a calibration curve for that agent. Lower limit of quantification (LLOQ) values for the ^{1}H NMR analysis of MGS were estimated on the 400 MHz Leicester School of Pharmacy spectrometer *via* the repeated analysis of phosphate-buffered (pH 7.10) standard solutions of this drug, which ranged in concentration from 10.0 - 80.0 μM.

Assay selectivity and matrix effects

To evaluate the accuracy of our quantification methodology based on the integration of selected resonance intensities, we investigated the matrix effects ascribable to those

resonances very close to the buckets employed for quantification. These resonances can interfere with those quantified, and therefore, generate inaccurate results. For this purpose, both blank or MGS-containing urine samples (collected from MGS-treated patients), were spiked with increasing concentrations of MGS (i.e. standard addition experiments involving the addition of final 0.16 - 0.83 and 1.13 - 5.00 mM levels of this agent), and then subjected to ^{1}H NMR analysis. Matrix effects on the intensity of the 0.93 - 0.97 ppm bucket were investigated by comparisons of the integral value of this bucket expressed relative to that of a pre-added TSP internal standard and/or internal urinary Cn, to those of 'neat' MGS solutions prepared in 0.10 M phosphate buffer (pH 7.10) at corresponding concentrations. These effects were monitored via determinations of variabilities of the concentration values attained. A series of 12 urine samples were investigated in this manner. The ^{1}H NMR resonance intensities of the 1-O-valproyl-β-glucuronide and Cn buckets selected were found not to be influenced by any such endogenous matrix effects.

Precision and accuracy

The within-, between-run precision (WRP and BRP respectively) and accuracy estimates of methods for the determination of MGS and 1-O-valproyl-β-glucuronide were evaluated on three separate days and five different quality control (QC) urine samples collected from NP-C1 patients treated with both MGS and valproate. An estimate of the BRP was obtained via the performance of a one-way (completely randomised design) ANOVA model for each sample tested, and employing analysis run (day) as the classification variable.

$$WRP = 100\%\ x\ \frac{\sqrt{MS_{within}}}{OM} \qquad \text{(A1)}$$

Where MS_{within} and OM represent the within-run mean square and overall mean values respectively. In order to estimate the BRP, 5 separate NP-C1 disease urine samples containing both ^{1}H NMR-detectable MGS and 1-O-valproyl-β-glucuronide were selected and analysed in triplicate on each of 3 separate runs (days), and for each sample examined, the between-days and within-days mean square (MS) values were estimated.

$$BRP = 100\%\ x\ \frac{\sqrt{\frac{MS_{between} - MS_{within}}{n}}}{OM} \quad \text{(A2)}$$

Where $MS_{between}$ and n are the between-groups mean square value and the number of replicate observations within each daily run (n = 3) respectively. These parameters were computed using XLSTAT 2015 software (Addinsoft). For such ANOVA estimates, the 'between-run' component of variance was found not to be statistically significant when tested against the 'within-run' one for each analyte and each sample analysed. The accuracy of analytical measurements was expressed as follows

$$ACC = 100\%\ x\ \frac{mean\ value - nominal\ value}{nominal\ value} \quad \text{(A3)}$$

Quantification results

MGS present in urine samples of patients treated with the standard dose of 200 mg (3 × daily) was quantified, yielding 208 ± 30 µmol MGS/mmol creatinine (mean ± SE, range 78 - 680 µmol MGS/mmol Cn; n = 25). In view of a potential minor interfering matrix effect, these levels only include values >70 µmol MGS/mmol Cn.

The concentration of 1-O-valproyl-β-glucuronide in these patient's samples was quantified, giving a value of 470 ± 61 µmol/mmol creatinine (mean ± SE, range 47 - 1,154 µmol/mmol Cn, n = 14).

Assay validation

***MGS and 1-O-valproyl-β-glucuronide assay selectivities, and investigations of the influence of matrix effects*:** Matrix effects arising from resonances close or overlaying those selected for MGS and 1-O-valproyl-β-glucuronide quantification did not affect the computation of these agents' concentrations, although this effect presented some minor interferences at the lower urinary MGS concentrations. Non-MGS-treated urine samples to which 1.00, 2.00, 3.00, 4.00 and 5.00 mM was added (Figure A1) gave increased MGS concentration values of 4.4 - 8.8, 3.0 - 6.8, 2.2 - 5.5, 1.5 - 3.4 and 0.9 - 2.6% respectively (Table A1).

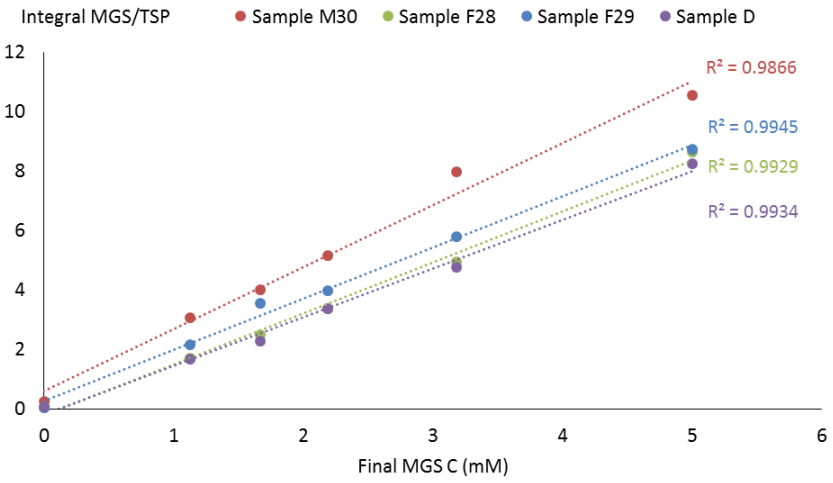

Figure A1. Non-treated urine samples spiked with MGS: plot of 4 urine samples after being spiked with MGS displaying their integral ratio MGS-CH_3:TSP-$(CH_3)_3$ *vs*. MGS final concentration.

Sample M30	Sample F28	Sample F29	Sample D
8.86%	4.37%	2.21%	5.16%
6.84%	2.99%	1.35%	3.80%
5.30%	2.20%	1.21%	2.57%
3.43%	1.51%	0.83%	1.81%
2.59%	0.86%	0.55%	1.05%

Table A1. Background contribution (matrix effect) to MGS concentration calculations on selected urine samples.

Linearity of calibration curves and lower limit of quantification (LLOQ): Calibration curves were generated with (1/concentration) regression weightings via least-squares linear regression analysis of MGS/TSP buckets intensity ratios *vs*. MGS concentration. Standard curves exhibited excellent linearity throughout the Cn-normalised MGS concentration range of 0 - 5.00 mM for phosphate-buffered (urine-free) standards. For the standard addition calibrations, MGS/Cn intensity ratios *v.* added MGS concentration plots (Figure A2) also demonstrated excellent linearity (r = 0.985 - 0.990). The estimated regression coefficient (calibration gradient) of these linear relationships was 1.72 ± 0.17 (estimated value ± 95% CIs) for plots of the above ratio versus added MGS concentration. For the *y* intercept, such 95% CIs always encompassed the zero concentration calibration point for plots obtained both with and without the inclusion of corresponding zero (blank) drug concentration data-points for both analytes, despite the presence of the minor matrix effect for urinary MGS determinations. The limit of detection (LOD) value was determined as 10.0 μM for the 400 MHz spectrometer utilised here; however, the achievement of a satisfactory signal-to-noise ratio for this concentration of MGS required 4096 spectral scans. Therefore, for a typical

bioanalytical ^{1}H NMR run performed on a typical NP-C1 disease urine sample, which involves 128 scans, a value of *ca*. 30 µM for this LOD value was determined. Absolute LLOQ values for the determination of MGS in phosphate-buffered aqueous solution and human urine samples were 50 and 80 µM respectively, and 80 M for that of 1-O-valproyl-β-glucuronide in human urine when analysed at an NMR operating frequency of 400 MHz.

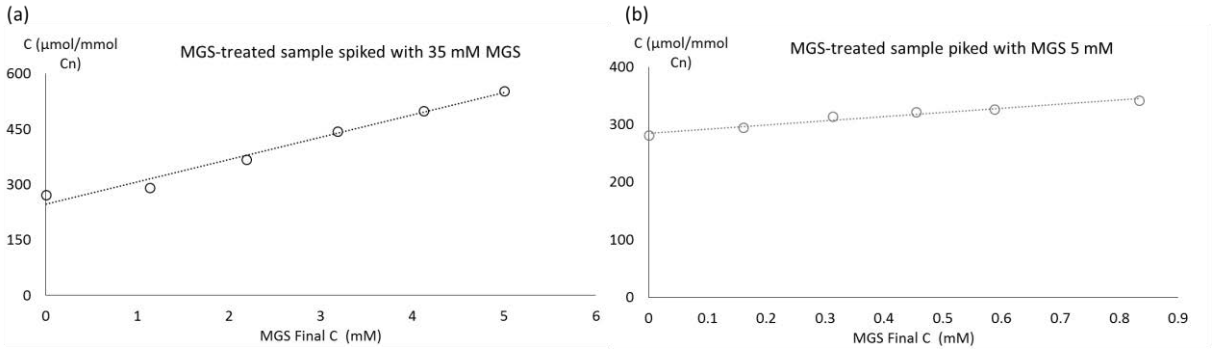

Figure A2. Standard addition experiments for 2 MGS-treated urine samples.

Assay precision and accuracies: Corresponding assay precision parameters for determinations of MGS and 1-O-valproyl-β-glucuronide are provided in Table A2; these values were determined by ^{1}H NMR analysis of the QC validation samples. The WRP of the assays were less than 6% and 4% for MGS and 1-O-valproyl-β-glucuronide respectively, and the BRP was less than 3% for both analytes on 5 QC samples. Assay accuracy was within the range of 95.3 - 107.4% for absolute urinary MGS concentrations which were > 0.10 mM, and 95.0 - 108.9% for urinary Cn-normalised ones for values >70 µmol/mmol Cn.

	MGS		1-O-valproyl-β-glucuronide	
Sample	WRP	BRP	WRP	BRP
1	5.49%	2.31%	3.15%	1.18%
2	2.26%	1.31%	3.11%	0.43%
3	3.96%	0.65%	0.17%	0.96%
4	2.71%	0.98%	0.20%	1.09%
5	2.87%	2.02%	1.45%	2.48%
Mean	3.46%	1.45%	1.62%	1.23%

Table A2. Within-run (WRP) and between-run precision (BRP) estimates (%) for ^{1}H NMR determinations of miglustat (MGS) and 1-O-valproyl-β-glucuronide. The buckets employed for these analytes were (a) 0.93 - 0.97 and (b) 5.53 - 5.57 ppm.

REFERENCES

1. Rabi II, Millman S, Kusch P, Zacharias JR. The Molecular Beam Resonance Method for Measuring Nuclear Magnetic Moments. The Magnetic Moments of $^{3}Li^{6}$, $^{3}Li^{7}$ and $^{9}F^{19}$. Phys Rev. 1939 Mar;55:526-35.

2. Slicter CP. Principles of Magnetic Resonance. 3rd ed. Heidelberg (Germany): Springer-Verlag; 1990.

3. Keller J. Understanding NMR Spectroscopy. 2nd ed. New Jersey (USA): John Wiley & Sons; 2010.

4. Bloch F, Hansen WW, Packard M. The Nuclear Induction Experiment. Phys Rev. 1946 Oct;70:474-85.

5. Ernst RR, Anderson WA. Application of Fourier transform spectroscopy to magnetic resonance. Rev Sci Instrum. 1966 Dec;37:93-102.

6. Lowe IJ, Norberg RE. Free-Induction Decays in Solids. Phys Rev. 1957 Jul;107:46-61.

7. Kumar A, Ernst RR, Wuthrich K. A two-dimensional nuclear Overhauser enhancement (2D NOE) experiment for the elucidation of complete proton-proton cross-relaxation networks in biological macromolecules. Biochem Biophys Res Commun. 1980 Jul;16;95(1):1-6.

8. Hoult DI. Solvent peak saturation with single phase and quadrature Fourier transformation. J Magn Reson. 1976 Feb;21:337-47.

9. Zheng G, Price WS. Solvent signal suppression in NMR. Prog Nucl Magn Reson Spectrosc. 2010 Apr;56(3):267-88.

10. Ross A, Schlotterbeck G, Dieterle F, Senn H. NMR Spectroscopy Techniques for Application to Metabolomics (55-112).In: The Handbook of Metabonomics and Metabolomics. Lindon JC, Nicholson JK, Holmes E, editors. 1st ed. Amsterdam (The Netherlands): Elsevier Science; 2007.

11. McKay RT. How the 1D-NOESY Suppresses Solvent Signal in Metabonomics NMR Spectroscopy: An Examination of the Pulse Sequence Components and Evolution. Concepts Magn Reson Part A. 2011 Sep;38A(5):197-220.

12. Carr HY, Purcell EM. Effects of diffusion on free precession in nuclear magnetic resonance experiments. Phys Rev. 1954 May;94:630-38.

13. Hahn EL. Spin echoes. Phys Rev. 1950 Nov;80:580-602.

14. Meiboom S, Gill DL. Modified spin-echo method for measuring nuclear relaxation times. Rev Sci Instrum. 1958 Aug;29:688-91.

15. Claridge TDW. High-resolution NMR techniques in organic chemistry. 2nd ed. Amsterdam (The Netherlands): Elsevier Science; 2009.

16. Aue WP, Bartholdi E, Ernst RR. Two-dimensional spectroscopy. Application to nuclear magnetic resonance. J Chem Phys. 1976 Mar;64:2229-46.

17. Friebolin H. Basic One- and Two-Dimensional NMR Spectroscopy. 5th ed. New Jersey (USA): John Wiley & Sons; 2011.

18. Braunschweiler L, Ernst RR. Coherence transfer by isotropic mixing: Application to proton correlation spectroscopy J Magn Reson. 1983 Jul;53(3):521-8.

19. Bax A, Davis DG. MLEV-17 based two-dimensional homonuclear magnetization transfer spectroscopy. J Magn Reson. 1985 Jul;65:355-60.

20. Hartmann SR, Hahn EL. Nuclear double resonance in the rotating frame. Phys Rev. 1962 Dec;128(5):2042-53.

21. Roberts JD. ABCs of FT-NMR. 1st ed. Sausalito(USA): University Science Book; 2000.

22. Bodenhausen G, Ruben DJ. Natural abundance nitrogen-15 NMR by enhanced heteronuclear spectroscopy. Chem Phys Lett. 1980 1 Jan;69(1):185-9.

23. Lindon JC, Nicholson JK, Holmes E, Everett JR. Metabonomics: Metabolic processes studied by NMR spectroscopy of biofluids. Concept Magn Res. 2000 Jan;12(5):289-320.

24. Poretsky L. Principles of diabetes mellitus. 2nd ed. New York (USA): Springer; 2010.

25. Jaques J. Greek Medicine from Hippocrates to Galen: Selected papers. 1st ed. Leiden (The Netherlands): Brill ; 2012.

26. Nicholson JK, Wilson ID. Opinion: understanding 'global' systems biology: metabonomics and the continuum of metabolism. Nat Rev Drug Discov. 2003 Aug;2:668-76.

27. Williams RJ. Introduction, General Discussion and Tentative Conclusions. In: Individual metabolic patterns and human disease: an exploratory study utilizing predominantly paper chromatographic methods (7-21). Austin, TX (USA): Biochemical Institute and the Dept. of Chemistry, the University of Texas, and the Clayton Foundation for Research; 1951.

28. Horning MG, Murakami S, Horning EC. Analyses of phospholipids, ceramides, and cerebrosides by gas chromatography and gas chromatography-mass spectrometry. Am J Clin Nutr. 1971 Sep;24(9):1086-96.

29. Horning EC, Devaux PG, Moffat AC, Pfaffenberger CD, Sakauchi N, Horning MG. Gas phase analytical separation techniques applicable to problems in clinical chemistry. Clin Chim Acta. 1971 Sep;34(2):135-44.

30. Horning MG, Hung A, Hill RM, Horning EC. Variations in urinary steroid profiles after birth. Clin Chim Acta. 1971 Sep;34(2):261-8.

31. Teranishi R, Mon TR, Robinson AB, Cary P, Pauling L. Gas chromatography of volatiles from breath and urine. Anal Chem. 1972 Jan;44(1):18-20.

32. McConnell ML, Rhodes G, Watson U, Novotny M. Application of pattern recognition and feature extraction techniques to volatile constituent metabolic profiles obtained by capillary gas chromatography. J Chromatogr. 1979 April;162:495-506.

33. Hoult DI, Busby SJ, Gadian DG, Radda GK, Richards RE, Seeley PJ. Observation of tissue metabolites using ^{31}P nuclear magnetic resonance. Nature. 1974 Nov;;252:285-7.

34. Barany M, Barany K, Burt CT, Glonek T, Myers TC. Structural changes in myosin during contraction and the state of ATP in the intact frog muscle. J Supramol Struct. 1975;3(2):125-40.

35. Cheng LL. High-resolution MAS NMR of Tissues and Cells. In: NMR in Pharmaceutical Science (117-28). Everett JR, Harris RK, Lindon JC, Wilson ID, editors.. 1st ed. Singapore (Singapore): Wiley; 2015. p. 117-28.

36. Rabenstein DL. ^{1}H NMR methods for the non-invasive study of metabolism and other processes involving small molecules in intact erythrocytes. J Biochem Biophys Methods. 1984 Sep;9(4):277-306.

37. Brown FF, Campbell ID, Kuchel PW, Rabenstein DC. Human erythrocyte metabolism studies by ^{1}H spin echo NMR. FEBS Lett. 1977 Oct;82(1):12-6.

38. Nicholson JK, Sadler PJ, Bales JR, Juul SM, MacLeod AF, Sonksen PH. Monitoring metabolic disease by proton NMR of urine. Lancet. 1984 Sep;2(8405):751-2.

39. Daniels A, Williams RJ, Wright PE. Nuclear magnetic resonance studies of the adrenal gland and some other organs. Nature. 1976 May;261(5558):321-3.

40. Bock JL. Analysis of serum by high-field proton nuclear magnetic resonance. Clin Chem. 1982 Sep;28(9):1873-7.

41. Arus C, Yen-Chang, Barany M. Proton nuclear magnetic resonance spectra of excised rat brain. Assignment of resonances. Physiol Chem Phys Med NMR. 1985;17(1):23-33.

42. Arus C, Barany M. Application of high-field ^{1}H-NMR spectroscopy for the study of perifused amphibian and excised mammalian muscles. Biochim Biophys Acta. 1986 May 29;886(3):411-24.

43. Wishart DS, Tzur D, Knox C, Eisner R, Guo AC, Young N, et al. HMDB: the Human Metabolome Database. Nucleic Acids Res. 2007 Jan;35(Database issue):D521-6.

44. Ulrich EL, Akutsu H, Doreleijers JF, Harano Y, Ioannidis YE, Lin J, et al. BioMagResBank. Nucleic Acids Res. 2008 Jan;36(Database issue):D402-8.

45. Bouatra S, Aziat F, Mandal R, Guo AC, Wilson MR, Knox C, et al. The human urine metabolome. PLoS One. 2013 Sep;8(9):e73076.

46. Psychogios N, Hau DD, Peng J, Guo AC, Mandal R, Bouatra S, et al. The human serum metabolome. PLoS One. 2011 Feb;;6(2):e16957.

47. Dame ZT, Aziat F, Mandal R, Krishnamurthy R, Bouatra S, Borzouie S, et al. The human saliva metabolome. Metabolomics. 2015 Dec;11(6):1864-83.

48. Bingol K, Li DW, Bruschweiler-Li L, Cabrera OA, Megraw T, Zhang F, et al. Unified and isomer-specific NMR metabolomics database for the accurate analysis of (13)C-(1)H HSQC spectra. ACS Chem Biol. 2015 Feb;10(2):452-9.

49. Ravanbakhsh S, Liu P, Bjorndahl TC, Mandal R, Grant JR, Wilson M, et al. Correction: Accurate, Fully-Automated NMR Spectral Profiling for Metabolomics. PLoS One. 2015 Jul ;10(7):e0132873.

50. Xia J, Sinelnikov IV, Han B, Wishart DS. MetaboAnalyst 3.0--making metabolomics more meaningful. Nucleic Acids Res. 2015 Jul;43(W1):W251-7.

51. Emwas AH, Luchinat C, Turano P, Tenori L, Roy R, Salek RM, et al. Standardizing the experimental conditions for using urine in NMR-based metabolomic studies with a particular focus on diagnostic studies: a review. Metabolomics. 2015 Aug;11(4):872-94.

52. Mallol R, Amigo N, Rodriguez MA, Heras M, Vinaixa M, Plana N, et al. Liposcale: a novel advanced lipoprotein test based on 2D diffusion-ordered ^{1}H NMR spectroscopy. J Lipid Res. 2015 Mar;56(3):737-46.

53. Nagana Gowda GA, Raftery D. Quantitating metabolites in protein precipitated serum using NMR spectroscopy. Anal Chem. 2014 Jun;86(11):5433-40.

54. Dona AC, Jimenez B, Schafer H, Humpfer E, Spraul M, Lewis MR, et al. Precision high-throughput proton NMR spectroscopy of human urine, serum, and plasma for large-scale metabolic phenotyping. Anal Chem. 2014 Oct;86(19):9887-94.

55. Salek RM, Steinbeck C, Viant MR, Goodacre R, Dunn WB. The role of reporting standards for metabolite annotation and identification in metabolomic studies. Gigascience. 2013 Oct ;2(1):13,217X-2-13.

56. MSI Board Members, Sansone SA, Fan T, Goodacre R, Griffin JL, Hardy NW, et al. The metabolomics standards initiative. Nat Biotechnol. 2007 Aug;25(8):846-8.

57. Emwas AH, Roy R, McKay RT, Ryan D, Brennan L, Tenori L, et al. Recommendations and Standardization of Biomarker Quantification Using NMR-Based Metabolomics with Particular Focus on Urinary Analysis. J Proteome Res. 2016 Feb;15(2):360-73.

58. Pathan M, Akoka S, Tea I, Charrier B, Giraudeau P. "Multi-scan single shot" quantitative 2D NMR: a valuable alternative to fast conventional quantitative 2D NMR. Analyst. 2011 Aug;136(15):3157-63.

59. Le Guennec A, Tea I, Antheaume I, Martineau E, Charrier B, Pathan M, et al. Fast determination of absolute metabolite concentrations by spatially encoded 2D NMR: application to breast cancer cell extracts. Anal Chem. 2012 Dec;84(24):10831-7.

60. Rai RK, Sinha N. Fast and accurate quantitative metabolic profiling of body fluids by nonlinear sampling of ^{1}H-^{13}C two-dimensional nuclear magnetic resonance spectroscopy. Anal Chem. 2012 Nov;84(22):10005-11.

61. Hotelling H. Analysis of a complex of statistical variables into principal components. J Educ Psychol. 1933 Sep;24(6):417-41.

62. Pearson K. On lines and planes of closest fit to systems of points in space. Philos Mag. 1901;2(11):559-72.

63. Rencher AC. Multivariate Statistical Inference and Applications. 1st ed. New Jersey (USA): John Wiley & Sons, Inc; 2002.

64. Abdi H, Williams LJ. Principal component analysis. Wiley Interdiscip Rev Comput Stat. 2010 Jun;2(4):433-59.

65. Kaiser HF. The varimax criterion for analytic rotation in factor analysis. Psychometrika. 1958 Sep;23(3):187-200.

66. Fisher RA. The use of multiple measurements in taxonomic problems. Ann Hum Genet. 1936 Sep;7(2):179-88.

67. Balakrishnam S, Ganapathiraju A. Linear Discriminant Analysis-A Brief Tutorial. Institute for Signal and Information Processing Department of Electrical and Computer Engineering, Mississippi State University. 1998:.

68. Borcard D, Gillet F, Legendre P. Numerical ecology with R. 3rd ed. Oxford (UK): Springer Science & Business Media; 2012.

69. Van den Wollenberg, A. L. Redundancy analysis: An alternative for canonical correlation analysis. Psychometrika. 1977 Jun;42(2):207-19.

70. Davies PT, Tso MK. Procedures for reduced-rank regression. Appl Stat. 1982 Mar;31:244-55.

71. Ter Braak CJF. Interpreting canonical correlation analysis through biplots of structure correlations and weights . Psychometrika. 1990 Sep;55(3):519-31.

72. Magidson J. Correlated component regression: re-thinking regression in the presence of near collinearity. In: New Perspectives in Partial Least Squares and Related Methods (65-78). 1st ed. New York (USA): Springer; 2013. p. 65-78.

73. Magidson J. A Fast Parsimonious Maximum Likelihood Approach for Predicting Outcome Variables from a Large Number of Predictors. COMPSTAT 2010 Proceedings; Aug 22-27; Paris; 2010.

74. Magidson J. Correlated Component Regression: A prediction/classification methodology for possibly many featuree. *Proceedings of the American Statistical Association*.

75. Magidson J, Bennett G. Correlated Component Regression (CCR) - A brief methodological description. 2011.

76. Consonni V, Ballabio D, Todeschini R. Evaluation of model predictive ability by external validation techniques. J Chemometrics. 2010 Feb;24:194-201.

77. Fawcett T. ROC Graphs: Notes and Practical Considerations for Data Mining Researchers. Mach Learn. 2003 Jan;31:1-38.

78. El Khouli RH, Macura KJ, Barker PB, Habba MR, Jacobs MA, Bluemke DA. Relationship of temporal resolution to diagnostic performance for dynamic contrast enhanced MRI of the breast. J Magn Reson Imaging. 2009 Nov;30(5):999-1004.

79. Breiman L. Random Forest. Mach Learn. 2001 Oct;45(1):5-32.

80. De'ath G, Fabricius KE. Classification and regression trees: a powerful yet simple technique for ecological data analysis. Ecology. 2000 Nov;81(11):3178-92.

81. Breiman L, Friedman JH, Olshen RA, Stone CJ. Classification and regression trees. 1st ed. Belmont (USA): Wadsworth & Brooks/Cole; 1984.

82. James G, Witten D, Hastie T, Tibshirani R. The Bootstrap. In: An introduction to statistical learning (187-90). 6th ed. New York (USA): Springer; 2013.

83. Felsenstein J. Confidence limits on phylogenies: an approach using the bootstrap. Evolution. 1985 Jul;39(4):783-91.

84. Efron B, Gong G. A leisurely look at the bootstrap the jackknife, and cross validation. Am Stat. 1983 Feb;37(1):36-48.

85. Vapnik V. Estimation of Dependences Based on Empirical Data. 1st ed. New York (USA): Springer Verlag; 1982.

86. Boser BE, Guyon IM, Vapnik VN. A training algorithm for optimal margin classifiers. In: Proceedings of the fifth annual workshop on Computational learning theory (144-52), ACM. 1992.

87. Vapnik V. Statistical Learning Theory. 1st ed. New York (USA): John Wiley and Sons, Inc; 1998.

88. Holland JH. Adaptation in Natural and Artificial Systems. 1st ed. Michigan (USA): University of Michigan Press; 1975.

89. Srinivas M, Patnaik LM. Adaptive probabilities of crossover and mutation in genetic algorithms. IEEE Trans Syst Man Cybern. 1994 Apr;24(4):656-67.

90. Lin X, Wang Q, Yin P. A method for handling metabonomics data from liquid chromatography/mass spectrometry: combinational use of support vector machine recursive feature elimination, genetic algorithm and random forest for feature selection. Metabolomics. 2011 Dec;7(4):549-58.

91. Vanier MT. Niemann-Pick disease type C. Orphanet J Rare Dis. 2010 Jun;5:16,1172-5-16.

92. Vanier MT, Millat G. Niemann-Pick disease type C. Clin Genet. 2003 Sep;64:269-81.

93. Sun X, Marks DL, Park WD, Wheatley CL, Puri V, O'Brien JF, et al. Niemann-Pick C variant detection by altered sphingolipid trafficking and correlation with mutations within a specific domain of NPC1. Am J Hum Genet. 2001 Jun;68(6):1361-72.

94. Sturley SL, Patterson MC, Balch W, Liscum L. The pathophysiology and mechanisms of NP-C disease. Biochim Biophys Acta. 2004 Oct;1685(1-3):83-7.

95. NP-C Guidelines Working Group, Wraith JE, Baumgartner MR, Bembi B, Covanis A, Levade T, et al. Recommendations on the diagnosis and management of Niemann-Pick disease type C. Mol Genet Metab. 2009 Sep-Oct;98(1-2):152-65.

96. Vance DE, Van den Bosch H. Cholesterol in the year 2000. Biochim Biophys Acta. 2000 Dec;1529(1-3):1-8.

97. Jurevics H, Morell P. Cholesterol for synthesis of myelin is made locally, not imported into brain. J Neurochem. 1995 Feb;64(2):895-901.

98. Riobo NA. Cholesterol and its derivatives in Sonic Hedgehog signaling and cancer. Curr Opin Pharmacol. 2012 Dec;12(6):736-41.

99. Briscoe J, Therond PP. The mechanisms of Hedgehog signalling and its roles in development and disease. Nat Rev Mol Cell Biol. 2013 Jul;14(7):416-29.

100. Weedon MN, Lango H, Lindgren CM, Wallace C, Evans DM, Mangino M, et al. Genome-wide association analysis identifies 20 loci that influence adult height. Nat Genet. 2008 May;40(5):575-83.

101. Ahn S, Joyner AL. In vivo analysis of quiescent adult neural stem cells responding to Sonic hedgehog. Nature. 2005 Oct;437(7060):894-7.

102. Oram JF, Vaughan AM. ATP-Binding cassette cholesterol transporters and cardiovascular disease. Circ Res. 2006 Nov;99(10):1031-43.

103. Liscum L, Munn NJ. Intracellular cholesterol transport. Biochim Biophys Acta. 1999 Apr;1438(1):19-37.

104. Vance JE. Dysregulation of cholesterol balance in the brain: contribution to neurodegenerative diseases. Dis Model Mech. 2012 Nov;5(6):746-55.

105. Bjorkhem I. Crossing the barrier: oxysterols as cholesterol transporters and metabolic modulators in the brain. J Intern Med. 2006 Dec;260(6):493-508.

106. Ikonen E. Cellular cholesterol trafficking and compartmentalization. Nat Rev Mol Cell Biol. 2008 Feb;9(2):125-38.

107. Karten B, Peake KB, Vance JE. Mechanisms and consequences of impaired lipid trafficking in Niemann-Pick type C1-deficient mammalian cells. Biochim Biophys Acta. 2009 Jul;1791(7):659-70.

108. Storch J, Xu Z. Niemann-Pick C2 (NPC2) and intracellular cholesterol trafficking. Biochim Biophys Acta. 2009 Jul;1791(7):671-8.

109. Peake KB, Vance JE. Defective cholesterol trafficking in Niemann-Pick C-deficient cells. FEBS Lett. 2010 Jul;584(13):2731-9.

110. Zhou S, Davidson C, McGlynn R, Stephney G, Dobrenis K, Vanier MT, et al. Endosomal/lysosomal processing of gangliosides affects neuronal cholesterol sequestration in Niemann-Pick disease type C. Am J Pathol. 2011 Aug;179(2):890-902.

111. Platt N, Speak AO, Colaco A, Gray J, Smith DA, Williams IM, et al. Immune dysfunction in Niemann-Pick disease type C. J Neurochem. 2015 Jan; 136 Suppl 1:74-80.

112. Stampfer M, Theiss S, Amraoui Y, Jiang X, Keller S, Ory DS, et al. Niemann-Pick disease type C clinical database: cognitive and coordination deficits are early disease indicators. Orphanet J Rare Dis. 2013 Feb;8:35,1172-8-35.

113. Sevin M, Lesca G, Baumann N, Millat G, Lyon-Caen O, Vanier MT, et al. The adult form of Niemann-Pick disease type C. Brain. 2007 Jan;130(Pt 1):120-33.

114. Madra M, Sturley SL. Niemann-Pick type C pathogenesis and treatment: from statins to sugars. Clin Lipidol. 2010 Jun;5(3):387-95.

115. Pineda M, Wraith JE, Mengel E, Sedel F, Hwu WL, Rohrbach M, et al. Miglustat in patients with Niemann-Pick disease Type C (NP-C): a multicenter observational retrospective cohort study. Mol Genet Metab. 2009 Nov;98(3):243-9.

116. Mengel E, Klunemann HH, Lourenco CM, Hendriksz CJ, Sedel F, Walterfang M, et al. Niemann-Pick disease type C symptomatology: an expert-based clinical description. Orphanet J Rare Dis. 2013 Oct;8:166,1172-8-166.

117. Wijburg FA, Sedel F, Pineda M, Hendriksz CJ, Fahey M, Walterfang M, et al. Development of a suspicion index to aid diagnosis of Niemann-Pick disease type C. Neurology. 2012 May;78(20):1560-7.

118. Kelly DA, Portmann B, Mowat AP, Sherlock S, Lake BD. Niemann-Pick disease type C: diagnosis and outcome in children, with particular reference to liver disease. J Pediatr. 1993 Aug;123(2):242-7.

119. Mieli-Vergani G, Howard ER, Mowat AP. Liver disease in infancy: a 20 year perspective. Gut. 1991 Sep;Suppl:S123-8.

120. Yerushalmi B, Sokol RJ, Narkewicz MR, Smith D, Ashmead JW, Wenger DA. Niemann-pick disease type C in neonatal cholestasis at a North American Center. J Pediatr Gastroenterol Nutr. 2002 Jul;35(1):44-50.

121. Garver WS, Jelinek D, Oyarzo JN, Flynn J, Zuckerman M, Krishnan K, et al. Characterization of liver disease and lipid metabolism in the Niemann-Pick C1 mouse. J Cell Biochem. 2007 May;101(2):498-516.

122. Beltroy EP, Richardson JA, Horton JD, Turley SD, Dietschy JM. Cholesterol accumulation and liver cell death in mice with Niemann-Pick type C disease. Hepatology. 2005 Oct;42(4):886-93.

123. Cluzeau CV, Watkins-Chow DE, Fu R, Borate B, Yanjanin N, Dail MK, et al. Microarray expression analysis and identification of serum biomarkers for Niemann-Pick disease, type C1. Hum Mol Genet. 2012 Aug;21(16):3632-46.

124. Loftus SK, Morris JA, Carstea ED, Gu JZ, Cummings C, Brown A, et al. Murine model of Niemann-Pick C disease: mutation in a cholesterol homeostasis gene. Science. 1997 Jul;277(5323):232-5.

125. Erickson RP, Bhattacharyya A, Hunter RJ, Heidenreich RA, Cherrington NJ. Liver disease with altered bile acid transport in Niemann-Pick C mice on a high-fat, 1% cholesterol diet. Am J Physiol Gastrointest Liver Physiol. 2005 Aug;289(2):G300-7.

126. McKay Bounford K, Gissen P. Genetic and laboratory diagnostic approach in Niemann Pick disease type C. J Neurol. 2014 Sep;261 Suppl 2:S569-75.

127. Bornig H, Geyer G. Staining of cholesterol with the fluorescent antibiotic "filipin". Acta Histochem. 1974 Feb;50(1):110-5.

128. Takamura A, Sakai N, Shinpoo M, Noguchi A, Takahashi T, Matsuda S, et al. The useful preliminary diagnosis of Niemann-Pick disease type C by filipin test in blood smear. Mol Genet Metab. 2013 Nov;110(3):401-4.

129. Vanier MT, Latour P. Laboratory diagnosis of Niemann-Pick disease type C: the filipin staining test. Methods Cell Biol. 2015 Jan;126:357-75.

130. Jiang X, Sidhu R, Porter FD, Yanjanin NM, Speak AO, te Vruchte DT. A sensitive and specific LC-MS/MS method for rapid diagnosis of NiemannPick C1 disease from human plasma. J Lipid Res. 2011 Jul;52(7):1435-45.

131. te Vruchte D, Speak AO, Wallom KL, Al Eisa N, Smith DA, Hendriksz CJ, et al. Relative acidic compartment volume as a lysosomal storage disorder-associated biomarker. J Clin Invest. 2014 Mar;124(3):1320-8.

132. Giese AK, Mascher H, Grittner U, Eichler S, Kramp G, Lukas J, et al. A novel, highly sensitive and specific biomarker for Niemann-Pick type C1 disease. Orphanet J Rare Dis. 2015 Jun;10:78,015-0274-1.

133. Sedel F, Barnerias C, Dubourg O, Desguerres I, Lyon-Caen O, Saudubray JM. Peripheral neuropathy and inborn errors of metabolism in adults. J Inherit Metab Dis. 2007 Oct;30(5):642-53.

134. Sandu S, Jackowski-Dohrmann S, Ladner A, Haberhausen M, Bachmann C. Niemann-Pick disease type C1 presenting with psychosis in an adolescent male. Eur Child Adolesc Psychiatry. 2009 Sep;18(9):583-5.

135. Heron B, Valayannopoulos V, Baruteau J, Chabrol B, Ogier H, Latour P, et al. Miglustat therapy in the French cohort of paediatric patients with Niemann-Pick disease type C. Orphanet J Rare Dis. 2012 Jun;7:36,1172-7-36.

136. Helquist P, Maxfield FR, Wiech NL, Wiest O. Treatment of Niemann--pick type C disease by histone deacetylase inhibitors. Neurotherapeutics. 2013 Oct;10(4):688-97.

137. Alvarez AR, Klein A, Castro J, Cancino GI, Amigo J, Mosqueira M, et al. Imatinib therapy blocks cerebellar apoptosis and improves neurological symptoms in a mouse model of Niemann-Pick type C disease. FASEB J. 2008 Oct;22(10):3617-27.

138. Davidson CD, Ali NF, Micsenyi MC, Stephney G, Renault S, Dobrenis K, et al. Chronic cyclodextrin treatment of murine Niemann-Pick C disease ameliorates neuronal cholesterol and glycosphingolipid storage and disease progression. PLoS One. 2009 Sep;4(9):e6951.

139. Liu B, Turley SD, Burns DK, Miller AM, Repa JJ, Dietschy JM. Reversal of defective lysosomal transport in NPC disease ameliorates liver dysfunction and neurodegeneration in the npc1-/- mouse. Proc Natl Acad Sci U S A. 2009 Feb;106(7):2377-82.

140. Pipalia NH, Cosner CC, Huang A, Chatterjee A, Bourbon P, Farley N, et al. Histone deacetylase inhibitor treatment dramatically reduces cholesterol accumulation in Niemann-Pick type C1 mutant human fibroblasts. Proc Natl Acad Sci U S A. 2011 Apr;108(14):5620-5.

141. Smith D, Wallom KL, Williams IM, Jeyakumar M, Platt FM. Beneficial effects of anti-inflammatory therapy in a mouse model of Niemann-Pick disease type C1. Neurobiol Dis. 2009 Nov;36(2):242-51.

142. Williams IM, Wallom KL, Smith DA, Al Eisa N, Smith C, Platt FM. Improved neuroprotection using miglustat, curcumin and ibuprofen as a triple combination therapy in Niemann-Pick disease type C1 mice. Neurobiol Dis. 2014 Jul;67:9-17.

143. Wada R, Tifft CJ, Proia RL. Microglial activation precedes acute neurodegeneration in Sandhoff disease and is suppressed by bone marrow transplantation. Proc Natl Acad Sci U S A. 2000 Sep;97(20):10954-9.

144. Stein VM, Crooks A, Ding W, Prociuk M, O'Donnell P, Bryan C, et al. Miglustat improves purkinje cell survival and alters microglial phenotype in feline Niemann-Pick disease type C. J Neuropathol Exp Neurol. 2012 May;71(5):434-48.

145. Butters TD, Dwek RA, Platt FM. Inhibition of glycosphingolipid biosynthesis: application to lysosomal storage disorders. Chem Rev. 2000 Nov;100:4683-96.

146. Ribas GS, Pires R, Coelho JC, Rodrigues D, Mescka CP, Vanzin CS, et al. Oxidative stress in Niemann-Pick type C patients: a protective role of N-butyl-deoxynojirimycin therapy. Int J Dev Neurosci. 2012 Oct;30(6):439-44.

147. Fu R, Yanjanin NM, Bianconi S, Pavan WJ, Porter FD. Oxidative stress in Niemann-Pick disease, type C. Mol Genet Metab. 2010 Oct-Nov;101(2-3):214-8.

148. Mattsson N, Zetterberg H, Bianconi S, Yanjanin NM, Fu R, Mansson JE, et al. Miglustat treatment may reduce cerebrospinal fluid levels of the axonal degeneration marker tau in niemann-pick type C. JIMD Rep. 2011 Sep;3:45-52.

149. Jeyakumar M, Butters TD, Cortina-Borja M, Hunnam V, Proia RL, Perry VH, et al. Delayed symptom onset and increased life expectancy in Sandhoff disease mice treated with N-butyldeoxynojirimycin. Proc Natl Acad Sci U S A. 1999 May;96(11):6388-93.

150. Cox T, Lachmann R, Hollak C, Aerts J, van Weely S, Hrebicek M, et al. Novel oral treatment of Gaucher's disease with N-butyldeoxynojirimycin (OGT 918) to decrease substrate biosynthesis. Lancet. 2000 Apr;355(9214):1481-5.

151. Lachmann RH. Miglustat. Oxford GlycoSciences/Actelion. Curr Opin Investig Drugs. 2003 Apr;4(4):472-9.

152. Di Rocco M, Dardis A, Madeo A, Barone R, Fiumara A. Early miglustat therapy in infantile Niemann-Pick disease type C. Pediatr Neurol. 2012 Jul;47(1):40-3.

153. Zervas M, Somers KL, Thrall MA, Walkley SU. Critical role for glycosphingolipids in Niemann-Pick disease type C. Curr Biol. 2001 Aug;11(16):1283-7.

154. Rottach KG, von Maydell RD, Das VE, Zivotofsky AZ, Discenna AO, Gordon JL, et al. Evidence for independent feedback control of horizontal and vertical saccades from Niemann-Pick type C disease. Vision Res. 1997 Dec;37(24):3627-38.

155. Solomon D, Winkelman AC, Zee DS, Gray L, Buttner-Ennever J. Niemann-Pick type C disease in two affected sisters: ocular motor recordings and brain-stem neuropathology. Ann N Y Acad Sci. 2005 Apr;1039:436-45.

156. Neville BG, Lake BD, Stephens R, Sanders MD. A neurovisceral storage disease with vertical supranuclear ophthalmoplegia, and its relationship to Niemann-Pick disease: A report of nine patients. Brain. 1973 Mar;96(1):97-120.

157. Patterson MC, Vecchio D, Prady H, Abel L, Wraith JE. Miglustat for treatment of Niemann-Pick C disease: a randomised controlled study. Lancet Neurol. 2007 Sep;6(9):765-72.

158. Wraith JE, Vecchio D, Jacklin E, Lucy R, Giorgino R, Patterson MC. Disease stability in patients with Niemann-Pick disease type C treated with Miglustat, in: Lysosomal Diseases Network WORLD Symposium, San Diego, California, USA, 2009.

159. Salek RM, Maguire ML, Bentley E, Rubtsov DV, Hough T, Cheeseman M, et al. A metabolomic comparison of urinary changes in type 2 diabetes in mouse, rat, and human. Physiol Genomics. 2007 Apr;29(2):99-108.

160. Martin FP, Dumas ME, Wang Y, Legido-Quigley C, Yap IK, Tang H, et al. A top-down systems biology view of microbiome-mammalian metabolic interactions in a mouse model. Mol Syst Biol. 2007 May;3:112.

161. Wishart DS, Jewison T, Guo AC, Wilson M, Knox C, Liu Y, et al. HMDB 3.0--The Human Metabolome Database in 2013. Nucleic Acids Res. 2013 Jan;41(Database issue):D801-7.

162. Hofmann AF, Mysels KJ. Bile acid solubility and precipitation in vitro and in vivo: the role of conjugation, pH, and Ca2+ ions. J Lipid Res. 1992 May;33(5):617-26.

163. Viau C, Lafontaine M, Payan JP. Creatinine normalization in biological monitoring revisited: the case of 1-hydroxypyrene. Int Arch Occup Environ Health. 2004 Apr;77(3):177-85.

164. Heavner DL, Morgan WT, Sears SB, Richardson JD, Byrd GD, Ogden MW. Effect of creatinine and specific gravity normalization techniques on xenobiotic biomarkers in smokers' spot and 24-h urines. J Pharm Biomed Anal. 2006 Mar;40(4):928-42.

165. Liaw A, Wiener M. Classification and regression by randomForest. R. News 2002. **2**:18-22.

166. Trevino V, Falciani F. GALGO: an R package for multivariate variable selection using genetic algorithms. Bioinformatics. 2006 May;22(9):1154-6.

167. Li M, Wang B, Zhang M, Rantalainen M, Wang S, Zhou H, et al. Symbiotic gut microbes modulate human metabolic phenotypes. Proc Natl Acad Sci U S A. 2008 Feb;105(6):2117-22.

168. Kemsley EK, Le Gall G, Dainty JR, Watson AD, Harvey LJ, Tapp HS, et al. Multivariate techniques and their application in nutrition: a metabolomics case study. Br J Nutr. 2007 Jul;98(1):1-14.

169. Xia J, Broadhurst DI, Wilson M, Wishart DS. Translational biomarker discovery in clinical metabolomics: an introductory tutorial. Metabolomics. 2013 Apr;9(2):280-99.

170. Kawai T, Yasugi T, Mizunuma K, Horiguchi S, Hirase Y, Uchida Y, et al. Methanol in urine as a biological indicator of occupational exposure to methanol vapor. Int Arch Occup Environ Health. 1991 Oct;63(5):311-8.

171. Slupsky CM, Rankin KN, Wagner J, Fu H, Chang D, Weljie AM, et al. Investigations of the effects of gender, diurnal variation, and age in human urinary metabolomic profiles. Anal Chem. 2007 Sep;79(18):6995-7004.

172. Rebouche CJ. Kinetics, pharmacokinetics, and regulation of L-carnitine and acetyl-L-carnitine metabolism. Ann N Y Acad Sci. 2004 Nov;1033:30-41.

173. Zuppi C, Messana I, Forni F, Ferrari F, Rossi C, Giardina B. Influence of feeding on metabolite excretion evidenced by urine ^{1}H NMR spectral profiles: a comparison between subjects living in Rome and subjects living at arctic latitudes (Svaldbard). Clin Chim Acta. 1998 Nov;278(1):75-9.

174. Solanky KS, Bailey NJ, Beckwith-Hall BM, Bingham S, Davis A, Holmes E, et al. Biofluid 1H NMR-based metabonomic techniques in nutrition research - metabolic effects of dietary isoflavones in humans. J Nutr Biochem. 2005 Apr;16(4):236-44.

175. Lukaski HC. Methods for the assessment of human body composition: traditional and new. Am J Clin Nutr. 1987 Oct;46(4):537-56.

176. Roche AF, Heymsfield SB, Lohma TG. Human body composition. 1st ed. Champaign (USA): Human Kinetics Publishers; 1996.

177. Selberg O, Sel S. The adjunctive value of routine biochemistry in nutritional assessment of hospitalized patients. Clin Nutr. 2001 Dec;20(6):477-85.

178. Azaroual N, Imbenotte M, Cartigny B, Leclerc F, Vallee L, Lhermitte M, et al. Valproic acid intoxication identified by 1H and 1H-(13)C correlated NMR spectroscopy of urine samples. MAGMA. 2000 Jul;10(3):177-82.

179. Meshitsuka S, Koeda T, Muro H. Direct observation of 3-keto-valproate in urine by 2D-NMR spectroscopy. Clin Chim Acta. 2003 Aug;334(1-2):145-51.

180. Booth CL, Pollack GM, Brouwer KL. Hepatobiliary disposition of valproic acid and valproate glucuronide: use of a pharmacokinetic model to examine the rate-limiting steps and potential sites of drug interactions. Hepatology. 1996 Apr;23(4):771-80.

181. Fisher E, Siemes H, Pund R, Wittfoht W, Nau H. Valproate metabolites in serum and urine during antiepileptic therapy in children with infantile spasms: abnormal metabolite pattern associated with reversible hepatotoxicity. Epilepsia. 1992 Jan-Feb;33(1):165-71.

182. Guitton J, Coste S, Guffon-Fouilhoux N, Cohen S, Manchon M, Guillaumont M. Rapid quantification of miglustat in human plasma and cerebrospinal fluid by liquid chromatography coupled with tandem mass spectrometry. J Chromatogr B Analyt Technol Biomed Life Sci. 2009 Jan;877(3):149-54.

183. Spieker E, Wagner-Redeker W, Dingemanse J. Validated LC-MS/MS method for the quantitative determination of the glucosylceramide synthase inhibitor miglustat in mouse plasma and human plasma and its application to a pharmacokinetic study. J Pharm Biomed Anal. 2012 Feb;59:123-9.

184. Lachmann RH, te Vruchte D, Lloyd-Evans E, Reinkensmeier G, Sillence DJ, Fernandez-Guillen L, et al. Treatment with miglustat reverses the lipid-trafficking defect in Niemann-Pick disease type C. Neurobiol Dis. 2004 Aug;16(3):654-8.

185. Treiber A, Morand O, Clozel M. The pharmacokinetics and tissue distribution of the glucosylceramide synthase inhibitor miglustat in the rat. Xenobiotica. 2007 Mar;37(3):298-314.

186. Gao S, Miao H, Tao X, Jiang B, Xiao Y, Cai F, et al. LC-MS/MS method for simultaneous determination of valproic acid and major metabolites in human plasma. J Chromatogr B Analyt Technol Biomed Life Sci. 2011 Jul;879(21):1939-44.

187. Argikar UA, Remmel RP. Effect of aging on glucuronidation of valproic acid in human liver microsomes and the role of UDP-glucuronosyltransferase UGT1A4, UGT1A8, and UGT1A10. Drug Metab Dispos. 2009 Jan;37(1):229-36.

188. Proenca P, Franco JM, Mustra C, Marcos M, Pereira AR, Corte-Real F, et al. An UPLC-MS/MS method for the determination of valproic acid in blood of a fatal intoxication case. J Forensic Leg Med. 2011 Oct;18(7):320-4.

189. Chen ZJ, Wang XD, Wang HS, Chen SD, Zhou LM, Li JL, et al. Simultaneous determination of valproic acid and 2-propyl-4-pentenoic acid for the prediction of clinical adverse effects in Chinese patients with epilepsy. Seizure. 2012 Mar;21(2):110-7.

190. Lyseng-Williamson KA. Miglustat: a review of its use in Niemann-Pick disease type C. Drugs. 2014 Jan;74(1):61-74.

191. Chen S, Beaton D, Nguyen N, Senekeo-Effenberger K, Brace-Sinnokrak E, Argikar U, et al. Tissue-specific, inducible, and hormonal control of the human UDP-glucuronosyltransferase-1 (UGT1) locus. J Biol Chem. 2005 Nov;280(45):37547-57.

192. Nicholson JK. Global systems biology, personalized medicine and molecular epidemiology. Mol Syst Biol. 2006 Oct;2:52-58.

193. Crockford DJ, Maher AD, Ahmadi KR, Barrett A, Plumb RS, Wilson ID, et al. ^{1}H NMR and UPLC-MS(E) statistical heterospectroscopy: characterization of drug metabolites (xenometabolome) in epidemiological studies. Anal Chem. 2008 Sep;80(18):6835-44.

194. Elstein D, Dweck A, Attias D, Hadas-Halpern I, Zevin S, Altarescu G, et al. Oral maintenance clinical trial with miglustat for type I Gaucher disease: switch from or combination with intravenous enzyme replacement. Blood. 2007 Oct;110(7):2296-301.

195. Kuter DJ, Mehta A, Hollak CE, Giraldo P, Hughes D, Belmatoug N, et al. Miglustat therapy in type 1 Gaucher disease: clinical and safety outcomes in a multicenter retrospective cohort study. Blood Cells Mol Dis. 2013 Aug;51(2):116-24.

196. Patterson MC, Vecchio D, Jacklin E, Abel L, Chadha-Boreham H, Luzy C, et al. Long-term miglustat therapy in children with Niemann-Pick disease type C. 2010 Mar;25:300-5.

197. Iturriaga C, Pineda M, Fernandez-Valero EM, Vanier MT, Coll MJ. Niemann-Pick C disease in Spain: clinical spectrum and development of a disability scale. J Neurol Sci. 2006 Nov;249(1):1-6.

198. Elstein D, Hollak C, Aerts JM, van Weely S, Maas M, Cox TM, et al. Sustained therapeutic effects of oral miglustat (Zavesca, N-butyldeoxynojirimycin, OGT 918) in type I Gaucher disease. J Inherit Metab Dis. 2004 Nov;27(6):757-66.

199. Santos ML, Raskin S, Telles DS, Lohr A,Jr, Liberalesso PB, Vieira SC, et al. Treatment of a child diagnosed with Niemann-Pick disease type C with miglustat: a case report in Brazil. J Inherit Metab Dis. 2008 Dec;31 Suppl 2:S357-61.

200. Chien YH, Lee NC, Tsai LK, Huang AC, Peng SF, Chen SJ, et al. Treatment of Niemann-Pick disease type C in two children with miglustat: initial responses and maintenance of effects over 1 year. J Inherit Metab Dis. 2007 Oct;30(5):826.

201. Platt FM, Boland B, van der Spoel AC. The cell biology of disease: lysosomal storage disorders: the cellular impact of lysosomal dysfunction. J Cell Biol. 2012 Nov;199(5):723-34.

202. Rosenbaum AI, Maxfield FR. Niemann-Pick type C disease: molecular mechanisms and potential therapeutic approaches. J Neurochem. 2011 Mar;116(5):789-95.

203. Engelke UF, Liebrand-van Sambeek ML, de Jong JG, Leroy JG, Morava E, Smeitink JA, et al. N-acetylated metabolites in urine: proton nuclear magnetic resonance spectroscopic study on patients with inborn errors of metabolism. Clin Chem. 2004 Jan;50(1):58-66.

204. Aerts JM, Hollak CE, Boot RG, Groener JE, Maas M. Substrate reduction therapy of glycosphingolipid storage disorders. J Inherit Metab Dis. 2006 Apr-Jun;29(2-3):449-56.

205. Lopez ME, Klein AD, Hong J, Dimbil UJ, Scott MP. Neuronal and epithelial cell rescue resolves chronic systemic inflammation in the lipid storage disorder Niemann-Pick C. Hum Mol Genet. 2012 Jul;21(13):2946-60.

206. Merrifield CA, Lewis M, Claus SP, Beckonert OP, Dumas ME, Duncker S, et al. A metabolic system-wide characterisation of the pig: a model for human physiology. Mol Biosyst. 2011 Sep;7(9):2577-88.

207. Soininen P, Kangas AJ, Wurtz P, Tukiainen T, Tynkkynen T, Laatikainen R, et al. High-throughput serum NMR metabonomics for cost-effective holistic studies on systemic metabolism. Analyst. 2009 Sep;134(9):1781-5.

208. Nicholson JK, Foxall PJ, Spraul M, Farrant RD, Lindon JC. 750 MHz ^{1}H and ^{1}H-^{13}C NMR spectroscopy of human blood plasma. Anal Chem. 1995 Mar;67(5):793-811.

209. Barton RH, Waterman D, Bonner FW, Holmes E, Clarke R, Procardis Consortium, et al. The influence of EDTA and citrate anticoagulant addition to human plasma on information recovery from NMR-based metabolic profiling studies. Mol Biosyst. 2010 Jan;6(1):215-24.

210. Sidhu D, Naugler C. Fasting time and lipid levels in a community-based population: a cross-sectional study. Arch Intern Med. 2012 Dec;172(22):1707-10.

211. te Vruchte D, Lloyd-Evans E, Veldman RJ, Neville DC, Dwek RA, Platt FM, et al. Accumulation of glycosphingolipids in Niemann-Pick C disease disrupts endosomal transport. J Biol Chem. 2004 Jun;279(25):26167-75.

212. Waters NJ, Holmes E, Williams A, Waterfield CJ, Farrant RD, Nicholson JK. NMR and pattern recognition studies on the time-related metabolic effects of alpha-naphthylisothiocyanate on liver, urine, and plasma in the rat: an integrative metabonomic approach. Chem Res Toxicol. 2001 Oct;14(10):1401-12.

213. Smilde AK, Jansen JJ, Hoefsloot HC, Lamers RJ, van der Greef J, Timmerman ME. ANOVA-simultaneous component analysis (ASCA): a new tool for analyzing designed metabolomics data. Bioinformatics. 2005 May;21(13):3043-8.

214. Townsend DM, Tew KD, Tapiero H. The importance of glutathione in human disease. Biomed Pharmacother. 2003 May-Jun;57(3-4):145-55.

215. Schafer FQ, Buettner GR. Redox environment of the cell as viewed through the redox state of the glutathione disulfide/glutathione couple. Free Radic Biol Med. 2001 Jun;30(11):1191-212.

216. Fan TW, Lane AN, Higashi RM, Farag MA, Gao H, Bousamra M, et al. Altered regulation of metabolic pathways in human lung cancer discerned by (13)C stable isotope-resolved metabolomics (SIRM). Mol Cancer. 2009 Jun;8:41,4598-8-41.

217. Fan TW, Lane AN. NMR-based stable isotope resolved metabolomics in systems biochemistry. J Biomol NMR. 2011 Apr;49(3-4):267-80.

218. Diaz-Uriarte R, Alvarez de Andres S. Gene selection and classification of microarray data using random forest. BMC Bioinformatics. 2006 Jan;7(1):1-13.

219. Saeys Y, Inza I, Larranaga P. A review of feature selection techniques in bioinformatics. 2007 Aug;23:2507-17.

220. Hastie T, Tibshirani R, Friedman J. The Elements of Statistical Learning: Data Mining, Inference and Prediction. 2nd ed. New York (USA): Springer-Verlag; 2009.

221. Bertini I, Luchinat C, Miniati M, Monti S, Tenori L. Phenotyping COPD by ^{1}H NMR metabolomics of exhaled breath condensate. Metabolomics. 2014 Apr;10(2):302-11.

222. Smolinska A, Klaassen EM, Dallinga JW, van de Kant KD, Jobsis Q, Moonen EJ, et al. Profiling of volatile organic compounds in exhaled breath as a strategy to find early predictive signatures of asthma in children. PLoS One. 2014 Apr;9(4):e95668.

223. Bureau A, Dupuis J, Hayward B, Falls K, Van Eerdewegh P. Mapping complex traits using Random Forests. BMC Genet. 2003 Dec;4 Suppl 1:S64.

224. Strobl C, Boulesteix AL, Zeileis A, Hothorn T. Bias in random forest variable importance measures: illustrations, sources and a solution. BMC Bioinform. 2007 Jan;8(1):1-25.

225. Bao L, Cui Y. Prediction of the phenotypic effects of non-synonymous single nucleotide polymorphisms using structural and evolutionary information. Bioinformatics. 2005 May;21(10):2185-90.

226. Genuer R, Poggi JM, Tuleau-Malot C. Variable selection using random forests. Pattern Recogn Lett. 2010 Oct;31(14):2225-36.

227. Hara N, Yamada K, Shibata T, Osago H, Hashimoto T, Tsuchiya M. Elevation of cellular NAD levels by nicotinic acid and involvement of nicotinic acid phosphoribosyltransferase in human cells. J Biol Chem. 2007 Aug;282(34):24574-82.

228. Lushchak VI. Glutathione homeostasis and functions: potential targets for medical interventions. J Amino Acids. 2012 Jan;2012:736837.

229. Penke M, Larsen PS, Schuster S, Dall M, Jensen BA, Gorski T, et al. Hepatic NAD salvage pathway is enhanced in mice on a high-fat diet. Mol Cell Endocrinol. 2015 Sep;412:65-72.

230. Chang WC, Jia H, Aw W, Saito K, Hasegawa S, Kato H. Beneficial effects of soluble dietary Jerusalem artichoke (Helianthus tuberosus) in the prevention of the onset of type 2 diabetes and non-alcoholic fatty liver disease in high-fructose diet-fed rats. Br J Nutr. 2014 Sep;112(5):709-17.

231. Kukla M, Ciupinska-Kajor M, Kajor M, Wylezol M, Zwirska-Korczala K, Hartleb M, et al. Liver visfatin expression in morbidly obese patients with nonalcoholic fatty liver disease undergoing bariatric surgery. Pol J Pathol. 2010;61(3):147-53.

232. Koliaki C, Roden M. Hepatic energy metabolism in human diabetes mellitus, obesity and non-alcoholic fatty liver disease. Mol Cell Endocrinol. 2013 Oct;379(1-2):35-42.

233. Jelinek DA, Maghsoodi B, Borbon IA, Hardwick RN, Cherrington NJ, Erickson RP. Genetic variation in the mouse model of Niemann Pick C1 affects female, as well as male, adiposity, and hepatic bile transporters but has indeterminate effects on caveolae. Gene. 2012 Jan;491(2):128-34.

234. Magni G, Amici A, Emanuelli M, Orsomando G, Raffaelli N, Ruggieri S. Enzymology of NAD+ homeostasis in man. Cell Mol Life Sci. 2004 Jan;61(1):19-34.

235. Moffett JR, Namboodiri MA. Tryptophan and the immune response. Immunol Cell Biol. 2003 Aug;81(4):247-65.

236. Guillemin GJ, Kerr SJ, Smythe GA, Smith DG, Kapoor V, Armati PJ, et al. Kynurenine pathway metabolism in human astrocytes: a paradox for neuronal protection. J Neurochem. 2001 Aug;78(4):842-53.

237. Lee MC, Ting KK, Adams S, Brew BJ, Chung R, Guillemin GJ. Characterisation of the expression of NMDA receptors in human astrocytes. PLoS One. 2010 Nov;5(11):e14123.

238. Braidy N, Grant R, Adams S, Brew BJ, Guillemin GJ. Mechanism for quinolinic acid cytotoxicity in human astrocytes and neurons. Neurotox Res. 2009 Jul;16(1):77-86.

239. Pierozan P, Goncalves Fernandes C, Ferreira F, Pessoa-Pureur R. Acute intrastriatal injection of quinolinic acid provokes long-lasting misregulation of the cytoskeleton in the striatum, cerebral cortex and hippocampus of young rats. Brain Res. 2014 Aug;1577:1-10.

240. Maddison DC, Giorgini F. The kynurenine pathway and neurodegenerative disease. Semin Cell Dev Biol. 2015 Apr;40:134-41.

241. Guillemin GJ, Smith DG, Smythe GA, Armati PJ, Brew BJ. Expression of the kynurenine pathway enzymes in human microglia and macrophages. Adv Exp Med Biol. 2003;527:105-12.

242. Speciale C, Schwarcz R. On the production and disposition of quinolinic acid in rat brain and liver slices. J Neurochem. 1993 Jan;60(1):212-8.

243. Saito K, Fujigaki S, Heyes MP, Shibata K, Takemura M, Fujii H, et al. Mechanism of increases in L-kynurenine and quinolinic acid in renal insufficiency. Am J Physiol Renal Physiol. 2000 Sep;279(3):F565-72.

244. Chen S, Burton C, Kaczmarek A, Shi H, Ma Y. Simultaneous determination of urinary quinolinate, gentisate, 4-hydroxybenzoate, and α-ketoglutarate by high-performance liquid chromatography-tandem mass spectrometry. Anal Methods. 2015 Jul;7:6572-8.

245. Kim K, Taylor SL, Ganti S, Guo L, Osier MV, Weiss RH. Urine metabolomic analysis identifies potential biomarkers and pathogenic pathways in kidney cancer. OMICS. 2011 May;15(5):293-303.

246. Zeden JP, Fusch G, Holtfreter B, Schefold JC, Reinke P, Domanska G, et al. Excessive tryptophan catabolism along the kynurenine pathway precedes ongoing sepsis in critically ill patients. Anaesth Intensive Care. 2010 Mar;38(2):307-16.

247. Ramirez CM, Lopez AM, Le LQ, Posey KS, Weinberg AG, Turley SD. Ontogenic changes in lung cholesterol metabolism, lipid content, and histology in mice with Niemann-Pick type C disease. Biochim Biophys Acta. 2014 Jan;1841(1):54-61.

248. Lahdou I, Sadeghi M, Oweira H, Fusch G, Daniel V, Mehrabi A, et al. Increased serum levels of quinolinic acid indicate enhanced severity of hepatic dysfunction in patients with liver cirrhosis. Hum Immunol. 2013 Jan;74(1):60-6.

249. Garver WS, Jelinek D, Meaney FJ, Flynn J, Pettit KM, Shepherd G, et al. The National Niemann-Pick Type C1 Disease Database: correlation of lipid profiles, mutations, and biochemical phenotypes. J Lipid Res. 2010 Feb;51(2):406-15.

250. Choi HY, Karten B, Chan T, Vance JE, Greer WL, Heidenreich RA, et al. Impaired ABCA1-dependent lipid efflux and hypoalphalipoproteinemia in human Niemann-Pick type C disease. J Biol Chem. 2003 Aug;278(35):32569-77.

251. De Meyer T, Sinnaeve D, Van Gasse B, Rietzschel ER, De Buyzere ML, Langlois MR, et al. Evaluation of standard and advanced preprocessing methods for the univariate analysis of blood serum ^{1}H-NMR spectra. Anal Bioanal Chem. 2010 Oct;398(4):1781-90.

252. Probert F, Rice P, Scudamore CL, Wells S, Williams R, Hough TA, et al. ^{1}H NMR metabolic profiling of plasma reveals additional phenotypes in knockout mouse models. J Proteome Res. 2015 May;14(5):2036-45.

253. Ganji SH, Tavintharan S, Zhu D, Xing Y, Kamanna VS, Kashyap ML. Niacin non-competitively inhibits DGAT2 but not DGAT1 activity in HepG2 cells. J Lipid Res. 2004 Oct;45:1835-45.

254. Kamanna VS, Kashyap ML. Nicotinic acid (niacin) receptor agonists: will they be useful therapeutic agents? Am J Cardiol. 2007 Dec;100(11 A):S53-61.

255. Schaefer EJ, Kay LL, Zech LA, Brewer HB,Jr. Tangier disease. High density lipoprotein deficiency due to defective metabolism of an abnormal apolipoprotein A-i (ApoA-ITangier). J Clin Invest. 1982 Nov;70(5):934-45.

256. Ginsberg HN, Le NA, Short MP, Ramakrishnan R, Desnick RJ. Suppression of apolipoprotein B production during treatment of cholesteryl ester storage disease with lovastatin. Implications for regulation of apolipoprotein B synthesis. J Clin Invest. 1987 Dec;80(6):1692-7.

257. Puzo J, Alfonso P, Irun P, Gervas J, Pocovi M, Giraldo P. Changes in the atherogenic profile of patients with type 1 Gaucher disease after miglustat therapy. Atherosclerosis. 2010 Apr;209(2):515-9.

258. Sechi A, Dardis A, Zampieri S, Rabacchi C, Zanoni P, Calandra S, et al. Effects of miglustat treatment in a patient affected by an atypical form of Tangier disease. Orphanet J Rare Dis. 2014 Sep9:143-50,

259. Thomas C, Pellicciari R, Pruzanski M, Auwerx J, Schoonjans K. Targeting bile-acid signalling for metabolic diseases. Nat Rev Drug Discov. 2008 Aug;7(8):678-93.

260. Lepercq P, Gerard P, Beguet F, Raibaud P, Grill JP, Relano P, et al. Epimerization of chenodeoxycholic acid to ursodeoxycholic acid by Clostridium baratii isolated from human feces. FEMS Microbiol Lett. 2004 Jun;235(1):65-72.

261. Kakiyama G, Ogawa S, Iida T, Fujimoto Y, Mushiake K, Goto T, et al. Nuclear magnetic resonance spectroscopy of 3 beta,7 beta-dihydroxy-5-cholen-24-oic acid multi-conjugates: unusual bile acid metabolites in human urine. Chem Phys Lipids. 2006 Apr;140(1-2):48-54.

262. Maekawa M, Misawa Y, Sotoura A, Yamaguchi H, Togawa M, Ohno K, et al. LC/ESI-MS/MS analysis of urinary 3beta-sulfooxy-7beta-N-acetylglucosaminyl-5-cholen-24-oic acid and its amides: new biomarkers for the detection of Niemann-Pick type C disease. Steroids. 2013 Oct;78(10):967-72.

263. Alvelius G, Hjalmarson O, Griffiths WJ, Bjorkhem I, Sjovall J. Identification of unusual 7-oxygenated bile acid sulfates in a patient with Niemann-Pick disease, type C. J Lipid Res. 2001 Oct;42(10):1571-7.

264. Garver WS, Francis GA, Jelinek D, Shepherd G, Flynn J, Castro G, et al. The National Niemann-Pick C1 disease database: report of clinical features and health problems. 2007 Jun;143A:1204-11.

265. Zarowski M, Steinborn B, Gurda B, Dvorakova L, Vlaskova H, Kothare SV. Treatment of cataplexy in Niemann-Pick disease type C with the use of miglustat. Eur J Paediatr Neurol. 2011 Jan;15(1):84-7.

266. Eisner R, Stretch C, Eastman T, Xia J, Hau D, Damaraju S, et al. Learning to predict cancer-associated skeletal muscle wasting from 1H-NMR profiles of urinary metabolites. Metabolomics. 2011;7(1):25-34.

267. Tom A, Nair KS. Assessment of branched-chain amino Acid status and potential for biomarkers. J Nutr. 2006 Jan;136(1 Suppl):324S-30S.

268. Pollitt RJ, Green A, Smith R. Excessive excretion of beta-alanine and of 3-hydroxypropionic, R- and S-3-aminoisobutyric, R- and S-3-hydroxyisobutyric and S-2-(hydroxymethyl)butyric acids probably due to a defect in the metabolism of the corresponding malonic semialdehydes. J Inherit Metab Dis. 1985;8(2):75-9.

269. Gartler SM. A metabolic investigation of urinary β-aminoisobutyric acid excretion in man. Arch Biochem Biophys. 1959 Feb;80(2):400-9.

270. Stumvoll M, Perriello G, Meyer C, Gerich J. Role of glutamine in human carbohydrate metabolism in kidney and other tissues. Kidney Int. 1999 Mar;55(3):778-92.

271. Lochs H, Roth E, Gasic S, Hubl W, Morse EL, Adibi SA. Splanchnic, renal, and muscle clearance of alanylglutamine in man and organ fluxes of alanine and glutamine when infused in free and peptide forms. Metabolism. 1990 Aug;39(8):833-6.

272. Gu H, Pan Z, Xi B, Hainline BE, Shanaiah N, Asiago V, et al. 1H NMR metabolomics study of age profiling in children. NMR Biomed. 2009 Oct;22(8):826-33.

273. Cummings JH, Englyst HN. Fermentation in the human large intestine and the available substrates. Am J Clin Nutr. 1987 May;45(5 Suppl):1243-55.

274. Stein TP, Koerner B, Schluter MD, Leskiw MJ, Gaprindachvilli T, Richards EW, et al. Weight loss, the gut and the inflammatory response in aids patients. Cytokine. 1997 Feb;9(2):143-7.

275. Louis P, Scott KP, Duncan SH, Flint HJ. Understanding the effects of diet on bacterial metabolism in the large intestine. J Appl Microbiol. 2007 May;102(5):1197-208.

276. Zhang AQ, Mitchell SC, Smith RL. Dietary precursors of trimethylamine in man: a pilot study. Food Chem Toxicol. 1999 May;37(5):515-20.

277. Dumas ME, Barton RH, Toye A, Cloarec O, Blancher C, Rothwell A, et al. Metabolic profiling reveals a contribution of gut microbiota to fatty liver phenotype in insulin-resistant mice. PNAS. 2006 Aug;103(33):12511-6.

278. Jiang XC, Li Z, Liu R, Yang XP, Pan M, Lagrost L, et al. Phospholipid transfer protein deficiency impairs apolipoprotein-B secretion from hepatocytes by stimulating a proteolytic pathway through a relative deficiency of vitamin E and an increase in intracellular oxidants. J Biol Chem. 2005 May;280(18):18336-40.

279. Dongowski G, Lorenz A, Anger H. Degradation of pectins with different degrees of esterification by Bacteroides thetaiotaomicron isolated from human gut flora. Appl Environ Microbiol. 2000 Apr;66(4):1321-7.

280. Lindinger W, Taucher J, Jordan A, Hansel A, Vogel W. Endogenous production of methanol after the consumption of fruit. Alcohol Clin Exp Res. 1997 Aug;21(5):939-43.

281. Schicho R, Shaykhutdinov R, Ngo J, Nazyrova A, Schneider C, Panaccione R, et al. Quantitative Metabolomic Profiling of Serum, Plasma, and Urine by ^{1}H NMR Spectroscopy Discriminates between Patients with Inflammatory Bowel Disease and Healthy Individuals. J Proteome Res. 2012 May;11(6):3344-57.

282. Osborne DL, Seidel ER. Gastrointestinal luminal polyamines: cellular accumulation and enterohepatic circulation. Am J Physiol. 1990 Apr;258(4 Pt 1):G576-84.

283. Lin HM, Barnett MP, Roy NC, Joyce NI, Zhu S, Armstrong K, et al. Metabolomic analysis identifies inflammatory and noninflammatory metabolic effects of genetic modification in a mouse model of Crohn's disease. J Proteome Res. 2010 Apr;9(4):1965-75.

284. Schwerd T, Pandey S, Yang HT, Bagola K, Jameson E, Jung J, et al. Impaired antibacterial autophagy links granulomatous intestinal inflammation in Niemann-Pick disease type C1 and XIAP deficiency with NOD2 variants in Crohn's disease. Gut. 2016 Mar;0:1-14.

285. Khor B, Gardet A, Xavier RJ. Genetics and pathogenesis of inflammatory bowel disease. Nature. 2011 Jun;474(7351):307-17.

286. Hugot JP, Chamaillard M, Zouali H, Lesage S, Cezard JP, Belaiche J, et al. Association of NOD2 leucine-rich repeat variants with susceptibility to Crohn's disease. Nature. 2001 May;411(6837):599-603.

287. Yazdanyar S, Kamstrup PR, Tybjaerg-Hansen A, Nordestgaard BG. Penetrance of NOD2/CARD15 genetic variants in the general population. CMAJ. 2010 Apr;182(7):661-5.

288. Prior RL, Rogers TR, Khanal RC, Wilkes SE, Wu X, Howard LR. Urinary excretion of phenolic acids in rats fed cranberry. J Agric Food Chem. 2010 Apr;58(7):3940-9.

289. Konishi Y. Transepithelial transport of microbial metabolites of quercetin in intestinal Caco-2 cell monolayers. J Agric Food Chem. 2005 Feb;53(3):601-7.

290. Marin L, Miguelez EM, Villar CJ, Lombo F. Bioavailability of dietary polyphenols and gut microbiota metabolism: antimicrobial properties. Biomed Res Int. 2015 Feb;2015:905215.

291. Lord RS, Bralley JA. Clinical applications of urinary organic acids. Part 2. Dysbiosis markers. Altern Med Rev. 2008 Dec;13(4):292-306.

292. Mardinoglu A, Shoaie S, Bergentall M, Ghaffari P, Zhang C, Larsson E, et al. The gut microbiota modulates host amino acid and glutathione metabolism in mice. Mol Syst Biol. 2015 Oct;11(10):834.

293. Tint GS, Pentchev P, Xu G, Batta AK, Shefer S, Salen G, et al. Cholesterol and oxygenated cholesterol concentrations are markedly elevated in peripheral tissue but not in brain from mice with the Niemann–Pick type C phenotype. J Inherit Metab Dis. 1998 Dec;21(8):853-63.

294. Vazquez MC, del Pozo T, Robledo FA, Carrasco G, Pavez L, Olivares F, et al. Alteration of gene expression profile in Niemann-Pick type C mice correlates with tissue damage and oxidative stress. PLoS One. 2011 Dec;6(12):e28777.

295. Cabre M, Camps J, Paternain JL, Ferre N, Joven J. Time-course of changes in hepatic lipid peroxidation and glutathione metabolism in rats with carbon tetrachloride-induced cirrhosis. Clin Exp Pharmacol Physiol. 2000 Sep;27(9):694-9.

296. Soga T, Sugimoto M, Honma M, Mori M, Igarashi K, Kashikura K, et al. Serum metabolomics reveals gamma-glutamyl dipeptides as biomarkers for discrimination among different forms of liver disease. J Hepatol. 2011 Oct;55(4):896-905.

297. Fu R, Wassif CA, Yanjanin NM, Watkins-Chow DE, Baxter LL, Incao A, et al. Efficacy of N-acetylcysteine in phenotypic suppression of mouse models of Niemann-Pick disease, type C1. Hum Mol Genet. 2013 Sep;22(17):3508-23.

298. Parasassi T, Brunelli R, Costa G, De Spirito M, Krasnowska E, Lundeberg T, et al. Thiol redox transitions in cell signaling: a lesson from N-acetylcysteine. ScientificWorldJournal. 2010 Jun;10:1192-202.

299. Wu YP, Mizukami H, Matsuda J, Saito Y, Proia RL, Suzuki K. Apoptosis accompanied by up-regulation of TNF-alpha death pathway genes in the brain of Niemann-Pick type C disease. Mol Genet Metab. 2005 Jan;84(1):9-17.

300. Fontana M, Giovannitti F, Pecci L. The protective effect of hypotaurine and cysteine sulphinic acid on peroxynitrite-mediated oxidative reactions. Free Radic Res. 2008 Apr;42(4):320-30.

301. Porter FD, Scherrer DE, Lanier MH, Langmade SJ, Molugu V, Gale SE, et al. Cholesterol oxidation products are sensitive and specific blood-based biomarkers for Niemann-Pick C1 disease. Sci Transl Med. 2010 Nov;2(56):56ra81.

302. Sakuragawa T, Hishiki T, Ueno Y, Ikeda S, Soga T, Yachie-Kinoshita A, et al. Hypotaurine is an energy-saving hepatoprotective compound against ischemia-reperfusion injury of the rat liver. J Clin Biochem Nutr. 2010 Mar;46(2):126-34.

303. Rimkunas VM, Graham MJ, Crooke RM, Liscum L. TNF-{alpha} plays a role in hepatocyte apoptosis in Niemann-Pick type C liver disease. J Lipid Res. 2009 Feb;50(2):327-33.

304. Rimkunas VM, Graham MJ, Crooke RM, Liscum L. In vivo antisense oligonucleotide reduction of NPC1 expression as a novel mouse model for Niemann Pick type C- associated liver disease. Hepatology. 2008 May;47(5):1504-12.

305. Friedman SL. Liver fibrosis -- from bench to bedside. J Hepatol. 2003;38 Suppl 1:S38-53.

306. Pinzani M, Rombouts K, Colagrande S. Fibrosis in chronic liver diseases: diagnosis and management. J Hepatol. 2005;42 Suppl(1):S22-36.

307. Dezortova M, Taimr P, Skoch A, Spicak J, Hajek M. Etiology and functional status of liver cirrhosis by ^{31}P MR spectroscopy. World J Gastroenterol. 2005 Nov;11(44):6926-31.

308. Kuriyama S, Yokoyama F, Inoue H, Takano J, Ogawa M, Kita Y, et al. Sequential assessment of the intrahepatic expression of epidermal growth factor and transforming growth factor-beta1 in hepatofibrogenesis of a rat cirrhosis model. Int J Mol Med. 2007 Feb;19(2):317-24.

309. Toyoki Y, Sasaki M, Narumi S, Yoshihara S, Morita T, Konn M. Semiquantitative evaluation of hepatic fibrosis by measuring tissue hydroxyproline. Hepatogastroenterology. 1998 Nov-Dec;45(24):2261-4.

310. Waters NJ, Waterfield CJ, Farrant RD, Holmes E, Nicholson JK. Metabonomic deconvolution of embedded toxicity: application to thioacetamide hepato- and nephrotoxicity. Chem Res Toxicol. 2005 Apr;18(4):639-54.

311. Ledda-Columbano GM, Coni P, Curto M, Giacomini L, Faa G, Oliverio S, et al. Induction of two different modes of cell death, apoptosis and necrosis, in rat liver after a single dose of thioacetamide. Am J Pathol. 1991 Nov;139(5):1099-109.

312. Sun F, Hayami S, Ogiri Y, Haruna S, Tanaka K, Yamada Y, et al. Evaluation of oxidative stress based on lipid hydroperoxide, vitamin C and vitamin E during apoptosis and necrosis caused by thioacetamide in rat liver. Biochim Biophys Acta. 2000 Feb;1500(2):181-5.

313. Constantinou MA, Theocharis SE, Mikros E. Application of metabonomics on an experimental model of fibrosis and cirrhosis induced by thioacetamide in rats. Toxicol Appl Pharmacol. 2007 Jan;218(1):11-9.

314. Rajendra W, Prasad GV, Indira K. Deviations in hepatic amino acid profiles of mouse following repeated hexachlorophene administration. J Environ Sci Health B. 1988 Aug;23(4):409-26.

315. Robenek H, Meiss R, Themann H, Hulsbusch R. Thin section and freeze-fracture studies of hexachlorophene induced alterations in the rat liver with special regard to intercellular junctions. Exp Pathol (Jena). 1980;18(5):257-68.

316. Ishigure K, Shimomura Y, Murakami T, Kaneko T, Takeda S, Inoue S, et al. Human liver disease decreases methacrylyl-CoA hydratase and beta-hydroxyisobutyryl-CoA hydrolase activities in valine catabolism. Clin Chim Acta. 2001 Oct;312(1-2):115-21.

317. Mato JM, Martinez-Chantar ML, Lu SC. Methionine metabolism and liver disease. Annu Rev Nutr. 2008 Mar;28:273-93.

318. Hutson SM, Sweatt AJ, Lanoue KF. Branched-chain [corrected] amino acid metabolism: implications for establishing safe intakes. J Nutr. 2005 Jun;135(6 Suppl):1557S-64S.

319. Varela-Rey M, Martinez-Lopez N, Fernandez-Ramos D, Embade N, Calvisi DF, Woodhoo A, et al. Fatty liver and fibrosis in glycine N-methyltransferase knockout mice is prevented by nicotinamide. Hepatology. 2010 Jul;52(1):105-14.

320. Mazagova M, Wang L, Anfora AT, Wissmueller M, Lesley SA, Miyamoto Y, et al. Commensal microbiota is hepatoprotective and prevents liver fibrosis in mice. FASEB J. 2015 Mar;29(3):1043-55.

321. Boenzi S, Deodato F, Taurisano R, Martinelli D, Verrigni D, Carrozzo R, et al. A new simple and rapid LC-ESI-MS/MS method for quantification of plasma oxysterols as

dimethylaminobutyrate esters. Its successful use for the diagnosis of Niemann-Pick type C disease. Clin Chim Acta. 2014 Nov;437:93-100.

322. Klinke G, Rohrbach M, Giugliani R, Burda P, Baumgartner MR, Tran C, et al. LC-MS/MS based assay and reference intervals in children and adolescents for oxysterols elevated in Niemann-Pick diseases. Clin Biochem. 2015 Jun;48(9):596-602.

323. Pajares S, Arias A, Garcia-Villoria J, Macias-Vidal J, Ros E, de las Heras J, et al. Cholestane-3beta,5alpha,6beta-triol: high levels in Niemann-Pick type C, cerebrotendinous xanthomatosis, and lysosomal acid lipase deficiency. J Lipid Res. 2015 Oct;56(10):1926-35.

324. Polo G, Burlina A, Furlan F, Kolamunnage T, Cananzi M, Giordano L, et al. High level of oxysterols in neonatal cholestasis: a pitfall in analysis of biochemical markers for Niemann-Pick type C disease. Clin Chem Lab Med. 2015 Dec; 9.

325. Welford RW, Garzotti M, Marques Lourenco C, Mengel E, Marquardt T, Reunert J, et al. Plasma lysosphingomyelin demonstrates great potential as a diagnostic biomarker for Niemann-Pick disease type C in a retrospective study. PLoS One. 2014 Dec;9(12):e114669.

326. Dodelson de Kremer R, Paschini de Capra A, Angaroni CJ, Giner de Ayala A. Plasma chitotriosidase activity in Argentinian patients with Gaucher disease, various lysosomal diseases and other inherited metabolic disorders. Medicina (B Aires). 1997;57(6):677-84.

327. Sheth JJ, Sheth FJ, Oza NJ, Gambhir PS, Dave UP, Shah RC. Plasma chitotriosidase activity in children with lysosomal storage disorders. Indian J Pediatr. 2010 Feb;77(2):203-5.

328. Guo Y, He W, Boer AM, Wevers RA, de Bruijn AM, Groener JE, et al. Elevated plasma chitotriosidase activity in various lysosomal storage disorders. J Inherit Metab Dis. 1995;18(6):717-22.

329. Hollak CE, van Weely S, van Oers MH, Aerts JM. Marked elevation of plasma chitotriosidase activity. A novel hallmark of Gaucher disease. J Clin Invest. 1994 Mar;93(3):1288-92.

330. Ries M, Schaefer E, Luhrs T, Mani L, Kuhn J, Vanier MT, et al. Critical assessment of chitotriosidase analysis in the rational laboratory diagnosis of children with Gaucher disease and Niemann-Pick disease type A/B and C. J Inherit Metab Dis. 2006 Oct;29(5):647-52.

331. Michelakakis H, Dimitriou E, Labadaridis I. The expanding spectrum of disorders with elevated plasma chitotriosidase activity: an update. J Inherit Metab Dis. 2004 Sep;27(5):705-6.

332. Palmer C, Bik EM, DiGiulio DB, Relman DA, Brown PO. Development of the human infant intestinal microbiota. PLoS Biol. 2007 Jul;5(7):e177.

333. Favier CF, Vaughan EE, De Vos WM, Akkermans ADL. Molecular monitoring of succession of bacterial communities in human neonates. Appl Environ Microbiol. 2002 Jan;68(1):219-26.